NASA TECHNICAL MEMORANDUM

NASA TM X-2508

NASA TM X-2508

SPACE SHUTTLE AEROTHERMODYNAMICS TECHNOLOGY CONFERENCE

Volume III - Aerodynamics

Held at
Ames Research Center
Moffett Field, California
December 15-16, 1971

NATIONAL AERONAUTICS AND SPACE ADMINISTRATION • WASHINGTON, D. C. • FEBRUARY 1972

1. Report No.	2. Government Accession No.	3. Recipient's Catalog No.
NASA TM X-2508		

4. Title and Subtitle	5. Report Date
SPACE SHUTTLE AEROTHERMODYNAMICS TECHNOLOGY CONFERENCE VOLUME III - AERODYNAMICS	February 1972
	6. Performing Organization Code
7. Author(s)	8. Performing Organization Report No. L-8136
9. Performing Organization Name and Address NASA Langley Research Center Hampton, Va. 23365	10. Work Unit No.
	11. Contract or Grant No.
12. Sponsoring Agency Name and Address National Aeronautics and Space Administration Washington, D.C. 20546	13. Type of Report and Period Covered Technical Memorandum
	14. Sponsoring Agency Code

15. Supplementary Notes

Held at NASA Ames Research Center, December 15-16, 1971.

16. Abstract

The conference encompasses four technology efforts, each published as a separate volume.

Volume I - Flow Fields (NASA TM X-2506)

Volume II - Heating (NASA TM X-2507)

Volume III - Aerodynamics (NASA TM X-2508)

Volume IV - Operational Flight Mechanics (NASA TM X-2509)

17. Key Words (Suggested by Author(s))	18. Distribution Statement
Flow fields Heating Aerodynamics Operational flight mechanics Space shuttle Aerothermodynamics	Unclassified - Unlimited

19. Security Classif. (of this report)	20. Security Classif. (of this page)	21. No. of Pages	22. Price*
Unclassified	Unclassified	305	$6.00

*For sale by the National Technical Information Service, Springfield, Virginia 22151

PREFACE

A Space Shuttle Technology Conference on Flow Fields, Heat Transfer, Aerodynamics, and Operational Flight Mechanics was held at the NASA Ames Research Center on December 15 and 16, 1971. The objective of this conference was to review the broad base of aerothermodynamics technology developed for the space shuttle during the period of the Phase B studies and, thereby, help focus attention on the technology required for further space shuttle development. This publication is a compilation of the conference papers. It has been divided into four volumes, one for each of the sessions. Five papers which were omitted from the oral presentation at the conference are included in this publication. Contributing organizations include U.S. Aerospace Contractors, Universities, Canadian and European Space Agencies, in addition to NASA Research Centers.

CONTENTS

VOLUME II.- HEATING

VOLUME III.- AERODYNAMICS

VOLUME IV.- OPERATIONAL FLIGHT MECHANICS

GLOSSARY

ABES	air breathing engines
ACPS	attitude control propulsion system
AEDC	Arnold Engineering Development Center
AFB	air force base
AFFDL	Air Force Flight Dynamics Laboratory
ALT	altitude
APS	auxiliary propulsion system
AR	aspect ratio
ARC	Ames Research Center
ARDC	Air Research and Development Command
BECO	booster engine cutoff
BLOW	booster lift-off weight
BV	body-vertical tail
BW	body-wing
BWV	body-wing-vertical tail
CAL	Cornell Aeronautical Laboratory
CALCS	calculations
CAL HST	Cornell Aeronautical Laboratory hypersonic shock tunnel
CFHT	continuous-flow hypersonic tunnel
CG; C.G.; c.g.	center of gravity
CONFIG	configuration
CRT	cathode ray tube
Cyl	cylinder
2-D	two-dimensional
3-D	three-dimensional

DAC	Douglas Aircraft Company
DCM	data control management
DEX	exit diameter
DIA	diameter
DIAT	diatomic
DIF. REFL.	differential deflection
3DMoC	three-dimensional method of characteristics
DOD	Department of Defense
DOF	degrees of freedom
DWO	delta-wing orbiter
EHT	external hydrogen tank
EOHT	external oxygen-hydrogen tank
EPL	emergency power level
EST	estimated
ETR	eastern test range
F&M	force and moment
FAR; F.A.R.	Federal Aircraft Regulation
FBS	flyback system
F.D.	finite difference
F/O	fuel-oxygen ratio
FO/FS	fail operational/fail safe
FPR	flight performance reserve
FPRE	flat-plate reference enthalpy
FR	fully reusable
FREQ	frequency
GAC	Grumman Aerospace Corporation

GD	General Dynamics
GDC	General Dynamics Corporation
GD/C	General Dynamics/Convair
G.E.	General Electric Company
GLOW	vehicle gross lift-off weight
GTOP	general trajectory optimization program
GW	gross weight
H	hydrogen
HCF	highly compacted fibers
HCR	high cross range
HeT	Mach 20 helium tunnel
HO	hydrogen-oxygen system
H.W.T.	hypersonic wind tunnel
IAC	industrial air center
IBFF	impulse base flow facility
ICD	interface control drawing
IFR	instrument flight rules
ILRV	integral launch and reentry vehicle
ILS	instrument landing system
IND	industrial
IR	infrared
IRAD	Independent Research and Development
KSC	Kennedy Space Center
L.E.	leading edge
LEE	leeward
LH_2	liquid hydrogen

LMSC	Lockheed Missiles & Space Company
LO_2; LOX	liquid oxygen
LRC; LaRC	Langley Research Center
LRU	link retraction unit
MAC	mean aerodynamic chord
MAC Exp	exposed mean aerodynamic chord
MARK I, MARK II	shuttle configurations
MAX	maximum
MC	Monte Carlo
MCAIR	a low-speed wind tunnel
MCAS	Marine Corps Air Station
MDAC	McDonnell Douglas Astronautics Company
MDC	McDonnell Douglas Corporation
MIL SPEC	military specification
MIN	minimum
MM HWT	Martin Marietta Corporation hotshot wind tunnel
MOC	method of characteristics
MPL	minimum power level
MSC	Manned Spacecraft Center
MSFC	Marshall Space Flight Center
MT.	mountain
NA	North American
NAE; N.A.E.	National Aeronautical Establishment
NAR; NARC; NR	North American Rockwell Corporation
NAS	Naval Air Station
NASA	National Aeronautics and Space Administration

NO.; No.	number
NOZ	nozzle
NPL	normal power level
O/F	oxygen-fuel ratio
OLOW	orbiter lift-off weight
OMS	orbiting maneuvering system
P/L	payload
PM	pitching moment
RCC	reinforced carbon carbon
RCS	reaction control system
Ref	reference
REQD	required
RFP	request for porposals
RGAS	real gas
R.H.	right hand engine
RSI	reusable surface insulation
RTV	room-temperature vulcanizing rubber
S&C	stability and control
SCT	shock capturing technique
SF	stick force
S.L.; SL	sea level
SM	service module
SPEC	specification
SRM	solid rocket motors
SS	stainless steel
SSV	space shuttle vehicle
ST	straight

STAR	strings and array computer; self-testing and repair computer
STD	standard
STI	Systems Technology, Incorporated
STOL	short take-off and landing
SW	southwest
SYM	symbol
T/C	thermocouple
T.E.	trailing edge
T.E.D.	trailing edge down
TEMP	temperature
T.E.U.	trailing edge up
THEO	theoretical
TPS	thermal protection system
TRAJ	trajectory
TVC	thrust vector control
Typ	typical
UPWT	Unitary Plan wind tunnel
USAF	U.S. Air Force
VAC HVWT	Vought Aeronautics Company hypervelocity wind tunnel
VAFB	Vandenburg Air Force Base
VDT	variable density tunnel
VFR	visual flight rules
V/STOL	vertical and short take-off and landing
w/o	without
WT	weight
WWD	windward
YM	yawing moment

AERODYNAMICS SESSION

INTRODUCTORY REMARKS OF SESSION CHAIRMAN

By Beverly Z. Henry
NASA Langley Research Center

The session this morning deals primarily with the aerodynamics of complete configurations; it deals with the orbiters and boosters as separate flight vehicles, and with the vehicles mated into the launch vehicle system. The discussions will cover a fairly wide range of aerodynamic considerations dealing with both the static and dynamic characteristics of several concepts.

You will see areas where the situation seems to be fairly well in hand, and we will also wave a few flags as to where additional effort is required.

STATUS OF LANGLEY STUDIES OF AERODYNAMICS AND INTERFERENCE EFFECTS OF TANDEM LAUNCH VEHICLES

By William I. Scallion and Kermit G. Pratt
NASA Langley Research Center

INTRODUCTION

In support of an overall system study of fully reusable tandem launch vehicles at Langley, an experimental and analytical program was initiated recently to investigate the aerodynamic and interference characteristics of several space shuttle launch configurations. The measured gross interference effects of the total configurations and the effects of each component on the other were obtained. The experimental data provide an opportunity to assess the application of a recently acquired analytical program for the calculation of aerodynamic loads on shuttle-type vehicles.

This paper presents some of the aerodynamic and interference effects measured from wind-tunnel tests of three fully reusable space shuttle configurations at transonic and low-supersonic speeds and the status of an assessment of the analytical approach to date. The three configurations tested were a low-fineness-ratio booster combined in tandem with a North American

Rockwell delta-wing orbiter, designated the "low-fineness-ratio configuration," and a phase B shuttle configuration consisting of the North American Rockwell delta-wing orbiter and the General Dynamics/Convair booster, designated the "stage-arrangement configuration," arranged in tandem and in parallel.

The force measurements obtained at a Mach number of 1.5 for the low-fineness-ratio configuration were representative of the transonic and low-supersonic speed ranges where the interference effects are predominant and were used for comparison with values calculated at the same Mach number. This comparison is the basis for a preliminary assessment of the initial application of the analytical approach.

SYMBOLS

$C_{A,min}$	minimum axial-force coefficient
C_m	pitching-moment coefficient
C_{m_α}	pitching-moment-curve slope
C_N	normal-force coefficient
C_{N_α}	normal-force-curve slope
$C_{p,b}$	base pressure coefficient
l	body length
q	dynamic pressure
x_{ac}/l	aerodynamic-center location
α	angle of attack, deg

LOW-FINENESS-RATIO CONFIGURATION

(Figure 1)

The low-fineness-ratio booster arranged in tandem with the North American Rockwell delta-wing orbiter is shown in figure 1. The booster was envisioned as a fully reusable vehicle using liquid hydrogen and liquid oxygen as fuel. Because of the emphasis placed on structural design with a large diameter tank, the booster is shorter than the orbiter. The lifting surfaces of the orbiter are almost equal in area (about 85 percent of the booster wing area) to those of the booster and would be expected to contribute a significant amount of the total vehicle load.

Six-component strain-gage balances were located in each model; the balance in the orbiter measured only the orbiter forces and moments, and the balance in the booster measured the total forces and moments of the combined vehicle. The orbiter measurements were referenced to the orbiter dimensions and to the orbiter launch center of gravity located 65.59 percent of the body length from the nose.

The ascent configuration, or total vehicle, forces and moments are referenced to the booster dimensions and the total-vehicle center of gravity corresponding approximately to the maximum αq condition. The distance between the centers of gravity of the orbiter and total vehicle is about 85 percent of the booster body length.

No interstage fairing was used, since it was assumed that a retractable interstage attachment would be used.

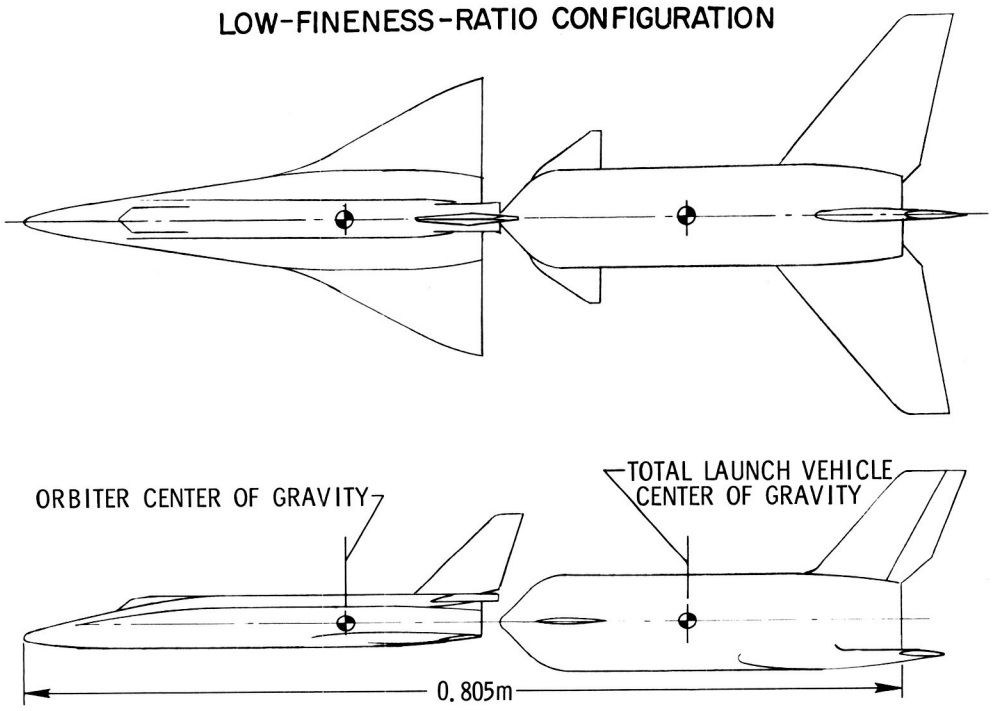
LOW-FINENESS-RATIO CONFIGURATION
ORBITER CENTER OF GRAVITY
TOTAL LAUNCH VEHICLE
CENTER OF GRAVITY
0.805m

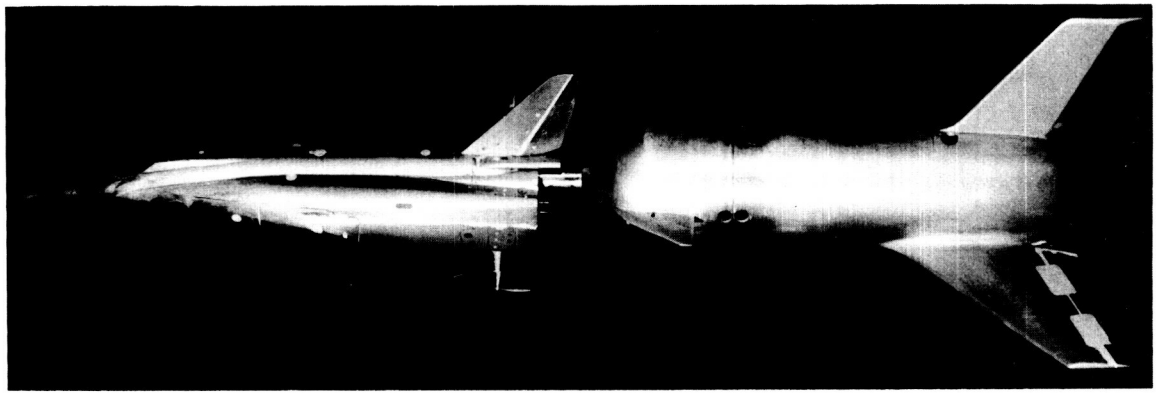

Figure 1

LOW-FINENESS-RATIO BOOSTER MODEL

(Figure 2)

A sketch of the low-fineness-ratio booster model is shown in figure 2. The principal dimensions for the full-scale vehicle and model are given in the table in the figure. The wing is a constant NACA 0012-64 airfoil section from root to tip. The exposed canard area was 6.3 percent of the wing reference area. The spherical segment used as a transition between the conical nose and the cylindrical section of the body enabled the canard to be deflected without unporting the canard root section ahead of the hinge line. The center of gravity indicated on the sketch represents the booster flyback and landing center-of-gravity location.

LOW FINENESS-RATIO BOOSTER MODEL

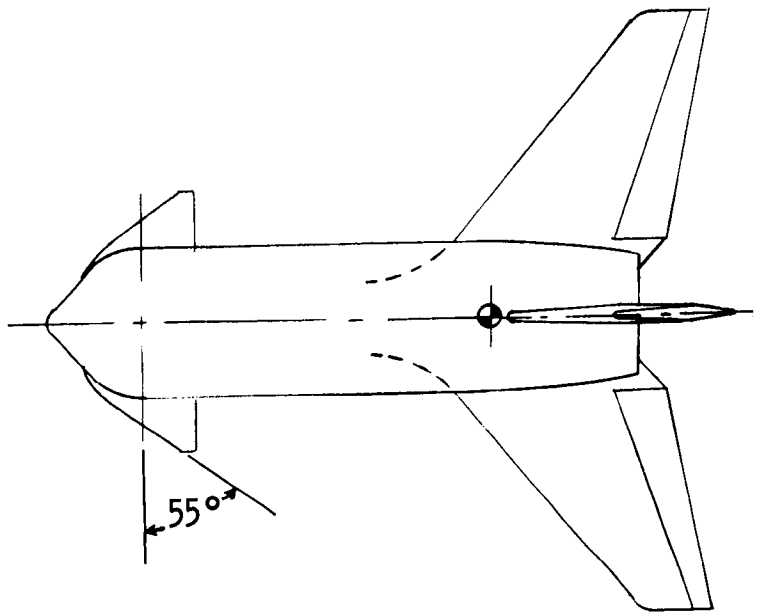

	FULL SCALE	MODEL
LENGTH	49.74 m	0.373 m
DIAMETER	12.19 m^2	0.091 m^2
WING AREA	697.0	0.039
ASPECT RATIO	3.56	3.56
SWEEP	40.0°	40.0°
TAPER RATIO	0.28	0.28
SPAN	49.45	0.371
T.E. DIHEDRAL	2.0°	2.0°

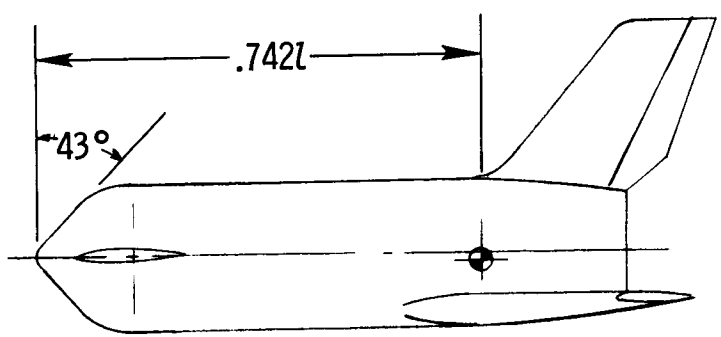

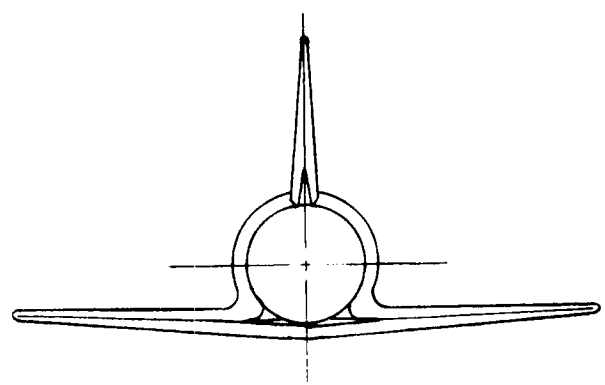

Figure 2

STAGE-ARRANGEMENT CONFIGURATION

(Figures 3, 4, and 5)

A sketch of the stage-arrangement configuration is shown in figure 3. This is a model of the phase B fully reusable North American Rockwell delta-wing orbiter and the General Dynamics/Convair booster. The model could be assembled in parallel (the phase B study configuration) or in tandem. (See figs. 4 and 5.) As in the low-fineness-ratio configuration, each component was instrumented with a strain-gage balance. Separate combined vehicle centers of gravity are indicated for the tandem and parallel configurations; they represent estimated locations for ascent flight conditions near maximum αq. The tandem and parallel centers of gravity were at stations 32.77 percent and 48.17 percent body length, respectively.

STAGE - ARRANGEMENT CONFIGURATION

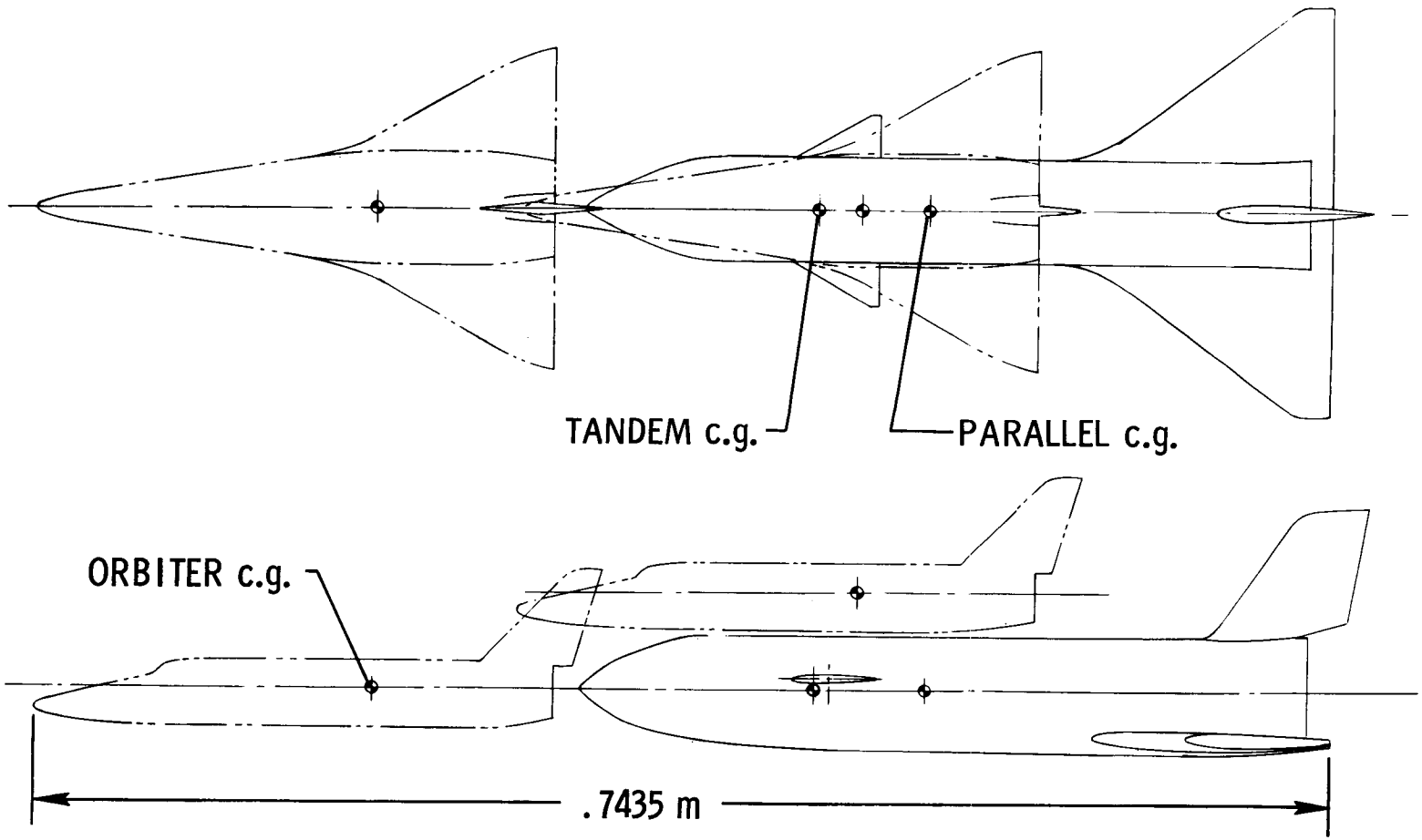

Figure 3

TANDEM STAGE-ARRANGEMENT CONFIGURATION

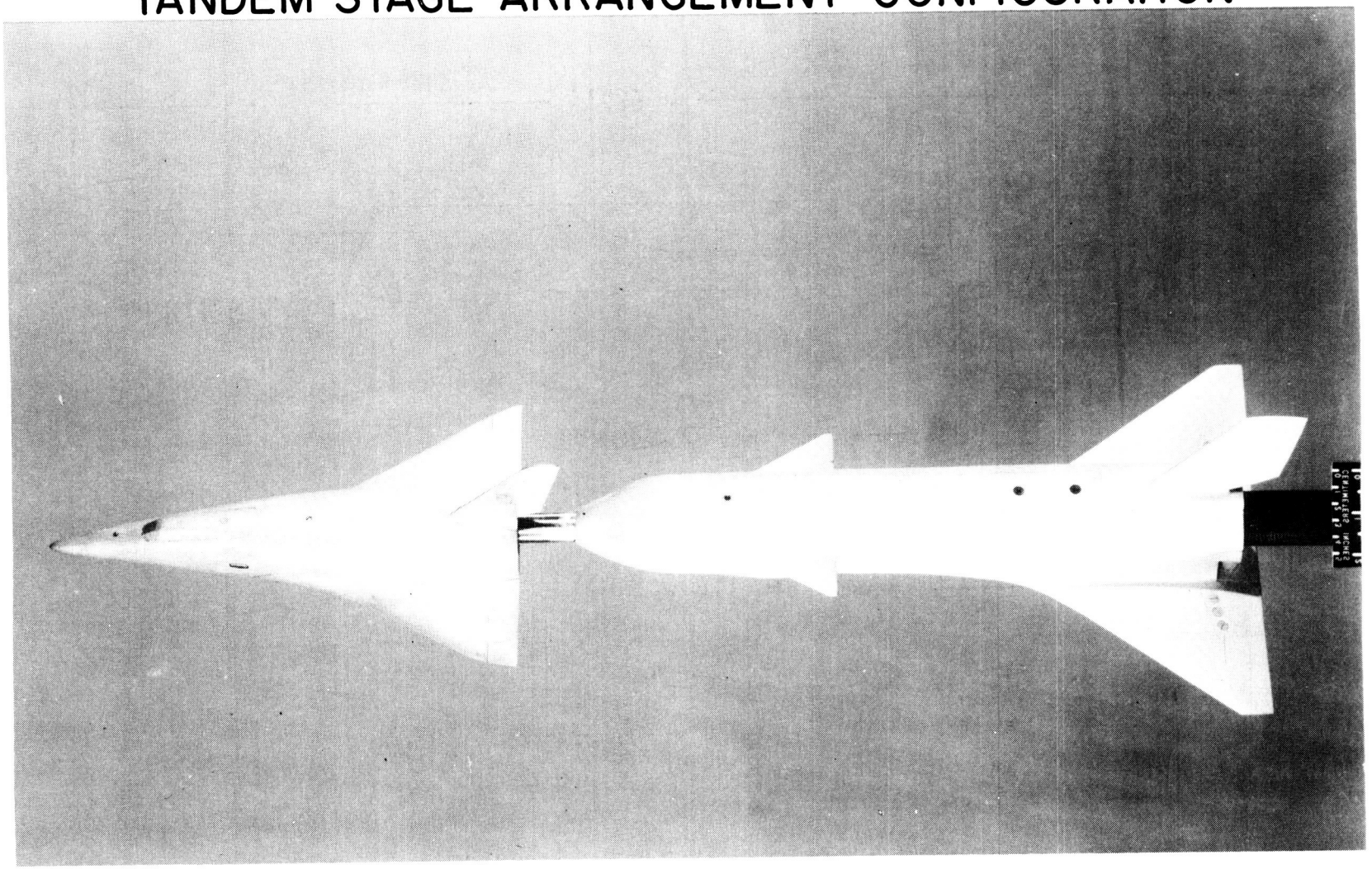

Figure 4

PARALLEL STAGE-ARRANGEMENT CONFIGURATION

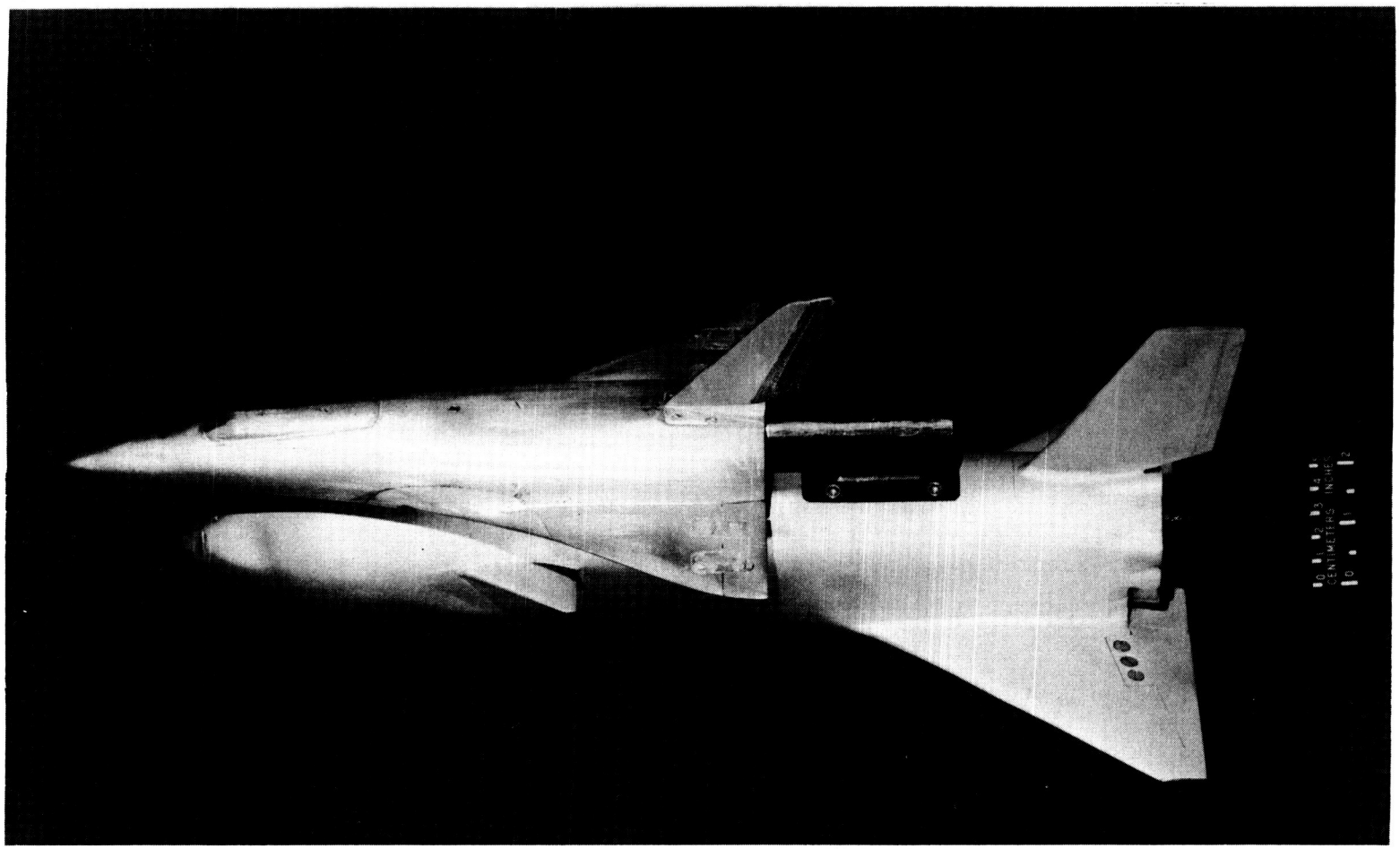

Figure 5

TEST CONDITIONS

(Figure 6)

The wind-tunnel test conditions for the low-fineness-ratio configuration are shown in figure 6. The tests were made at subsonic, transonic, and low-supersonic Mach numbers. Transition strips were applied to the forebodies and lifting surfaces for the transonic and supersonic tests (Mach 0.4 to 2.16).

The stage-arrangement-configuration tests were limited to Mach numbers ranging from 1.6 to 2.16. The components were tested separately and combined in tandem for the low-fineness-ratio configuration and combined in tandem and in parallel for the stage-arrangement configuration. Thus, the influence of each component on the other could be isolated algebraically. The influence of the booster on the orbiter can be found by subtracting the orbiter-alone coefficients from the coefficients of the orbiter mated with the booster, or by simply comparing the data for the orbiter alone and the orbiter mated with the booster directly. The data for the booster in the presence of the orbiter were isolated by subtracting the mated orbiter data (adjusted by the appropriate dimensional constants) from the total vehicle data. The influence of the orbiter on the booster can then be determined in the same manner as the influence of the booster on the orbiter, either by subtraction or by direct comparison with the booster-alone data.

TEST CONDITIONS FOR LOW-FINENESS-RATIO CONFIGURATION

CONFIGURATION	MACH NO.	REYNOLDS NO.
BOOSTER ALONE TANDEM	0.25	2.9×10^6 TO 17.1×10^6
ORBITER ALONE BOOSTER ALONE TANDEM	0.4 TO 1.2	2.9×10^6 TO 5.1×10^6
ORBITER ALONE BOOSTER ALONE TANDEM	1.5 TO 2.16	2.2×10^6 TO 2.9×10^6

BOOSTER IN PRESENCE OF ORBITER = TOTAL VEHICLE - MATED ORBITER

Figure 6

TANDEM AXIAL INTERFERENCE EFFECTS

(Figure 7)

The axial interference effects of the components of the low-fineness-ratio configuration on each other are illustrated in figure 7. Minimum axial-force coefficient is plotted against Mach number for the orbiter alone, the orbiter in the presence of the booster, the booster alone, the booster in the presence of the orbiter, and the total vehicle. The minimum drag $C_{A,min}$ of the orbiter in the presence of the booster is significantly less than that of the orbiter alone. A comparison of the orbiter base pressure coefficients $C_{p,b}$ plotted against Mach number shows that the base pressure coefficient becomes positive when the orbiter is in the presence of the large blunt nose of the booster. Previous wind-tunnel experience has shown that a large model support sting behind the base of a model has a significant effect on the model base pressures and, consequently, on the overall drag measurement. It is recognized that the shape of the orbiter-booster interface has a large influence on the interference effects on both the orbiter and booster in a tandem configuration. An interstage fairing or a booster forebody that was less blunt than the present configuration would tend to reduce the interference effects.

The minimum drag of the booster in presence of the orbiter and the total-vehicle drag are both greater than that of the booster alone at subsonic speeds, whereas the opposite is true for Mach numbers greater than 1. At subsonic speeds, the interference effects of the orbiter-booster interface tend to predominate; whereas, at supersonic speeds, the increased effective fineness ratio of the total vehicle tends to reduce the effect of the interstage region on overall drag.

TANDEM AXIAL INTERFERENCE EFFECTS

LOW-FINENESS-RATIO CONFIGURATION

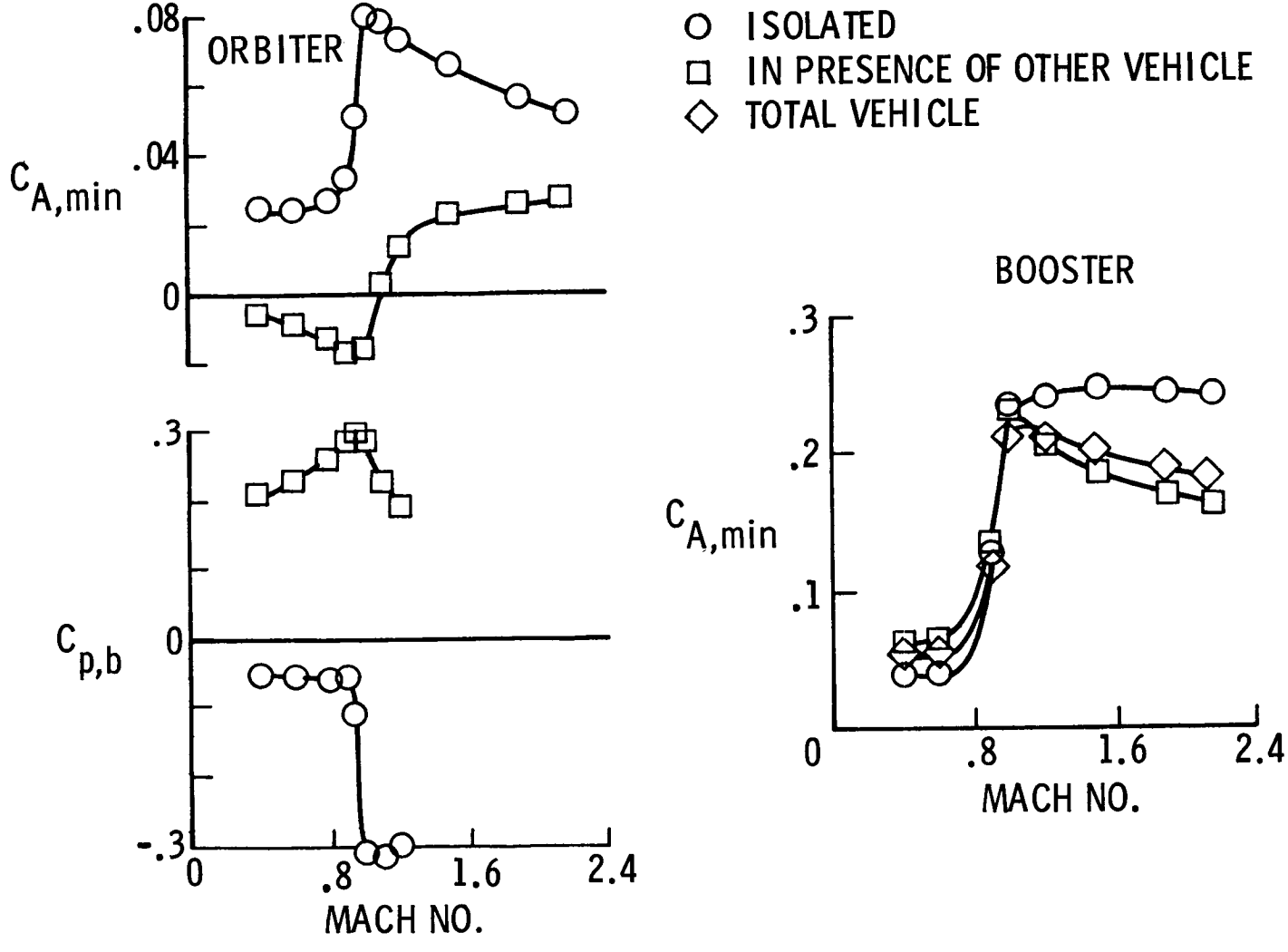

Figure 7

TANDEM LONGITUDINAL INTERFERENCE EFFECTS

(Figure 8)

The longitudinal interference effects of the low-fineness-ratio configuration are shown in figure 8. The variation of C_N and C_m with angle of attack at a Mach number of 1.5 is presented for the total vehicle, the orbiter, and the booster. The data at a Mach number of 1.5 are considered representative of the interference effects at transonic and low-supersonic speeds.

The total-vehicle interference effects are shown by a comparison of the measured values with the sum of the isolated components. The reduction in C_{N_α} caused by interference of both the orbiter and booster in the presence of each other contributes directly to the reduction in C_{N_α} of the total vehicle. The additive reductions in C_{m_α}, however, are moderated by the interference effect on C_{N_α} of the orbiter which contributed an opposite increment to the total-vehicle C_{m_α}. The orbiter and the booster interference effects are shown by a comparison of C_{N_α} and C_{m_α} of the isolated vehicle with those of the vehicle in the presence of the other. The interference effects of the booster on the orbiter are a result of the forward movement of the pressure field at the interstage region onto the aft portion of the orbiter. The relatively small increment in C_N compared with the increment in C_m tends to confirm that the interference is concentrated on the aft portion of the orbiter. The interference effects shown for the booster are a result of the orbiter downwash acting on the booster lifting surfaces.

TANDEM LONGITUDINAL INTERFERENCE EFFECTS

LOW-FINENESS-RATIO CONFIGURATION; MACH 1.5

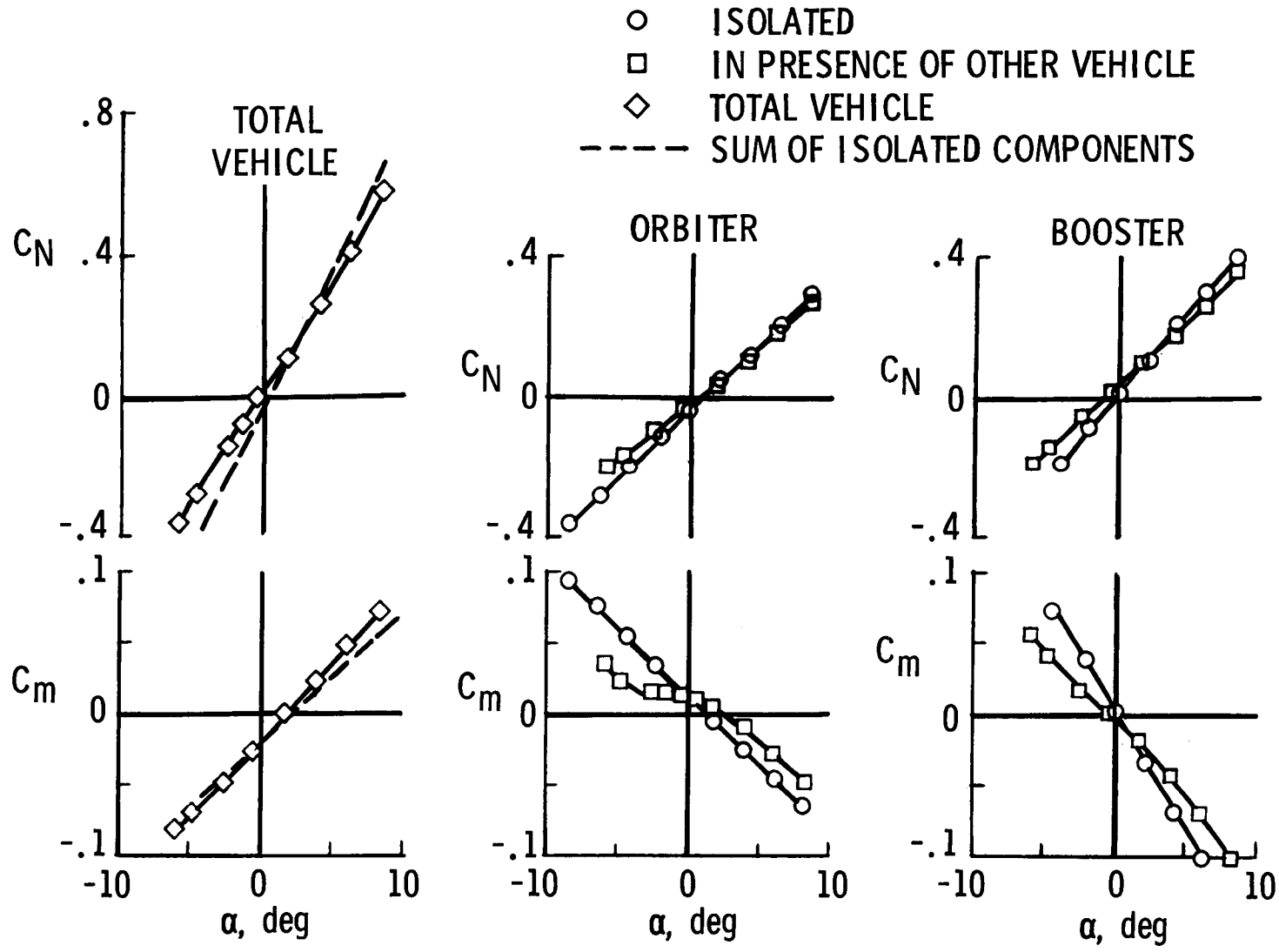

Figure 8

TANDEM STAGE-ARRANGEMENT CONFIGURATION

(Figure 9)

The longitudinal interference effects of the tandem stage-arrangement configuration (North American Rockwell orbiter and General Dynamics/Convair booster) are presented in figure 9. In contrast to the low-fineness-ratio configuration, the interference effects of the booster on the orbiter characteristics are very small. Almost all the gross interference shown for the total vehicle is caused by the effect of the orbiter downwash on the booster lifting surfaces. The linear sum of the isolated component C_m values indicates a longitudinally stable total vehicle, but the measured values show a nonlinear variation in C_{m_α} and a longitudinally unstable total vehicle.

TANDEM STAGE-ARRANGEMENT CONFIGURATION

LONGITUDINAL INTERFERENCE EFFECTS; MACH 1.6

○ ISOLATED

□ IN PRESENCE OF OTHER VEHICLE

◇ TOTAL VEHICLE

--- SUM OF ISOLATED COMPONENTS

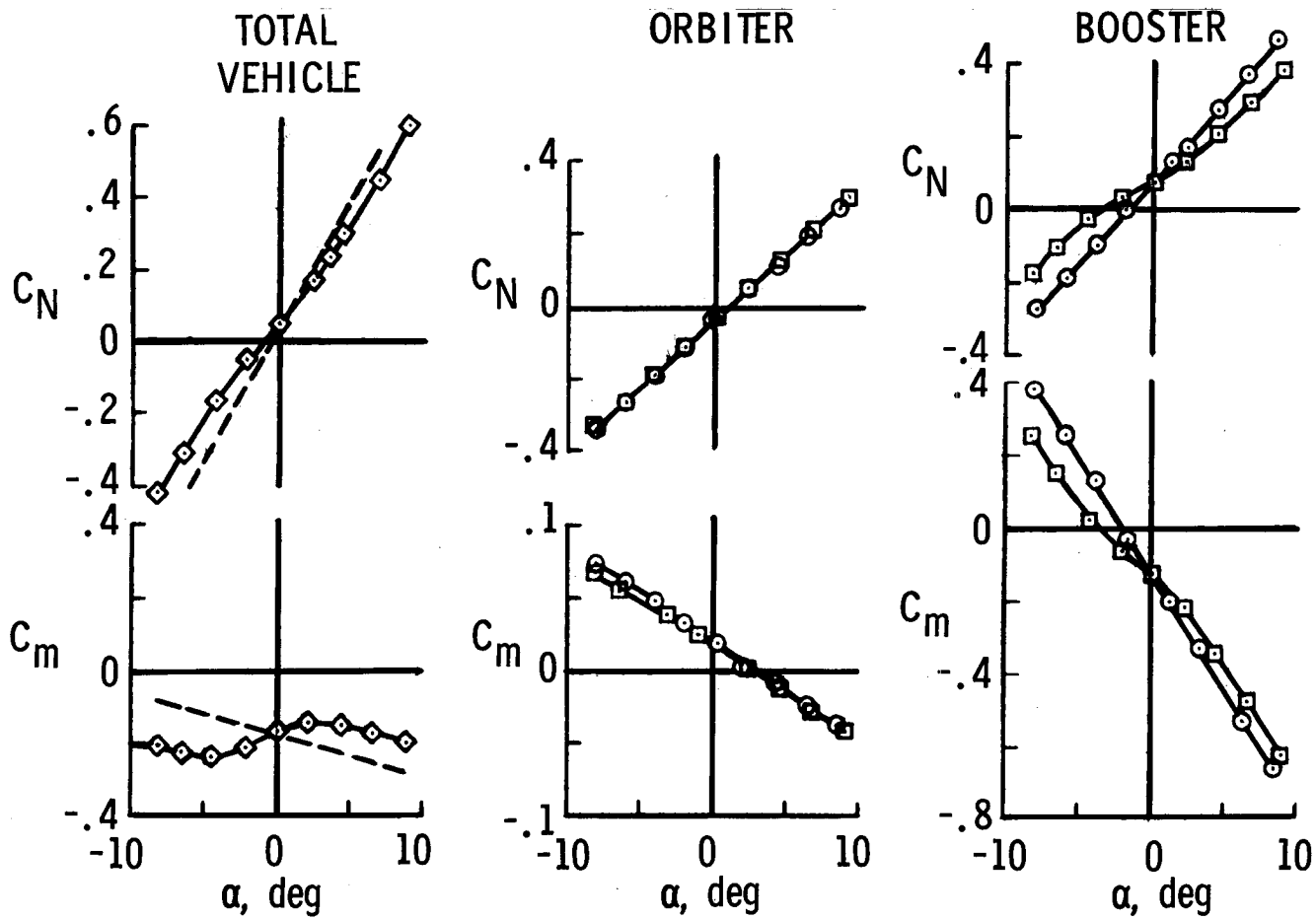

Figure 9

PARALLEL STAGE-ARRANGEMENT CONFIGURATION
(Figure 10)

The longitudinal interference effects of the parallel stage-arrangement configuration are presented in figure 10. The interference effects of the parallel arrangement are characterized by large incremental changes in C_N and C_m of the orbiter and booster in the presence of each other. A sizable reduction in C_{N_α} for the orbiter in the presence of the booster is also noted.

The parallel arrangement, in contrast to the tandem arrangements, is longitudinally stable. The gross interference effect on C_{N_α} is a result of mutual interference of both components on each other, both tending to reduce C_{N_α}. The negative contribution of interference effect on C_m from the booster to the total vehicle is somewhat offset by the positive contribution from the orbiter. The stabilizing interference effect on C_{m_α} for the total vehicle was contributed by the negative interference increment in C_{N_α} shown for the orbiter.

PARALLEL STAGE-ARRANGEMENT CONFIGURATION

LONGITUDINAL INTERFERENCE EFFECTS; MACH 1.6

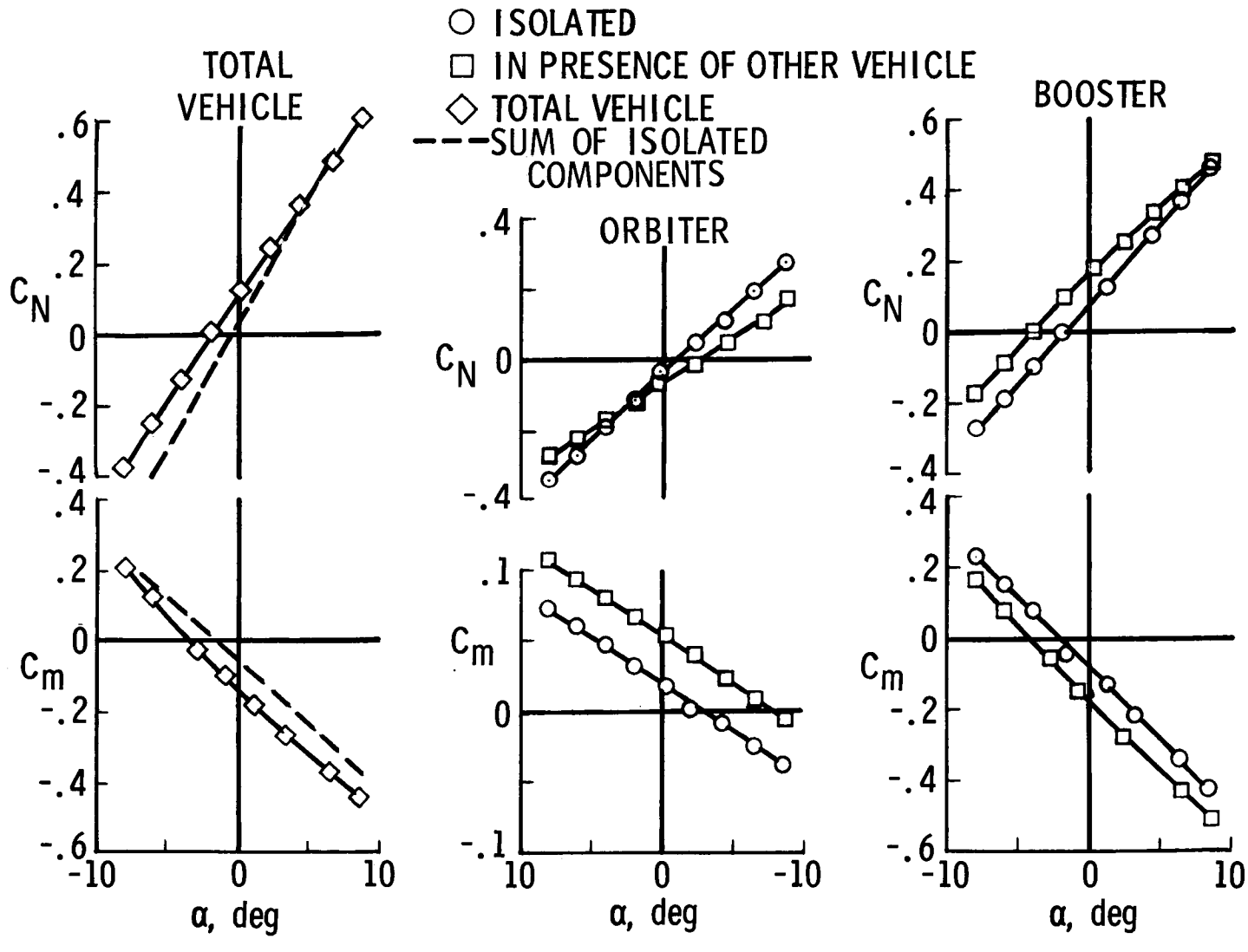

Figure 10

AMES WING-BODY PROGRAM

(Figure 11)

An outline of the features of the analytical method used to predict the aerodynamic normal force and aerodynamic center of each component of the low-fineness-ratio configuration is shown in figure 11. This program is the Carmichael version of the Woodward program (ref. 1). Based on linearized aerodynamic equations, the program is designed for vehicles in steady-state flow for both subsonic and supersonic flight conditions. Various wing-body configurations can be utilized, including multiple lifting surfaces; however, several limitations are pertinent to the present configuration. First, the body must be a figure of revolution; second, the cross section of the body must be constant over the region of wing-body interference.

The results of the program can be read out in the form of running loads on the body and each of the lifting surfaces, aerodynamic centers, shears and bending moments, and the total forces and moments.

AMES WING–BODY PROGRAM

- LINEAR THEORY
- STEADY-STATE FLOW: SUBSONIC AND SUPERSONIC
- WING-BODY VEHICLES
  - WINGS: MULTIPLE LIFTING SURFACES
  - BODY: CIRCULAR CROSS SECTION; CONSTANT AREA OVER INTERFERENCE REGION
- OUTPUT
  - RUNNING LOADS
  - SHEARS AND BENDING MOMENTS
  - AERODYNAMIC CENTERS
  - TOTAL FORCES AND MOMENTS

Figure 11

LOW-FINENESS-RATIO CONFIGURATION

Mathematical and Wind-Tunnel Models
(Figure 12)

The mathematical model of the tandem low-fineness-ratio configuration used in the calculations is illustrated in figure 12(a). The aerodynamics of the several lifting surfaces and the mutual interference effects of the wings and body are treated by panels distributed as indicated in the figure.

Several features of the mathematical model differ from those of the wind-tunnel model (fig. 12(b)). The wind-tunnel model has a paraboloid-cone nose, whereas the mathematical model has a stock nose built into the computer program. The mathematical-model orbiter body is essentially circular in cross section, whereas the orbiter body of the actual model is more flattened or elliptical. Because of the restriction that requires a constant body cross section through the interference region, the interstage area between the orbiter and booster could not be simulated. The conical nose of the mathematical booster was sharper than the nose of the wind-tunnel model since the forebody of the wind-tunnel model was too blunt for the program to accept. Finally, the mathematical-model orbiter wing was planar and located on the vehicle center line, whereas the wing of the wind-tunnel model had 5° of twist and was located slightly below the vehicle center line.

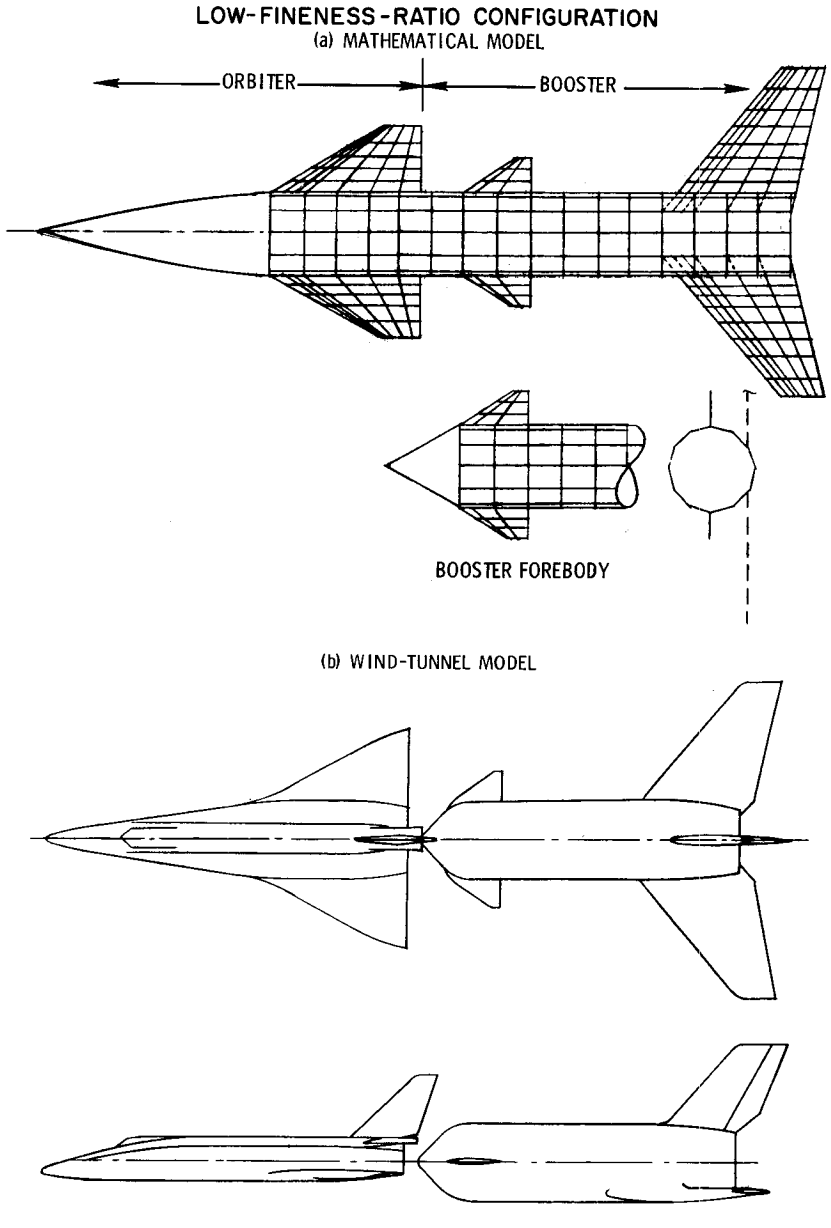
LOW-FINENESS-RATIO CONFIGURATION
(a) MATHEMATICAL MODEL
ORBITER
BOOSTER
BOOSTER FOREBODY
(b) WIND-TUNNEL MODEL

Figure 12

ISOLATED AND TANDEM VEHICLE INTERFERENCE AT MACH 1.5

(Figure 13)

Calculated values of C_{N_α} and of aerodynamic-center location for the low-fineness-ratio configuration in terms of the body length, obtained by the Carmichael analytical method, are compared with the measured values at Mach 1.5 in figure 13. These results are shown for the orbiter and booster alone (represented by the circular symbols) and for the vehicles in tandem (represented by the square symbols). The open and solid symbols represent the calculated and measured values of C_{N_α}, respectively.

The calculated values of C_{N_α} and aerodynamic-center location for the orbiter alone agree closely with the measured values. The calculated value of C_{N_α} for the booster alone is about 30 percent larger than the measured value, although the aerodynamic-center location was correctly predicted.

Considering the values of C_{N_α} for the vehicles in tandem, the calculations could not predict interference effects on the orbiter from the booster. The wind-tunnel data indicate a decrease in C_{N_α} and a forward aerodynamic-center movement on the orbiter in presence of the booster. The interference effect is represented by the difference in values between the solid square and solid circle symbols on the left-hand plot. As stated previously, the interference on the orbiter is caused by the forward propagation of the pressure field from the orbiter-booster interface region onto the aft portion of the orbiter. The interference on the orbiter is likely to be highly dependent on the shape of the orbiter-booster interface. An interstage fairing might reduce the interference in this region to an insignificant value.

The calculated C_{N_α} on the booster in the tandem arrangement is somewhat larger and farther aft than the measured value. Again the interference effects from the orbiter are indicated by the difference between the circular and square symbols. These results indicate that the predicted effect of orbiter downwash on the booster forebody and canard relative to the downwash on the wing is larger than the effect measured on the wind-tunnel model. If the mathematical orbiter wing vertical position was adjusted closer to the model wing position, the trend of the calculated results might improve.

ISOLATED AND TANDEM VEHICLE INTERFERENCE

LOW-FINENESS-RATIO CONFIGURATION; MACH 1.5

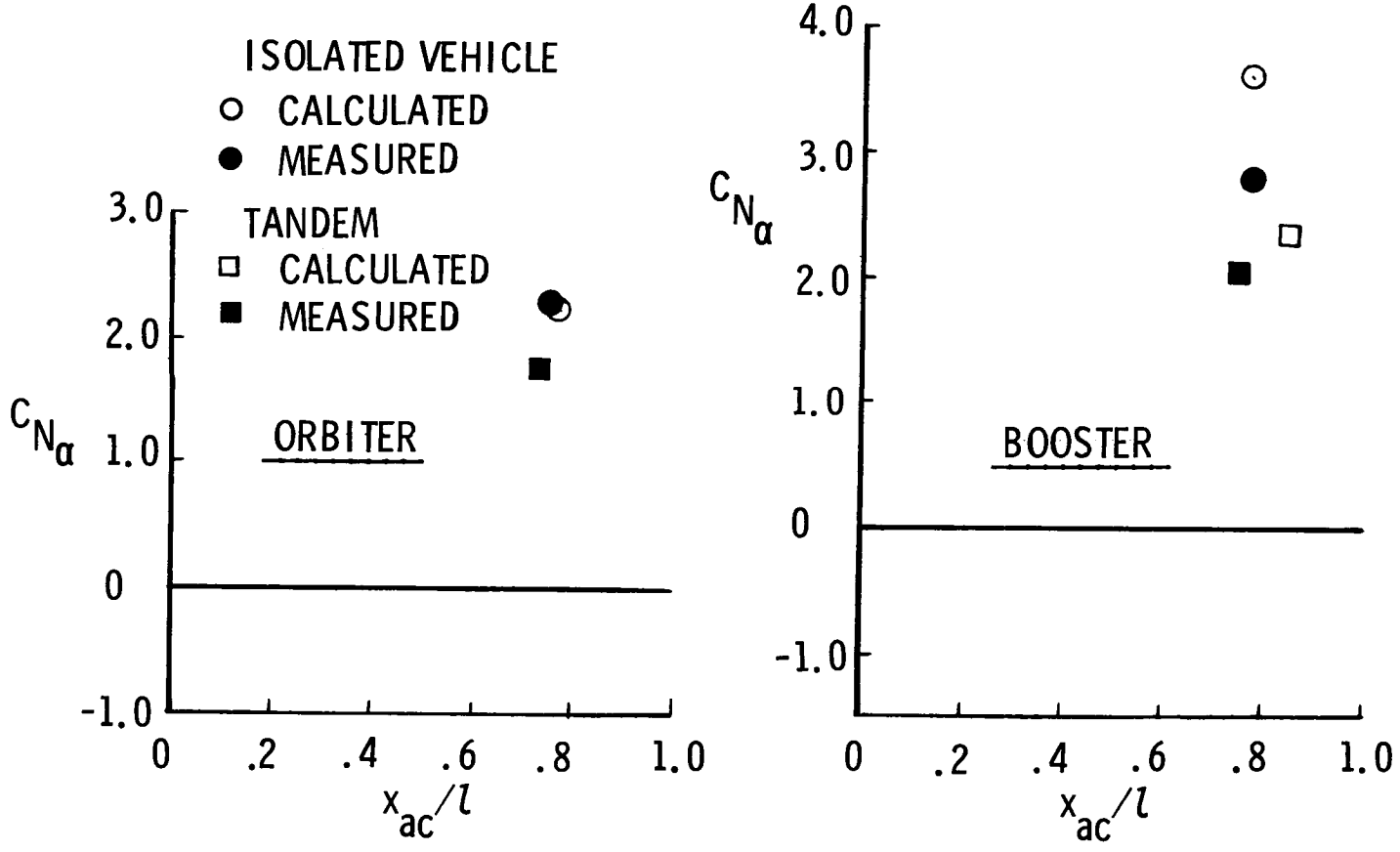

Figure 13

STATUS OF ASSESSMENT TO DATE

The application of the Carmichael method to loads estimation on tandem launch vehicles is in an early phase and, as yet, has not been completely exercised. The preliminary assessment indicated that although the analytical approach approximately predicted the tandem launch vehicle forces, the prediction was not adequate for loads estimation. The calculated results for the isolated orbiter indicated that useful estimates of the loads on the orbiter alone may be obtained, but a satisfactory estimate for the isolated booster forces was not obtained. A better representation of the booster nose might improve the booster-alone estimate. Since the orbiter downwash effects on the booster lifting surfaces are liable to be sensitive to their relative position in the orbiter downwash field, relocating the orbiter wing in the mathematical model closer to the actual position would possibly improve the estimate of the orbiter interference effects on the booster. The inability to represent the interstage discontinuity precluded calculation of the interstage interference effects on the booster. Even with the discontinuity represented, the program could not calculate its effects on the orbiter at supersonic speeds. If an interstage fairing was used, the interference effects in the interstage region might be negligible, and the analytical predictions would be more applicable. Further exploration of analytical methods is necessary before the prediction of loads on combined vehicles can be improved.

REFERENCE

1. Carmichael, Ralph L.; Castellano, Charles R.; and Chen, Chuan F.: The Use of Finite Element Methods for Predicting the Aerodynamics of Wing-Body Combinations. Analytic Methods in Aircraft Aerodynamics, NASA SP-228, 1970, pp. 37-51.

IMPACT OF SUBSONIC AERODYNAMIC CONSIDERATIONS ON A SPACE SHUTTLE BOOSTER CONFIGURATION

By R. L. Roensch
Douglas Aircraft Company
Long Beach, California

and R. L. Odenbaugh
McDonnell Douglas Astronautics Company-West
Huntington Beach, California

McDonnell Douglas Corporation

INTRODUCTION

With conventional launch vehicles, the subsonic aerodynamic characteristics are usually of little importance. With the Space Shuttle Booster, however, the configuration must be an adequate aircraft as well as an efficient launch vehicle. This paper discusses how these aircraft considerations influenced the Booster configuration developed by the McDonnell Douglas Corporation during Phase B of the Shuttle Program.

SUBSONIC AERODYNAMIC CONFIGURATION DRIVERS

(Figure 1)

Listed in the figure are the major items which influence the aerodynamic configuration of any subsonic aircraft. First and foremost are the mission requirements. The engine bypass ratio will be strongly influenced by the cruise-back range. The total thrust required and therefore the number of currently available engines will be determined by the cruise altitude, the go-around requirements and possibly the ferry requirements. The wing area is driven primarily by the landing distance. The aspect ratio is influenced by the cruise-back range and flying qualities (e.g. adequate roll control), but it also impacts on the go-around capability and the landing distance. Flying qualities influence the vertical tail size and the longitudinal location of the wing with respect to the center of gravity.

The very far aft location of the center of gravity of a space shuttle booster has a significant impact on the configuration geometry.

Finally, the configuration which meets the subsonic aerodynamic requirements must be compatible with the launch, reentry and transition requirements, and vice-versa.

SUBSONIC AERODYNAMICS CONFIGURATION DRIVERS

- **REQUIREMENTS**
  - CRUISE-BACK RANGE
  - CRUISE ALTITUDE
  - GO-AROUND CAPABILITY
  - LANDING DISTANCE
  - FLYING QUALITIES
  - FERRY
- **CENTER-OF-GRAVITY LOCATION**
- **LAUNCH AND REENTRY COMPATIBILITY**

Figure 1

JET CANARD BOOSTER UNIQUE CONFIGURATION CHARACTERISTICS

(Figure 2)

Shown here is a sketch of the final configuration of the Booster developed during Phase B. Shown are some of the unique configuration characteristics.

The high wing was selected as a result of a system trade study which considered the impact of the lower cruise-back fuel and better hypersonic stability with a high wing compared to the lower weight of the thermal protection system with a low wing. Likewise, the aspect ratio was selected to minimize vehicle weight considering cruise-back fuel and wing weight and to provide adequate aileron authority during subsonic flight. The dorsal tip fins were sized to provide sufficient lateral-directional stability and control during reentry. This was found to be a lighter system than the combination of a central vertical tail, sized for subsonic flight, and the additional reaction control system which such a configuration would require for control during hypersonic reentry at high angles of attack. The ventral tip fins, which result in the lazy-Y tip fins, were incorporated to provide satisfactory stability and control during subsonic cruise and landing, and this configuration was found to be lighter than the central vertical and reaction control system. These subsonic considerations will be discussed in more detail later.

The jet canard, which houses the cruise-back jet engines, provides a very effective high lift capability canard for longitudinal trim and control. This, too, will be discussed in more detail later.

JET CANARD BOOSTER
UNIQUE CONFIGURATION CHARACTERISTICS

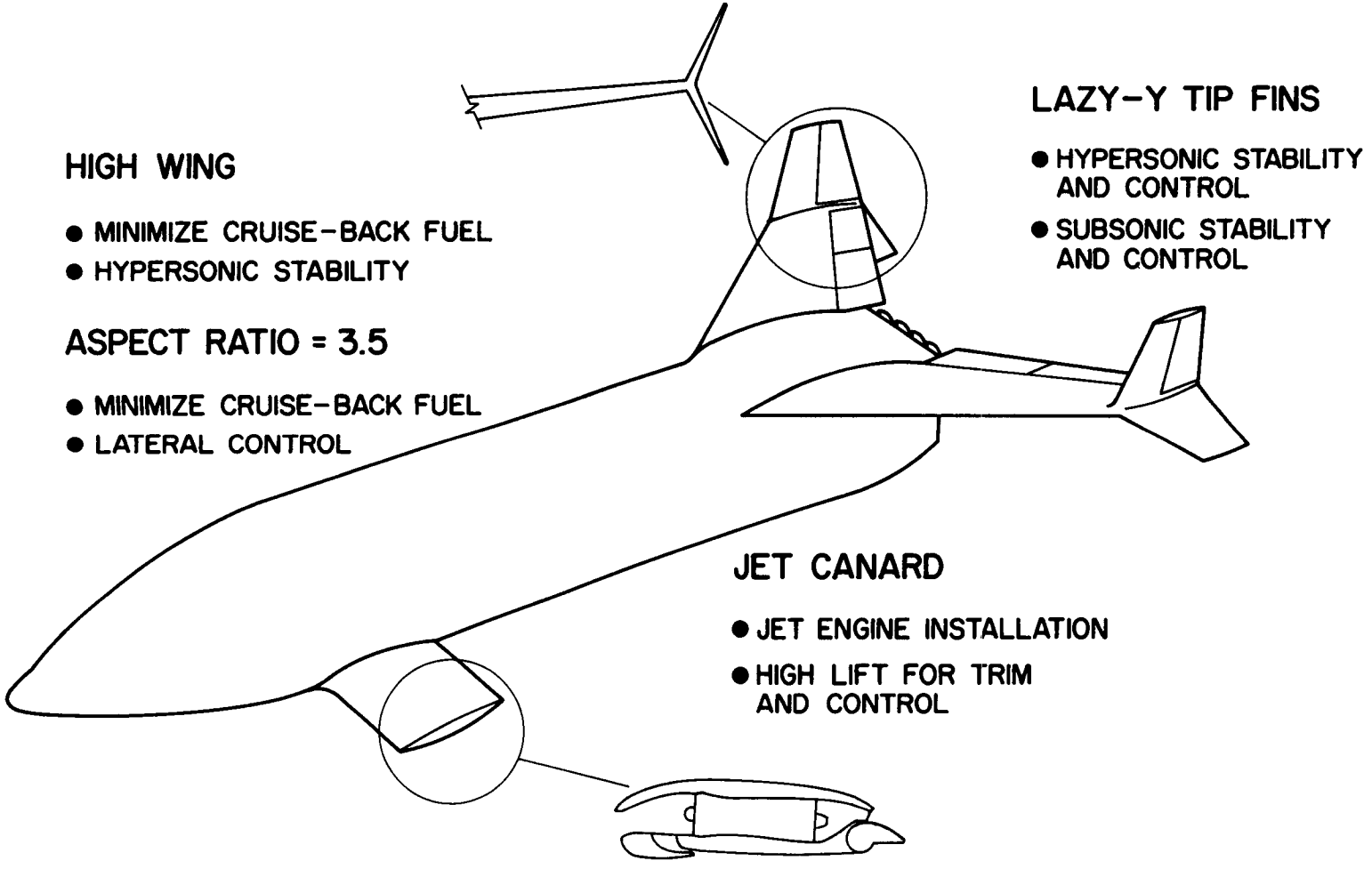

Figure 2

C.G. EVOLUTION

(Figure 3)

The wing and the horizontal tail on an aircraft are normally located so that the resultant vehicle meets certain longitudinal stability and control requirements. This is usually achieved by placing the wing near the center of gravity and the horizontal tail as far away as possible.

This figure illustrates the development of the Booster center-of-gravity location and why it is so far aft. The heavy rocket engines contribute to most of the shift from about 55-percent of body length for the tankage alone to the complete vehicle center-of-gravity location without the jet canard of about 73-percent of body length. The addition of the jet canard between the LOX and Hyrdogen tanks moves the center of gravity forward to about 71-percent of body length.

CG EVOLUTION

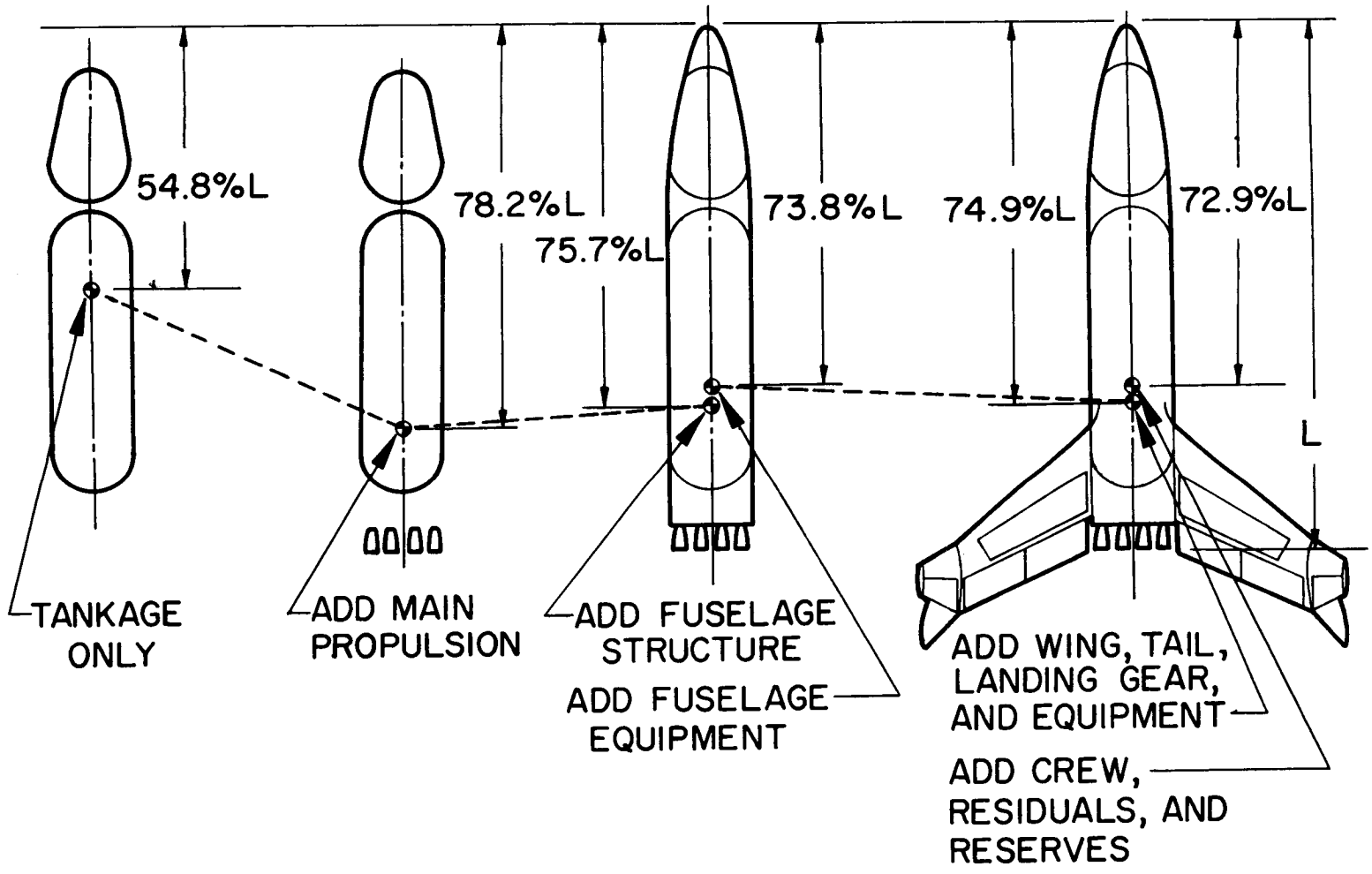

Figure 3

TRENDS IN C.G. LOCATION AND TAIL/WING SURFACE RELATIONSHIPS

(Figure 4)

This figure illustrates how the final Booster configuration center-of-gravity location compares with that of present day commercial transports and some earlier Booster configurations. It is fairly obvious that there is no room for an aft horizontal tail and that either a delta wing configuration or a canard configuration should be considered.

TRENDS IN CG LOCATION AND TAIL/WING SURFACE RELATIONSHIPS

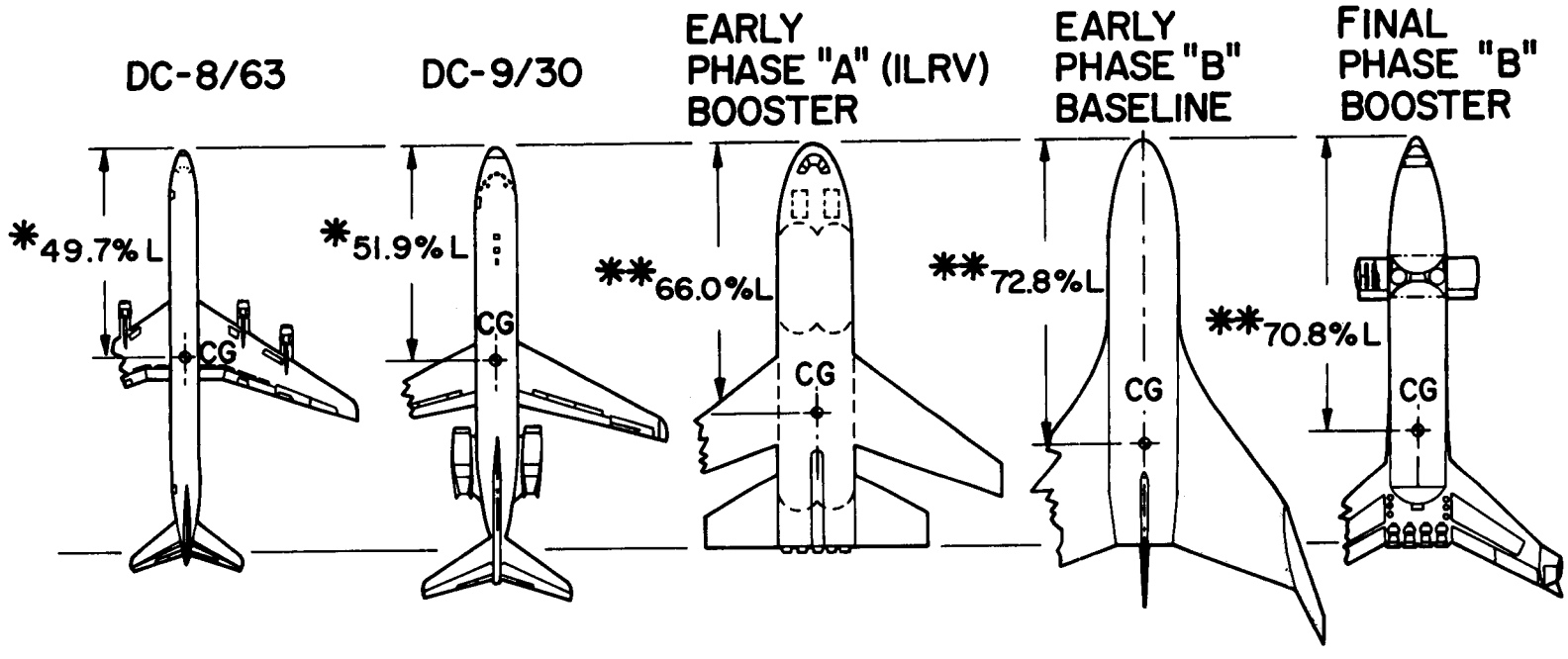

$\frac{S_H}{S_W} = \frac{559}{2,927} = 0.191$ $\frac{S_H}{S_W} = \frac{276}{1,001} = 0.276$ $\frac{S_H}{S_W} = \frac{3,200}{5,500} = 0.577$ $\frac{S_H}{S_W} = \frac{0}{10,000} = 0$ $\frac{S_H}{S_W} = \frac{1,630}{6,020} = 0.271$

S_H THEORETICAL TAIL AREA (FT^2)

S_W THEORETICAL WING AREA (FT^2)

*AFT CG LOCATION

**CG LOCATION AT START OF CRUISE

Figure 4

WING LOCATION CONSIDERATIONS
(Figure 5)

While several diverse requirements led to the final configuration, of primary importance was the requirement to minimize weight, which, within the accuracy of the cost model, means minimum vehicle cost. This figure and several of those following will illustrate why this consideration led to the selection of a canard configuration. Illustrated below are two possible wing-tail combinations. A delta wing configuration with the elevons providing the "tail" authority and a canard configuration. Both configurations are required to exhibit positive static longitudinal stability. Shown in the sketch are the wing spars and their location with respect to the rocket engine thrust structure and the hydrogen tank. It can be seen that the wing carry-through structure with the delta wing must either penetrate or go around the tank. With the further aft wing permitted by the use of the canard, this configuration can use the thrust structure as the carry-through structure. This duplication of structural function saves more than 10,000 pounds of inert weight.

WING LOCATION CONSIDERATIONS

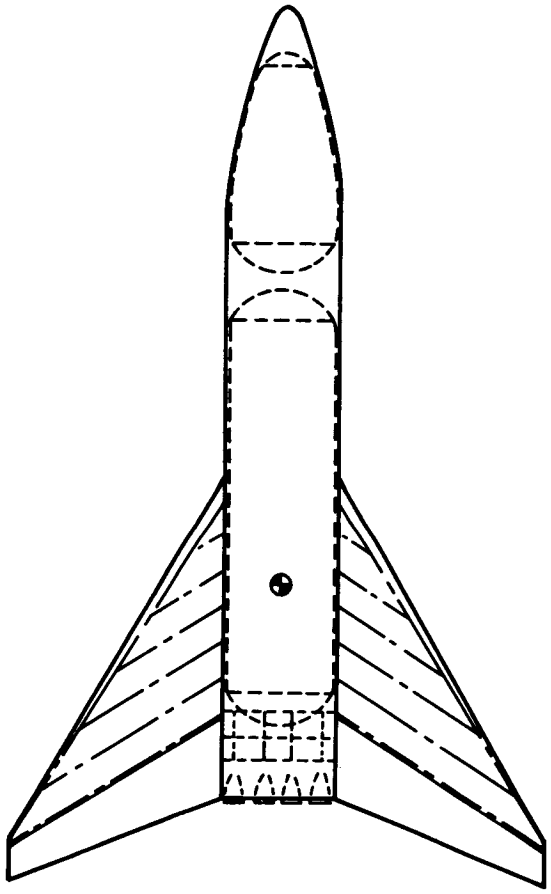

DELTA WING

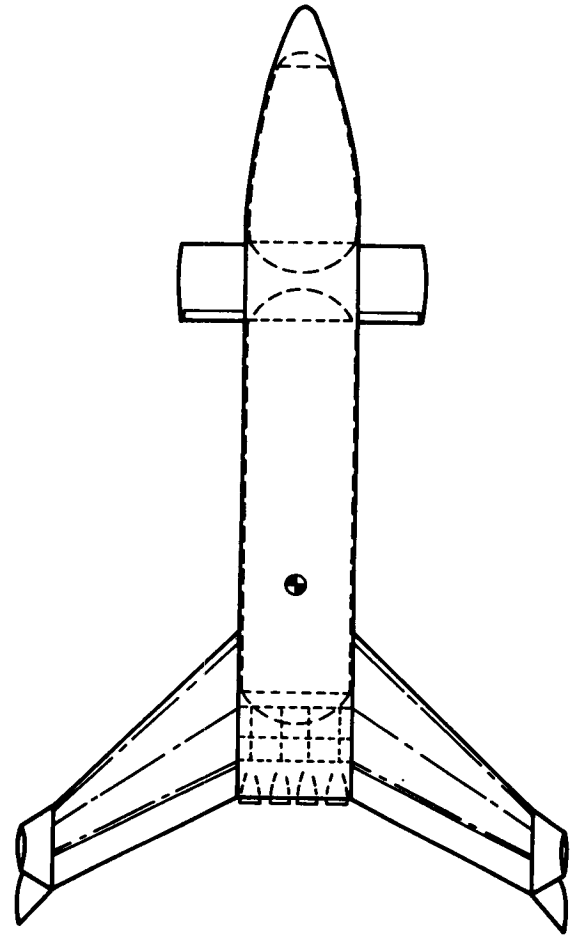

CANARD

Figure 5

DELTA WING BOOSTER - TYPICAL PITCHING MOMENT CHARACTERISTICS
(Figure 6)

The next few figures will illustrate why additional weight savings can be realized by the use of a canard configuration, compared to a delta wing configuration. To meet a required landing distance, either vehicle must touch down at the same speed. Due to the trim penalities associated with a delta wing, it will require a larger wing area to achieve the same speed.

Illustrated in this figure are the lift and pitching moment characteristics of a stable delta wing configuration. The static margin is five-percent of the wing mean aerodynamic chord. The trim penalty is readily apparent. Trailing edge up elevon deflections are required to trim, and the resulting lift loss at a given angle of attack is significant due to the short "tail length" of the elevons.

DELTA WING BOOSTER
TYPICAL PITCHING MOMENT CHARACTERISTICS

$AR = 2.4$

STATIC MARGIN = 5 % MAC

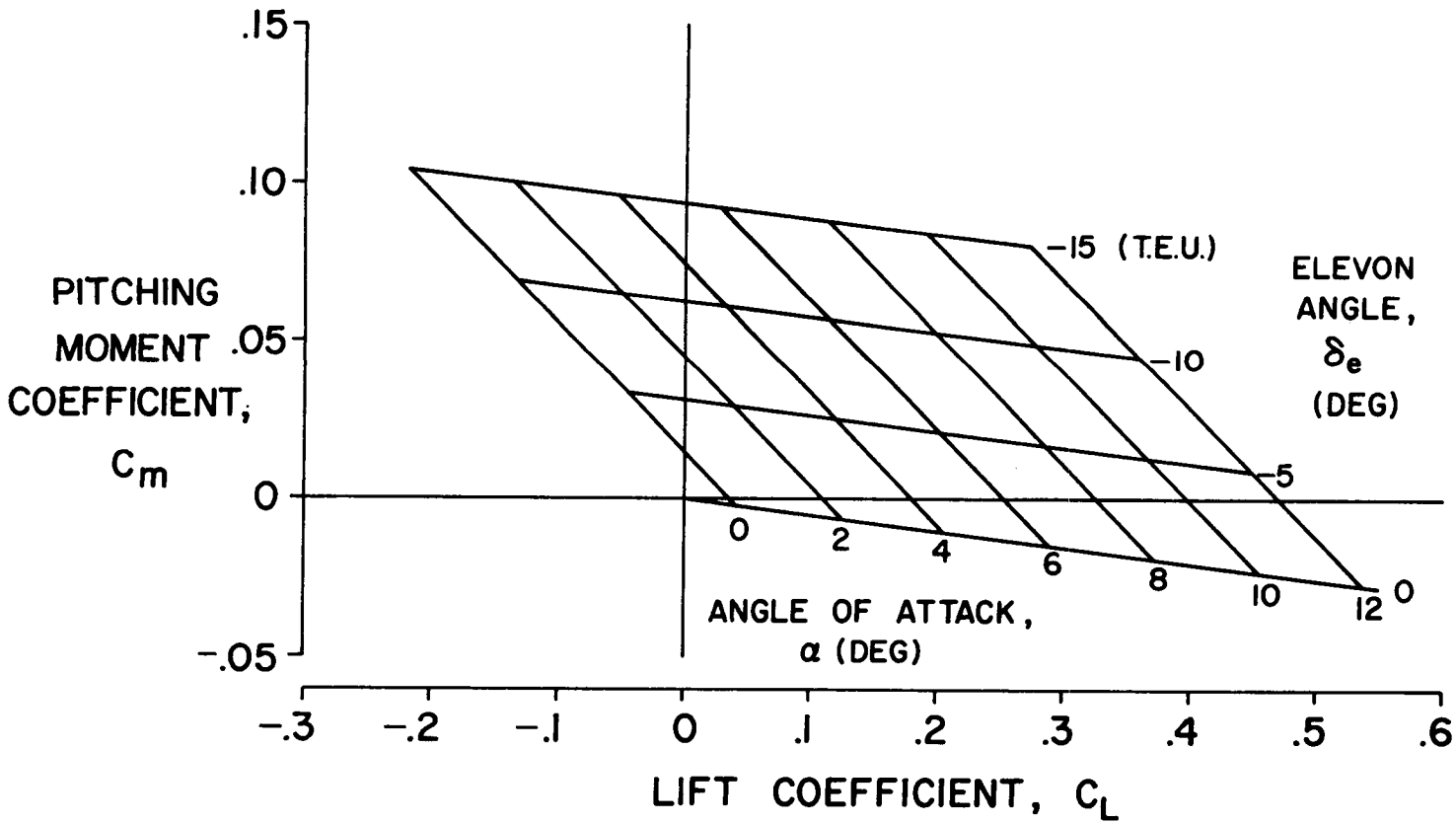

Figure 6

DELTA WING BOOSTER - TYPICAL LIFT CURVES

(Figure 7)

The pitching-moment data from the previous figure were used to prepare the trimmed and untrimmed lift curves shown here. The reduction in lift-curve slope due to trim is obvious. Only by going to an unstable configuration could this trim penalty be avoided. However, this would result in a whole new set of problems which are not within the scope of this presentation.

DELTA WING BOOSTER
TYPICAL LIFT CURVES

$AR = 2.4$

STATIC MARGIN = 5% MAC

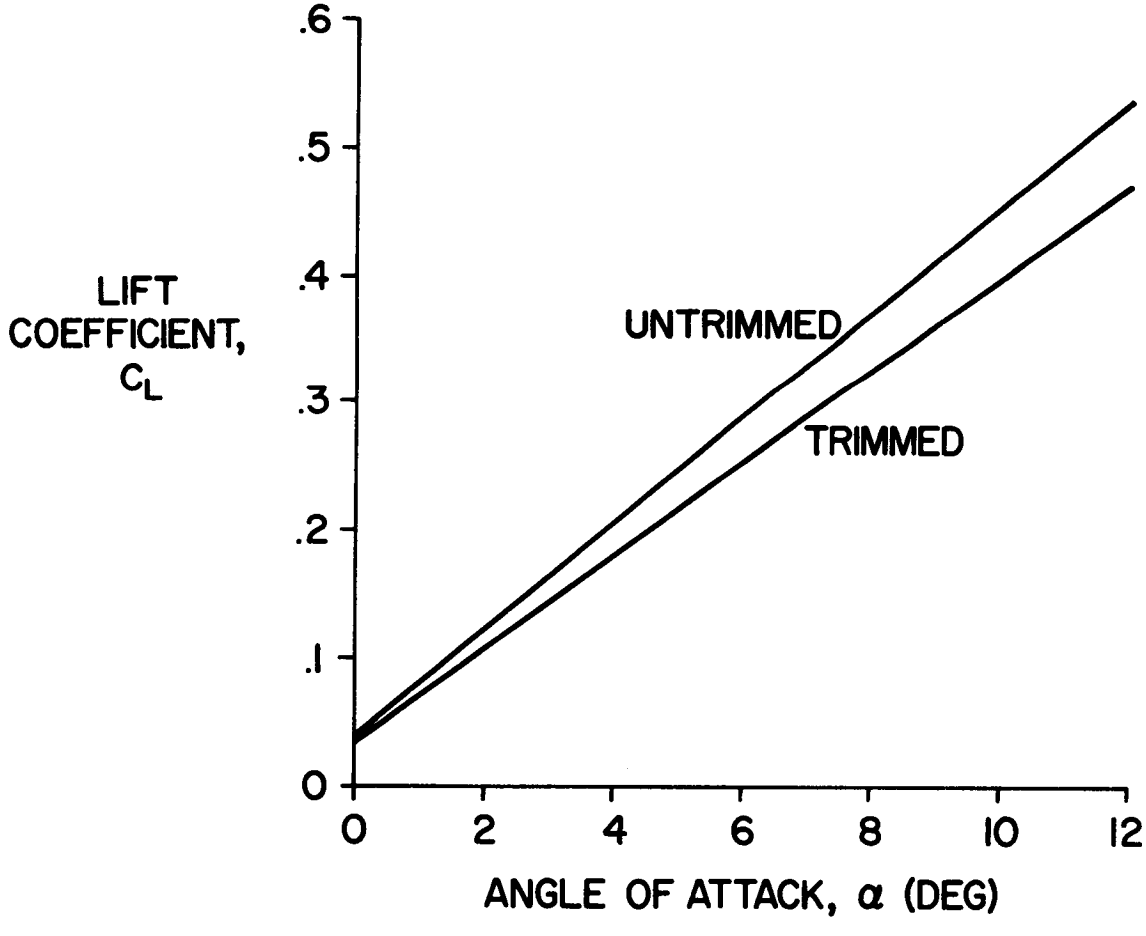

Figure 7

CANARD BOOSTER - TYPICAL PITCHING MOMENT CHARACTERISTICS

(Figure 8)

With a canard vehicle, both elevons and canard deflections can be used for trim. Illustrated in the figure, for a stable vehicle with a static margin of five-percent wing mean aerodynamic chord, is a way to combine the two. As can be seen, canard incidence alone can result in a modest increase in lift at a given angle of attack. Additional lift can be gained by trailing edge down deflection of the elevons. The analysis used to prepare this figure took into account both the net lift loss due to the wing in the canard downwash and the resulting nose-up pitching moment due to this lift loss.

CANARD BOOSTER
TYPICAL PITCHING MOMENT CHARACTERISTICS

$AR = 3.5$

STATIC MARGIN = 5 % MAC

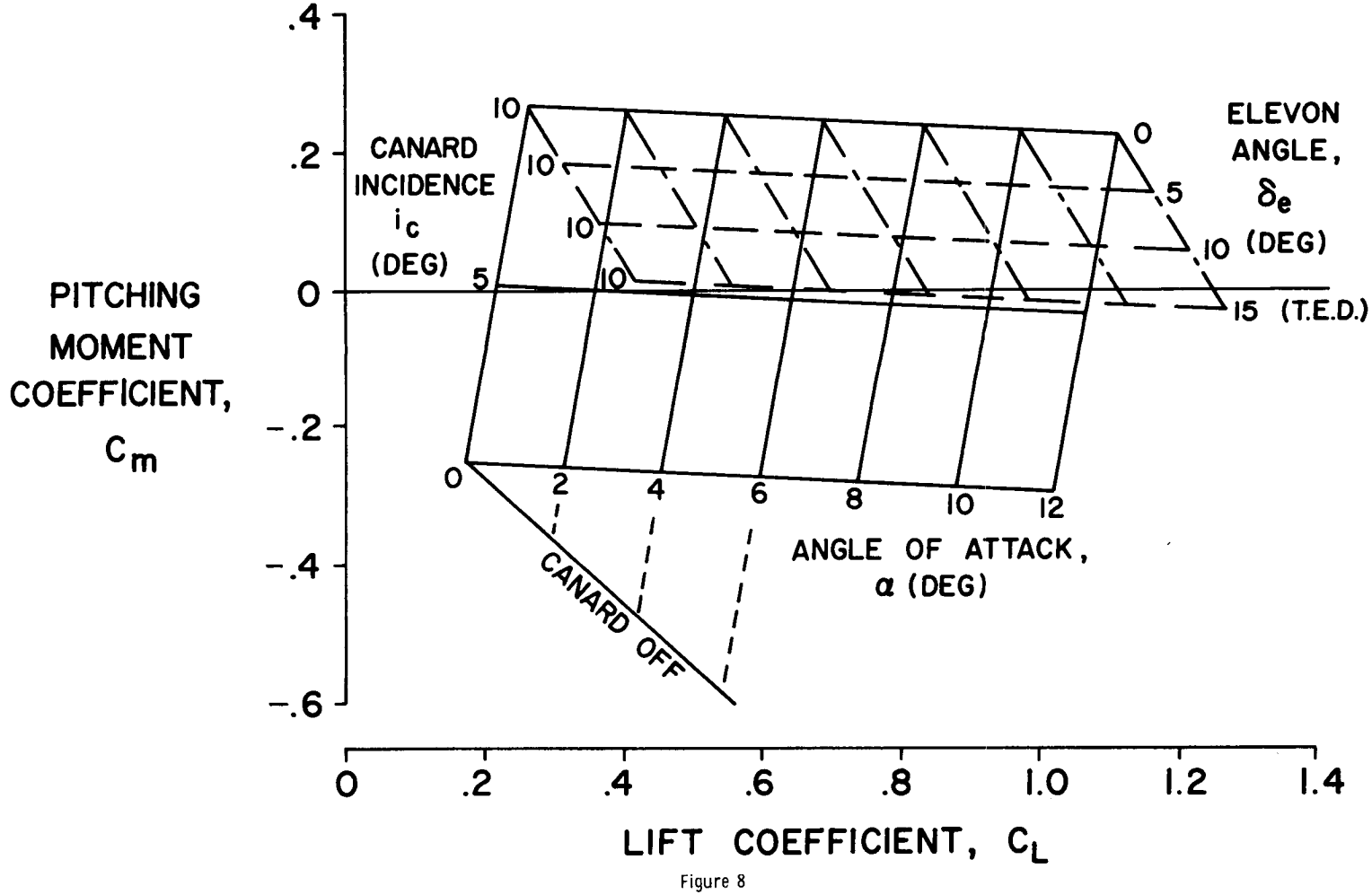

Figure 8

CANARD BOOSTER - TYPICAL LIFT CURVES

(Figure 9)

The data from the previous figure are presented here to show the real advantage of a canard for the generation of high airplane lift coefficients at moderate angles of attack. Unlike that for a delta wing, the trimmed lift-curve slope is greater than the untrimmed slope. Additional trimmed lift is available with the elevons biased trailing edge down. These two effects can be used to advantage to permit a canard configuration to operate to much higher useable lift coefficients than is possible with a delta wing configuration. This allows the canard configuration to meet the landing performance requirements with a smaller wing area. As a result, with a powerful enough canard, the configuration should be lighter than a delta wing configuration by as much as 50,000 pounds. Obviously, if this wing area is too small to meet the reentry requirements, this large a weight saving cannot be realized. At present, however, the landing requirement is sizing the wing.

CANARD BOOSTER TYPICAL LIFT CURVES

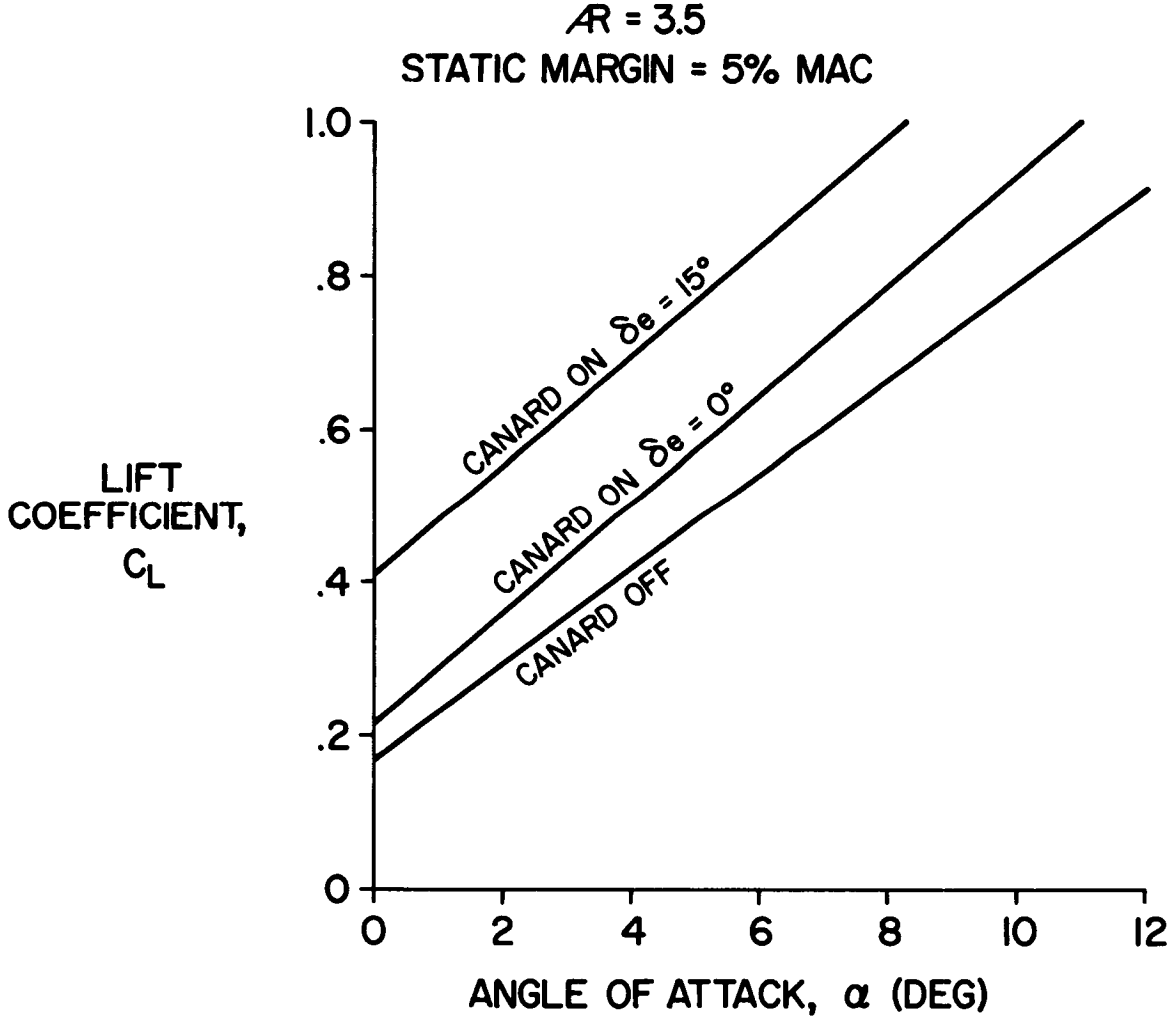

Figure 9

CANARD BOOSTER - CANARD LIFT REQUIREMENTS
(Figure 10)

In order to realize the benefits of the canard, it must be able to generate enough lift to trim out the nose down pitching moment of the wing and, if used, down elevons. Presented here is the required canard lift coefficient, based on the canard planform area, as a function of trimmed aircraft lift coefficient. The wing stall indicated corresponds to an angle of attack of 12 degrees.

Indicated on the figure are the estimated maximum lift coefficients for an all moveable aerodynamic canard with and without a leading edge device. The additional $C_{L_{MAX}}$ needed to trim to wing stall with the elevons down 15 degrees can be obtained by the incorporation of a large chord double slotted trailing edge flap. This, along with a leading edge device (the leading edge flap is only one of several alternatives) on an all moveable surface which must survive the reentry environment and still generate high $C_{L_{MAX}}$ is a tall order.

As a result, we chose to seriously examine a fixed incidence jet-flap canard, which offers the possibility of more than sufficient canard $C_{L_{MAX}}$ when one includes the lift due to flap deflection, jet reaction, and supercirculation. As envisioned, the cruise-back jet engines would be buried in the canard. The inlet, with retractable doors to protect the engines during launch and reentry, would be at the leading edge of the canard and all the engine airflow would be exhausted over a flap to provide the necessary jet turning.

CANARD BOOSTER
CANARD LIFT REQUIREMENTS
STATIC MARGIN = 5% MAC

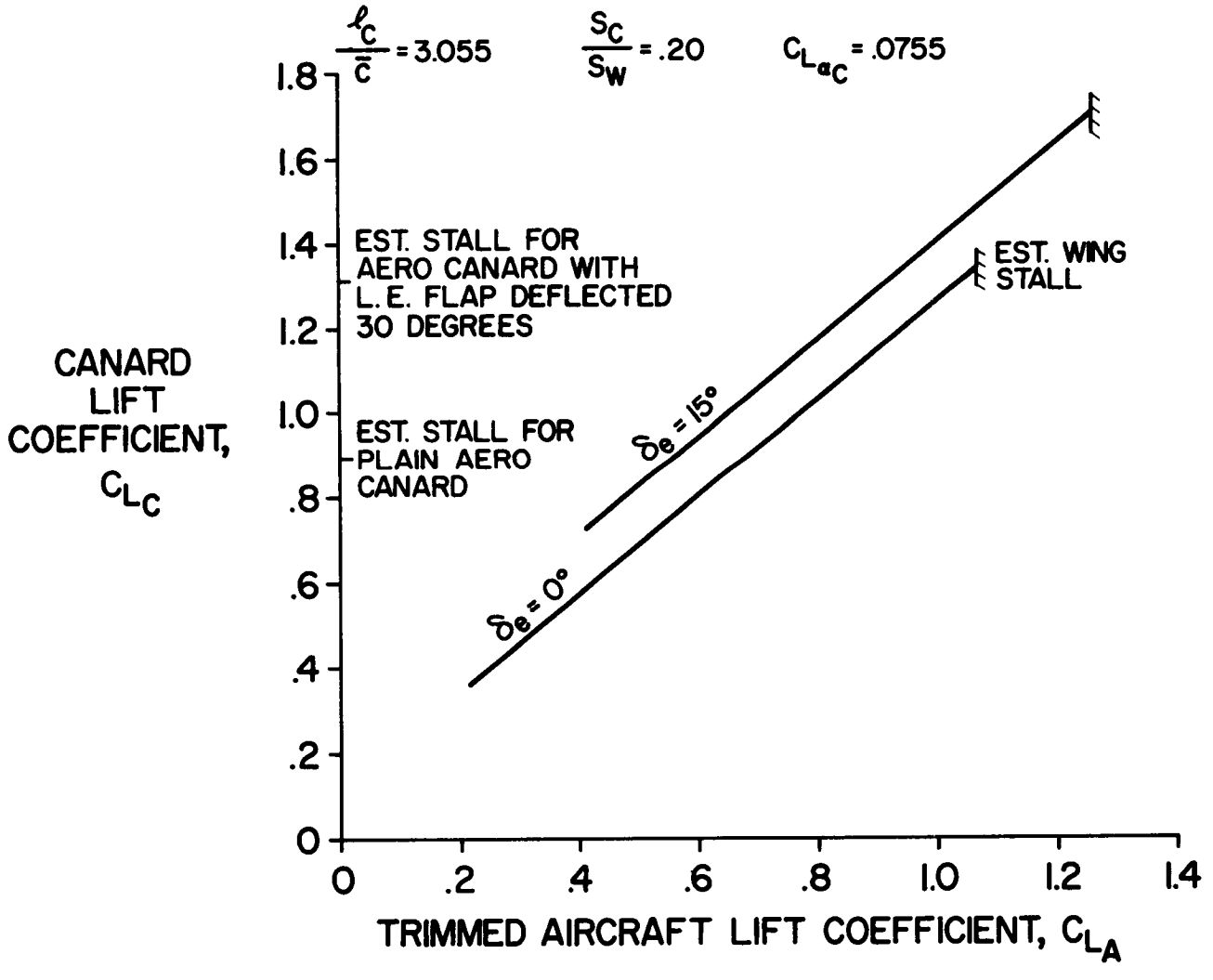

Figure 10

CANARD BOOSTER - JET CANARD CONSIDERATIONS

(Figure 11)

Tabulated here are some of the advantages and some of the risks associated with the jet-flap canard concept when compared to an aerodynamic canard.

The jet canard offers the potential for the high lift necessary to allow the landing performance requirement to be met with a minimum wing area without the problems associated with providing a variable incidence surface with leading and trailing edge devices.

The jet canard is an ideal airbreathing engine installation since the engines can be protected from launch and reentry heating by a simple inlet door. With an aerodynamic canard, other ways must be found to install and protect the engines, with probably the next best alternative being the deployable engine concept.

Due to the thickness of the canard required to house the engines (with the inlet closed the equivalent thickness ratio is almost 20 percent) the leading edge radius is quite large. As a result, the leading edge heating should be much less than with an aerodynamic canard of reasonable thickness turned into the wind.

While it is true that the concept of the jet canard is not a flight proven system, the unique advantages offered by the "power profile" concept are being seriously considered by both the Navy and the Air Force (e.g. the Air Deflection And Modulation Program) for application to V/STOL.

The wind tunnel data obtained to date with an unpowered jet canard show a reduction in directional stability due to the pressure of the canard. This would suggest that an additional reduction might be incurred due to the jet wake. Unfortunately, the powered testing to date has not been able to provide reliable directional characteristics.

The limited amount of wind tunnel data relative to ground effects with jet flaps indicate a reduction in lift near the ground. The magnitude of this reduction may determine the amount of jet deflection required for control during the landing flare.

CANARD BOOSTER
JET CANARD CONSIDERATIONS

ADVANTAGES

- HIGH CANARD LIFT WITHOUT EXOTIC HIGH LIFT DEVICES
- IDEAL AIR-BREATHING ENGINE INSTALLATION
- LOWER REENTRY HEATING

RISKS

- NOT A FLIGHT PROVEN SYSTEM
- POSSIBLE YAW INSTABILITY DUE TO JET WAKE
- GROUND EFFECTS

Figure 11

JET CANARD BOOSTER - JET CANARD TURNING EFFICIENCY MEASURED IN WIND TUNNEL

(Figure 12)

The jet flap canard concept envisioned for application to the Booster requires that the engine exhaust flow be turned by the flap. While such "Coanda" turning has been easily achieved with low Mach number jets, this particular application requires the turning of a supersonic jet.

Presented in this figure are the measurements of the static turning angles and efficiencies obtained with a rather unsophisticated model of the jet flap canard. These data were obtained during a test with a three-percent-scale Booster model in the MCAIR Low Speed Wind Tunnel. The data were reduced to coefficient form based on a q of 100 pounds per square foot. The momentum coefficient is defined by $C_\mu = \frac{T_{ideal}}{q\ S}$, where T_{ideal} is the ideal gross thrust for the measured airflow based on an isentropic expansion to free stream static pressure. Indicated on the figure is the full scale turning efficiency which we believe can be achieved with further analyses and tests. At the pressure ratios shown, the flow remained attached to the flap. At pressure ratios in excess of these the flow separated and the turning angle was significantly reduced.

JET CANARD BOOSTER
JET CANARD TURNING EFFICIENCY MEASURED IN WIND TUNNEL
STATIC CONDITIONS

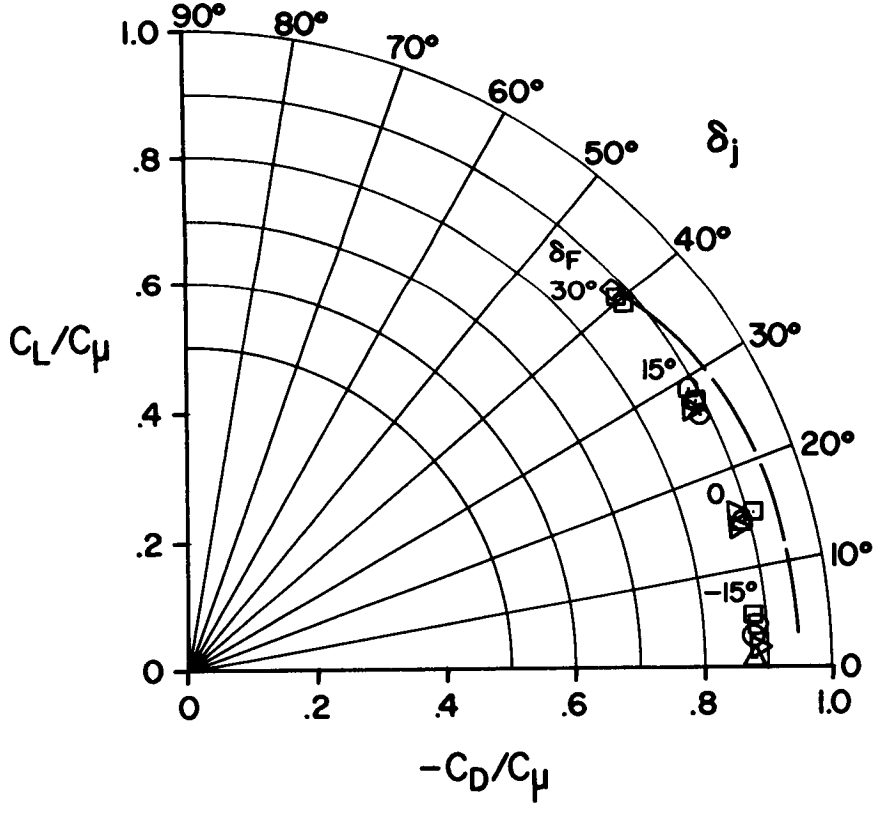

SYM	PRESSURE RATIO
○	1.9
□	2.0
◇	2.1
△	2.2
⬠	2.3
⬡	2.4
▷	2.6
◇	2.7
◇	2.8

—— —— FULL SCALE ANTICIPATED TURNING EFFICIENCY

Figure 12

JET CANARD BOOSTER - DEMONSTRATED JET FLAP FLOW ATTACHMENT

(Figure 13)

The data presented in the previous figure were for static conditions in which the flow did not separate. At a tunnel q of 100 pounds per square foot (Mach number of about 0.26) the flow did separate at the higher pressure ratios. Presented in this figure are the data obtained and the estimated separation boundary for this configuration based on these data. Also indicated are the engine pressure ratios for the General Electric engine and jet deflection angles appropriate for cruise and landing approach as well as the pressure ratio for the engine at takeoff conditions.

This figure shows that more flap design work needs to be done to achieve a satisfactory configuration. However, the partial success with the first cut design suggests that the task is a relatively easy one.

JET CANARD BOOSTER
DEMONSTRATED JET FLAP FLOW ATTACHMENT

BASED ON LOW-SPEED WIND TUNNEL TEST
OF UNSOPHISTICATED JET FLAP DESIGN

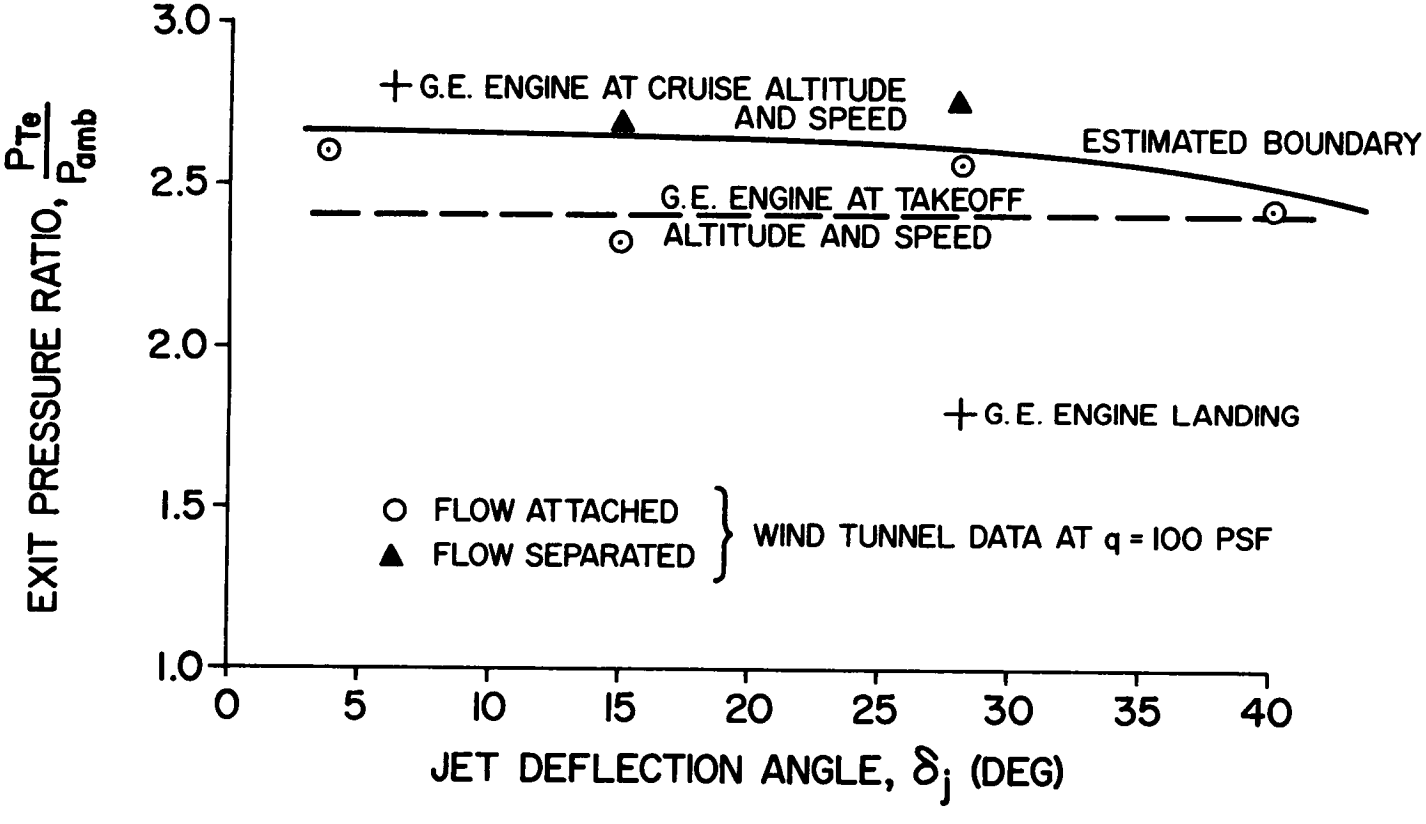

Figure 13

JET CANARD BOOSTER - LANDING FLIGHT PATH CONTROL CAPABILITY

(Figure 14)

Associated with the use of the jet canard is the need to develop unconventional analysis and data presentation procedures. The deflected jet engine gross thrust provides both an increase in lift and a reduction in propulsive force. The optimum jet deflection angle and elevon angle is a function of the parameter to be optimized. Once these characteristics are recognized, it then is the aerodynamicist's task to incorporate these interactions into a workable computer program to solve the problem.

Illustrated in the figure are the results of the analysis for the landing configuration. With the elevons fixed at 15 degrees trailing edge down, the jet deflection angle and power setting required to fly at a particular speed and flight path angle can be determined, as well as the corresponding angle of attack. With the vehicle trimmed along the three-degree glide slope at 180 knots, the angle of attack is slightly less than five degrees, the jet deflection angle is not quite 35 degrees and the power setting is a little less than 50-percent of maximum thrust. At this power setting, the stall speed (angle of attack equal to 12 degrees) is about 138 knots. During a landing abort, the angle of attack reduces only slightly and the jet deflection angle is reduced to less than 25 degrees. Flight simulator demonstrations showed that by using the jet flap as the primary longitudinal trim and control surface, landing aborts could easily be accomplished. The pilots had no difficulty in retrimming the vehicle after application of power during the go-around.

Note that at no time are large jet deflection angles required, so that the jet flap design task is significantly simplified.

JET CANARD BOOSTER
LANDING FLIGHT PATH CONTROL CAPABILITY

GW = 610,000 LB SEA LEVEL STD + 10 °C

GEAR DOWN

ELEVON DEFLECTION = 15°

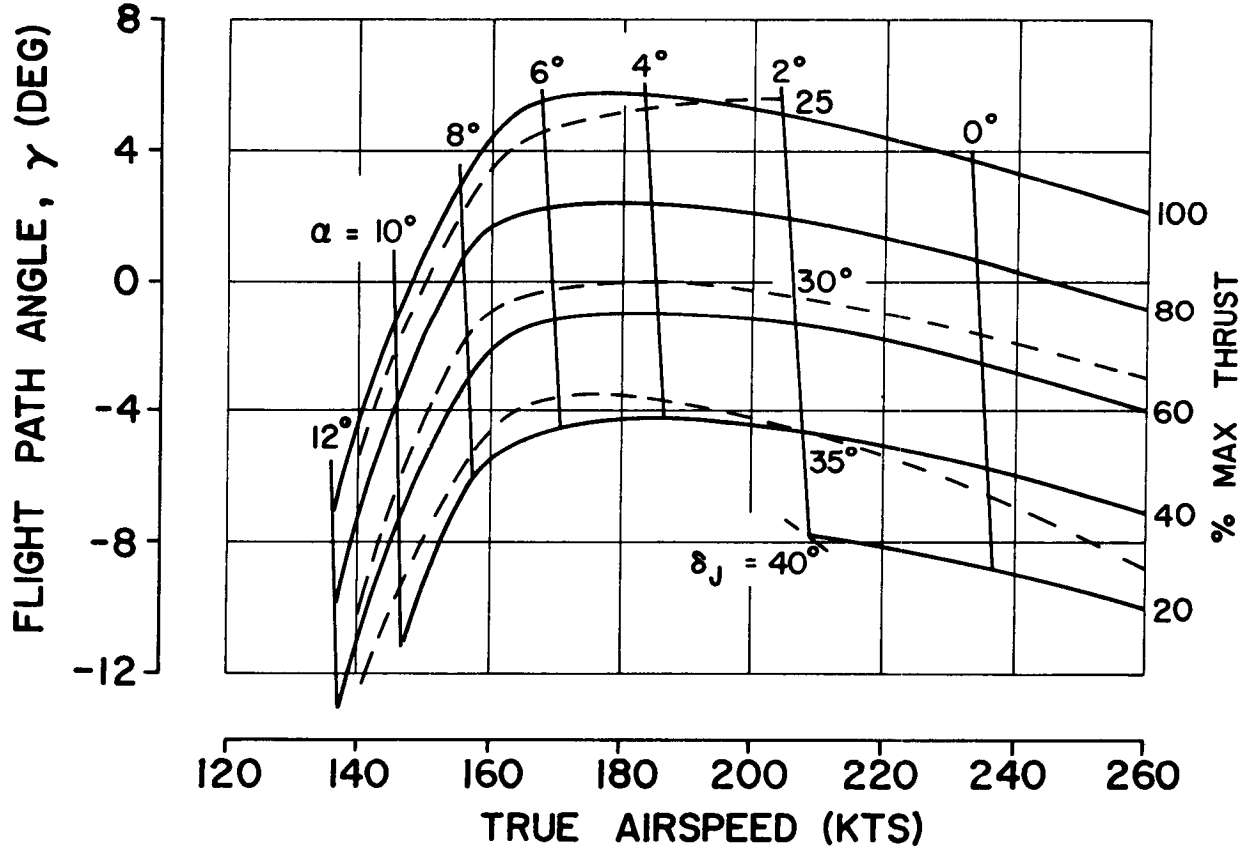

Figure 14

JET CANARD BOOSTER - LONGITUDINAL TIME HISTORIES DURING A FLARE MANEUVER - ELEVON CONTROL
(Figure 15)

As already indicated, the jet flap was shown on the simulator to offer an acceptable means for both longitudinal trim and control. Both the elevon and the jet flap were evaluated during the simulator studies and the jet flap control was preferred by the pilots. The next two figures illustrate why.

Shown here are time histories during a flare maneuver obtained for a three degree of freedom digital solution of the equations of motion. With the vehicle trimmed along the three-degree glide slope a step in elevon deflection, $\Delta\delta_e$, of the magnitudes indicated on the figure was initiated after one second and held at this level for the remainder of the time history. Even though the negative elevon deflection is a "fly-up" command, for almost two seconds after the command the vehicle flies down. With a 7.5-degree trailing-edge-up elevon command, the vehicle reaches the stall angle of attack of 12 degrees before completing the flare maneuver. With -5.0 degrees of elevon deflection, the flare is completed about 70 feet below the height at time zero and the angle of attack is slightly greater than 11 degrees.

JET CANARD BOOSTER LONGITUDINAL TIME HISTORIES DURING A FLARE MANEUVER ELEVON CONTROL

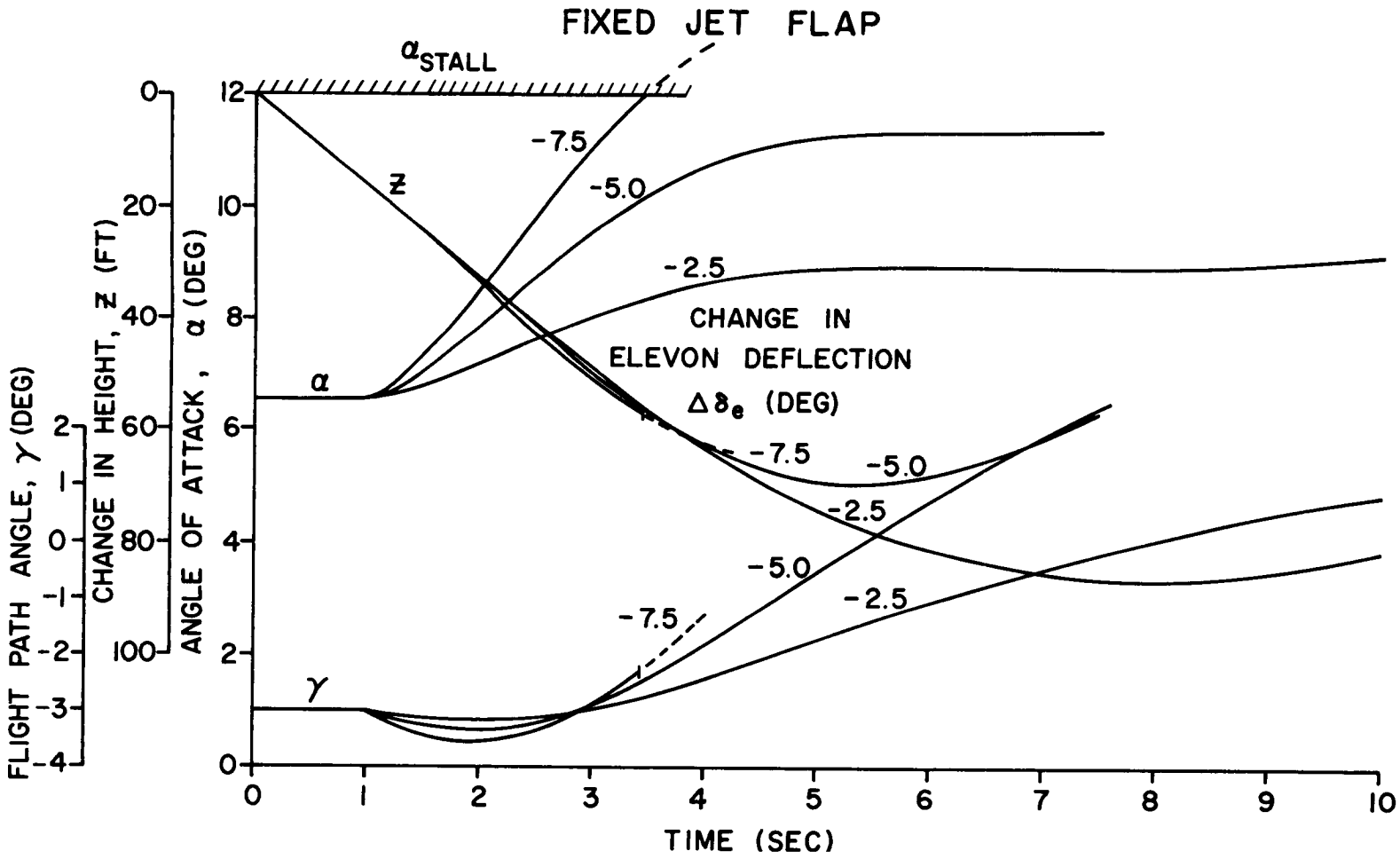

Figure 15

JET CANARD BOOSTER - LONGITUDINAL TIME HISTORIES DURING A FLARE MANEUVER - JET FLAP CONTROL
(Figure 16)

For the same initial conditions shown in the previous figure the jet flap has been given a step command, $\Delta\delta_F$, after one second and held. This positive deflection is a "fly up" command and the vehicle immediately responds in the desired direction. With a 10.0-degree trailing-edge-down flap command the flare is completed 50 feet below the height at time zero and the angle of attack is equal to about 10 degrees. With a 5.0-degree flap command, the flare requires less than 70 feet and the angle of attack is less than nine degrees. Compared with the results shown in the previous figure, it is clear that the jet flap is the preferred control device.

JET CANARD BOOSTER LONGITUDINAL TIME HISTORIES DURING A FLARE MANEUVER JET FLAP CONTROL

FIXED ELEVON

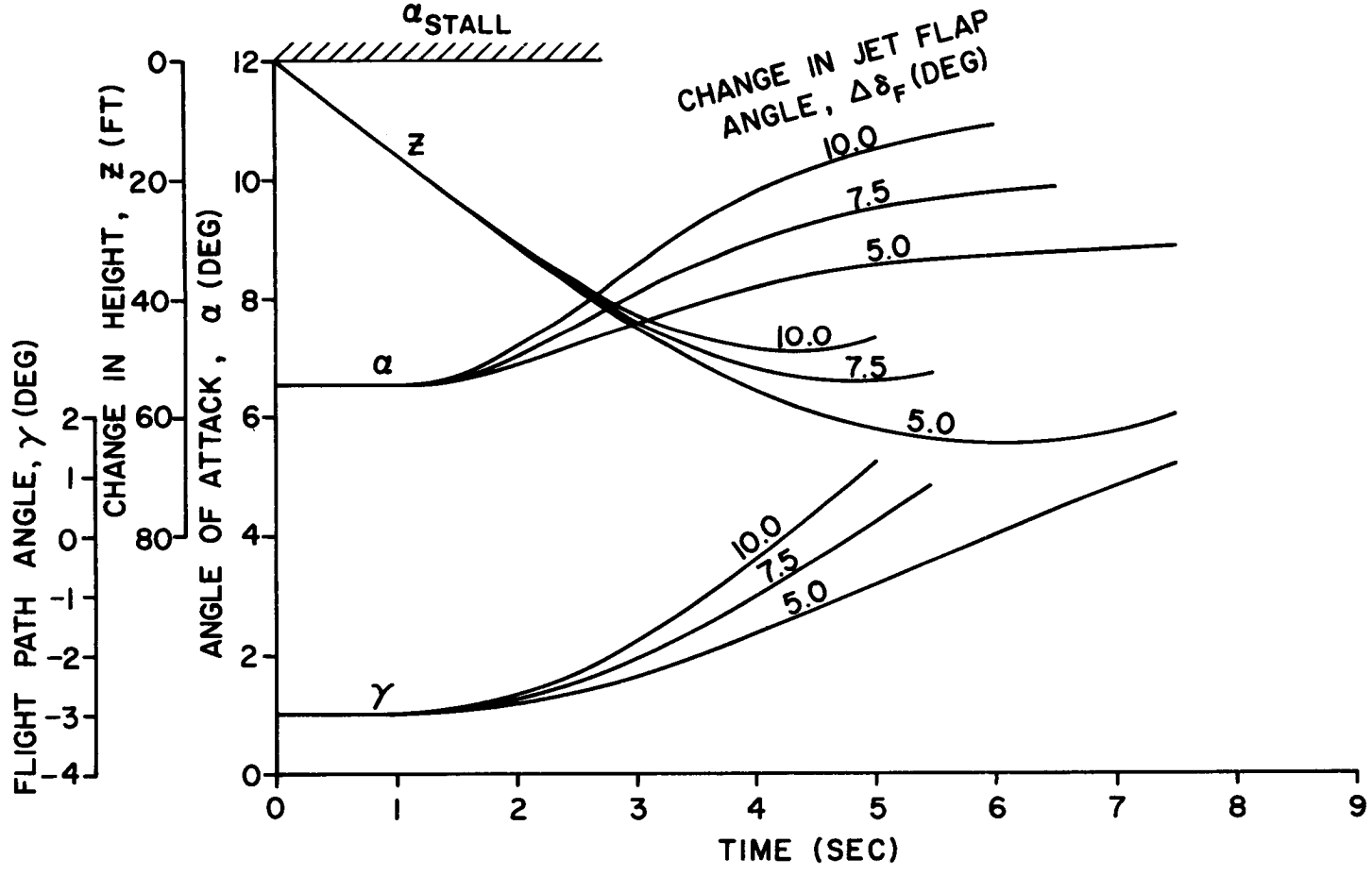

Figure 16

JET CANARD BOOSTER - LONGITUDINAL DYNAMIC CHARACTERISTICS

(Figure 17)

While vehicle response to step control commands can be used to assess the flying qualities of a particular vehicle, there are other requirements which, according to the military specification, must be examined. Shown in this figure are some of the dynamic longitudinal parameters of interest for the jet canard Booster in the landing configuration. The phugoid characteristics are well within the Level I requirements of the specification, i.e. positive damping. The short-period damping ratio exceeds the Level I specification requirement of 0.35, but the period and time to one-half amplitude are not explicity called out by the specification. Rather, a parameter which is supposed to relate to the ability of the pilot to maintain flight path control, $\frac{\omega_n^2}{n/\alpha}$, is used. The frequency, ω_n, is independent of the control device, since it is the frequency of the stick-fixed short-period motion. The load factor per angle of attack, n/α, is essentially the trimmed lift-curve slope. Because the trimmed lift-curve slope using elevon control is less than that using jet flap control, the parameter $\frac{\omega_n^2}{n/\alpha}$ is greater with the elevon control. With either control the parameter is greater than the Level III specification requirement of 0.096, and with the elevon control the parameter exceeds the Level I specification requirement of 0.16. This implies that the elevon control is to be preferred over the jet flap control. However, based on the flare time histories, this is not true. Obviously, no one parameter can be used to determine if a vehicle has satisfactory flying qualities. This little exercise has been used merely to emphasize the point and does not represent an indictement of the flying qualities specification.

JET CANARD BOOSTER
LONGITUDINAL DYNAMIC CHARACTERISTICS
LANDING CONFIGURATION

GROSS WEIGHT = 601,000 LB

V_T = 180 KTS

α = 6.5 DEG

	PERIOD (SEC)	DAMPING RATIO	$T_{1/2}$ (SEC)	$\frac{\omega_{n^2}}{n/\alpha}$		
				JET FLAP CONTROL	ELEVON CONTROL	SPEC. (LEVEL III)
SHORT PERIOD	9.04	0.538	1.57	0.138	0.206	0.096
PHUGOID	74.4	0.094	86.7	———	———	———

Figure 17

JET CANARD BOOSTER - JET CANARD DEVELOPMENT PROGRAM

(Figure 18)

As a result of the analyses conducted during Phase B, we have concluded that the jet-flap canard offers some unique advantages for a flyable Space Shuttle Booster. Since it is not a currently flying system, additional development work must be done prior to its application to the Shuttle Program. Listed in the figure is a proposed development program.

To define the flap geometry which will turn the jet exhaust flow over the ranges of pressure ratio and jet angle required, both theoretical analyses and tests are required. Two-dimensional shock-expansion theory of the static case, along with an analysis of the boundary layer growth on the flap, would be used first. Scale model static tests would then be conducted to check the validity of these analyses. The analyses would be further refined by the inclusion of the effect of the external airflow, followed by experimental verification.

With the flap geometry now defined, those analyses and tests required to provide canard-vehicle integration would be undertaken. Potential flow analysis techniques are readily available to treat the problems associated with the inlet design. A relatively simple inlet-exit test could then be conducted to insure that the presence of the inlet at the leading edge of the canard does not prevent the canard from developing the required circulation lift. Wind tunnel tests would then be conducted with models of the complete configuration to obtain data in both pitch and yaw. The models would be complete with a powered jet-flap canard and also inlet simulation when possible. Such a program would include tests at high Reynolds numbers (e.g. Ames 12-foot). Ground proximity tests would also be conducted including tests with a moving ground plane (e.g. Langley 14.5 x 21.75).

The program outlined thus far has involved only static tests. If deemed necessary, dynamic tests could be conducted in the wind tunnel, but probably not with a powered canard. If the dynamics of the jet-flap canard are of concern they can best be explored by conducting scale model flight tests. The size of the model would depend on the availability of suitable jet engines. Such a model might have other applications to the Space Shuttle program. It could be used to explore some of the unknowns in other flight regimes and thus assist in the development of a satisfactory Space Shuttle Booster.

JET CANARD BOOSTER
JET CANARD DEVELOPMENT PROGRAM

FLAP GEOMETRY

- THEORETICAL ANALYSIS
  2 DIMENSIONAL, NO EXTERNAL AIRFLOW
- SCALE MODEL STATIC TEST
- THEORETICAL ANALYSIS
  2 DIMENSIONAL WITH EXTERNAL AIRFLOW
- TEST WITH EXTERNAL AIRFLOW

CANARD INTEGRATION

- INLET DESIGN
- INLET – EXIT COMPATIBILITY TEST
- COMPLETE VEHICLE POWERED TEST
- SCALE MODEL FLIGHT TEST

Figure 18

LATERAL-DIRECTIONAL CONSIDERATIONS

(Figure 19)

A satisfactory flying machine must satisfy certain longitudinal and lateral-directional requirements. Listed are some of the major items which are influenced by the lateral-directional characteristics.

A configuration which requires a large bank angle to maintain a steady sideslip will require either a crosswind landing gear or must be designed to touchdown in a crabbed attitude.

The static lateral-directional stability and control characteristics will determine the magnitude of the steady sideslip which can be achieved. In addition, the response of the vehicle to lateral gusts is intimately related to the lateral-directional characteristics and the stability augmentation system used to meet desired flying qualities.

Obviously, the lateral-directional characteristics will determine the bare airframe flying qualities and thus establish the degree and sophistication of the stability augmentation system.

LATERAL DIRECTIONAL CONSIDERATIONS

LATERAL DIRECTIONAL STABILITY CHARACTERISTICS IMPACT ON:

- CROSS WIND LANDING
- STEADY SIDESLIP
- GUST RESPONSE
- FLYING QUALITIES

Figure 19

LATERAL-DIRECTIONAL REQUIREMENTS

(Figure 20)

Listed are two of the lateral-directional requirements which have been used to evaluate proposed configuration designs.

The vehicle must be able to land safely in a 30 knot crosswind if the suggested adaptation of the military flying qualities specification (MIL-F-8785B (ASG)) is applied. Douglas Aircraft Company experience would suggest that no more than five degrees of bank should be allowed during the crosswind demonstration.

The military specification requires that the vehicle be able to maintain a steady sideslip of ten degrees in the landing configuration. With the elevator and aileron functions provided by elevons, only part of the individual surface throw of 30 degrees is available for each function and a 50-50 split between elevator and aileron was selected. This results in a total aileron deflection ($\delta a_{left} - \delta a_{right}$) available of 30 degrees. The rudder throw has been set at $\pm$ 30 degrees, but the round-over in rudder effectiveness results in a maximum effectiveness for a linear analysis equivalent to $\pm$ 25 degrees.

LATERAL-DIRECTIONAL REQUIREMENTS

CROSS WIND LANDING REQUIREMENTS

- 30KT. CROSS WIND (MIL SPEC)
- BANK ANGLE $\leq 5°$ (DAC)

STEADY SIDESLIP REQUIREMENTS

- 10° SIDESLIP DURING LANDING APPROACH (MIL SPEC)
- TOTAL AILERON DEFLECTION AVAILABLE = 30°
- TOTAL RUDDER DEFLECTION AVAILABLE = 30° (EQUIVALENT TO 25° FOR LINEAR ANALYSIS)

Figure 20

JET CANARD BOOSTER - COMPARISON OF STEADY SIDESLIP CHARACTERISTICS

(Figure 21)

The figure shows how hypersonic and subsonic design considerations resulted in the final Booster configuration.

The results of a hypersonic reentry control trade study led to the selection of rolled out dorsal tip fins so that the vehicle could be flown with aerodynamic controls rather than using a large number of reaction control thrusters. However, as can be seen from the figure, this configuration had insufficient aileron authority to achieve the required ten degrees of steady sideslip. In fact, as the sign of the rudder deflection indicates, the configuration was unstable and had insufficient rudder and aileron to keep it from exceeding about six degrees of sideslip.

The addition of the ventrals to form the lazy-Y tip fins resulted in a configuration which easily met the steady sideslip requirement. Incidently, this configuration was also satisfactory in the hypersonic flight regime.

Neither configuration can meet the 30-knot crosswind landing requirement without crab. With five degrees of bank angle and no crab, the allowable crosswind is about nine knots. About nine degrees of crab would be required for a wings level landing in a 30-knot crosswind. With five degrees of bank the crab angle is reduced to about six degrees.

JET CANARD BOOSTER
COMPARISON OF STEADY SIDESLIP CHARACTERISTICS
DORSAL TIP FINS AND LAZY-Y TIP FINS

LANDING APPROACH

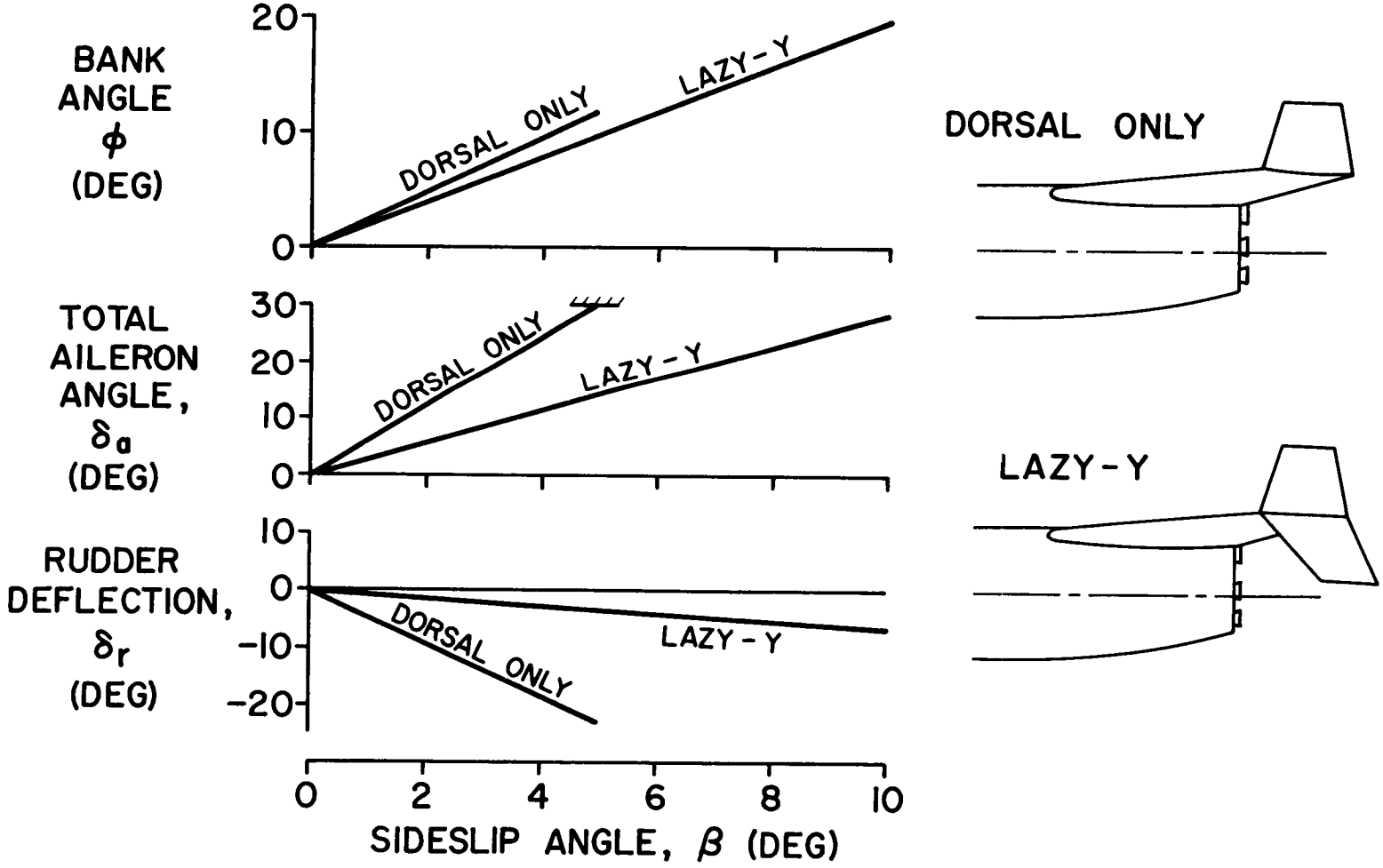

Figure 21

JET CANARD BOOSTER - COMPARISON OF GUST RESPONSE TO A THUNDERSTORM LEVEL DISCRETE GUST
(Figure 22)

Military flying quality specifications have long required that an aircraft have the capability to achieve at least ten degrees of steady sideslip in the landing configuration. Commercial practices have also used this requirement as a design-to goal. With a directionally unstable vehicle, the requirement has less meaning, since the problem is not one of enough control to obtain ten degrees of sideslip, but rather is one of preventing the sideslip from exceeding ten degrees. Only after detailed gust analyses have been conducted is it possible to determine if this requirement need not be met. However, based on the limited gust analyses conducted to date, the requirement seems to work. This is best illustrated by comparing the dynamic response to a discrete (1 - cos type) thunderstorm gust for the two Booster configurations shown in the previous figure. The results are shown below for the case where the surface deflections and the aileron rate for the dynamic response were unlimited, but the rudder rate was limited to 30 degrees per second. Both configurations were augmented so that the Dutch-roll mode was well damped. As can be seen, with the dorsal tip fins, the configuration needed more aileron and rudder than was available to handle the gust, while the lazy-Y configuration had control authority left over. During the configuration development phase of a program there is seldom time to conduct these detailed gust response studies. As a result of the exercise just discussed we would recommend that, during a preliminary design phase, the ten degree steady sideslip requirement be maintained.

JET CANARD BOOSTER
COMPARISON OF GUST RESPONSE TO A THUNDERSTORM LEVEL DISCRETE GUST

DORSAL TIP FINS AND LAZY-Y TIP FINS STABILITY AUGMENTATION AS REQUIRED TO MEET LEVEL I DUTCH-ROLL CHARACTERISTICS

GUST VELOCITY = 42 FPS

V_T = 180 KTS

GUST PERIOD = 5.2 SEC

α = 4°

	PEAK RESPONSES			
	DORSAL TIP FINS		LAZY-Y TIP FINS	
SIDESLIP ANGLE (DEG)	6.2	- 5.6	6.0	- 4.9
RUDDER DEFLECTION (DEG)	41.8	-37.6	8.2	- 8.8
RATE (DEG/SEC)	30.0	-26.2	9.6	- 6.2
AILERON DEFLECTION (DEG)	43.6	-45.4	19.0	- 16.8
RATE (DEG/SEC)	29.8	-41.2	13.0	- 20.2
BANK ANGLE (DEG)	4.6	- 3.2	2.3	- 2.0
HEADING CHANGE (DEG)	4.7	- 0.1	3.7	- 0.2

Figure 22

JET CANARD BOOSTER - UNAUGMENTED DUTCH-ROLL CHARACTERISTICS

(Figure 23)

The unaugmented Dutch-roll characteristics of the Booster with the lazy-Y tip fins are tabulated here. The configuration is slightly undamped during cruise due, primarily, to the aft location of the c.g. associated with the cruise configuration. With the c.g. further forward, in the landing configuration, the damping is slightly positive. For comparison purposes, the minimum military specification requirements are tabulated, along with the characteristics of the aircraft often used as the "standard of the world" for-jet transport flying qualities, the DC-8. This table indicates that with these unaugmented characteristics, a relatively unsophisticated augmentation system can be implemented to provide the Booster with adequate Dutch-roll damping.

JET CANARD BOOSTER
UNAUGMENTED DUTCH ROLL CHARACTERISTICS
CRUISE AND LANDING

LAZY-Y TIP FINS

GROSS WEIGHT = 601,000 LB

CONDITION	ALT (FT)	SPEED (KTAS)	α (DEG)	FREQ (RAD/SEC)	PERIOD (SEC)	DAMPING RATIO	$T_{1/2}$ (SEC)	T_2 (SEC)
CRUISE	20,000	334	5	0.403	15.6	-0.069	--	25
LANDING	SL	180	6	0.504	12.5	0.037	37	--
MIL SPEC (LEVEL III)				0.4	15.7	0.02		
DC-8 LANDING				0.9	7.0	0		

Figure 23

SUMMARY

It has been shown how considerations of cruise-back efficiency and subsonic flying qualities resulted in a configuration with an aft high wing of moderate aspect ratio and with the vertical tails located at the wing tips. The need to protect the air breathing engines during ascent and re-entry and the desire for a low trim penalty longitudinal control surface led to consideration of a jet-flap canard. The advantages of this application of STOL technology to a space system were examined and the results of both wind tunnel tests and flight simulations were discussed. Since the use of the jet-flap canard concept offers the potential for a minimum weight vehicle, a proposed technology development program was outlined in order that the full benefit of this concept may be realized.

AERODYNAMIC STUDIES OF DELTA-WING SHUTTLE ORBITERS

PART I – LOW SPEED

By Delma C. Freeman, Jr., and James C. Ellison
Langley Research Center

INTRODUCTION

(Figure 1)

As part of the continuing effort to develop technology for the space shuttle, numerous wind tunnel tests, both contractor requested and in-house, have been conducted at Langley on the evolving delta-wing orbiters. These tests have generated a fairly large aerodynamic data base over the entire entry operation range of these vehicles. The recent changes in design philosophy have resulted in changes in the shuttle system. Although, as shown in figure 1, there are changes in the orbiter vehicle, experience in other programs has shown that while there are configuration differences, the existing aerodynamic data base for this generic class vehicle should be very useful in pointing out the problem areas uncovered in the preliminary studies giving insight into the design of the new generation orbiters. With the proper application of the results of the phase B studies, the emerging vehicle designs should be reasonably mature from the outset.

In this presentation a limited assessment will be made of some of the aerodynamics of the current HO type orbiters. Several specific problem areas have been selected for discussion from the broad available data base. These include, from a subsonic viewpoint, discussion of trim drag effect; effects of the installation of main rocket engine nozzles, OMS and RCS packages, Reynolds number effects, lateral-directional stability characteristics, and landing characteristics. The second part of the paper will discuss nose shape effects and lateral-directional stability and control in the hypersonic regime.

DATA BASE APPLICATION

PHASE B CONFIGURATIONS

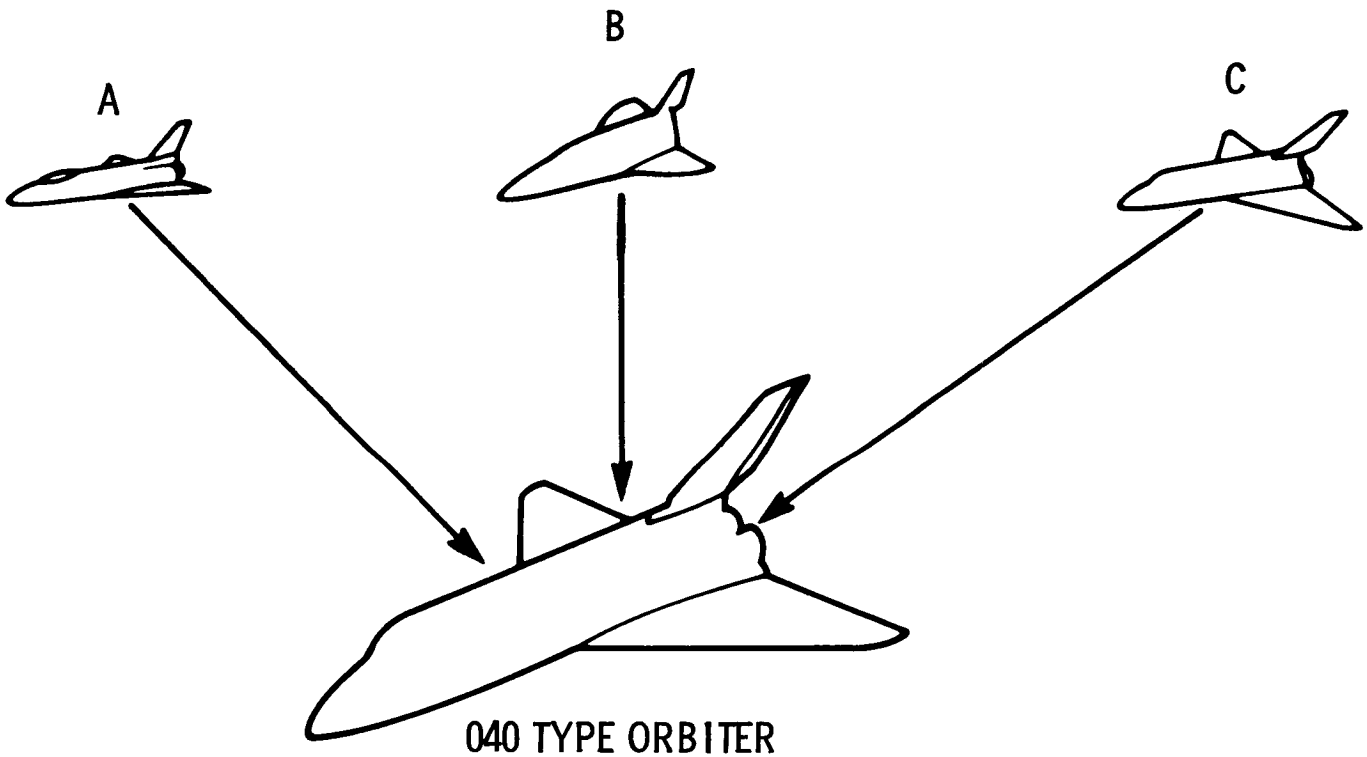

040 TYPE ORBITER
EXTERNAL LO_2/LH_2 TANK
MARK I - MARK II APPROACH

Figure 1

EFFECT OF TRIM ON SUBSONIC PERFORMANCE

(Figure 2)

The phase B orbiter studies to date have produced a diversity of generically similar vehicle concepts. Significant differences exist in these vehicles, however, and result primarily from considerations other than aerodynamics such as structural design concepts and internal arrangement philosophy. Differences exist also in the approaches taken by the various designers in matching the lifting components to the bodies of these vehicles. The results shown here are representative of some of the resulting aerodynamic characteristics for three configurations; on the left, the performance change associated with trimming the vehicles and on the right the basic longitudinal stability characteristics of each. The differences in trim penalty are relatively large but the indication is that these penalties can be minimized. Configuration C has essentially no penalty at lift coefficients above the somewhat artitrary lower operating boundary of 0.25, and does in fact show improvement at $C_L > 0.3$. This characteristic is associated first with the lower static margin of the concept with the attendant smaller out-of-trim moments and corresponding lower control deflections required to trim. Secondly, a favorable choice of wing twist, camber, incidence, and sweep, in conjunction with the reduced base drag impact of the small elevon deflection, minimizes the penalty. On the basis of these and other results, the proper design approaches to minimizing the trim penalties now appears to be understood.

EFFECT OF TRIM ON SUBSONIC PERFORMANCE

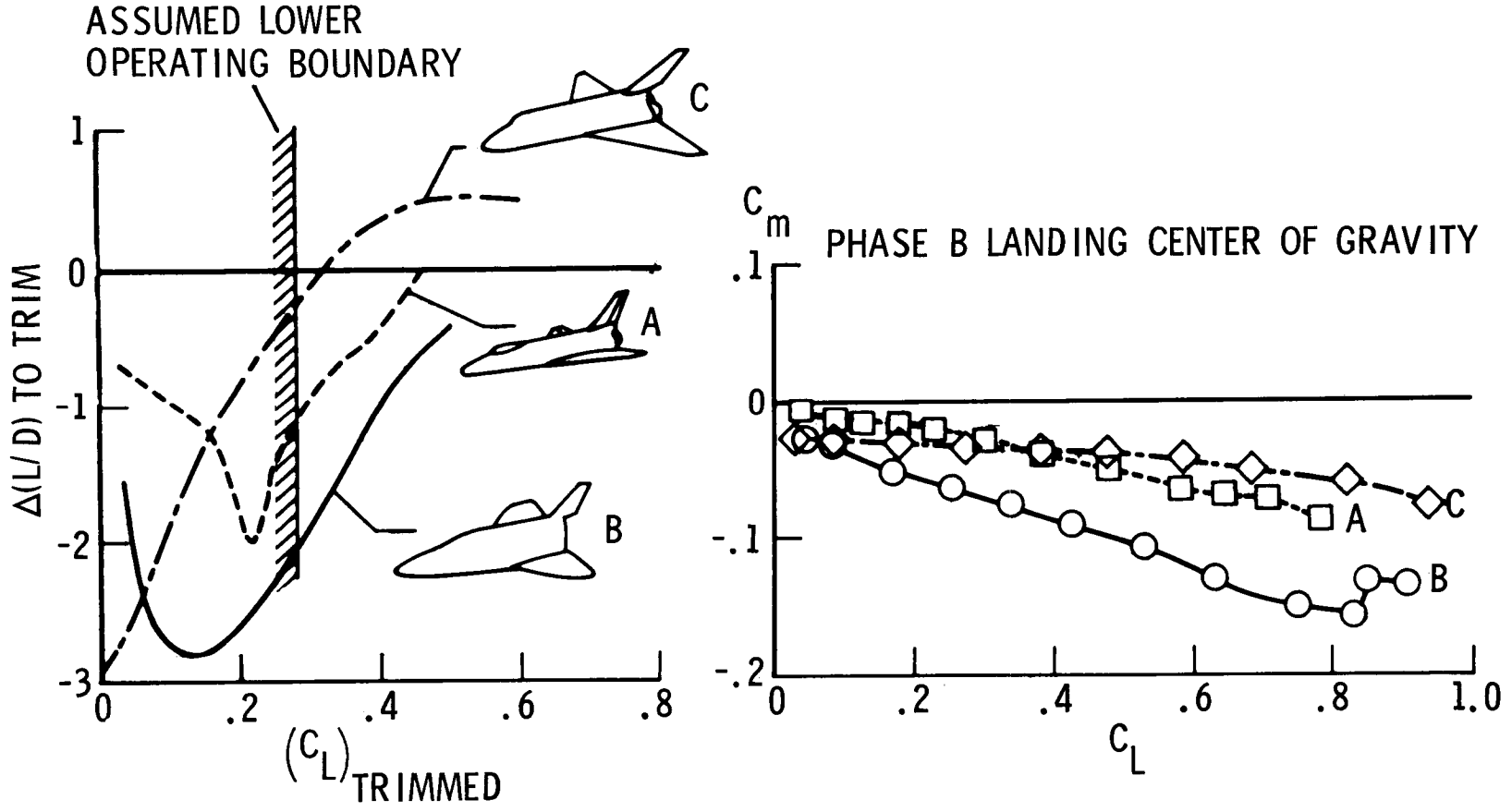

Figure 2

NOZZLE, OMS, AND RCS EFFECTS

(Figures 3 and 4)

An indication of the effect of externally podded OMS and RCS installation on subsonic performance has been derived from tests of an in-house parametric delta-wing orbiter and the influence of main rocket engine nozzles from tests of one of the phase B orbiters. The results on the left (fig. 3) show that the installation of OMS packages (see fig. 4), decreased the maximum untrimmed L/D by 0.5. Installing RCS pods on the wing tips and the tip of the vertical fin decreased the maximum untrimmed L/D by 1.0. The data on the right show that the installation of the main rocket engine nozzles on the phase B configuration had no effect on the subsonic performance. Results from wind-tunnel tests just completed on the MSC 040A tend to support some of these findings; they show a decrement in maximum untrimmed L/D of about 1.7 for OMS and RCS installation which is similar to that shown in figure 4. Previous results, not shown, have indicated that OMS packages can, by proper placement, be utilized to improve the $C_{m,o}$ characteristics of the vehicles. It is not to be implied that the performance levels of the orbiter vehicles will necessarily be reduced by this amount, but it is felt, that the compromises to the external shape for installation of these devices should be kept to a minimum. These effects can be minimized by proper shaping and location of the pods. This condition becomes more important with the elimination of airbreathing engines and go-around capability, since the addition of uncertainties such as surface roughness and base drag effects to the effects just discussed may reduce the performance levels of these vehicles to the point that approach glide slope margins may become the critical design case.

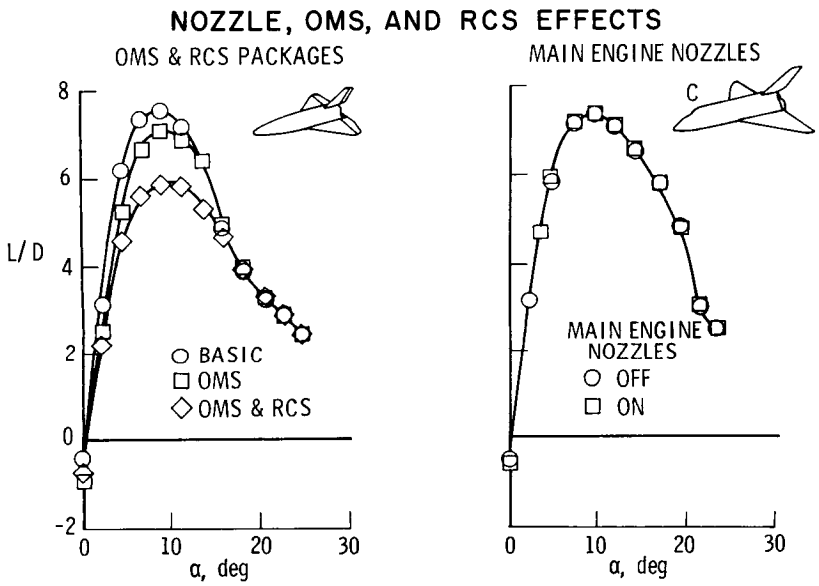

Figure 3

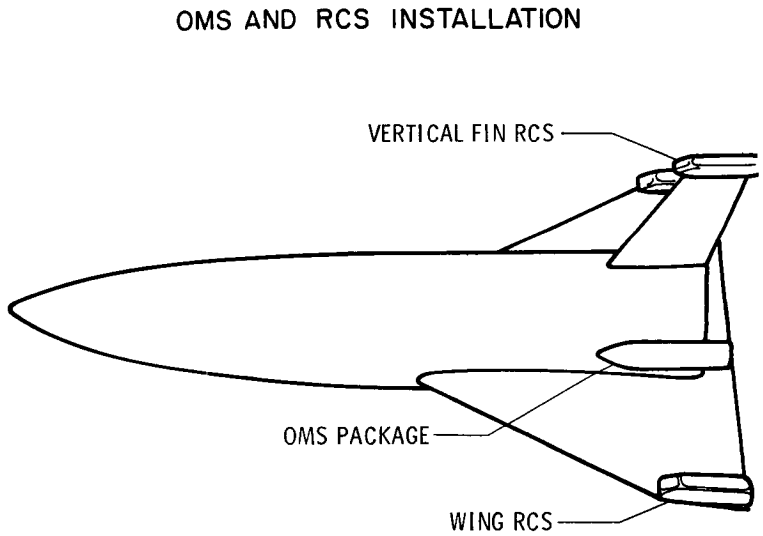

Figure 4

SUBSONIC LATERAL-DIRECTIONAL CHARACTERISTICS

(Figures 5 and 6)

During the phase B studies, one of the major aerodynamic design problems has been the achievement of desired levels of directional stability. These problems have been complicated by the close coupling of the vertical tail and center of gravity combined with bodies having a large lateral area ahead of the center of gravity. Figure 5 shows the results of some subsonic wind-tunnel tests made to determine the effect of vehicle components (body, body vertical tail, body-wing, and body-wing-vertical tail combinations) on the directional stability of two of the phase B orbiters – one representative of a high profile body design (configuration B) and one representative of a low profile body (configuration A). From the data it can be seen that configuration B is about 50 percent more unstable than configuration A. Adding the wing to the body had very little effect on configuration A; however, it had a very large destabilizing effect on configuration B and resulted in directional instability at an angle of attack of about 8° for the complete configuration (BWV). Figure 6 is an illustration of the origin of the large wing-body instability, as determined from tuft studies. With the model yawed, a vortex forms in the windward wing fuselage juncture and sweeps rearward along the body; as a result, a negative pressure gradient with a resulting destabilizing yawing moment is created. Efforts by MDAC and ERNO to improve the directional stability of the orbiter by altering the wing fuselage juncture by changing planform shape, body cross section, thickness, and camber combined with a high-aspect-ratio vertical tail made the configuration directionally stable. Experience has shown that the wing-body juncture must be shaped to reduce the strength of the vortex (by increased leading-edge radius with less sweep or shorter transition into the body nose) and/or reshaping the body sides to minimize the vortex interaction in this region.

SUBSONIC LATERAL–DIRECTIONAL CHARACTERISTICS

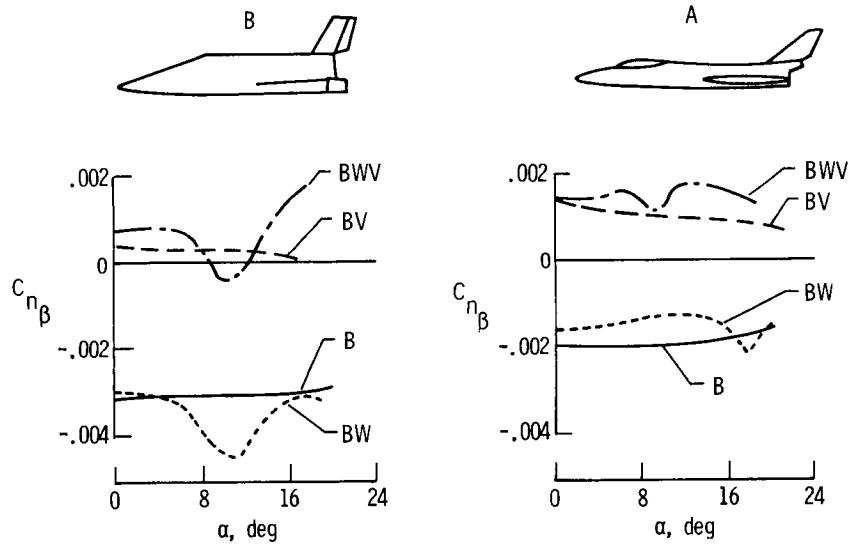

Figure 5

VORTEX IMPINGEMENT

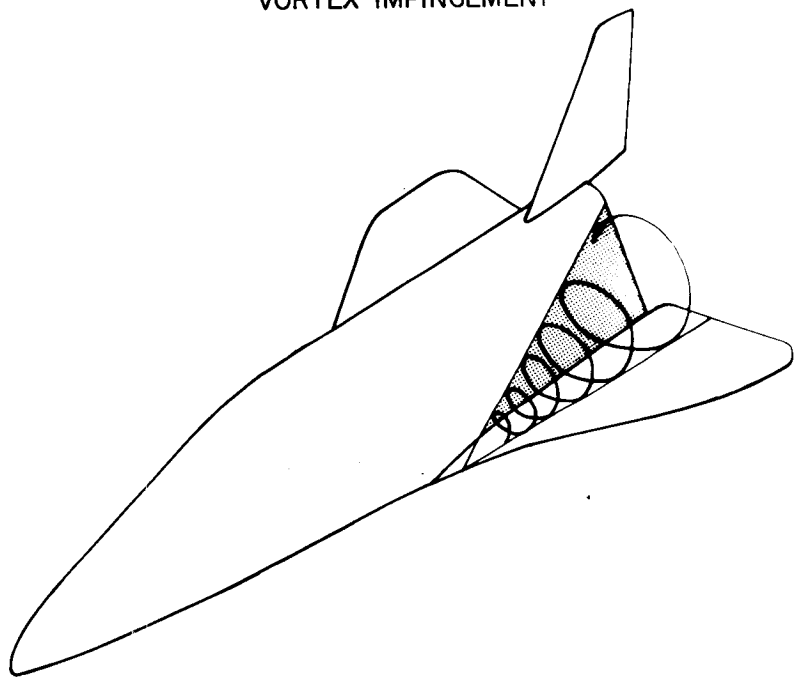

Figure 6

ERNO TEST RESULTS

(Figure 7)

As previously discussed, considerable effort has been expended by the contractor of configuration B in his own facilities and at ERNO in Germany. The results of these tests presented in figure 7 show that by altering the wing fuselage juncture, the directional instability of the wing-body combination was greatly reduced. The reduced wing-body instability in combination with the addition of a high aspect ratio vertical tail eliminated the directional instability for this configuration.

ERNO TEST RESULTS

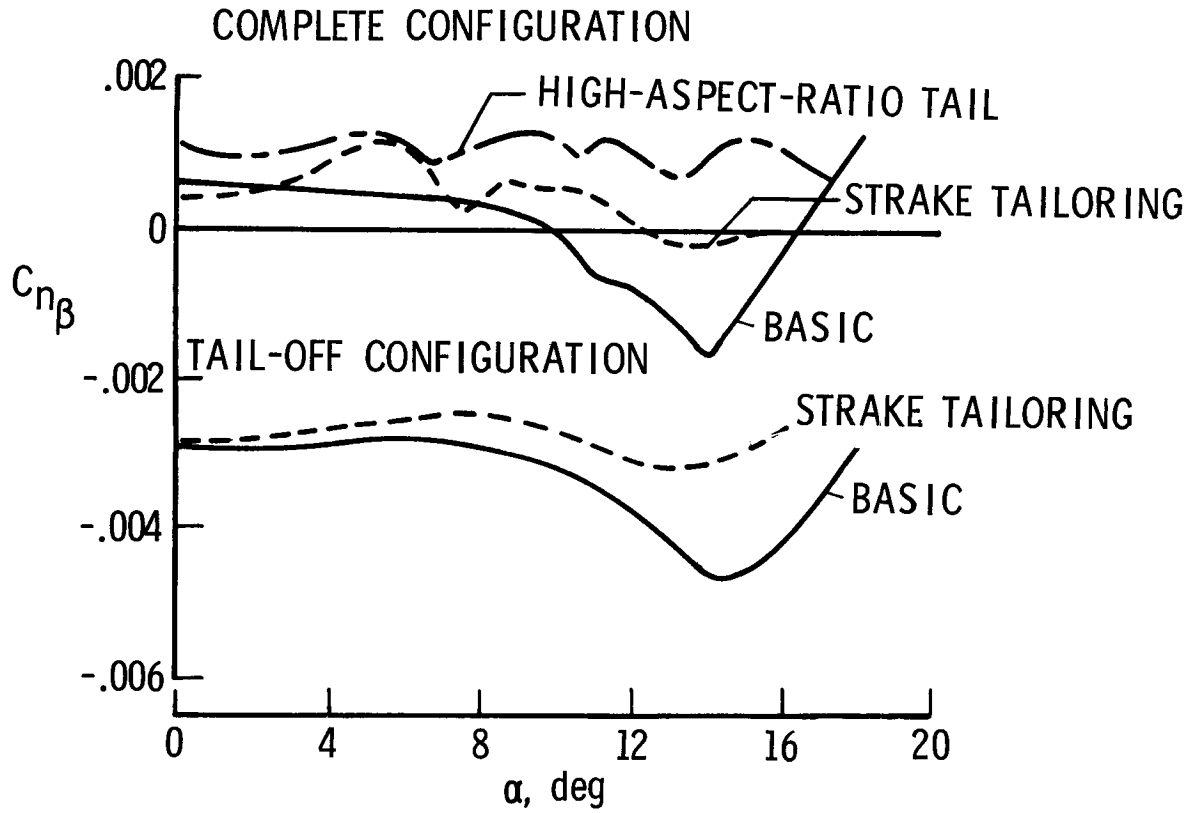

Figure 7

SUBSONIC REYNOLDS NUMBER EFFECTS

(Figure 8)

Since the results presented in figure 5 indicate that lateral-directional characteristics are influenced by vortex formation, tests have been made to determine the effects of Reynolds number on the lateral-directional characteristics of one of the phase B configurations. At a Reynolds number of 15×10^6, based on body length, $(L/D)_{max}$ and C_A at $(L/D)_{max}$ indicate that supercritical Reynolds numbers have been achieved and any changes above this Reynolds number are small and result from reductions in skin-friction drag. The lateral-directional data are presented on the right for angles of attack of 0° and 17° which was the proposed landing attitude for this configuration. These results indicate that increasing the Reynolds number from 15×10^6 to 30×10^6 resulted in a 25 percent increase in C_{n_β} and a large decrease in C_{l_β} at $\alpha = 17^\circ$. These effects are the results of the weakening of the wing vortex as the Reynolds number is increased; thus, the vertical tail is more effective in one case and causes tip stall on the leading wing in the other case. For this configuration, both of the Reynolds number effects discussed are favorable; increased C_{n_β} results in more directional stability at landing and decreased C_{l_β} would give better Dutch roll damping and cross-wind landing characteristics. In addition to those discussed, Reynolds number effects have been seen on the lateral-directional characteristics of the other phase B configurations; thus, increased emphasis should be placed in this area because of a greater sensitivity of these parameters relative to the longitudinal characteristics. This certainly must be the case as the configurations mature since it has been shown that most of the stability and control problems for this class of vehicle appear in the lateral-directional mode.

SUBSONIC REYNOLDS NUMBER EFFECTS

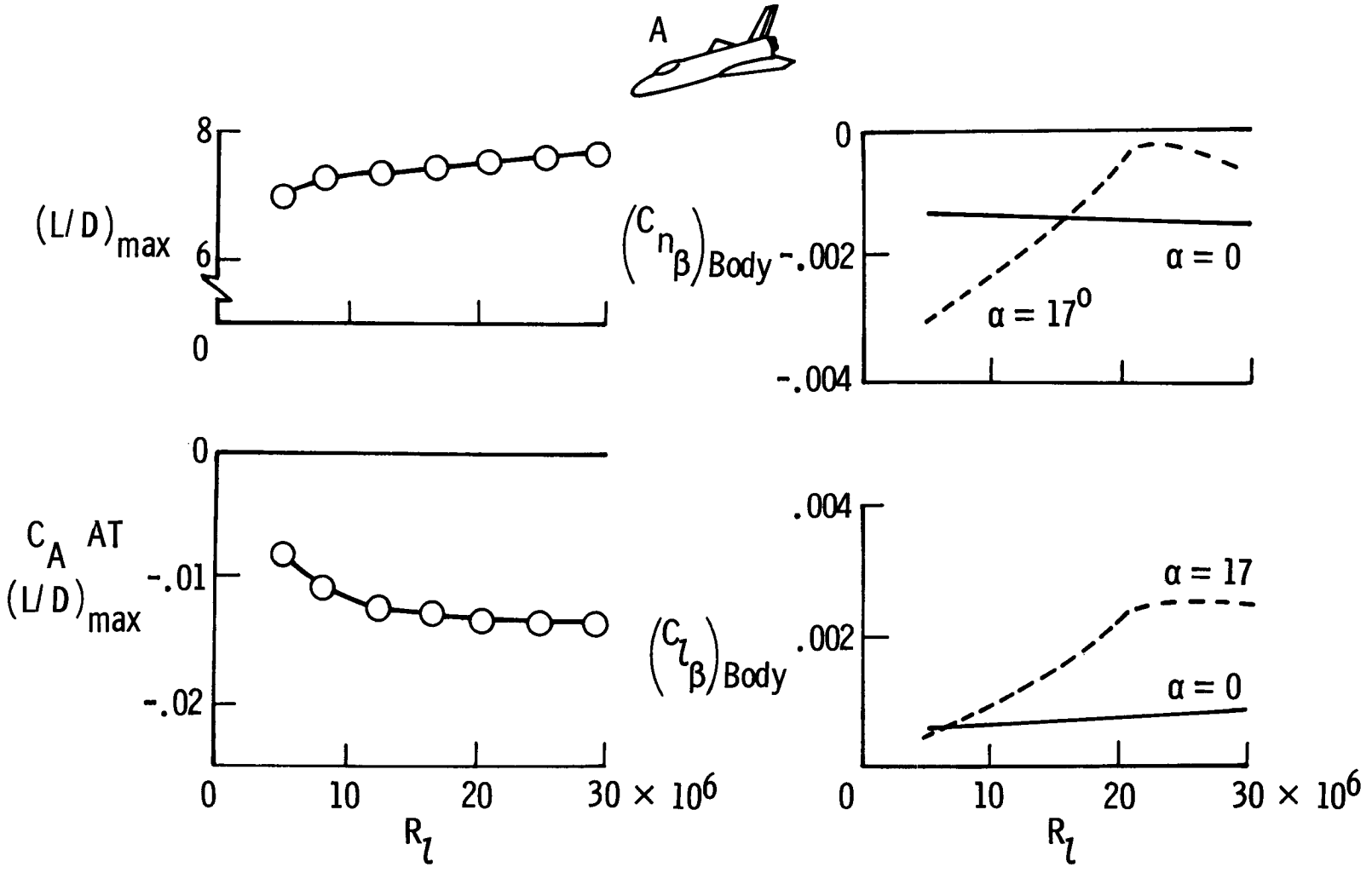

Figure 8

ORBITER LANDING PARAMETERS

(Figures 9 and 10)

Landing calculations have been made to define some of the terminal area requirements of three of the phase B configurations and an 040 type orbiter. For the purpose of these calculations, phase B aerodynamics and weights, along with estimated aerodynamics and weights, of an 040 type orbiter were used. The input for these calculations is presented in figure 9. The calculations were made to determine the effect of the W/SC_L and approach speed margins on wet FAR landing-field length using constant normal load factor flares. For this purpose, approach speed margin is referenced to $(V_{MIN})_{DES}$ as defined in the figure. Note that this value is not the normal V_{stall}. The approach speed margins were calculated for all the configurations at an assumed angle of attack of 17° for comparison purposes, since this value is approximately the landing attitude of two of the phase B configurations. The results presented in figure 10 were calculated for an approach glide slope of 12° with a constant normal load factor flare of 1.4. The set of conditions used for the calculations is just one of any number of conditions that could be flown by these vehicles, but it is felt that these conditions are representative, and are valid for comparison purposes. Results indicate that as W/SC_L is increased, the range of approach speed margins available is decreased for all weather operations on a specific runway, in this case 3048 meters (10 000 ft). This narrowing of the corridor of available approach speed margins is important in the transition from the Mark I to the Mark II vehicle since, because of the increased landed payload weight, the W/SC_L of the Mark II vehicle will be increased and thus it will be the critical design case.

ORBITER LANDING PARAMETERS

PAYLOAD, 18 144 kg (40 000 lb); AIRBREATHING ENGINES OUT

ORBITER TYPE	A FR	B FR	C H	D * HO
α_{max}, deg	17	17	17	17
W/S, kg/m^2	202.1	203.6	243.1	271.5
W/SC$_L$, kg/m^2	396.4	442.8	398.4	420.9
$(V_{MIN})_{DES}$, kts	155	163.5	155	159

* ESTIMATED AERODYNAMICS AND WEIGHTS

Figure 9

LANDING CALCULATION RESULTS

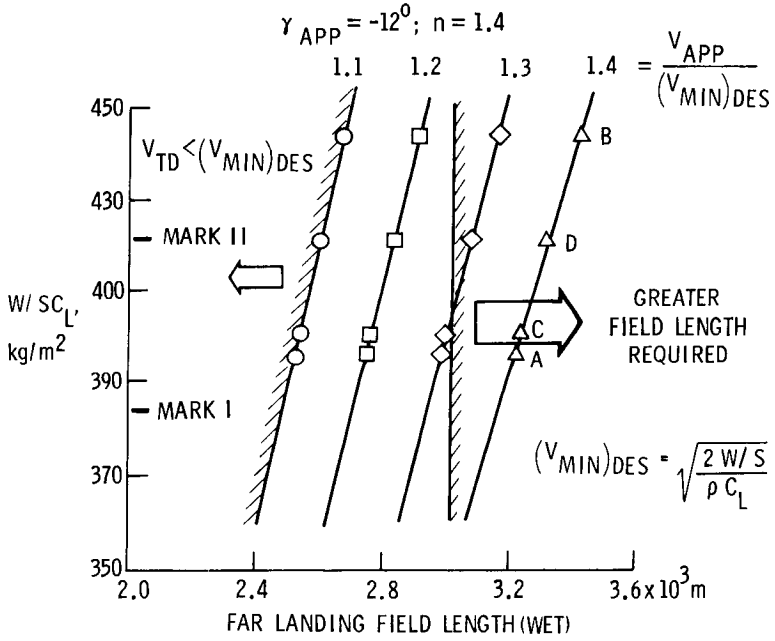

Figure 10

CONCLUSIONS

The assessment of the phase B orbiter data base has pointed out several problem areas of the delta-wing orbiter. Many of these problems are not new to the aerodynamists, but an effort has been made to relate these problems specifically to the design of the HO type orbiters. Examples of these problem areas are:

(1) Installation of main engine nozzles, OMS and RCS packages decrease subsonic performance considerably. Adding the effect of surface roughness and base drag to the effects of OMS and RCS installation could result in performance level so low the approach glide slope margin could be the critical design case for these vehicles.

(2) The indications are that increased emphasis should be placed on lateral-directional characteristics as affected by Reynolds number due to an increased sensitivity of these parameters relative to the longitudinal characteristics. This certainly must be the case as configurations mature since it has been shown that most of the stability and control problems for this class vehicle appears in the lateral-directional mode.

(3) As expected, the results of landing calculations show that the narrowing of the corridor of available approach speed margins is important since in the transition from the Mark I to the Mark II vehicle because of increased landed payload weight, the Mark II vehicle would have a smaller range of approach speed margins available, making the Mark II vehicle the critical design case.

SYMBOLS

C_A	axial-force coefficient
C_L	lift coefficient
C_{l_β}	rolling moment due to sideslip
C_m	pitching moment
$C_{m,o}$	pitching moment at zero lift
C_{n_β}	yawing moment due to sideslip
L/D	lift-drag ratio
$\Delta(L/D)$	incremental lift-drag ratio
n	normal load factor
R_l	Reynolds number based on body length
S	wing area
W	weight
α	angle of attack
ρ	density

Subscripts:

max	maximum
MIN	minimum
DES	design
APP	approach

AERODYNAMIC STUDIES OF DELTA-WING SHUTTLE ORBITERS

PART II – HYPERSONICS

By Howard W. Stone and James P. Arrington
Langley Research Center

BASELINE STUDY CONFIGURATION

(Figure 1)

An early (September 1971) version of an external hydrogen-oxygen tank orbiter, derived by MSC and designated 040A, has been used as a baseline vehicle to experimentally evaluate: (1) nose shape and canopy effects on longitudinal, lateral, and directional stability and trim, and (2) yaw due to aerodynamic roll control at hypersonic speeds. Nose alterations were examined since this part of the vehicle may be subject to modifications because of internal packaging requirements, alleviation of potential high heating areas, and/or possible improvements in aerodynamic stability and control. There was also some concern about the effect of the rather high profile canopy on the aerodynamics; therefore, its removal was examined. In addition, roll-yaw coupling was investigated because of its impact on the RCS fuel requirements for entry maneuvers.

The configuration shown in figure 1 was tested with OMS pods on the sides of the body and RCS pods on the tips of the wings and vertical tail. The 0.005-scale model had a reference area of 73.28 cm^2, a mean aerodynamic chord of 7.74 cm, and a span of 11.2 cm. The center of gravity was at 66 percent of the body length (l = 16.7 cm) along the reference payload center line.

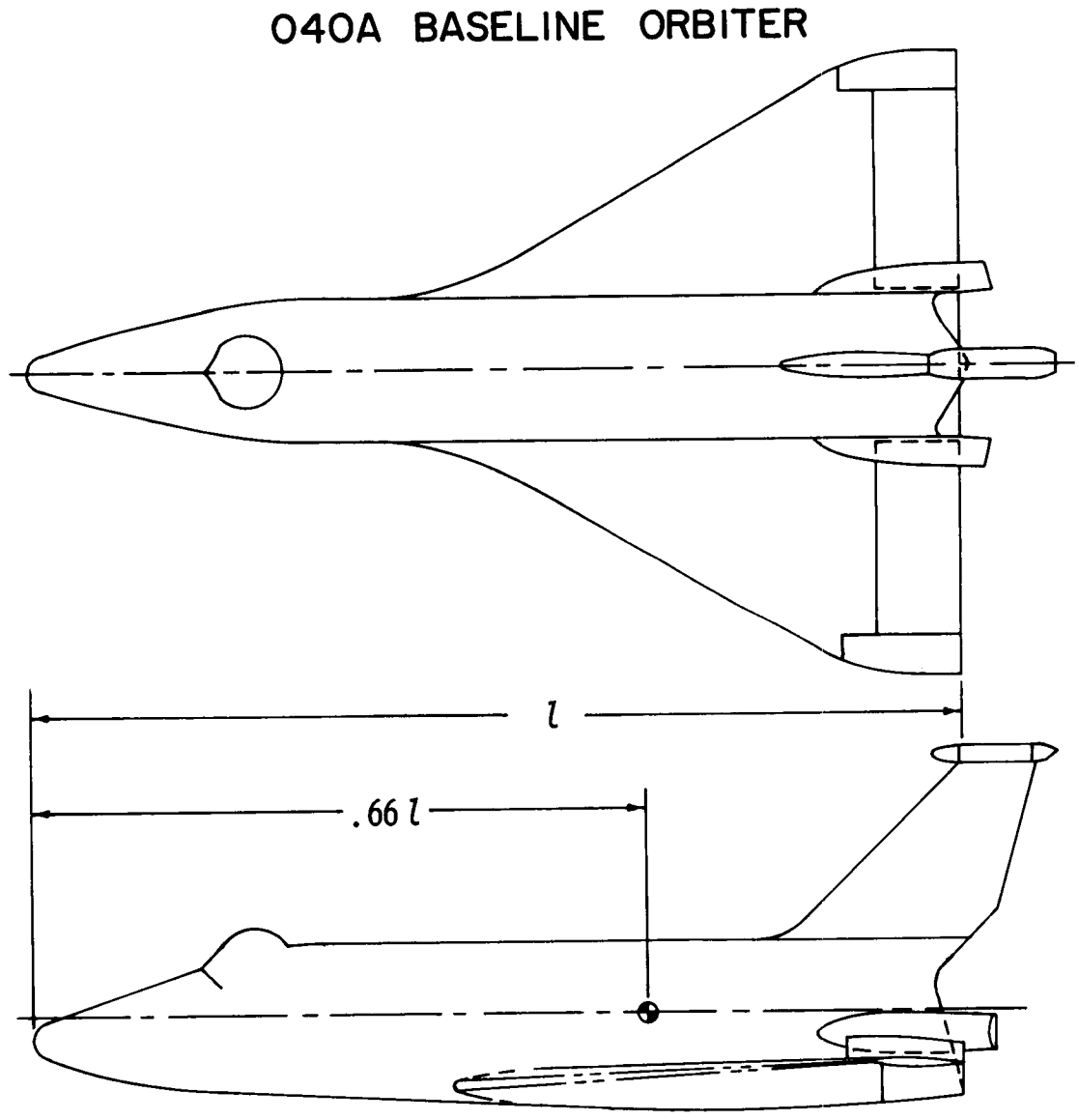

Figure 1

ELEVON-CONTROL EFFECTS OF BASELINE ORBITER

(Figure 2)

The tests were conducted at $M = 20$ and at a Reynolds number of 2.4×10^6, based on body length, in the Langley 22-inch helium tunnel. The results of the elevon control effectiveness of the baseline orbiter show that the vehicle trimmed with longitudinal static stability from angles of attack for $(L/D)_{max}$ to $C_{L,max}$ without positive elevon deflections. The OMS pods in their original location prevented the elevons from deflecting further than -30^o; however, the elevons-off case gave an indication of the maximum trim capability. With this wide longitudinal trim angle range and the L/D capability $\left((L/D)_{max} = 1.9\right)$, the vehicle meets the shuttle high cross-range aerodynamic requirements.

ELEVON-CONTROL EFFECTS ON BASELINE ORBITER

$M = 20,\ R_l = 2.4 \times 10^6$

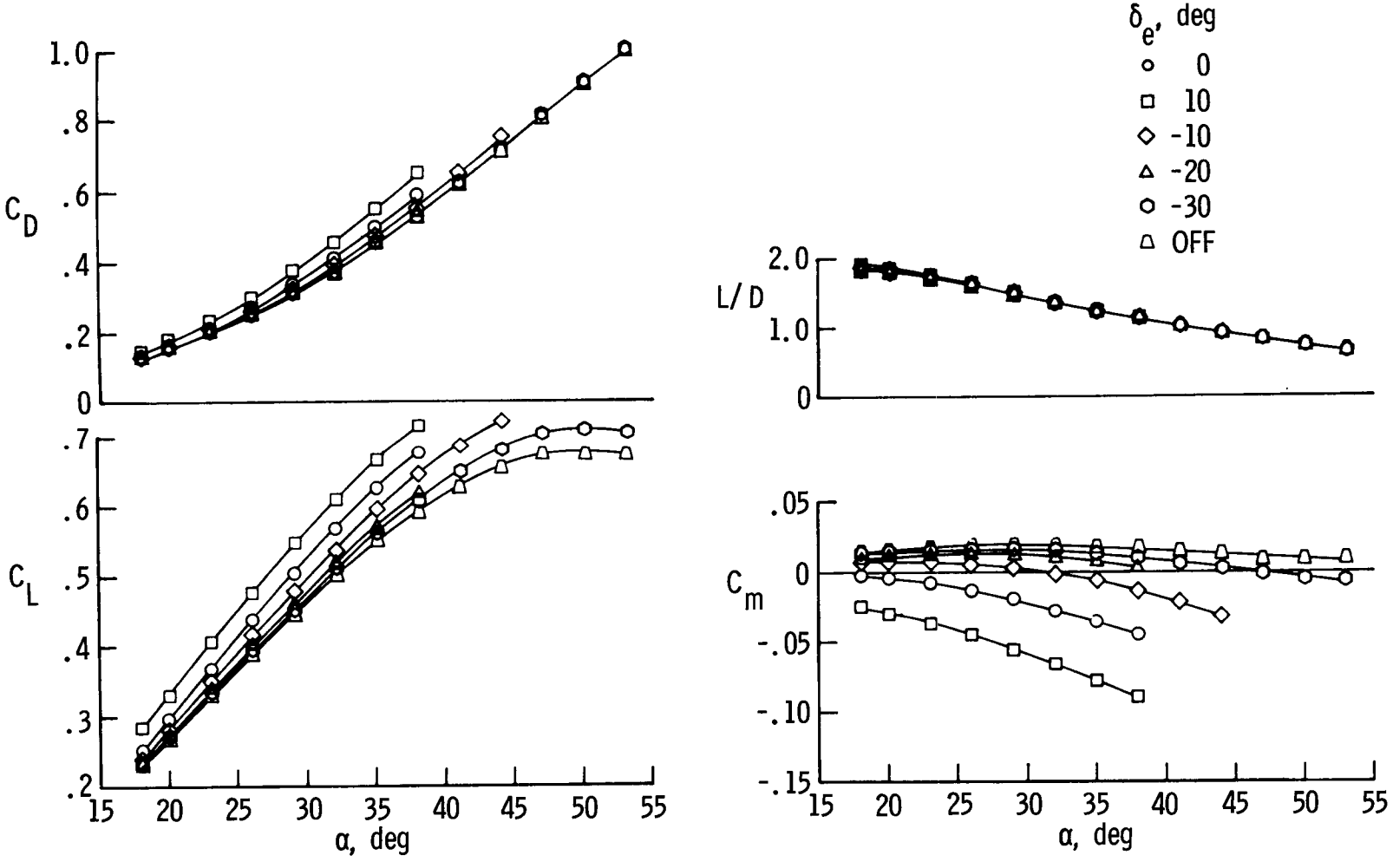

Figure 2

NOSE SHAPE VARIATIONS

(Figure 3)

The baseline nose was altered by changing the cross section and the profile from x/l stations of 0 to 0.3 while the planform remained the same. As shown on the right of figure 3, the cross-sectional changes included square, circular, and trapezoidal shapes with the same baseline planform and profile. Therefore, the effects of nose cross section on the longitudinal and lateral-directional aerodynamics could be isolated. The baseline nose was also tested with and without the canopy.

The trapezoidal cross section was also evaluated on a nose with the lower foreramp removed (the body lower surface was extended forward at a 3° angle as shown in the left-hand part of the figure) to indicate the extent of the camber effect on the longitudinal trim angles. This nose also had the same planform as the others tested, and the cross-sectional heights were identical. However, the canopy was removed.

NOSE SHAPE VARIATIONS

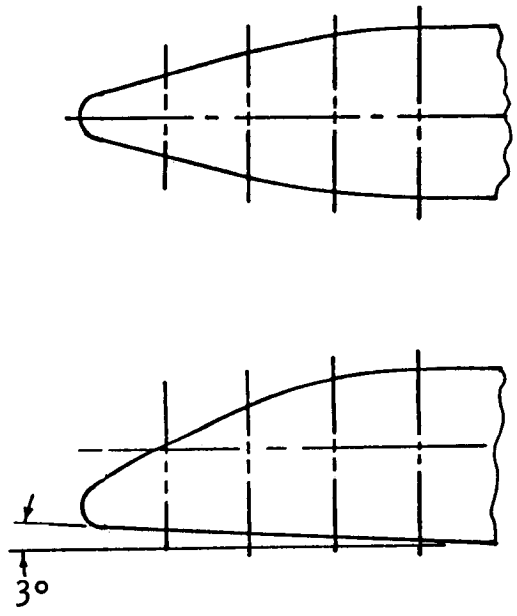

TRAPEZOIDAL
FORERAMP REMOVED

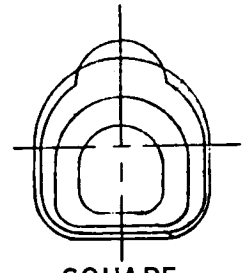

SQUARE

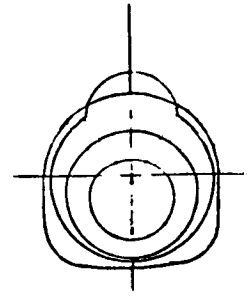

CIRCULAR

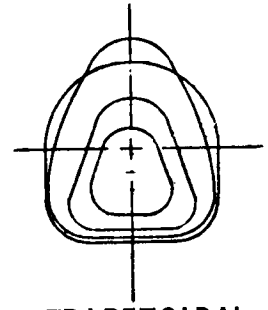

TRAPEZOIDAL

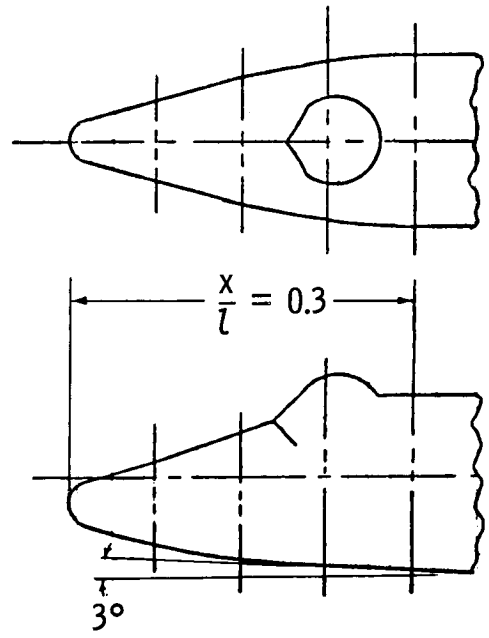

BASELINE
(CANOPY ON AND OFF)

Figure 3

NOSE CROSS-SECTION EFFECTS

(Figures 4 and 5)

Little effect of nose cross section on the longitudinal stability and trim characteristics is shown for trim angles of attack corresponding to near $C_{L,max}$ and high cross-range entry conditions (elevon deflections of -30° and -10°, respectively). Other data not presented indicated that the various cross sections also had no effect on the normal force and had only a small effect on axial force at the higher angles of attack.

The effect of nose cross section on the lateral and directional stability derivatives are indicated in figure 5 for $\delta_e = -10^{\circ}$. The results show a negligible effect of nose cross section on the lateral stability derivative C_{l_β}; but the level of the directional instability was reduced by using the square and trapezoidal shapes. Similar results (not presented) were obtained for these nose cross sections at a longitudinal trim angle of attack near 50° ($\delta_e = -30^{\circ}$). This improvement in the directional instability can be attributed to a reduction of the destabilizing flow component on the nose due to turning the sides inward. Additional heating benefits would also result from sloping the sides inward.

A linearized lateral-directional motion analysis was performed for the configuration using the baseline and trapezoidal nose shapes. The assumed flight conditions were a velocity of 6100 m/sec (20 000 ft/sec), an altitude of 64 km (210 000 ft), and angles of attack of 32° and 53°. The analysis showed that the improvement in the directional stability derivative by going to the trapezoidal nose shape resulted in a negligible change in the vehicle responses.

This study has shown that for the types of shapes tested, the nose cross section can be altered because of design requirements without a major impact on the hypersonic aerodynamics. The selection of a particular cross section should therefore depend on other considerations such as aerodynamic heating and effects on aerodynamics at lower speeds.

NOSE-CROSS-SECTION EFFECT ON THE LONGITUDINAL STABILITY OF THE BASELINE ORBITER

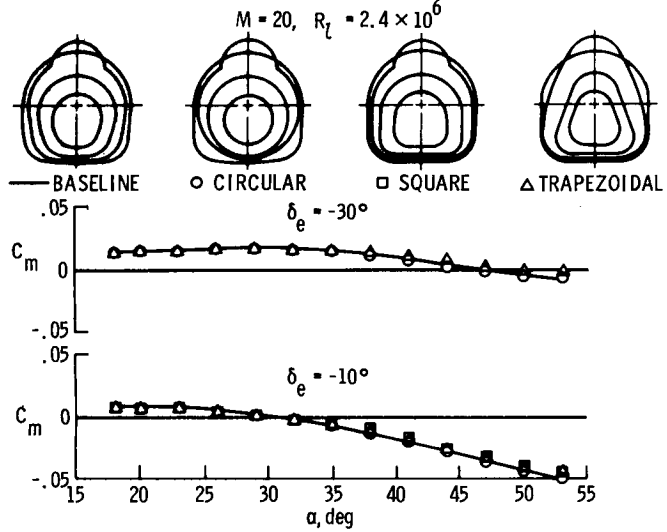

Figure 4

EFFECT OF NOSE CROSS SECTION ON LATERAL-DIRECTIONAL STABILITY DERIVATIVES OF BASELINE ORBITER

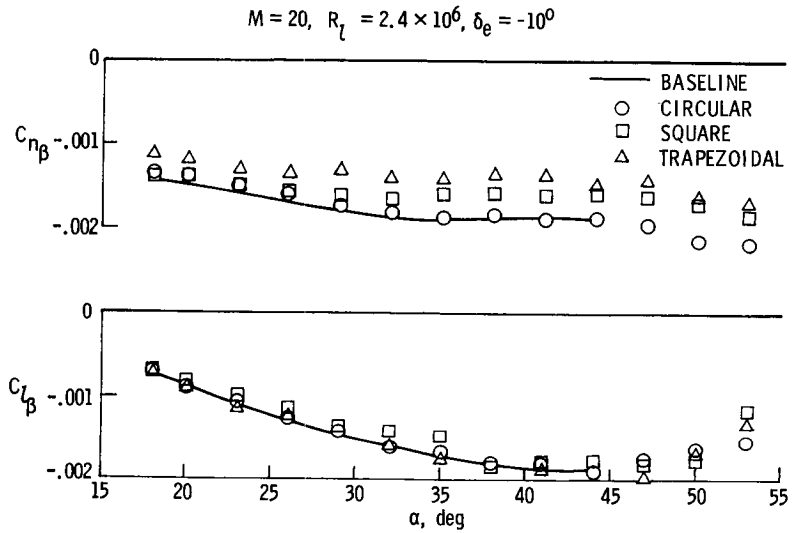

Figure 5

CANOPY EFFECTS ON THE BASELINE ORBITER

(Figure 6)

The effect of the baseline canopy on the aerodynamics at low angles of attack is shown in the figure where the canopy-off data are compared with the baseline data for $\delta_e = 0^o$. The comparison shows that the characteristics were affected at the lower angles of attack with the effects on C_m continuing up to $\alpha = 17^o$. At higher angles of attack (data not shown), there was no effect due to removal of the canopy for the longitudinal and lateral-directional parameters. Thus the canopy is effectively shielded from the flow at operational angles of attack. Therefore, selection of the canopy design will depend on other considerations such as heating due to shock impingement on the mated configuration and effects on aerodynamics at lower speeds.

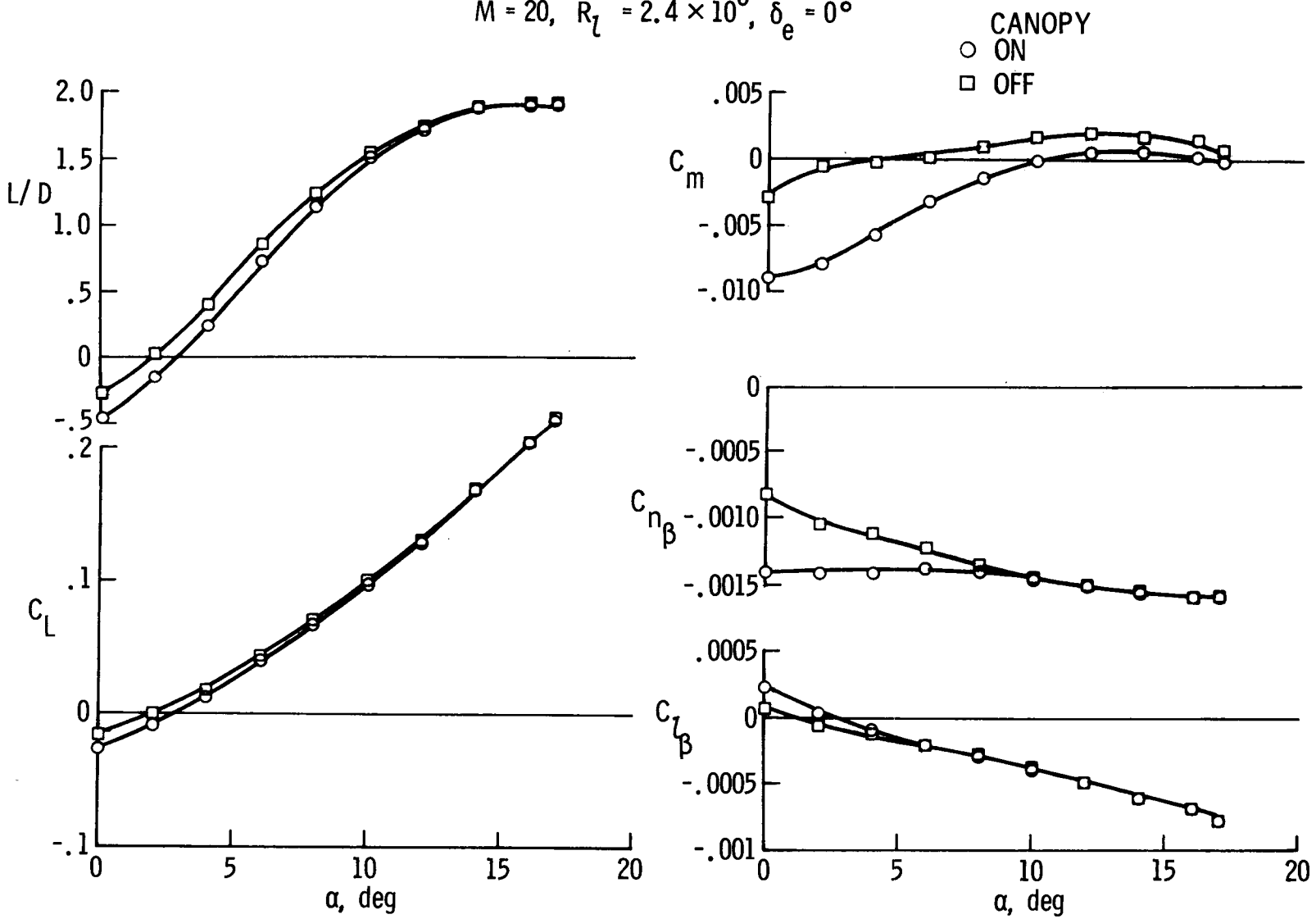
CANOPY EFFECTS ON THE BASELINE ORBITER
M = 20, $R_\ell = 2.4 \times 10^6$, $\delta_e = 0°$
CANOPY
ON
OFF
L/D
C_m
C_L
C_{n_β}
C_{ℓ_β}
α, deg
α, deg

Figure 6

NOSE-PROFILE EFFECTS ON THE LONGITUDINAL STABILITY OF THE BASELINE ORBITER

(Figure 7)

Removing the nose lower surface ramp on the vehicle with trapezoidal nose cross sections decreased the trim angle of attack by approximately 9° and reduced the stability level at trim. This rather large change in trim angle was realized because the vehicle had nearly neutral stability in this angle-of-attack range where a small change in C_m greatly affects the trim angle. There were negligible differences in the lateral and directional stability derivatives for these two nose shapes over an angle-of-attack range of 17° to 53°; thus, nose-profile modifications of this type can be used to tailor longitudinal trim aerodynamics over the shuttle hypersonic angle-of-attack range without affecting lateral and directional parameters. Major changes in trim and stability would require other configurational modifications in conjunction with nose alterations.

NOSE PROFILE EFFECT ON THE LONGITUDINAL STABILITY OF THE BASELINE ORBITER

$M = 20,\ R_l = 2.4 \times 10^6,\ \delta_e = -10°$

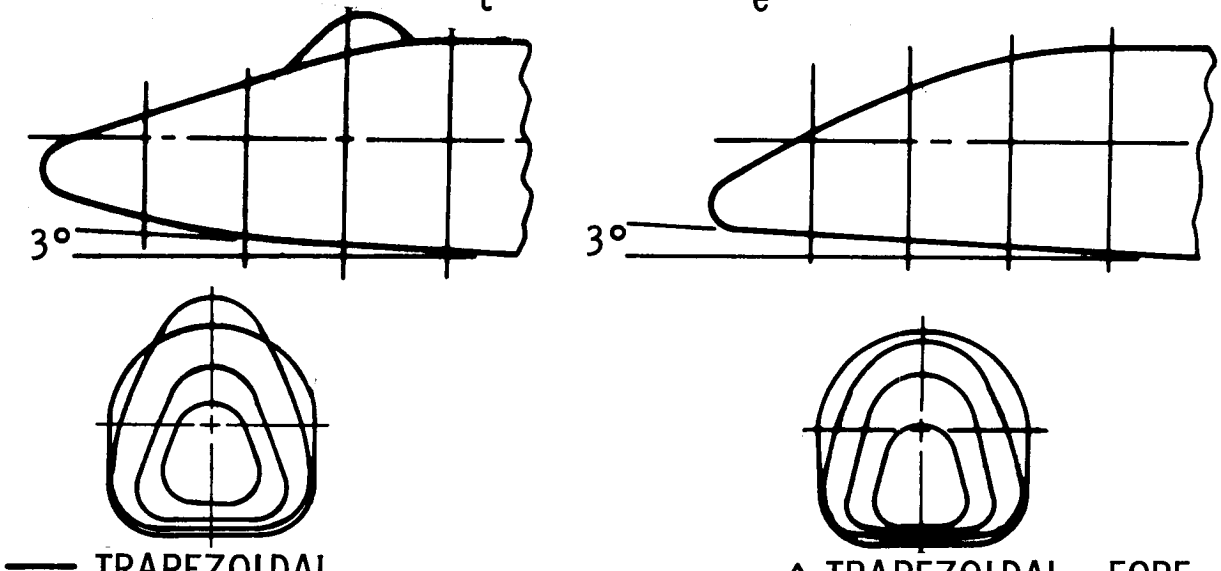

— TRAPEZOIDAL

△ TRAPEZOIDAL - FORE RAMP REMOVED

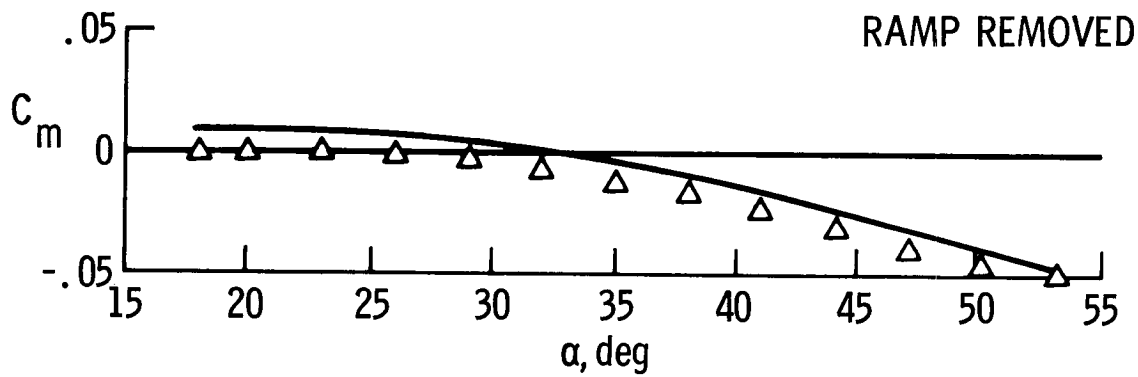

Figure 7

YAW DUE TO ROLL CONTROL

(Figure 8)

During the hypersonic part of the entry, the vehicle angle of attack is such that the center dorsal fin is ineffective. In the absence of an effective directional stability and control device, the Phase B designs use the reaction control systems (RCS) generally in combination with the ailerons to accomplish the required lateral-directional control for maneuvers such as banking for cross range. The control effectiveness resulting from aileron deflection (herein defined as differential elevon deflection, $\delta_a = \frac{\delta_{e,L} - \delta_{e,R}}{2}$) was obtained on the baseline orbiter at two elevon deflection angles.

The results presented in figure 8 show that the yawing moment due to aileron was adverse for an elevon angle $\left(\delta_e = \frac{\delta_{e,L} + \delta_{e,R}}{2}\right)$ of -10° and negligible for $\delta_e = -20^\circ$. (Similar results have been obtained on Phase B orbiter concepts.) The longitudinal trim angle of attack for $\delta_e = -10^\circ$ is near that required for high cross-range entry. Thus, elimination of this adverse yawing moment would be desirable to improve the vehicle handling qualities and reduce RCS fuel requirements. Methods for reducing or eliminating adverse yaw due to aileron are presented in the following discussion.

YAW DUE TO ROLL CONTROL ON THE BASELINE ORBITER

$M = 20,\ R_\ell = 2.4 \times 10^6,\ \delta_a = 10°$

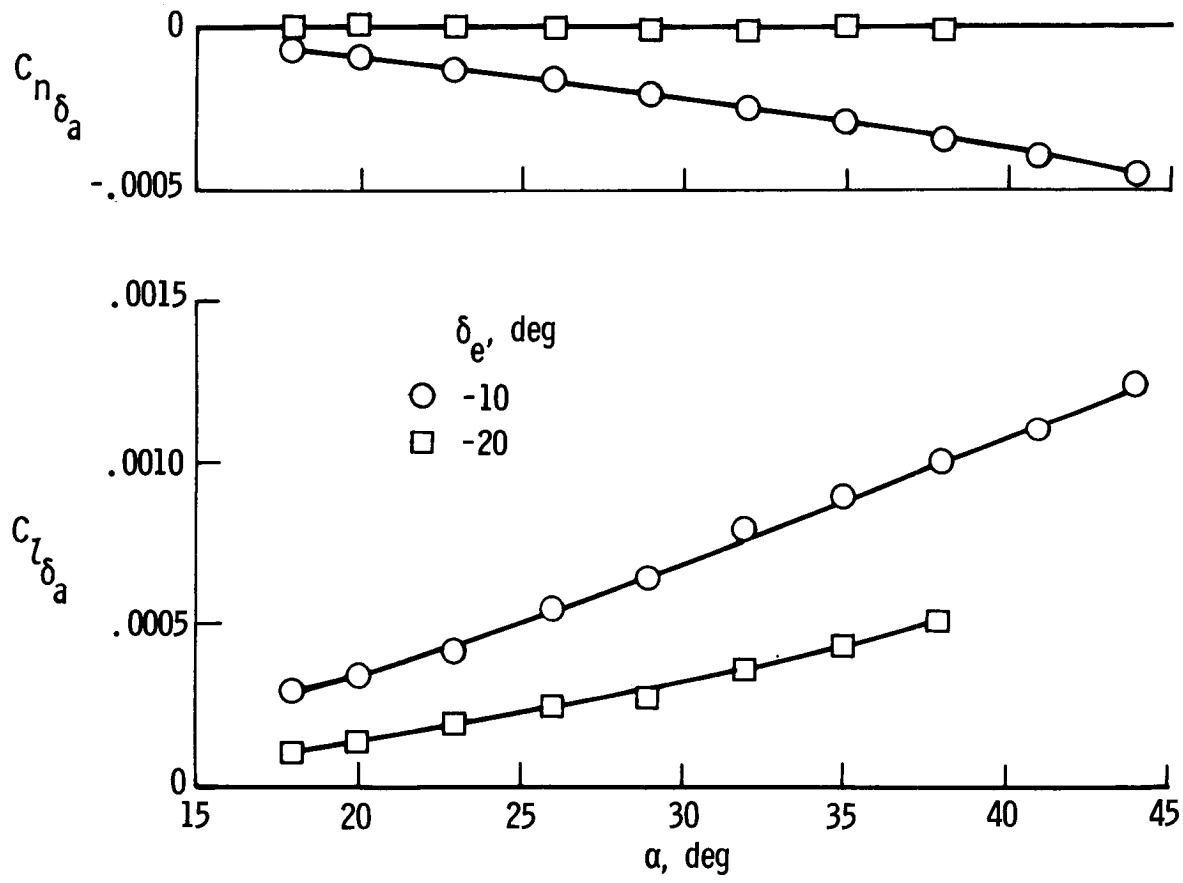

Figure 8

SPLIT ELEVON EFFECTIVENESS

(Figure 9)

The reduced level of adverse yaw obtained for negatively deflected elevons shown in the previous figure can also be obtained at lower trim angles of attack by the use of split elevons. In this case, the outer elevons were deflected negatively and differentially to provide roll control and the inner elevons were deflected positively to maintain the desired trim α. To evaluate this method experimentally, the inner elevon panels of the unswept hinge-line wing of an in-house parametric orbiter model were deflected in unison to 0°, 5°, and 10° while the outer elevon panels were deflected to 0°, 5°, and -10°, respectively. Thus, the average elevon angle in all cases was 0° and the trim angle of attack was about 23°. The outer elevon panels were then differentially deflected for roll control ($\delta_a = 10^\circ$) about the 0°, -5°, and -10° deflection angles. The in-house parametric orbiter model was 0.279 m (11.0 in.) long and the center of gravity was at 67 percent of the body length. The coefficients were nondimensionalized by using the total projected planform area, 0.0232 m^2 (0.249 ft^2) and the actual span, 0.197 m (7.74 in.).

Data obtained in the Langley continuous-flow hypersonic tunnel at $M = 10$ show that the adverse yaw was reduced and the roll control effectiveness decreased at the more negative outer elevon angles. As the left outer elevon angle became more negative (see sketches in figure), the axial-force component on it decreased which, in turn, reduced the adverse body-axis yawing moment. Oil-flow test results showed some tendency for flow impingement on the upper surface of the elevon differentially deflected upward (right outer elevon in sketches); this condition increased the axial force and resulted in a proverse yawing-moment increment.

SPLIT-ELEVON EFFECTS

UNSWEPT ELEVON HINGE LINE; M = 10

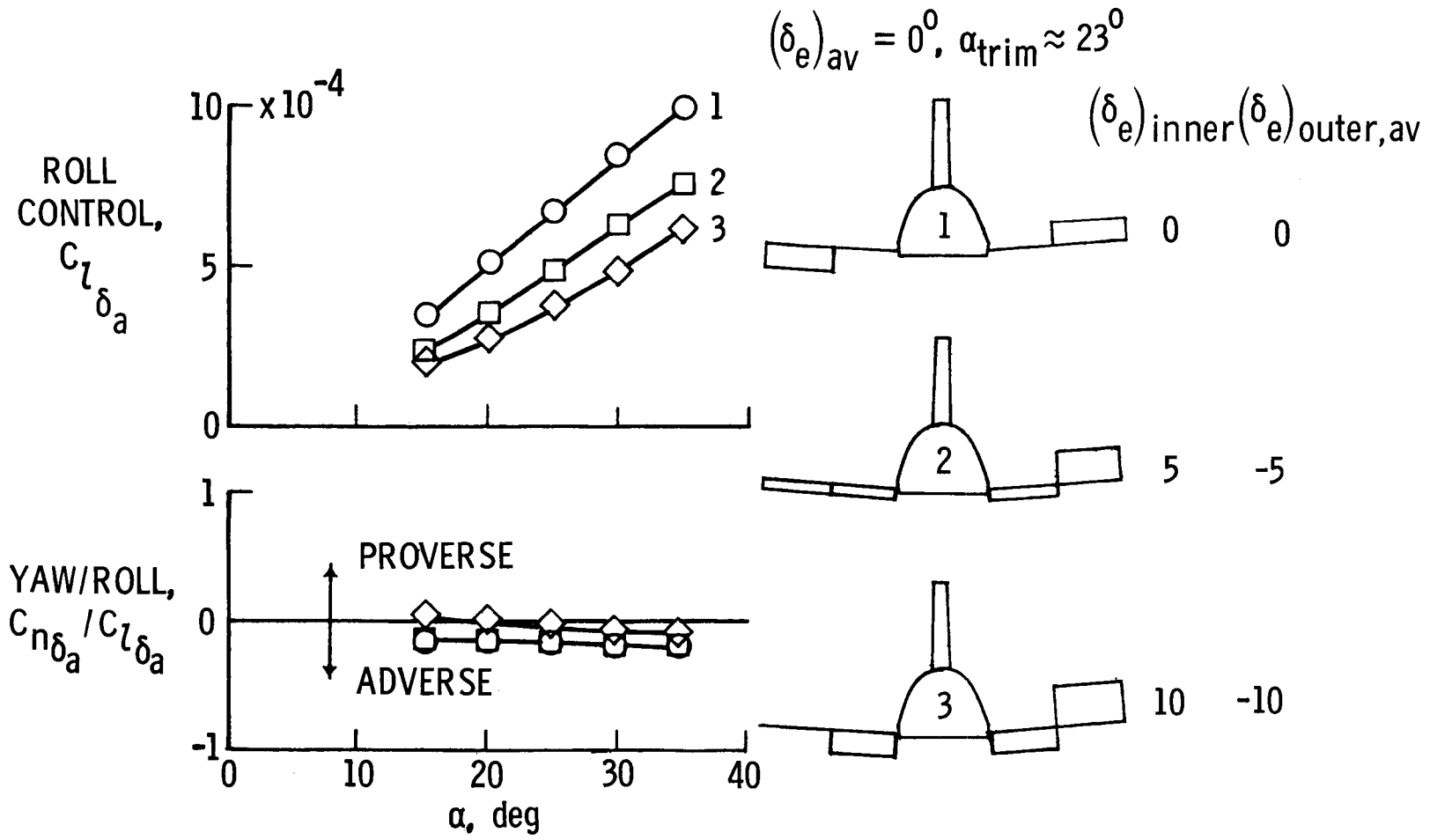

Figure 9

ELEVON HINGE-LINE SWEEP EFFECTS

(Figure 10)

Sweeping the elevon hinge line forward has been used previously on other types of configurations to reduce the adverse yaw. To assess the applicability of this method to the shuttle orbiter, three elevon configurations have been tested on the in-house parametric orbiter model. In this investigation, outer elevons of equal area were differentially deflected for roll control. The data shown in the figure are for an elevon deflection angle of 0° which results in a trim angle of attack of about 25°. Sweeping the elevon hinge line forward reduced the adverse yaw and initially increased and then decreased the roll control effectiveness; these effects were the result of the variation of the elevon orientation with the local flow direction and of the length of the lateral moment arms.

Although the adverse yaw due to aileron can be reduced and with refinement eliminated, a vehicle rolling about the body axis at shuttle-operational angles of attack generates significant adverse sideslip angles. Since the vehicles have a negative C_{l_β}, a rolling moment is generated in the direction of the sideslip. Thus, the resulting motion is a roll initially in one direction which reverses to a roll in the opposite direction. A motion analysis shows that a significant yawing moment is required at the operational angles of attack to alter this trend. This requirement cannot be met by the ailerons. When a mixed control system (RCS + aileron) is used, eliminating the adverse yaw will save RCS fuel and improve vehicle handling qualities.

ELEVON HINGE-LINE SWEEP EFFECTS

$M = 10;\ \delta_e = 0^0$

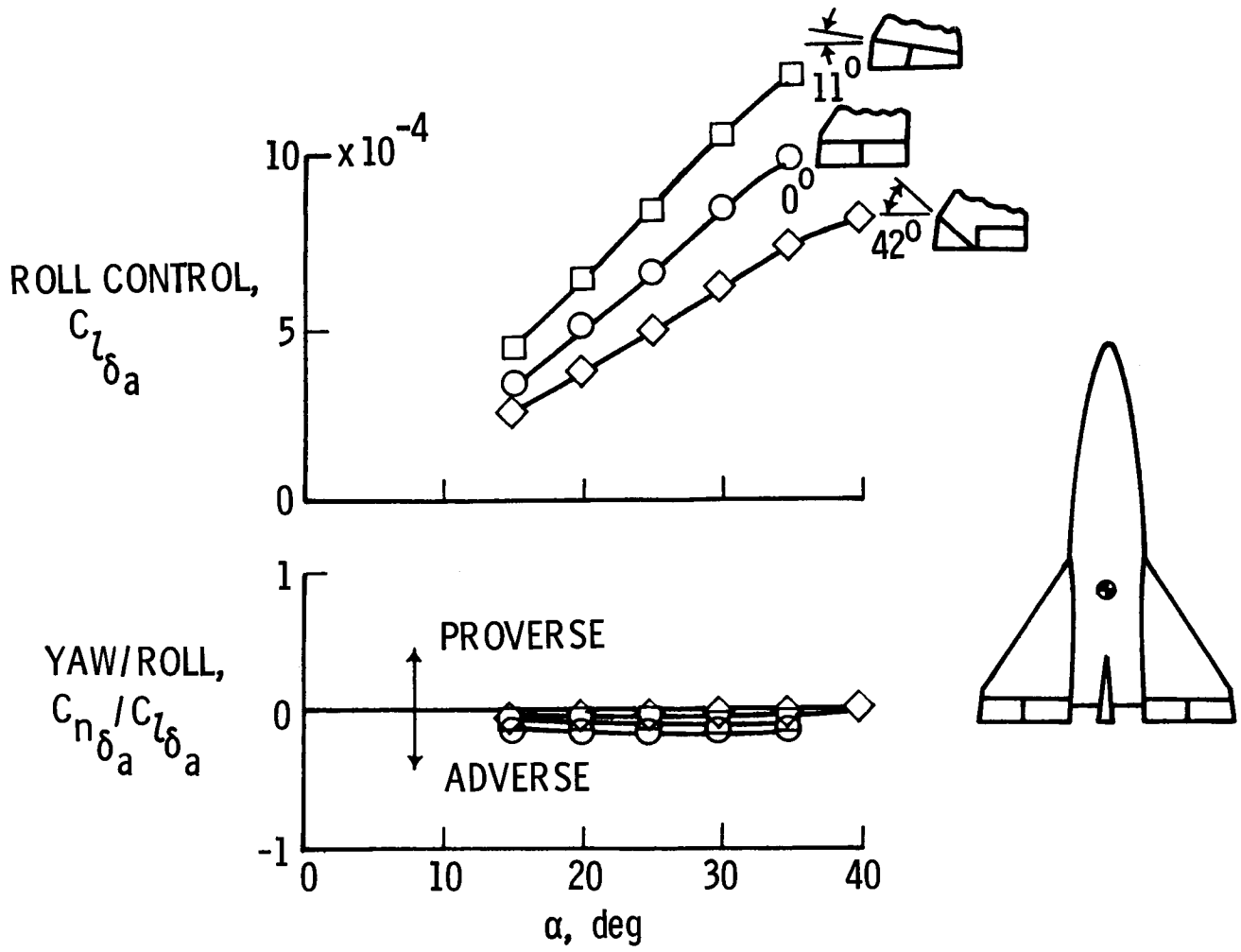

Figure 10

AERODYNAMIC YAW CONTROL

(Figure 11)

Aerodynamic yaw control can be provided hypersonically by a wing upper-surface flap. This device is an element of the wing upper surface that rotates up into the wind about a hinge line parallel to and just behind the wing leading edge (hinges probably at the front of the wing box). Although the angle of rotation between the flap and the wing upper surface δ_{WF} is large, at the operational angles of attack, this highly swept device has relatively low flow impingement angles. Data obtained at $M = 10$ shows that the yawing moment is larger than the rolling moment and both have the same sign or the control is proverse.

A limited amount of data at $M = 2$ indicated that the control was still proverse but the yawing and rolling moments were about the same level. Possible benefits of the flap at $M = 2$ and at lower speeds have not been examined. When the flap is not needed during the entry, it would remain flush with the wing upper surface.

A six-degree-of-freedom motion analysis has been conducted for several deflection modes of the wing-upper-surface flap by using the $M = 10$ data. The results for flap-deflection angles of 45° and 75° are shown in figure 11. The flap was deflected first on one wing to start the motion and then deflected on the other wing to stop the motion. Substantial bank angles were obtained for both flap deflection angles with sideslip angle oscillations of less then 1°. The angle-of-attack oscillations due to this motion were also very small.

EFFECTIVENESS OF WING-UPPER-SURFACE FLAP

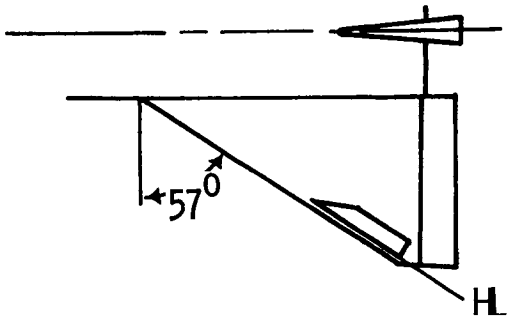

STATIC CONTROL EFFECTIVENESS

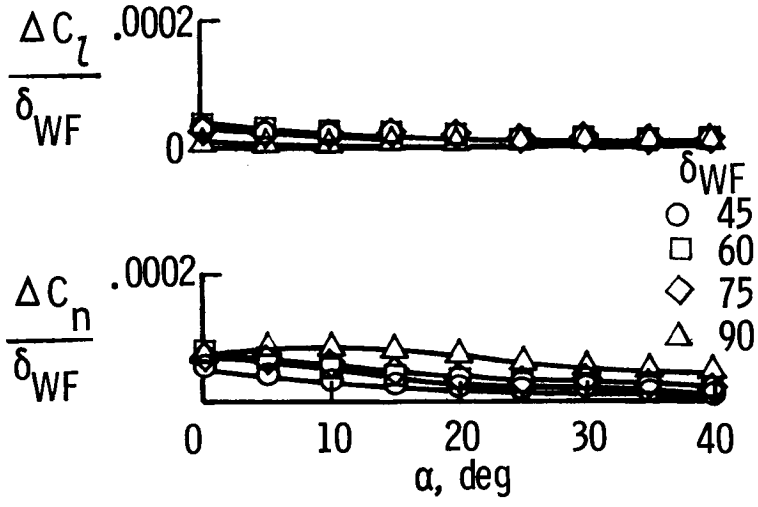

6-DEGREE-OF-FREEDOM MOTION ANALYSIS
INITIAL CONDITION: $\alpha = 25^0$; M = 10.2;
h = 52 km (170 000 ft)

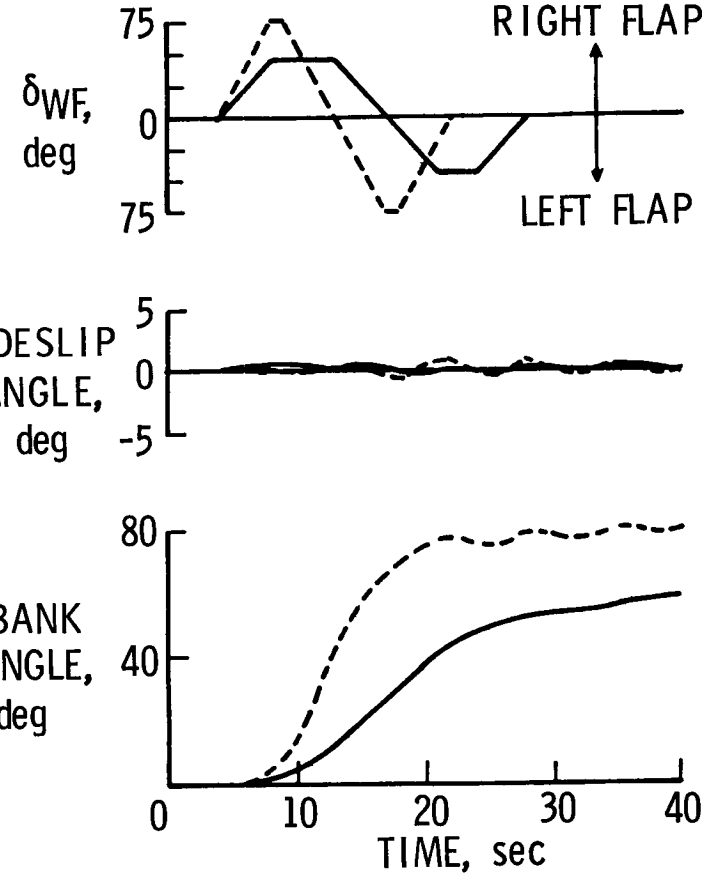

Figure 11

VEHICLE RESPONSE

(Figure 12)

The augmentation capability of the wing-upper-surface flap is illustrated by comparison of the vehicle responses for the bare airframe, airframe augmented with aileron, and airframe augmented with aileron and flap. The bare airframe and aileron static force and moment data used in this calculation were obtained from $M = 4.9$ wind-tunnel tests of a Phase B contractor fully reusable configuration which were in close agreement with $M = 10$ data. The flap data was obtained from $M = 10$ wind-tunnel tests of the in-house parametric orbiter model. This Mach number and model difference should not significantly affect these results.

The NASA Flight Research Center has investigated proposed flying qualities specifications for space shuttle vehicles and recommends the following conditions for satisfactory flying qualities during entry; Dutch roll frequency greater than 0.4 rad/sec, Dutch roll damping ratio greater than 0.08, no roll-spiral oscillation, and a roll-mode time constant less than 1.4 seconds. These conditions can be compared with those presented in the figure.

VEHICLE RESPONSE

ASSUMED FLIGHT CONDITION; M = 4.7; α = 30°; h = 46km (150000ft)

	DUTCH ROLL FREQUENCY, rad/sec	DUTCH ROLL DAMPING RATIO	ROLL-MODE TIME CONSTANT, sec	SPIRAL-MODE TIME CONSTANT, sec	ROLL-SPIRAL OSCILLATION FREQUENCY, rad/sec	ROLL-SPIRAL DAMPING RATIO
BARE AIRFRAME	0.7	0.003	100	600	—	—
AIRFRAME AUGMENTED WITH AILERON	0.7	0.08	—	—	0.011	-0.72
AIRFRAME AUGMENTED WITH AILERON AND FLAP	0.97	0.28	2.0	2500	—	—

Figure 12

PRELIMINARY SIMULATOR EVALUATION

(Figure 13)

To more fully assess the control systems with and without the wing-upper-surface flap, a preliminary simulator evaluation was conducted under the direction of James J. Adams at the Langley Research Center. The simulator task was a typical shuttle entry with 1850 km (1000 miles) cross range. The reaction control system used proportional body rate feedback to provide a rate command system. The jets were sized to provide an angular acceleration of $1\frac{1}{2}^{\circ}$/second and the system deadband was $\frac{1}{2}^{\circ}$/second on all axes. The low Dutch roll damping which is characteristic of this class of vehicle was augmented to an acceptable level by a roll-rate feedback to the aileron (assumed to have no adverse yaw). This feedback caused a divergent roll-spiral oscillation to occur and resulted in unsatisfactory pilot ratings on the Cooper-Harper scale.

The added augmentation capability offered by the wing-upper-surface flap plus the yaw control resulted in satisfactory pilot ratings when the flap was coupled with the RCS and aileron control systems. The flap has low control power which resulted in satisfactory to unsatisfactory pilot ratings for the flap alone. The difference in pilot ratings for the flap alone depended upon how precisely the bank angle was maintained.

The control system demand for the RCS over the entire simulator flight was used to determine the RCS fuel requirements for all three control modes by assuming a specific impulse of 350 seconds. In the flap-alone flights, the RCS was turned off when the dynamic pressure reached 480 N/m^2 (10 psf). The RCS fuel savings resulting from incorporating the wing-upper-surface flap in the control system is shown in the figure.

It should be pointed out that Dutch roll damping augmentation would have been provided by the yaw jets if the yaw axis deadband had been much smaller. This augmentation would have reduced the adverse effects in the roll-spiral mode and thus improved the handling qualities for the RCS + aileron mode. This augmentation was not simulated since the much smaller yaw axis deadband would have significantly increased the RCS fuel requirements.

A heat-transfer analysis showed that radiation equilibrium temperatures slightly below 1020° C (1900° F) could result from a turbulent boundary layer at the higher flap deflection angles. A structural analysis using this operating temperature resulted in total system weights of 910 kg (2000 lbs) for a replaceable or refurbishable flap and 1360 kg (3000 lbs) for a metallic fully reusable flap. The flap was sized for a fully reusable size vehicle and was about one-third of the elevon area.

The wing-upper-surface flap provides sufficient yaw control to improve significantly the vehicle handling qualities in the hypersonic part of the entry. There does not appear to be a significant weight advantage either with or without the flap.

PRELIMINARY SIMULATOR EVALUATION WITH AUGMENTATION

6-DEGREES-OF-FREEDOM FIXED-BASE SIMULATOR

TASK: SHUTTLE ENTRY WITH 1850 km (1000 MILES) CROSS RANGE

FLIGHT CONTROL MODES	PILOT RATINGS	RCS FUEL SAVINGS kg (lb)	SYSTEM WEIGHT INCREASE kg (lb)	REMARKS
RCS + AILERON	UNSATISFACTORY	———	———	LOW DUTCH ROLL DAMPING, ROLL-SPIRAL OSCILLATION
RCS + AILERON + FLAP	SATISFACTORY	1000 (2200)	910 - 1360 (2000 - 3000)	DIRECTIONAL STABILITY AND YAW DAMPING AUGMENTATION
FLAP ALONE	SATISFACTORY TO UNSATISFACTORY	1360 (3000)	910 - 1360 (2000 - 3000)	LOW CONTROL POWER

Figure 13

CONCLUSIONS

Recent tests and analyses of hypersonic data and simulator studies have led to the following conclusions:

(1) The baseline orbiter trimmed with longitudinal static stability from angles of attack at $(L/D)_{max}$ to $C_{L,max}$ with sufficient L/D to perform the shuttle high cross-range mission.

(2) The effects of the baseline canopy on the aerodynamics became negligible in the hypersonic operational angle-of-attack range.

(3) Reducing the nose ramp lowered the pitching moment and changed the trim angle. Nose shapes studied did not have a major impact on the hypersonic aerodynamics.

(4) Adverse yaw due to aileron for roll control can be reduced and probably eliminated, and thus the fuel requirements for a mixed RCS plus aileron control mode is reduced; however, this mode has unsatisfactory handling qualities. Adding the wing-upper-surface flap significantly improved the handling qualities without a significant change in weight.

SYMBOLS

C_A axial-force coefficient

C_D drag coefficient

C_L lift coefficient

C_l rolling-moment coefficient

$C_{l_\beta} = \frac{\Delta C_l}{\Delta \beta}$ per degree

C_m pitching-moment coefficient

C_n yawing-moment coeffidient

$C_{n_\beta} = \frac{\Delta C_n}{\Delta \beta}$ per degree

$C_{n_{\delta_a}} = \frac{\Delta C_n}{\Delta \delta_a}$ per degree

$C_{l_{\delta_a}} = \frac{\Delta C_l}{\Delta \delta_a}$ per degree

h altitude

L/D lift-drag ratio

l length

M Mach number

R_l Reynolds number based on body length

α angle of attack, degrees

β angle of sideslip, degrees

$\delta_a = \frac{\delta_{e,L} - \delta_{e,R}}{2}$ where L denotes left and R, right

δ_e elevon deflection, positive when trailing edge is down, degrees

$(\delta_e)_{av} = \frac{(\delta_e)_{outer,L} + (\delta_e)_{inner,L} + (\delta_e)_{inner,R} + (\delta_e)_{outer,R}}{4}$, degrees

$(\delta_e)_{inner}$ inner split-elevon deflection, positive when trailing edge is down, degrees

$(\delta_e)_{outer,av} = \frac{(\delta_e)_{outer,L} + (\delta_e)_{outer,R}}{2}$, degrees

δ_{WF} wing-upper-surface flap deflection angle, degrees

Subscripts:

max maximum

trim trimmed value

av average

WING OPTIMIZATION FOR SPACE SHUTTLE ORBITER VEHICLES

by T. E. Surber, W. E. Bornemann, W. D. Miller
Space Division, North American Rockwell Corporation
Downey, California

INTRODUCTION

This paper presents the results of a parametric study performed to determine the optimum wing geometry for a Space Shuttle Orbiter proposed by North American Rockwell Corporation. The results of this study establish the minimum weight wing for a series of wing-fuselage combinations subject to constraints on aerodynamic heating, wing trailing edge sweep, and wing over-hang. The study consists of a generalized design evaluation which has the flexibility of arbitrarily varying those wing parameters which influence the vehicle system design and its performance. The study is structured to allow inputs of aerodynamic, weight, aerothermal, structural and material data in a general form so that the influence of these parameters on the design optimization process can be isolated and identified. This procedure displays the sensitivity of the system design to variations in wing geometry. The parameters of interest are varied in a prescribed fashion on a selected fuselage and the effect on the total vehicle weight is determined. The primary variables investigated are: wing loading, aspect ratio, leading edge sweep, thickness ratio, and taper ratio. These parameter variations specify a 75 element wing matrix. Constraints imposed by leading edge temperature, balance trim, subsonic lifting characteristics and transonic buffet place boundaries on the weight, balance and wing geometry matrix. Wing size (area) is specified by the requirement for a 150 knot minimum touchdown speed. The thermal protection system weights are specified on the basis of the thermal environment determined from trajectory information. The wing geometry matrix and the wing size information are then processed through a generalized wing weight matrix to determine wing weights for each wing specified in the wing geometry matrix. Each wing-fuselage system is then checked for subsonic and hypersonic balance (2% subsonic static margin and hypersonic trim over required center of gravity and angle of attack range). The selection of the minimum weight candidate wings is made from the weight, balance and geometry matrix subject to the previously mentioned constraints.

WING SELECTION FOR SHUTTLE ORBITERS
(Figure 1)

The evaluation of the effects of wing planform shape on the overall wing system performance utilizes a baseline configuration as a starting point. The baseline body shape is held constant; since it may be assumed that the body design is prescribed by factors other than aerodynamic performance, such as payload size and packaging efficiency. The minimum weight wing system defined for a fixed body is thereby the optimum wing for that particular wing-body configuration. However, it is probable that the optimum wing shape will also be a good selection for other configurations generally similar to the nominal design for which the evaluation is made.

Aerodynamic factors that must be included in the analysis are the size and location on the body of the candidate wings. Wing size is based on specified landing performance requirements; and the wing location is dictated by balance and trim considerations. The wing size affects the aerothermodynamic entry environment, requiring an analysis of thermal protection system (TPS) requirements to protect the aluminum primary structure. The weight of the TPS materials is combined with the basic structural weight of the wing to define the total weight of the wing system. Evaluation of the total weight results then identifies the most favorable candidate wing planform concepts.

WING SELECTION FOR SHUTTLE ORBITER

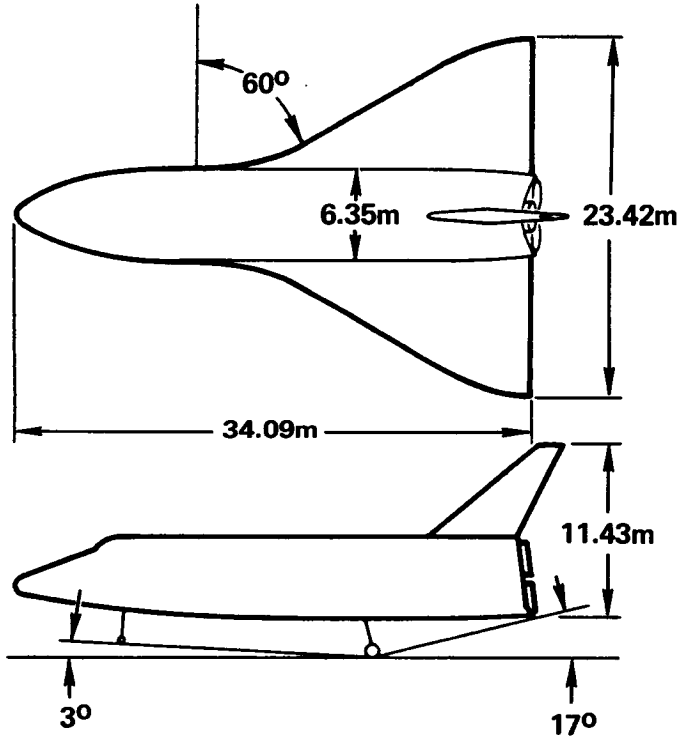

BASELINE VEHICLE

TRADE FACTORS CONSIDERED

- WING GEOMETRY
  - LEADING EDGE SWEEP 40°–60°
  - ASPECT RATIO 1.8–4
  - TAPER RATIO .1–.3
  - THICKNESS .04–.10
- WING SIZE
  - 150 KNOT TOUCHDOWN SPEED
- WING LOCATION ON BODY
  - SUBSONIC STATIC MARGIN 2% L OR GREATER
- AEROTHERMODYNAMIC ENVIRONMENT
- WING STRUCTURAL WEIGHT
  - ALUMINUM STRUCTURE
- WING TPS WEIGHT
- EFFECT OF WING ON BODY TPS WEIGHT

Figure 1

WING SIZING
(Figure 2)

The determination of wing size is based on the requirement of providing equivalent subsonic aerodynamic performance at landing for each candidate planform shape. The landing requirement that defines the wing size is the desired design touchdown speed of 150 knots at sea level elevation on a standard day. A further constraint arises from the FAR Part 25 specification that requires this landing speed to occur at a velocity not less than 1.1 V_{stall}. The general characteristics of swept wings cause the corresponding touchdown angle-of-attack to increase with increasing leading edge sweep. In order to maintain reasonable proportions for the landing gear geometry, the maximum allowable landing angle is arbitrarily limited to 17 degrees. As a result, configurations with high leading edge sweep have a design landing lift coefficient that is less than the fully attainable value that could be achieved by using the 1.1 V_{stall} criterion.

The landing lift coefficient and the resulting wing area have been evaluated by calculating the wing-body lift curve slope and maximum lift characteristics for each wing planform. The required wing area increases for wings with low leading edge sweep because of the earlier stall and lower maximum lift coefficient properties of these planforms. For wing configurations constrained by the maximum landing angle of 17 degrees, the required wing area increases with increasing leading edge sweep due to a decrease in wing-body lift curve slope.

WING SIZING

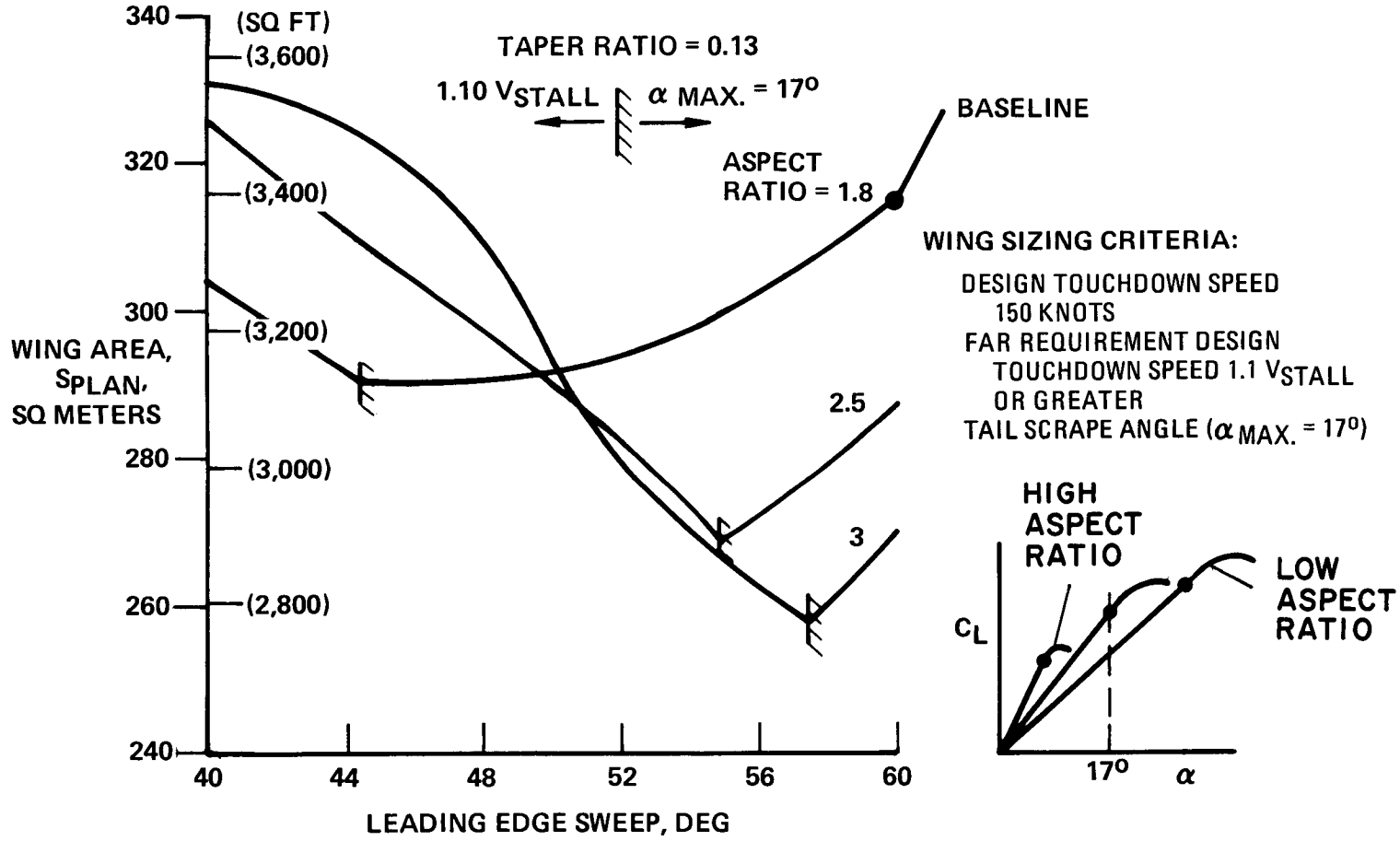

Figure 2

WING GEOMETRY
(Figure 3)

The range of wing shapes considered in the study is illustrated for representative values of planform geometrical parameters. The generalized wing has varying amounts of trailing edge sweep. The delta planform with zero trailing edge sweep is a special case of the parametric wing family, with any two of the three independent variables (leading edge sweep, aspect ratio, or taper ratio) uniquely defining the third.

WING GEOMETRY

TAPER RATIO = 0.13

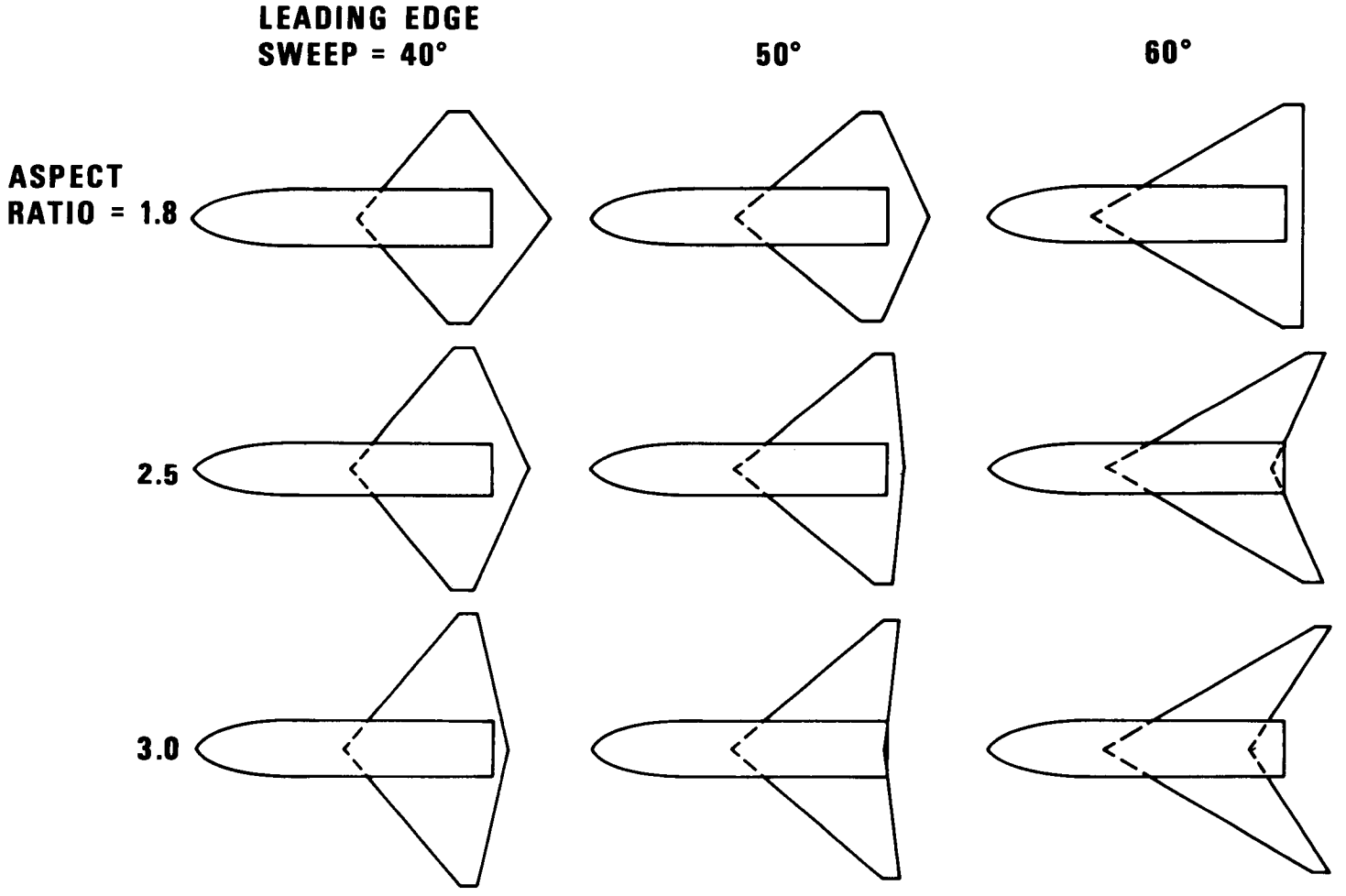

Figure 3

AEROTHERMODYNAMIC ENTRY ENVIRONMENT
(Figure 4)

The entry environment map for a given configuration displays the peak heating rate - heat load values for an entire range of possible entry trajectories. Peak heating rate can be traded off against heat load along a line of constant lateral cross-range. The "nominal" entry heating environment for a specified lateral cross-range is defined to be at the "knee" of such a curve. Increasing the entry lift loading (W/C_LS) by reducing the wing size causes an increase in both peak heating rate and heat load for the nominal entry environment of the modified configuration. The range of entry lift loading resulting from the variation of wing geometry and size causes the indicated change in entry heating environment.

Wing and body surface heating have been calculated for the range of entry environments encountered. The results show that the variation of body heating with W/C_LS is primarily influenced by the change in the extent of turbulent heating over the body lower surface. Transition to turbulent flow on the wing lower surface is similarly affected by W/C_LS. The effect of W/C_LS on wing leading edge temperature is relatively small in comparison to the effect of the variation of leading edge radius with wing geometry.

AEROTHERMODYNAMIC ENTRY ENVIRONMENT

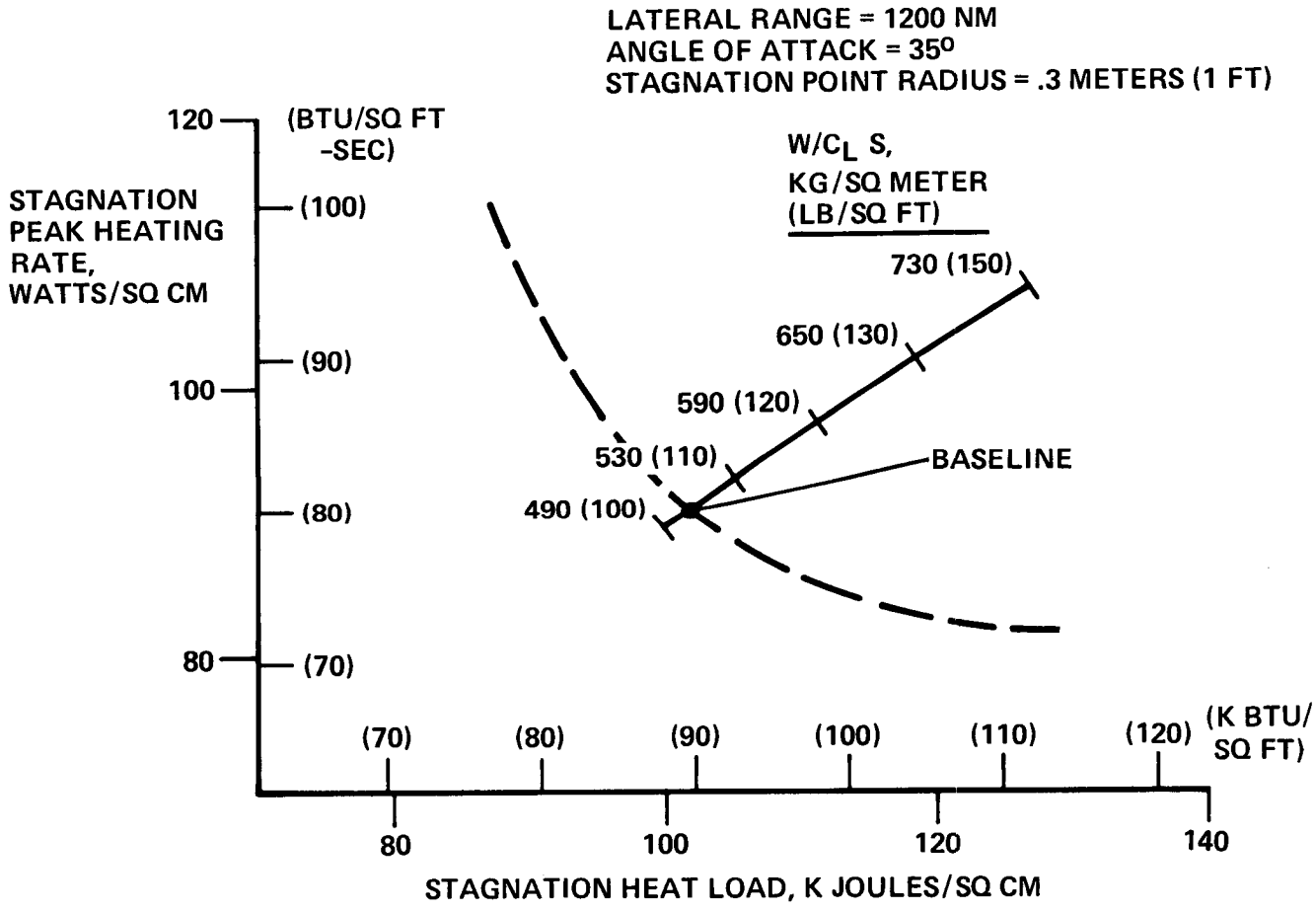

Figure 4

WING SYSTEM WEIGHT BREAKDOWN
(Figure 5)

The total wing system weight is composed of the wing structural weight, the wing thermal protection system (TPS) weight, and the incremental change in body TPS weight due to the change in entry W/C_LS. The TPS consists of a reusable surface insulation (RSI) which covers the vehicle in areas whose surface temperatures do not exceed 1500°K (2300°F). For regions such as leading edges which are above 1500°K (2300°F), a reinforced carbon carbon (RCC) material is employed. The wing structural weight evaluation employs a weight analysis program to calculate the torque box material dimensions required to support the shear and bending loads acting on the wing.

The variation of the body TPS weight increment with leading edge sweep is related to the change in wing size and entry W/C_LS. A similar variation is obtained for the unit weight of the wing TPS. However, the change in wing TPS unit weight is compensated for by the change in wing area; so that the net wing TPS weight is essentially constant with leading edge sweep. The wing structural weight generally minimizes for a value of leading edge sweep near the low end of the sweep range. However, when the wing and body TPS weight components are added to the structural weight to obtain the total wing system weight, a minimum weight point is not obtained within the range of sweep angles considered.

WING SYSTEM WEIGHT BREAKDOWN

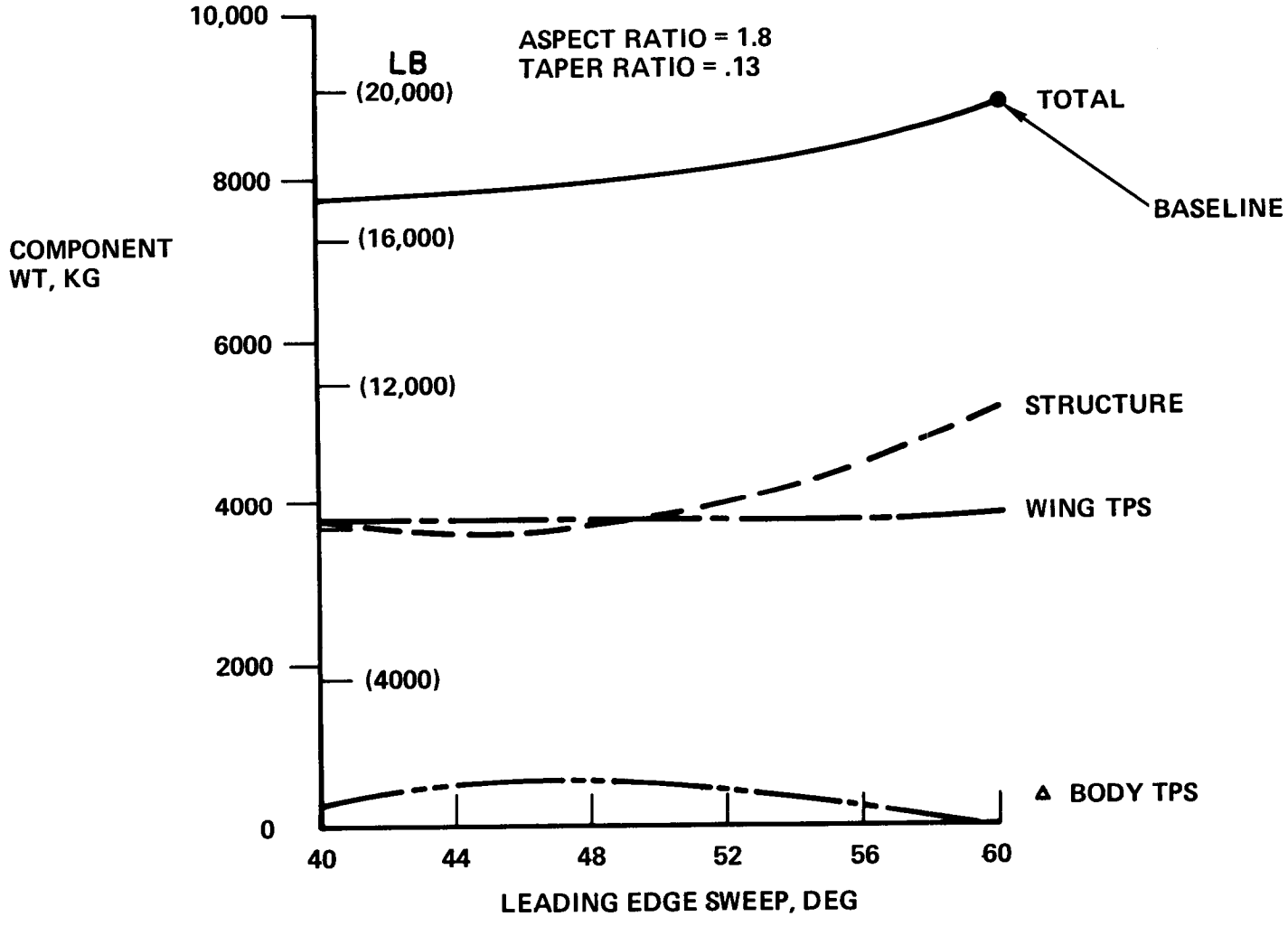

Figure 5

TOTAL WING WEIGHT
(Figure 6)

The general trend of the total wing weight results for a range of planform geometry indicates a significant driving effect of aspect ratio on wing weight. Evaluation of the unit structural weight of the exposed wing panels indicates that these trends are due to the effect of aspect ratio on structural weight. The variations in total wing weight due to changes in wing area are relatively small in comparison. In addition, any expected saving in wing weight obtained by incorporating the smallest, most efficient subsonic wing into the vehicle design is partially compensated for by an increase in body TPS weight due to the higher entry $W/C_L S$ associated with the smaller wing.

Maximum leading edge temperature constraints do not appear useful as criteria for wing geometry selection, since the majority of candidate wings fall between the temperature limits of 1920°K (3460°R) and 2480°K (4460°R). The lower temperature limit of 1920°K (3460°R) permits reuse of the leading edge material for 100 flights without refurbishment. If the upper material operating limit of 2480°K (4460°R) is reached, refurbishment is required after every flight. Intermediate temperatures require inspection and periodic refurbishment of the leading edge TPS.

TOTAL WING WEIGHT

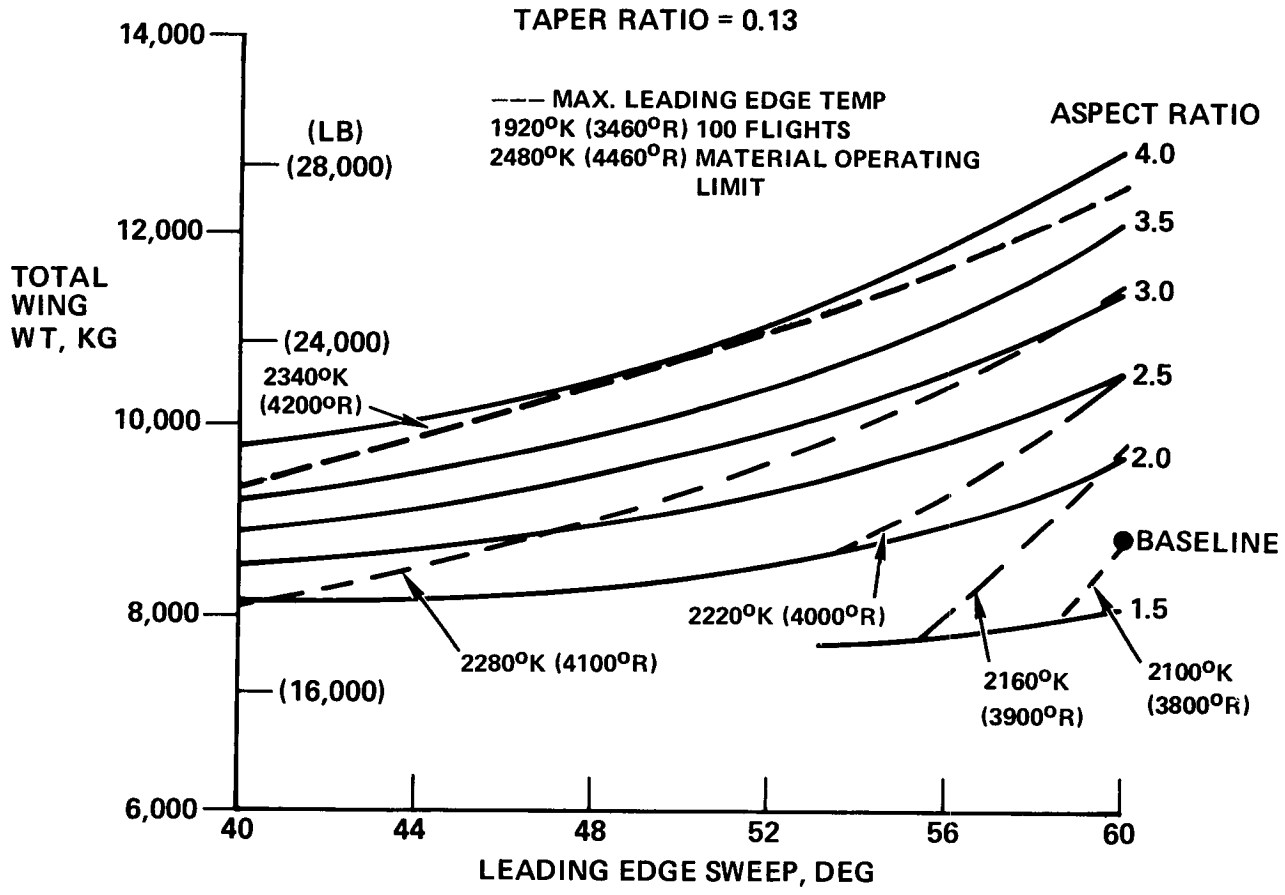

Figure 6

WING LOCATION CRITERIA
(Figure 7)

In order for the vehicle to be stable and trimmable for both hypersonic and subsonic velocities, the wing must be located so that the elevons can provide enough control to meet the upper and lower attitude requirements for the specified center-of-gravity (CG) range. With the wing in this location, it is also required that the subsonic stability limit (aerodynamic center) be aft of the furthest aft CG to provide longitudinal stability. Evaluation of previous results shows that for an angle-of-attack range of from 20 to 40 degrees, the hypersonic center of pressure location for an angle-of-attack of 35 degrees and zero elevon deflection falls very near the middle of the CG range. The wing location is therefore selected so that the center of pressure at an angle-of-attack of 35 degrees and zero elevon deflection coincides with the desired nominal CG of .66L. This procedure always provided subsonic stability for the range of wing geometry considered.

WING LOCATION CRITERIA

HYPERSONIC TRIM
ANGLE OF ATTACK = 35°
ELEVON DEFLECTION = 0

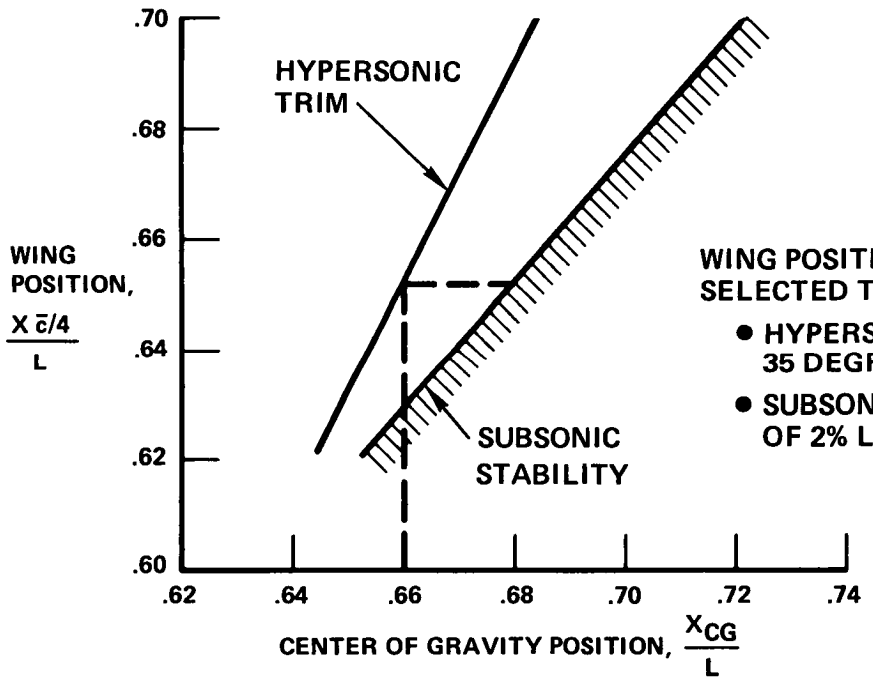

WING POSITION ON BODY SELECTED TO GIVE:

- HYPERSONIC TRIM AT 35 DEGREES ANGLE OF ATTACK
- SUBSONIC STATIC MARGIN OF 2% L OR GREATER

Figure 7

TOTAL WING WEIGHT
(Figure 8)

In addition to the requirements for hypersonic trim and subsonic stability, other factors such as structural constraints and possible undesirable dynamic characteristics may decide the acceptability or unacceptability of a given wing. The total wing weight results are repeated here to illustrate the effect of such constraints.

Until this point, the value of the wing trailing edge sweep has been unrestricted. However, the sweep of the elevon hinge line is directly related to the sweep of the wing trailing edge; and large amounts of elevon sweep introduce undesirable roll-yaw coupling into the handling characteristics of the vehicle. Therefore, the wing trailing edge sweep is arbitrarily constrained to values between $\pm$20 degrees, and any wing whose trailing edge sweep exceeds this range is deemed unacceptable. For the range of wing geometry considered, the -20 degree trailing edge sweep constraint is not critical, and so only the +20 degree sweep boundary is indicated.

TOTAL WING WEIGHT

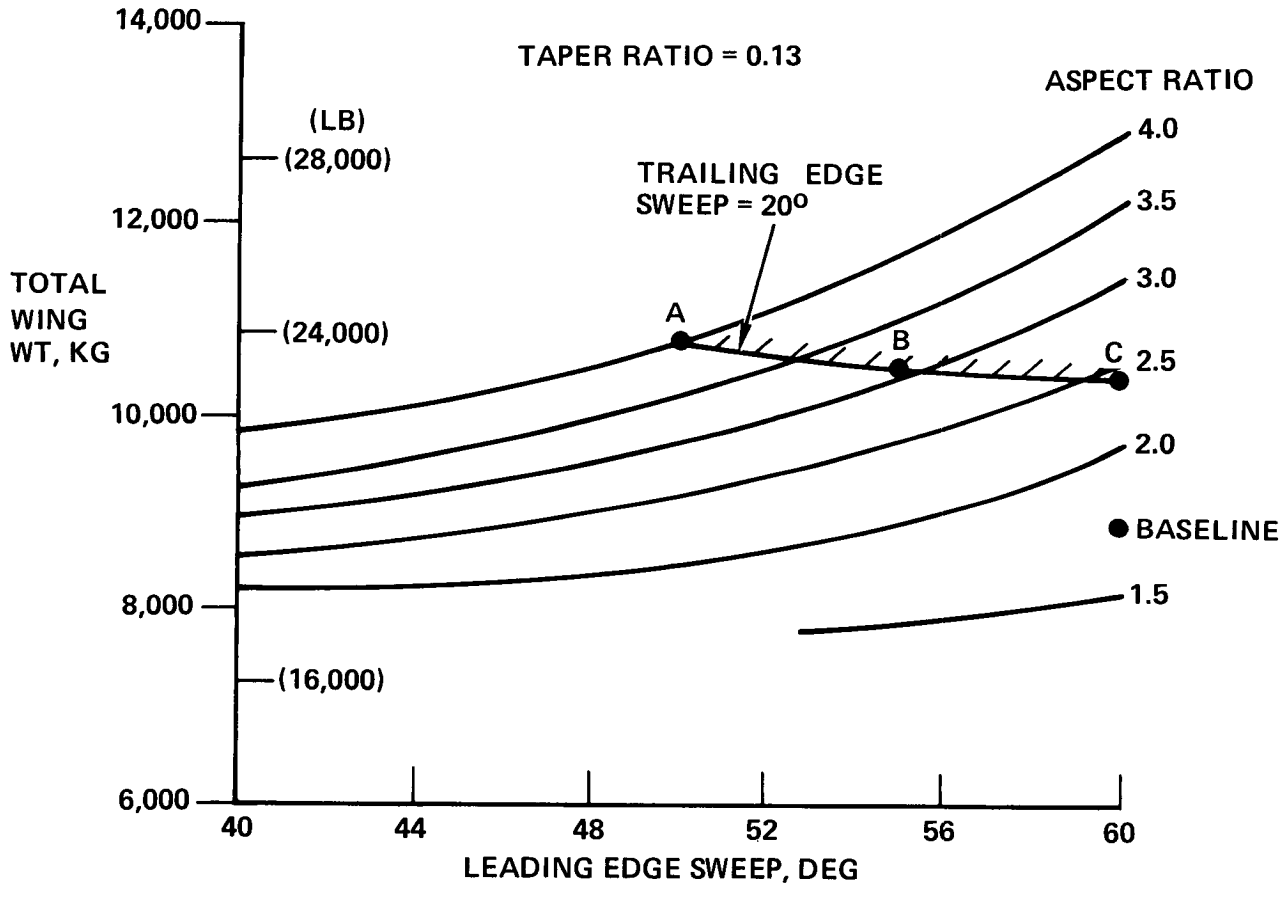

Figure 8

WING LOCATION CONSTRAINTS
(Figure 9)

Representative planform shapes are illustrated for configurations constrained by the +20 degree trailing edge sweep boundary.

WING LOCATION CONSTRAINTS

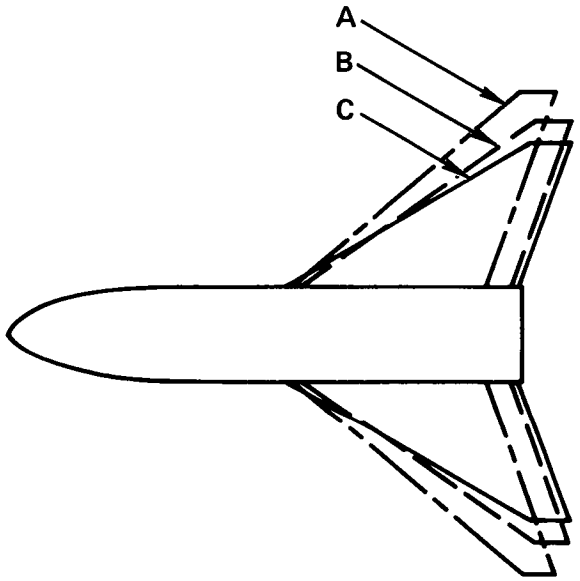

TRAILING EDGE SWEEP 20^{o}

Figure 9

TOTAL WING WEIGHT
(Figure 10)

Plume impingement heating considerations constrain the position of the wing trailing edge relative to the exit plane of the main propulsion exhaust nozzles. The wing torque box must also be forward of the main rocket engine for structural reasons, thereby limiting the aft movement of the wing. To limit this aft movement, an arbitrary limit of 1.3 meters (50 inches) is placed on the wing overhang relative to the base of the fuselage; and any wing which exceeds this limit to meet the hypersonic trim requirements is deemed unacceptable. The wing overhang is measured from the end of the fuselage to the trailing edge of the exposed root chord, and is positive for aft movement of the wing.

Excessive forward wing movement is also undesirable in that it reduces the moment arm of the elevon and therefore requires a larger elevon size to provide the same tail volume. Another arbitrary limit of -3.8 meters (-150 inches) is placed on the forward movement of the wing. The -3.8 meter (-150 inch) forward wing limit boundary is not indicated, since it is less critical than the +20 degree trailing edge sweep boundary.

The trailing edge sweep and wing overhang boundaries define a region of acceptable wing geometry.

TOTAL WING WEIGHT

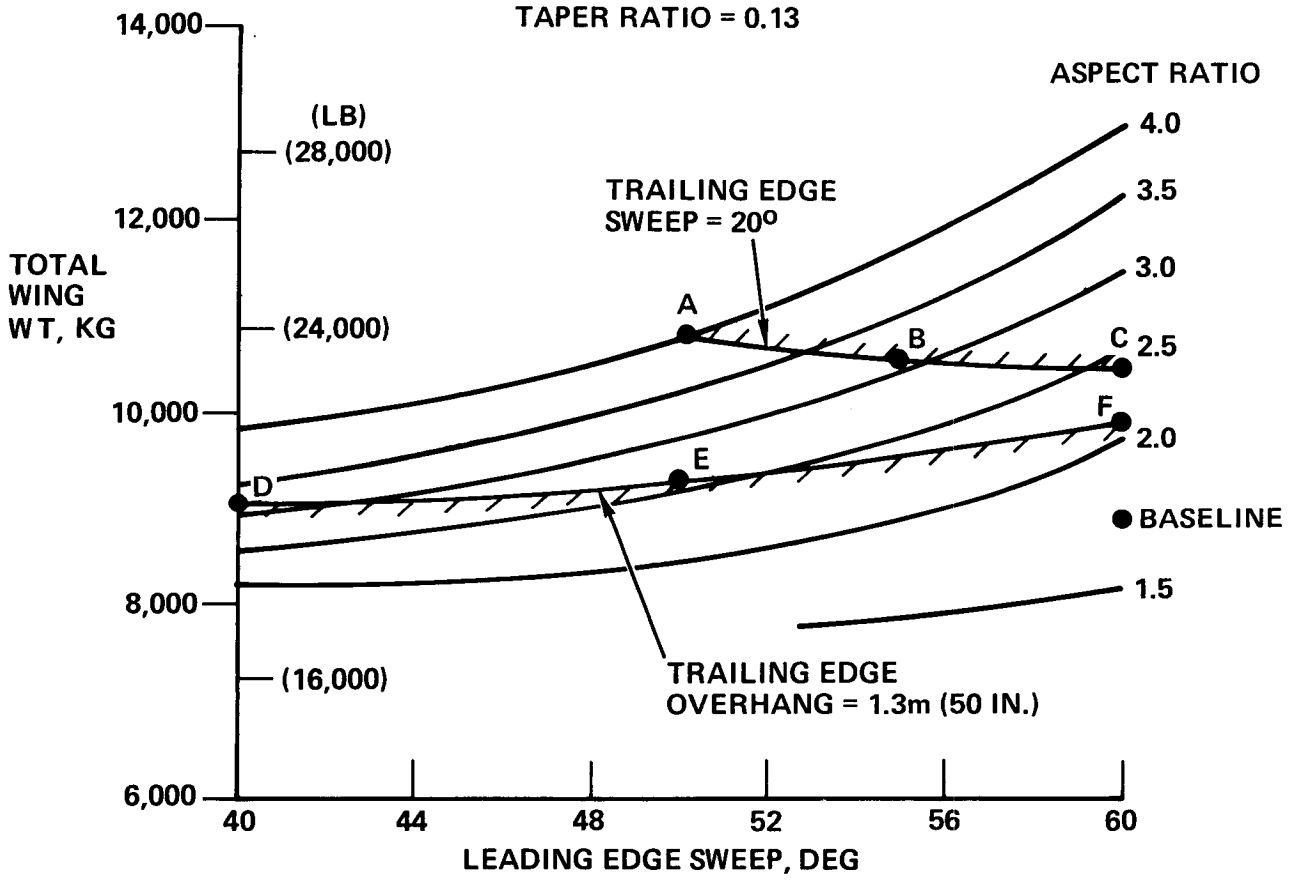

Figure 10

WING LOCATION CONSTRAINTS
(Figure 11)

Representative planform shapes are illustrated for configurations constrained by the 1.3 meter (50 inches) trailing edge overhang boundary.

WING LOCATION CONSTRAINTS

TRAILING EDGE SWEEP BETWEEN ± 20°

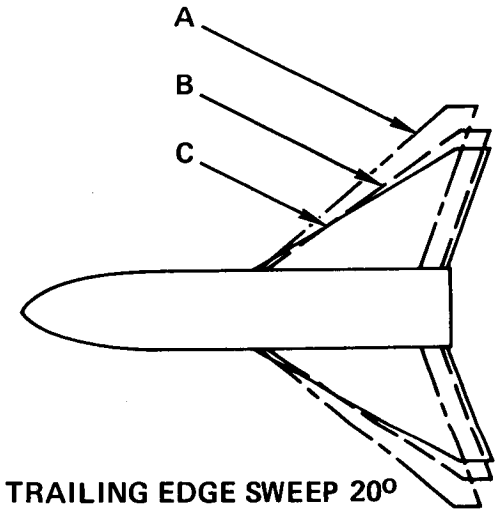

TRAILING EDGE SWEEP 20°

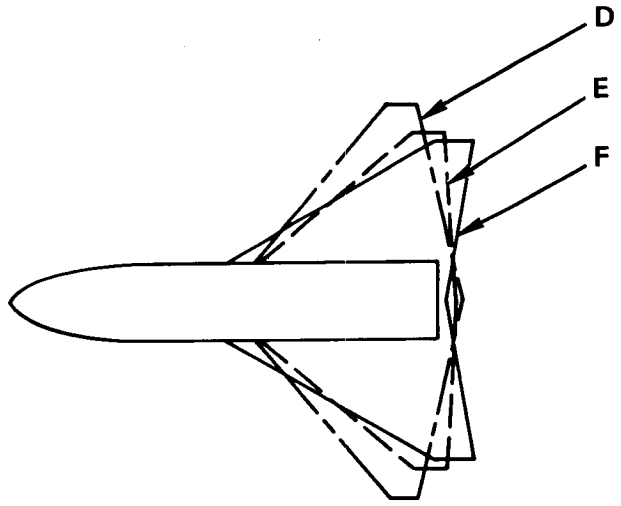

TRAILING EDGE POSITION LIMITED TO -3.8 METERS (-150 IN.) FWD & 1.3 METERS (50 IN.) AFT OF BASE OF BODY

Figure 11

SELECTION OF MINIMUM WEIGHT WING
(Figure 12)

The region of acceptable wing geometry defined by the trailing edge sweep and wing overhang constraints is evaluated for a range of taper ratio to identify the minimum weight wing concept. The wing weight minimizes for a leading edge sweep of 60 degrees, but only a slight weight penalty is incurred for wings with leading edge sweep as low as 50 degrees. For configurations with leading edge sweep greater than 60 degrees, the region of allowable wing geometry shrinks to a very small operating area.

SELECTION OF MINIMUM WEIGHT WING

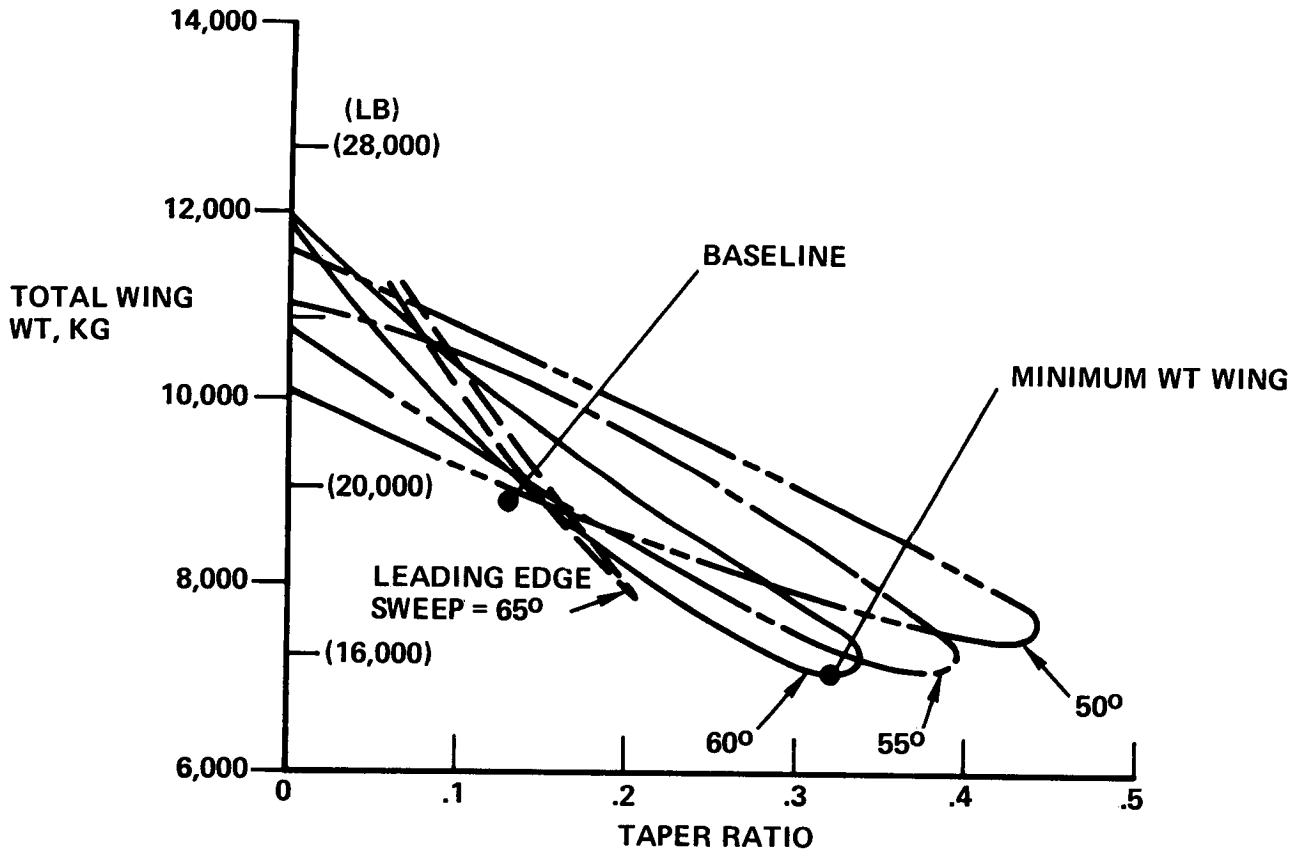

Figure 12

STUDY RESULTS
(Figure 13)

The planform of the minimum weight wing identified in the wing geometry evaluation is characterized as having a lower aspect ratio and higher taper ratio than the baseline configuration. The trailing edge sweep of 19 degrees is the most notable departure from the original delta planform. The weight difference of 1800 kg (4000 lb) relative to the baseline design is actually fairly small in comparison to the weight extremes obtained from the range of wing geometry considered.

STUDY RESULTS

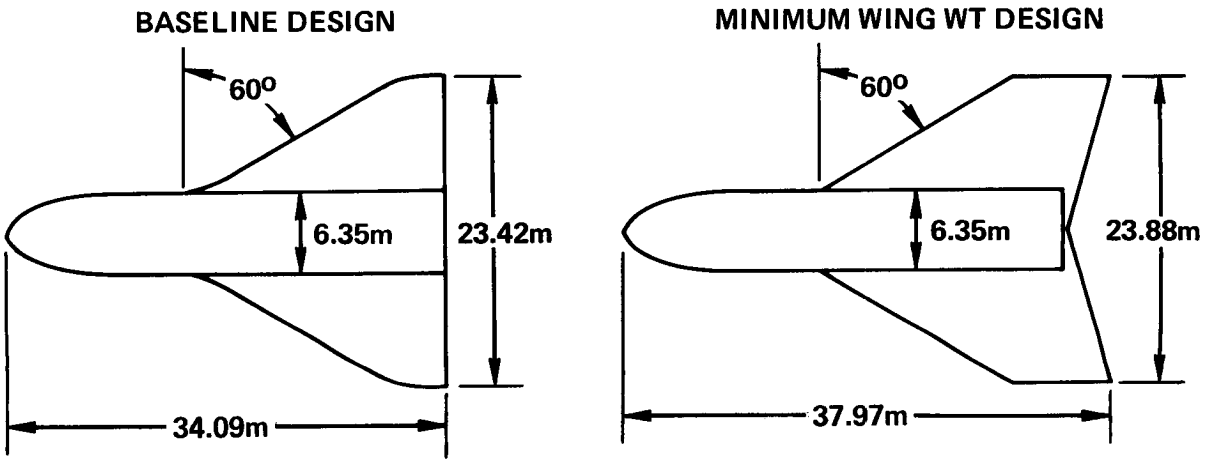

	BASELINE DESIGN	MIN WING WT DESIGN
LEADING EDGE SWEEP, DEG	60	60
ASPECT RATIO	1.8	1.5
TAPER RATIO	.13	.32
THICKNESS, PERCENT	.06-.09	.10
AREA, SQ METERS	314	383
TOTAL WING WT, KG	8890	7076

Figure 13

CONCLUSIONS
(Figure 14)

The minimum weight wing identified by the optimization procedure allows a 20% reduction in the wing weight of the baseline vehicle. However, selection of the minimum weight wing requires a change in the planform shape (lower aspect ratio, higher taper ratio, swept back wing trailing edges) that is outside the range of the delta planforms previously used. The wing selection procedure is also sensitive to the design constraints on aft wing movement, as related to the hypersonic wing-body center of pressure location. Additional analytical and wind tunnel investigations are called for to extend the data base to include the more general wing planforms identified here, in order to verify the potential weight reduction benefits of these wings.

CONCLUSIONS

- OPTIMIZATION RESULTED IN A 20% REDUCTION IN WING WEIGHT
- MINIMUM WEIGHT WINGS REQUIRE LOW ASPECT RATIO AND HIGH TAPER RATIO
- WEIGHT REDUCTION LIMITED BY DESIGN CONSTRAINT ON AFT WING MOVEMENT
- THE STUDY HAS IDENTIFIED AN AREA FOR ADDITIONAL WORK
- IT IS RECOMMENDED THAT ANALYTICAL AND WIND TUNNEL INVESTIGATIONS ON HIGH SWEEP, HIGH TAPER RATIO WING–BODY COMBINATIONS BE INITIATED

Figure 14

REVIEW OF DELTA WING SPACE SHUTTLE VEHICLE DYNAMICS*

By J. Peter Reding and Lars E. Ericsson
Lockheed Missiles & Space Company

The unsteady aerodynamics of the delta planform, high cross range, shuttle orbiter have been investigated. It has been found that these vehicles are subject to five unsteady flow phenomena that could compromise the flight dynamics. They are: (1) leeside shock induced separation, (2) sudden leading edge stall, (3) vortex burst, (4) bow shock-flap shock interaction, (5) forebody vorticity.

Trajectory shaping is seen as the most powerful means of avoiding the detrimental effects of the stall phenomena. However, stall must be fixed or controlled when traversing the stall region. The other phenomena may be controlled by carefully programmed control deflections and some configuration modification. Ways to alter the occurrence of the various flow conditions are explored.

INTRODUCTION

The high cross range, delta wing, space shuttle configurations present the flight dynamicist with a challenging set of flight conditions. These vehicles must fly at speeds from hypersonic down to low subsonic, they must traverse altitudes from orbit to sea level, and are required to fly at angles of attack from zero to as high as 50° in some cases. The angle of attack requirements probably cause the most severe aerodynamic stability problems since the vehicle is stalled, or, what is worse, nearly stalled, for much of the trajectory. There is the danger of experiencing a sudden, discontinuous change in stability when flying near incipient stall (either stalled or unstalled) which will raise havoc with the flight dynamics.

Because of past experience with the effects of unsteady aerodynamics on vehicle dynamics (Refs. 1-17), Lockheed was chosen by the NASA Manned Spacecraft Center to investigate the unsteady aerodynamics of the high cross range, delta planform, shuttle vehicles. This work, reported herein, is exploratory in nature. Possible problem areas are identified, their impact on the flight dynamics is explored, and fixes are suggested.

The major portion of this report deals with the North American Rockwell (NAR) delta orbiter. This is wholly the result of the availability of wind tunnel data at the time of the study. The problems discussed are by no means peculiar to the NAR orbiter. They are, in fact, common to the various delta wing designs, the only difference being minor shifts of the ranges of the instabilities.

* The results reported herein were obtained in study conducted for the NASA Manned Spacecraft Center under Contract NAS 9-11445.

ENTRY ATTITUDE HISTORIES
(FIGURE 1)

Generally the various delta orbiters follow a similar angle of attack-Mach number profile (Figure 1 and Ref. 18). Entry occurs at a high initial angle of attack (up to 53 degrees). At $M \approx 20.0$ pitchover to between 20 and 35 degrees is accomplished where a bank angle program is initiated to achieve the required cross range. This continues to $M \approx 7.0$ where pitchover to the subsonic cruise attitude, which varies between 5° and 10°, is initiated. The pitchover maneuver may last down to $M \approx 1.0$. A very important part of the trajectory is flown at high angle of attack and high Mach number.

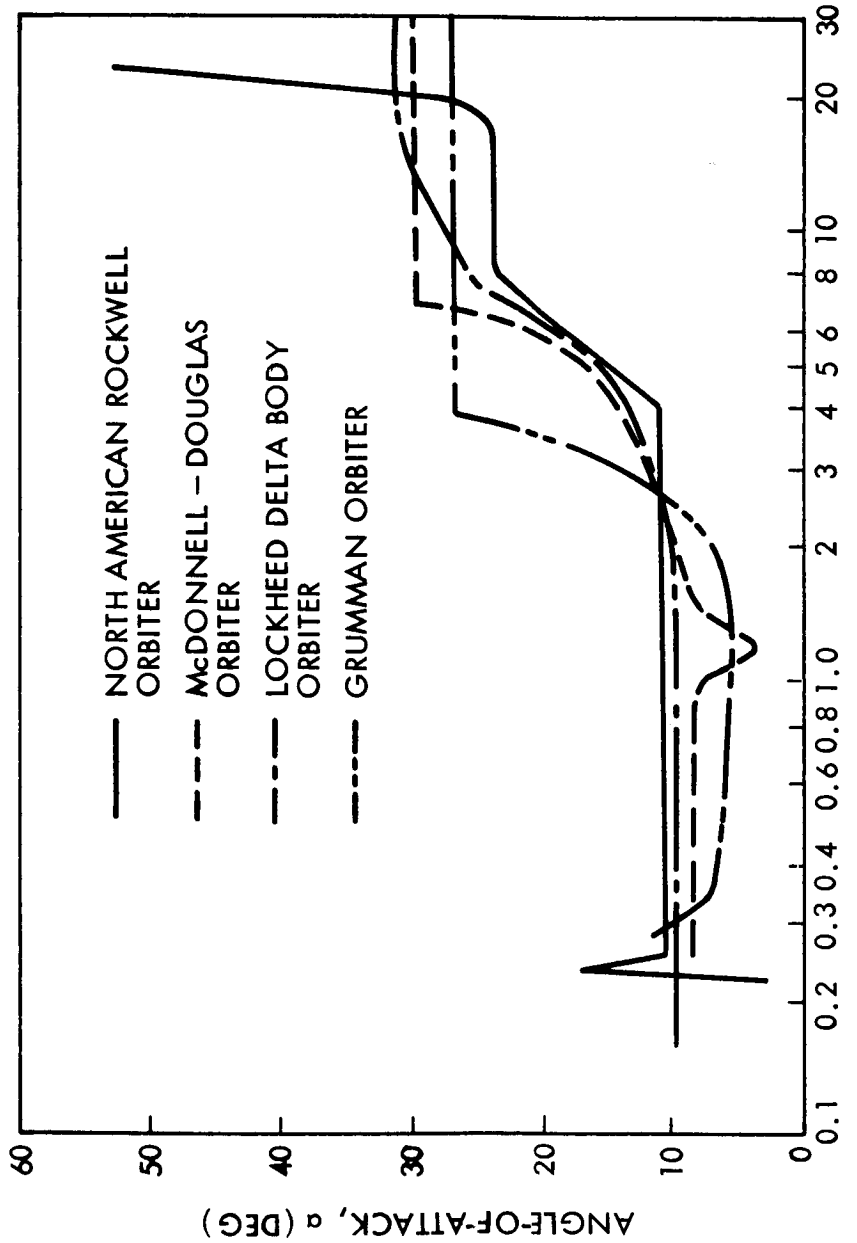
ENTRY ATTITUDE HISTORIES
NORTH AMERICAN ROCKWELL ORBITER
McDONNELL – DOUGLAS ORBITER
LOCKHEED DELTA BODY ORBITER
GRUMMAN ORBITER
ANGLE-OF-ATTACK, α (DEG)
MACH NUMBER, M
0
10
20
30
40
50
60
0.1
0.2
0.3
0.4
0.6
0.8
1.0
2
3
4
5
6
8
10
20
30

Figure 1

HYPERSONIC LEESIDE FLOW PATTERNS

(FIGURE 2)

It is quite possible to arrive at some very erroneous conclusions if one approaches the high α -M regime with Newtonian theory in mind. Leeside effects are not negligible as Seegmiller's excellent flow photographs demonstrate (Figure 2 and Ref. 19). At moderate angle of attack a significant region of attached flow exists on the leeward side of the delta wing (Figure 2a). Also relatively strong reattachment zones may be seen on the sides of the fuselage at all angles of attack. Furthermore, a reattachment zone exists on the leeward fuselage, which, like the region of attached flow on the wing, is sensitive to yaw angle.* As angle of attack is increased the wing separation grows until nearly the entire wing -- in fact, nearly the entire leeside of the vehicle -- is separated (Figures 2b and 2c). However, this does not occur until very high angles of attack.

* Note the asymmetry of both due to the negative yaw angle of Figure 2b.

HYPERSONIC LEESIDE FLOW PATTERNS (NAR ORBITER, M = 7.4)

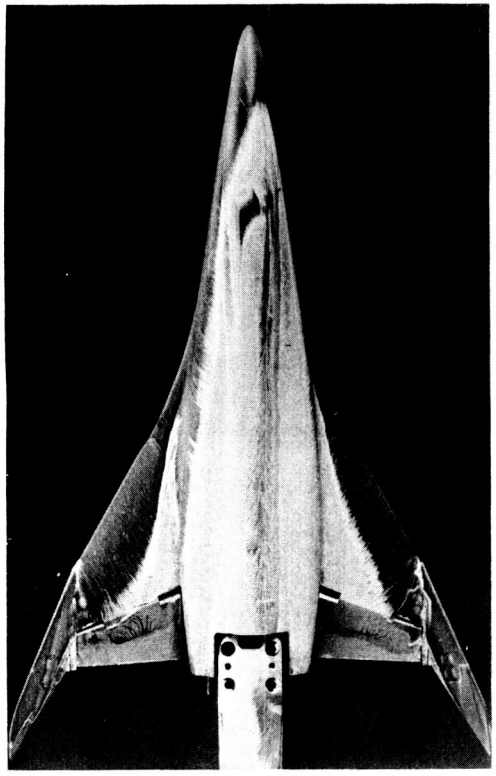

A. α = 15 DEG, β = -5 DEG

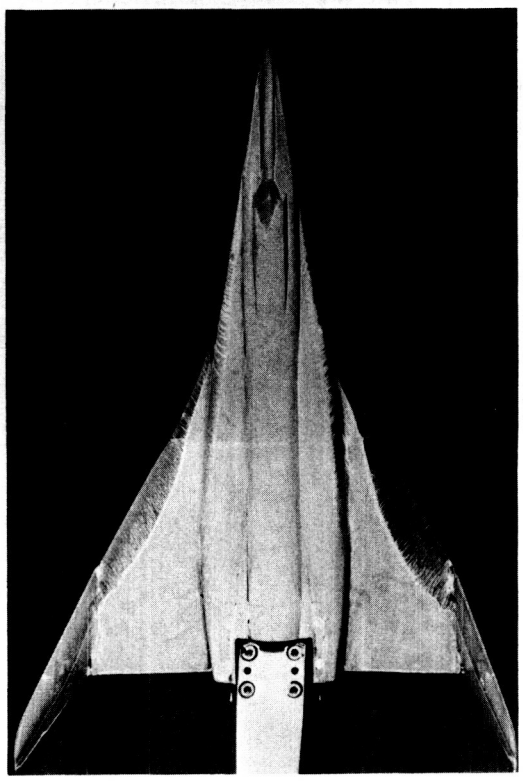

B. α = 30 DEG, β = 0 DEG

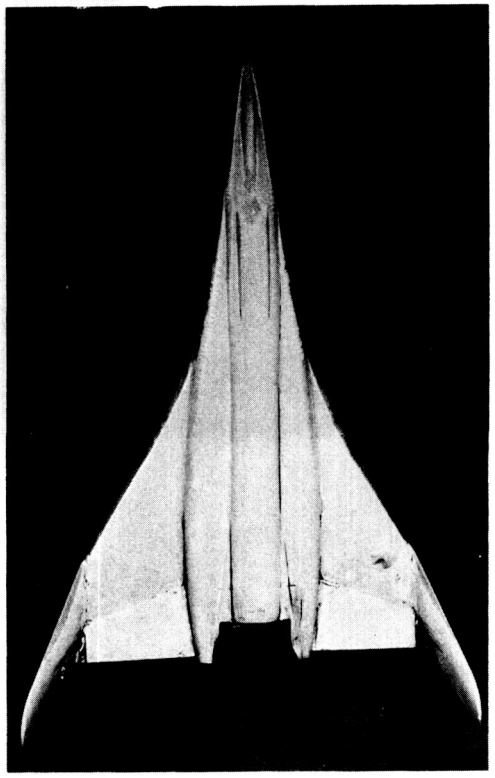

C. α = 45 DEG, β = 0 DEG

Figure 2

HYPERSONIC LEESIDE FLOW FIELD
(FIGURE 3)

The salient features of the leeside flow are illustrated in Figure 3. The strong leeside flows have a significant, sometimes a dominant, effect on orbiter stability as the following discussion will demonstrate.

HYPERSONIC LEESIDE FLOWFIELD

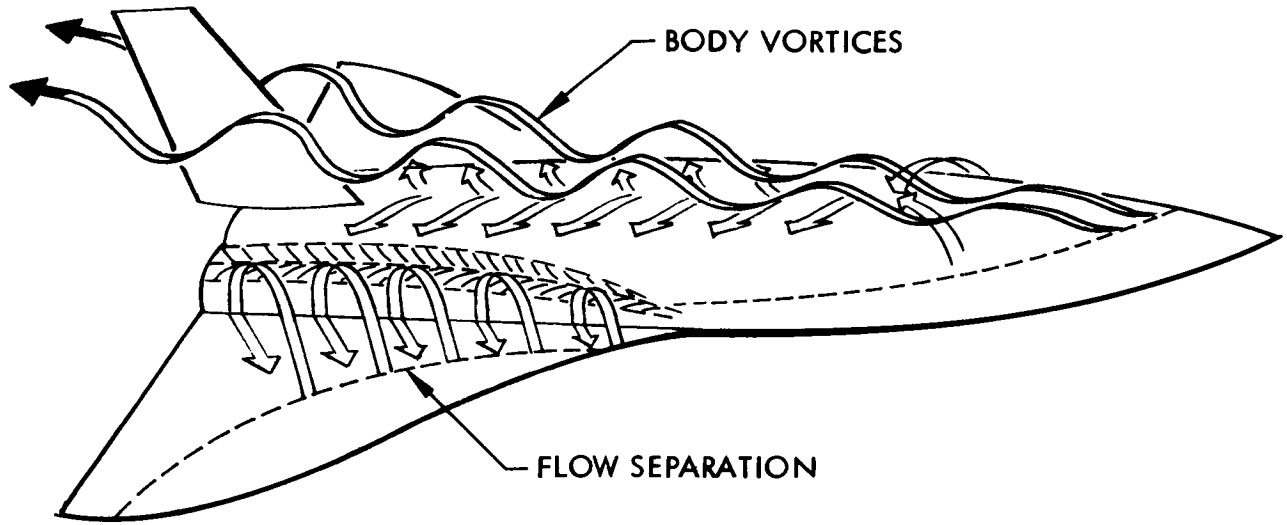

Figure 3

HYPERSONIC LEESIDE FLOWS ON A PURE DELTA WING (M = 10.16) (FIGURE 4)

The surface flow patterns presented by Cross (Ref. 20) suggest a number of distinct flows on the leeside of a delta wing at hypersonic speeds (Figure 4). At low angles of attack the flow converging from opposite wing panels (in the case of the pure delta wing) or from wing and fuselage (in the case of the shuttle) is turned parallel to the free stream by a weak shock (Type 1). When the angle of attack is great enough to cause the wing leading edge shock to detach the embedded terminal leeside shock becomes strong enough to separate the boundary layer (Type 2). That is, the subsonic flow aft of the detached shock expands around the leeward leading edge reattaining supersonic speeds. The flow is still constrained to turn downstream near the root as before. This turning is accomplished by a strong shock that causes the boundary layer to separate. The wake begins to affect the flow patterns at higher angle of attack, causing a secondary separation (Type 3). This is undoubtedly promoted by the thick, laminar, leeside boundary layer. As angle of attack is increased further the leeward boundary layer is weakened. This couples with the increased leeside expansion to promote separation. The separation region, therefore, grows until it reaches the leading edge (Type 4). This type of flow is somewhat similar to the subsonic delta wing flow with a vortex bound to the leading edge. Increasing the angle of attack still further results in a breakdown or burst of the bound vortex near the trailing edge. Finally, at still larger angles of attack, the leeward flow separation takes on a complicated three-dimensional, wake-like character (Type 5).

HYPERSONIC LEESIDE FLOWS ON A PURE DELTA WING (M = 10.16)

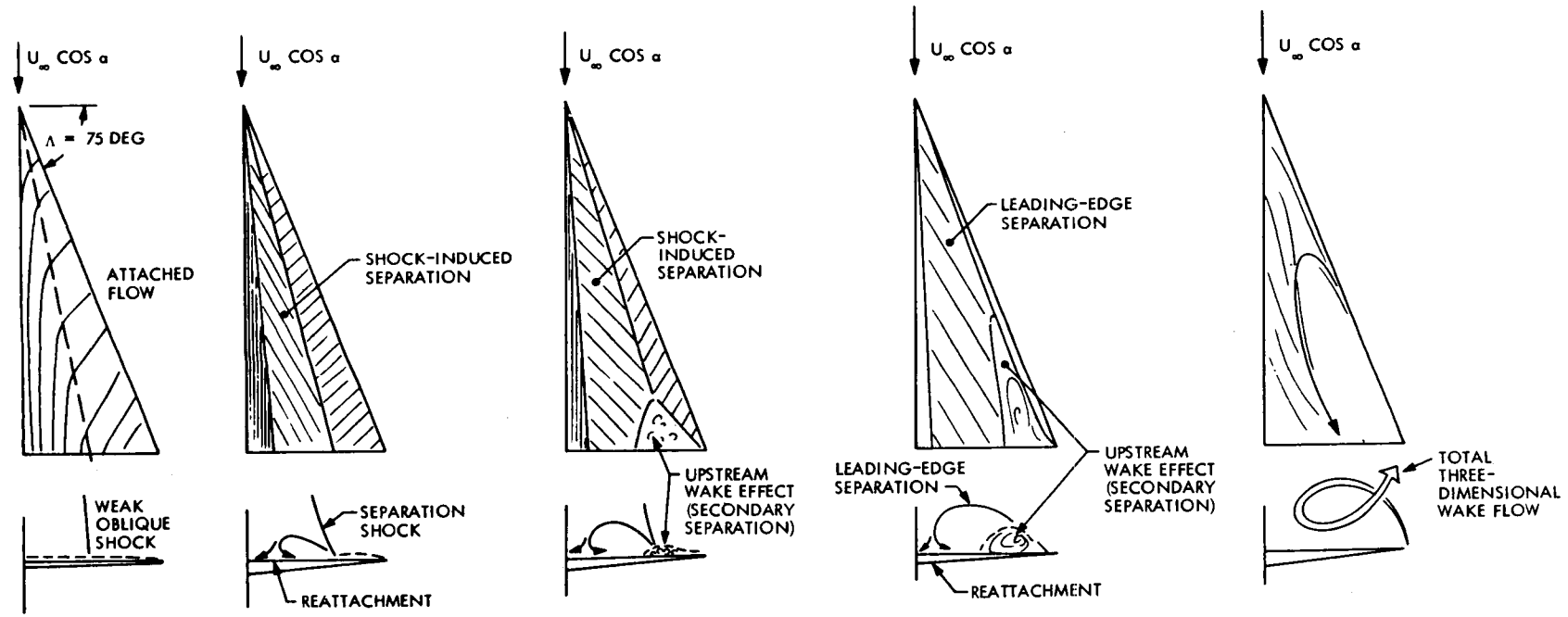

Figure 4

COMPARISON OF EXPERIMENTAL LEESIDE FLOW BOUNDARIES
(FIGURE 5)

The changes in flow type observed by Cross correlate with discontinuities in the α -dependence in the location of the terminal shock position (Figure 5a). The shock position is determined by the Mach angle until leeside shock induced separation occurs. The shock then moves outboard rapidly at constant rate until it nears the leading edge. Here the shock position becomes less sensitive to angle of attack as separation becomes fixed to the leading edge. Of course the delta wing space shuttle orbiter experiences similar flow phenomena (Compare Figures 5a and 5b).* The shuttle data seem to indicate the possibility of a hysteresis region associated with the occurrence of shock induced separation. Again the occurrence of leeside shock induced separation correlates with wing bow shock detachment.

* The data in Figure 5b were measured on a double tail configuration (Ref. 19). However, the relative spanwise shock position (b_s/b) was measured at a chord station that appeared to be unaffected by the leading edge-fuselage interaction or by the wing-tail interaction; that is, where the separation line was relatively straight.

COMPARISON OF EXPERIMENTAL LEESIDE FLOW BOUNDARIES

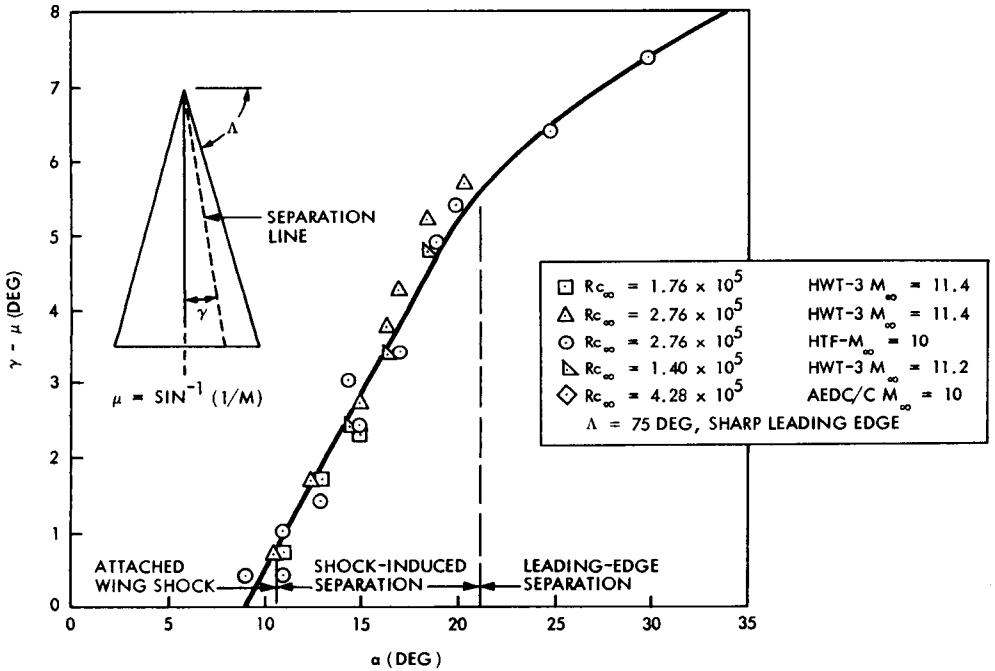

A) PURE DELTA WING, M = 10.16 (REF. 20)

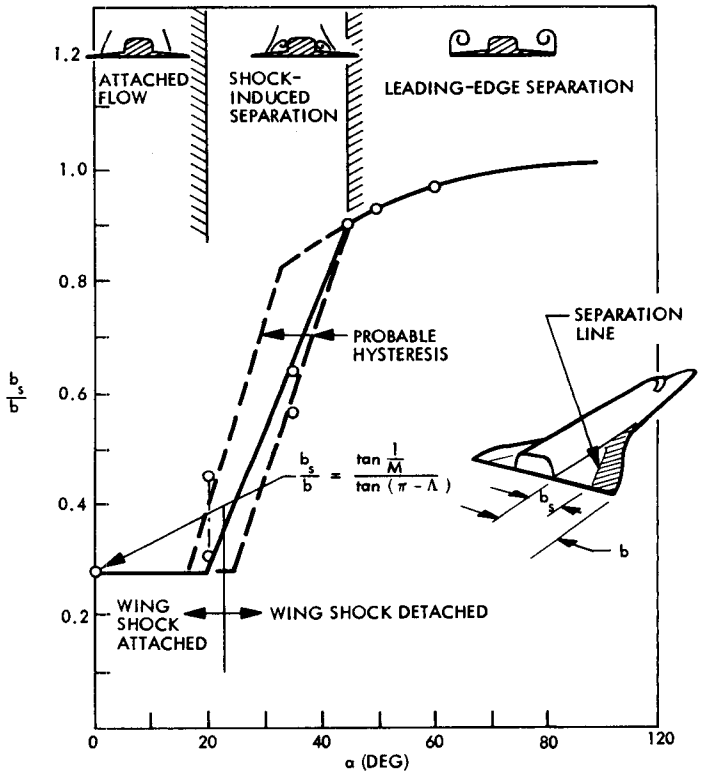

B) NAR DELTA ORBITER, M = 7.4 (REF. 19)

Figure 5

EFFECT OF LEESIDE SEPARATION ON LONGITUDINAL STABILITY
(FIGURE 6)

As one would expect the leeside flow separation affects the shuttle stability. The angle of attack of shock detachment correlates the discontinuity of the wing pitching moment, (Figure 6 and Refs. 21-23). The change to a more stable pitching moments slope is the result of the subsonic leading edge suction that occurs when the wing bow shock detaches. In addition, there is reduction in the lift over the wing area aft of separation (see sketches in Figure 6). Due to the increasing leading edge sweep towards the trailing edge, the center of pressure is more aft for the lift gain (due to L.E. suction) than for the lift loss (due to shock induced pressure increase aft of separation line). Thus, the wing pitching moment becomes more stable (Figure 6a) although the incremental lift remains nearly linear (Figure 6b).

EFFECTS OF LEESIDE SEPARATION ON LONGITUDINAL STABILITY

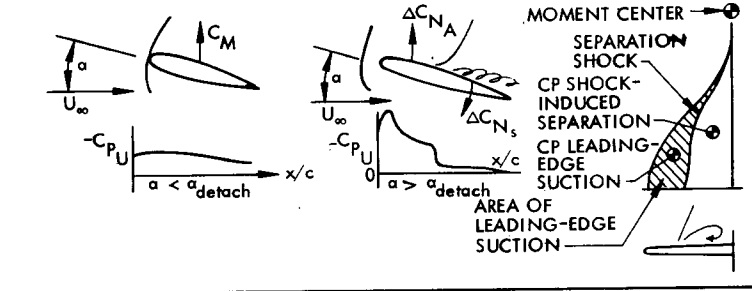

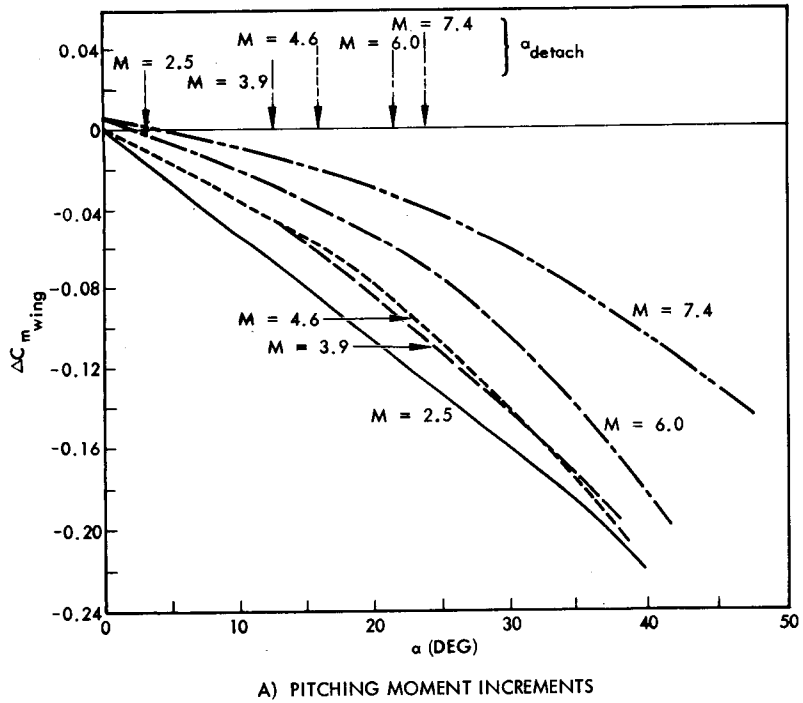

A) PITCHING MOMENT INCREMENTS

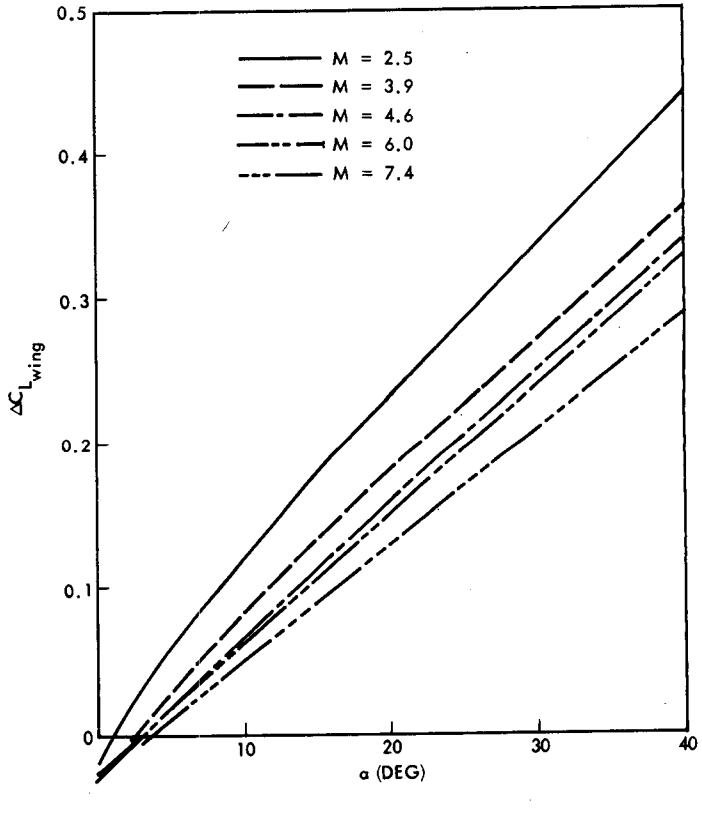

B) LIFT INCREMENTS

Figure 6

EFFECT OF LEESIDE SEPARATION ON ROLL STABILITY
(FIGURE 7)

The lift redistribution also explains the nonlinear wing induced roll characteristics (Ref. 24). As the body is yawed the shock induced separation becomes asymmetric. The separation grows on the leeward side giving a negative incremental lift, and shrinks on the windward side causing a positive incremental lift. The result is a stable (negative) incremental roll moment of a larger magnitude than for attached flow. When leading edge separation occurs the growth of the negative lift increment is arrested and a less negative C_{ℓ_β} results (Figure 7). Thus, the non-linearity in the roll curve indicates the occurrence of leading edge separation. Likewise, a non-linearity in the incremental wing pitching moment occurs due to leading edge separation, although the discontinuity is less distinct than that for the roll moment characteristics. Thus, the α -M range of shock induced separation may be obtained directly from the static data. Shock induced separation is characterized by an extreme (maximum) sensitivity of shock position and wing loading to angle of attack. This is undoubtedly due to the sensitivity of the boundary layer, hence the separation, to angle of attack. This dominance of viscous effects indicates that the separation extent, and thus the wing loads, will be extremely sensitive to all factors affecting boundary layer strength (e.g., angle of attack, yaw angle, Reynolds number, pitch rate, yaw rate, etc.). The dominance of viscous effects will have a particularly strong impact on the dynamic characteristics.

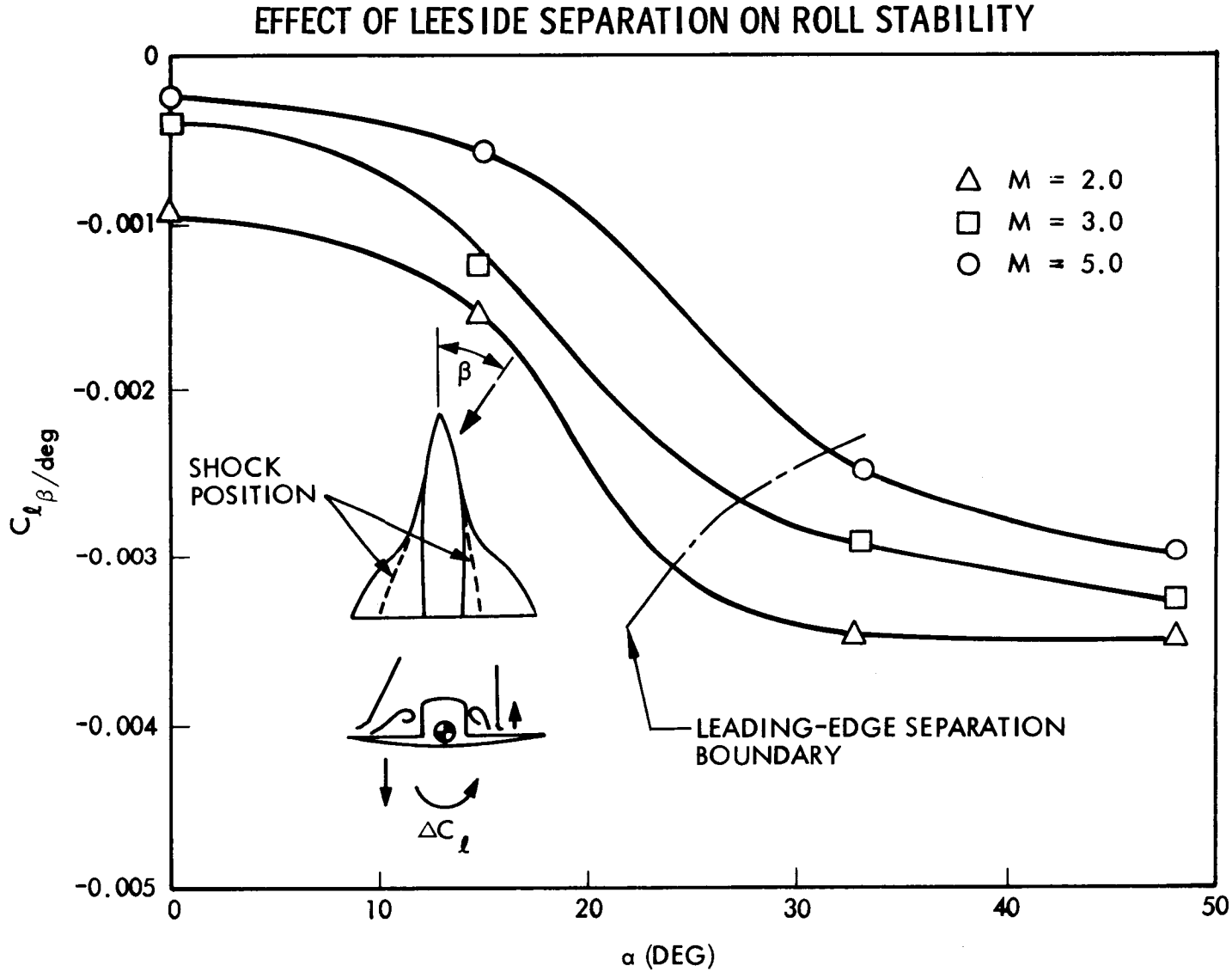
EFFECT OF LEESIDE SEPARATION ON ROLL STABILITY
0
-0.001
-0.002
-0.003
-0.004
-0.005
$C_{l_\beta/deg}$
0
10
20
30
40
50
α (DEG)
M = 2.0
M = 3.0
M = 5.0
β
SHOCK POSITION
ΔC$_l$
LEADING-EDGE SEPARATION BOUNDARY

Figure 7

COMPARISON OF LEESIDE FLOW BOUNDARIES WITH α_{TRIM} SCHEDULE (FIGURE 8)

The fundamental principle in the application of quasi-steady theory to the dynamics of bodies dominated by separated flow is that of the time lag (Refs. 1-17). In the case of leeside shock induced separation the time lag due to the finite convection speed within the boundary layer is amplified by accelerated flow effects, which change the boundary layer strength. Because of this lag, one can apply the so called reversed reactions rule. That is, if the induced load is statically stabilizing it will be undamping dynamically. It was shown earlier that the shock induced separation produced statically stabilizing contribution to the pitching and roll moments. Consequently, the shuttle vehicle will experience degraded pitch and roll damping if it experiences shock induced separation. If the trajectories of References 24 and 28 are representative, the shuttle will indeed experience leeside shock induced separation with the attendant dynamic difficulties.

COMPARISON OF LEESIDE FLOW BOUNDARIES WITH α_{TRIM} SCHEDULE

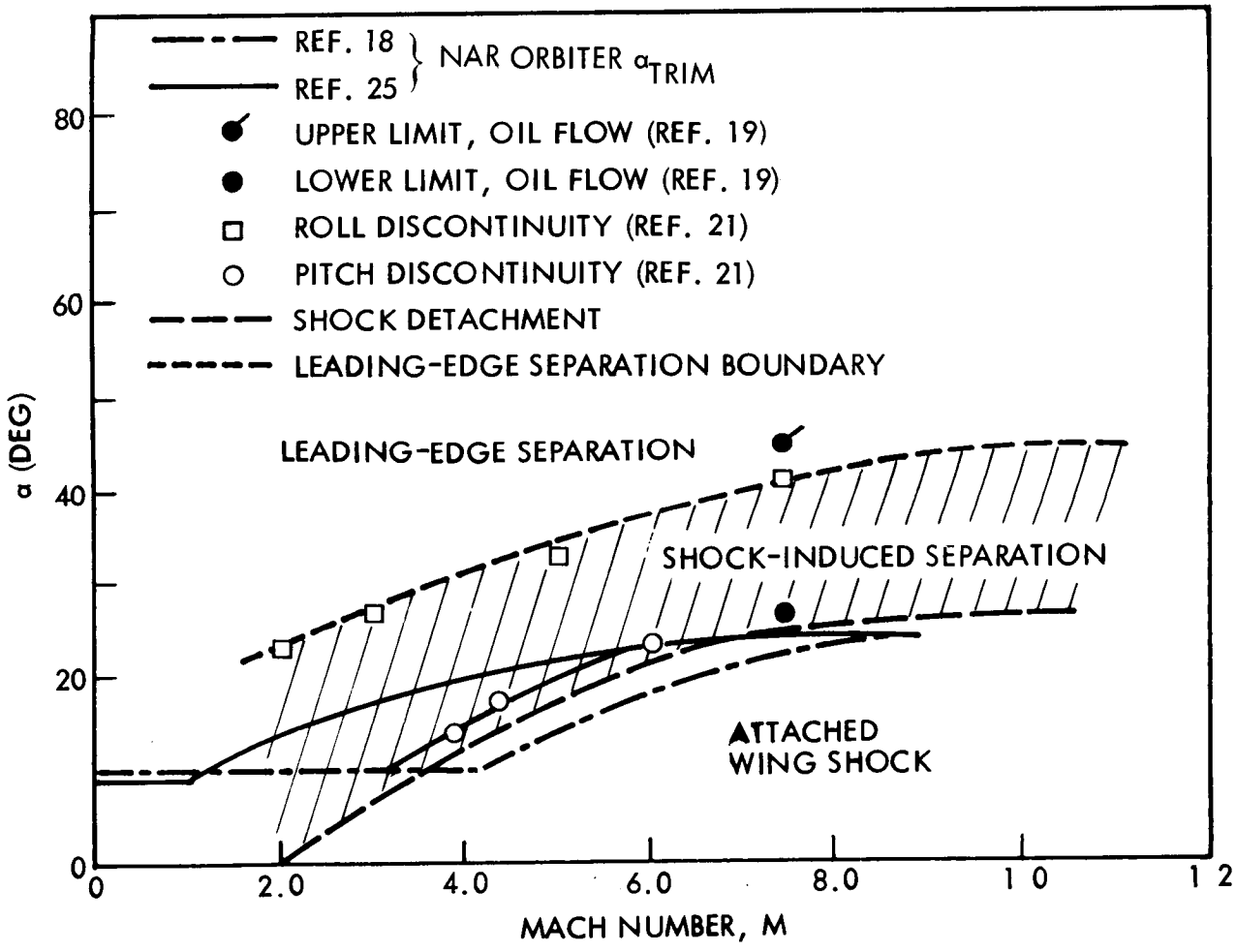

Figure 8

LEADING EDGE VORTEX LAG MEASUREMENTS
(FIGURE 9)

A damping degradation may also result from the leading edge separation. Leading edge separation at high Mach numbers is similar to subsonic delta wing flow, since in both cases a vortex is bound to the wing leading edge. Lambourne (Ref. 26) has shown that the leading edge vortex position lags dynamically (Figure 9a). On the upstroke the vortex is closer to the wing and further outboard relative to the static position. This results in greater lift, due to increased leading edge suction, which is located further outboard. The incremental moment, therefore, is in the direction of the motion and is undamping. Similarly the smaller, further inboard, downstroke load is also undamping. The lag in the vortex position is the result of the finite vortex convection speed. That is, the vortex travels downstream with free stream speed as Lambourne et al, (Ref. 27) have shown (Figure 9b).

LEADING EDGE VORTEX LAG MEASUREMENTS

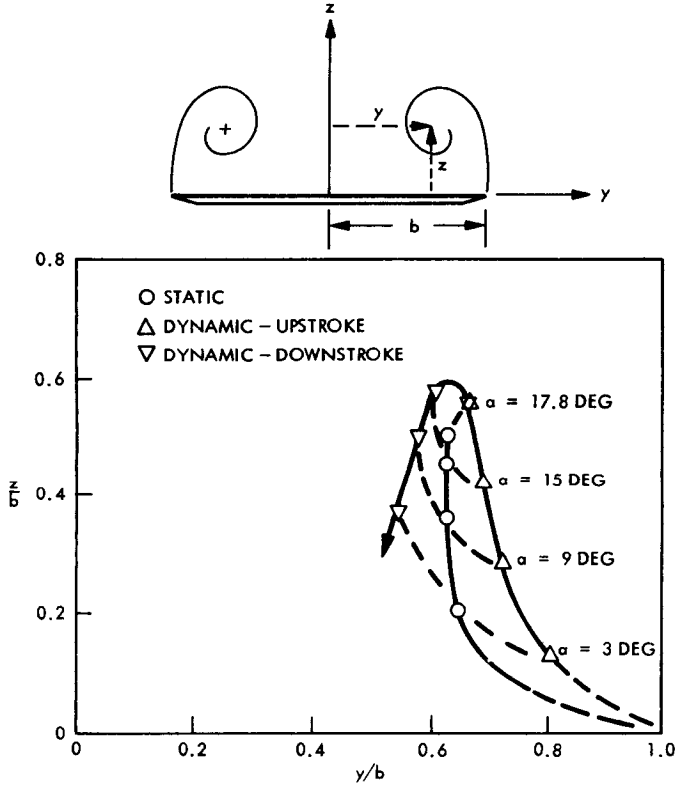

A) COMPARISON OF STEADY AND UNSTEADY VORTEX POSITIONS (REF. 26)

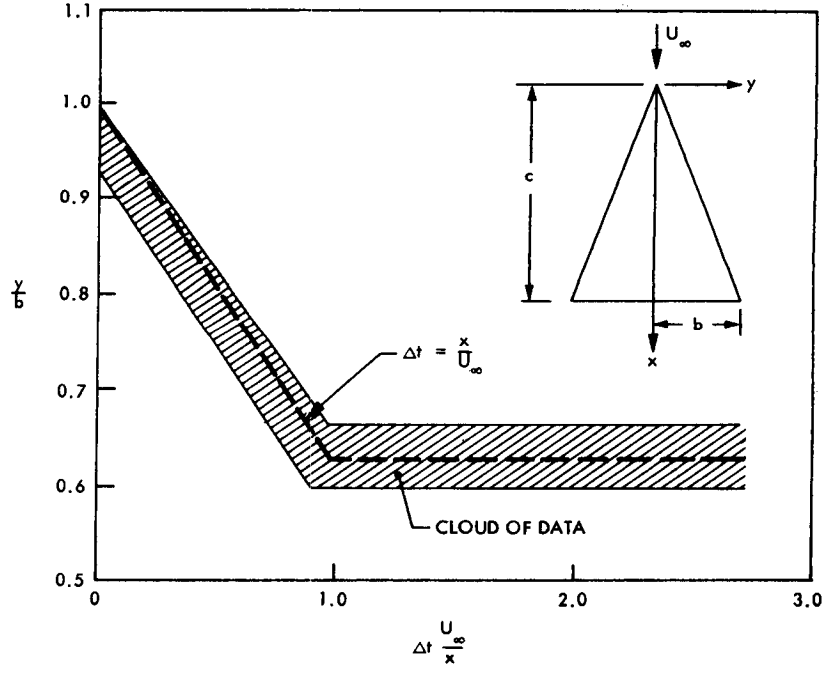

B) VORTEX POSITION AS FUNCTION OF TIME FOR PLUNGING DELTA WING (REF. 27)

Figure 9

ESTIMATED ROLL DAMPING CHARACTERISTICS AT M = 6.0 FOR NAR ORBITER
(FIGURE 10)

By applying the shock induced time lag and accelerated flow effect derived in Ref. 15 (from the data of Ref. 28) to the crossflow normal to the leading edge, and using free stream speed for the vortex convection velocity also at supersonic Mach numbers (measured for subsonic Mach numbers in Ref. 29), it is possible to get an estimate of the leeward side contribution to the roll damping. The estimated leeside damping ($C_{\ell_\beta} \cdot \tan \alpha$) is obtained by assuming that the large statically stabilizing roll derivative measured in wind tunnel tests is in totality the result of the separation induced loads. In Figure 10 this is compared to the windward side damping derivative ($-C_{\ell_p}$) as given by hypersonic small disturbance theory (Ref. 29). It is evident that roll undamping can result due to shock induced separation, and for the trajectory given in Ref. 25 it could exist over a considerable Mach number range (Figure 8). While the results are only approximate, they do demonstrate that shock induced separation could cause roll undamping of the shuttle orbiter.

ESTIMATED ROLL DAMPING CHARACTERISTICS AT M = 6.0 FOR NAR ORBITER

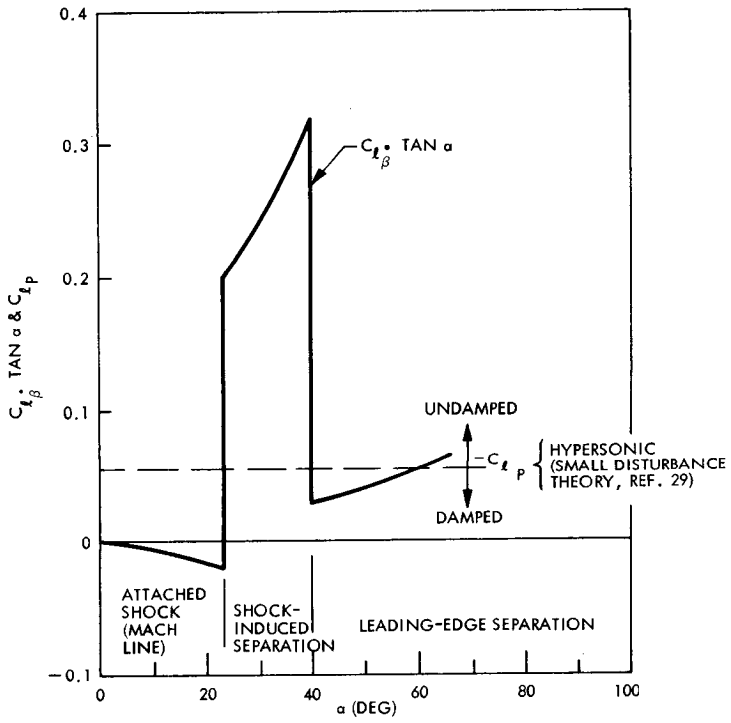

Figure 10

SUDDEN LEADING EDGE STALL
(FIGURE 11)

When the Mach number normal to the leading edge is slightly less than unity (M = 2.0 for NAR shuttle) the separation can suddenly switch from the shock induced variety to leading edge separation with a corresponding discontinuous change in wing loading. This phenomenon is analogous to the switch between transonic flow attachment and leading edge stall and is, therefore, dependent upon the airfoil section configuration (Ref. 30). Typical boundaries for sudden leading edge stall are shown in Figure 11 for a practical airfoil section. The disconcerting feature of this plot is that the jump is from an aft shock position (transonic attachment) to L. E. separation which implies a very large change in loading.

For some rather thin airfoils the flow was observed to oscillate between L.E. separation and transonic attachment followed by a region where the terminal normal shock position was unsteady. This behavior is reminiscent of the results of Chevalier and Robertson (Ref. 31). They observed that the flow aft of the shoulder of a cone-cylinder body switched between totally separated and attached. The body of revolution results are simply the three-dimensional analog of the airfoil results. The discontinuous jump from attached to separated flow occurs when the terminal normal shock enters the near nose region with its adverse pressure gradient. At some point the shock induced pressure rise, coupled with the near nose adverse pressure gradient, is just too much for the boundary layer, and separation jumps to the shoulder (in the case of cone-cylinder) or to the point where the boundary layer encounters a pressure gradient that it can tolerate.

SUDDEN LEADING EDGE STALL

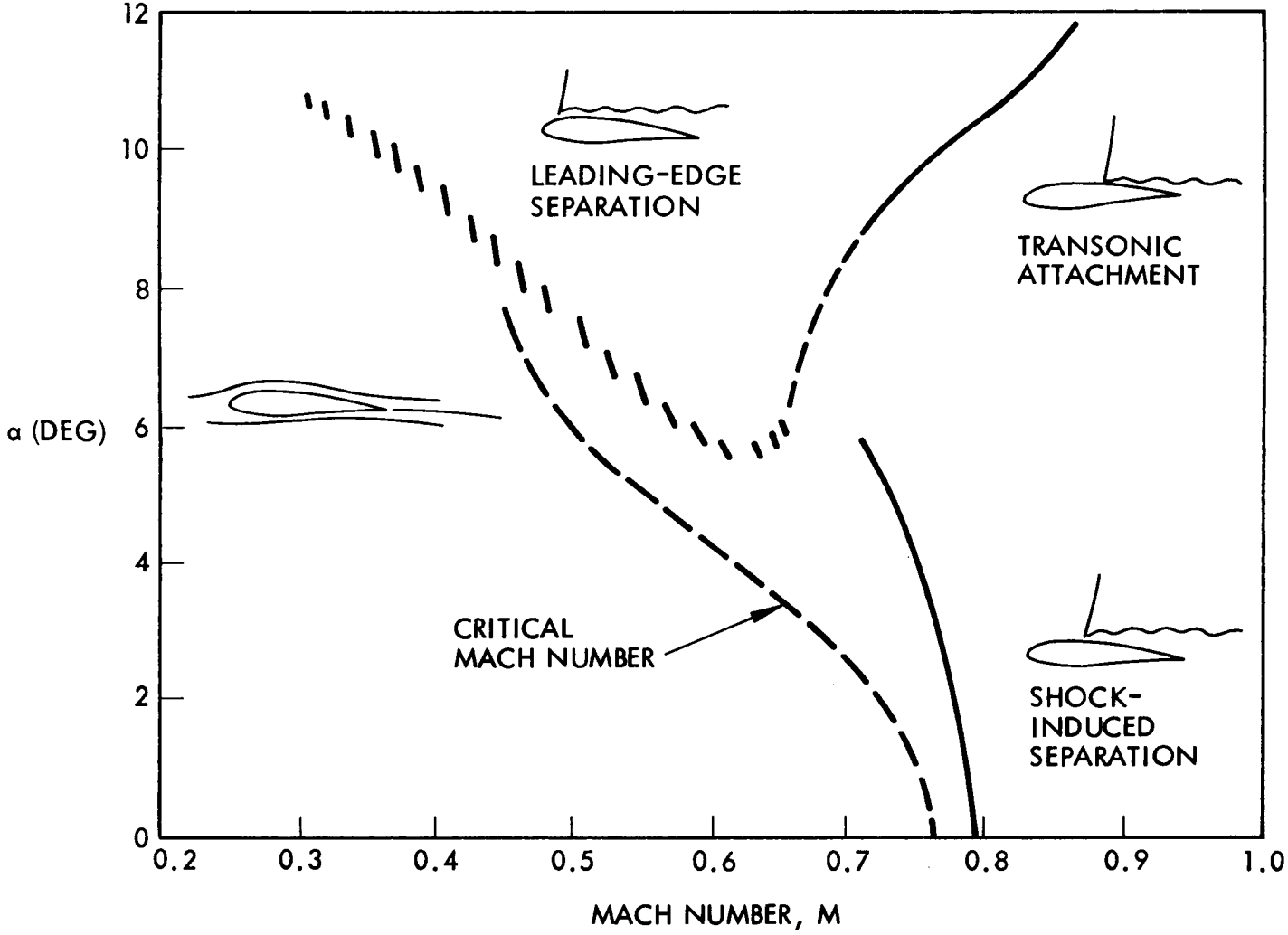

Figure 11

COMPARISON OF PRESSURE DISTRIBUTIONS FOR SUDDEN SEPARATION (FIGURE 12)

The similarity between the two- and three-dimensional flows is illustrated in Figure 12. Both result in large discontinuous, statically stabilizing, pitching moments when the sudden nose stall is established. For the cone-cylinder body it has been shown that dynamically the jump will lag the body motion, due mainly to the accelerated flow relief of the adverse pressure gradient, and, to a lesser extent, due to the delay of boundary layer buildup on the leeward side (as a result of a finite convection speed in the boundary layer, Refs. 4 and 5). Likewise, pitch rate induced camber and accelerated flow effects have a large influence on the jump to leading edge stall, perhaps even larger than their influence on regular (low speed) dynamic airfoil stall (Refs. 14-16 and 32).

COMPARISON OF PRESSURE DISTRIBUTIONS FOR SUDDEN SEPARATION

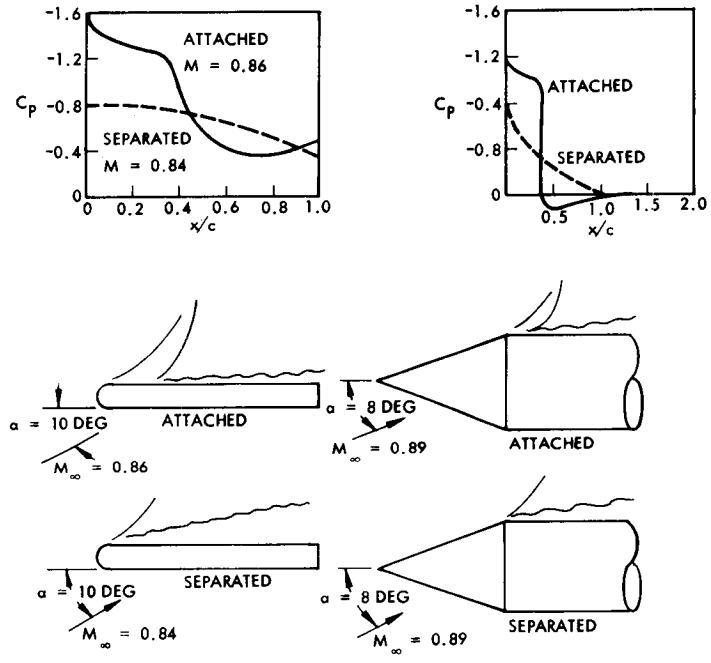

(a) SLAB WING (REF. 30) (b) 15-DEG CONE-CYLINDER (REF. 31)

Figure 12

DYNAMIC EFFECTS OF SUDDEN SEPARATION ON BODIES OF REVOLUTION (FIGURE 13)

The jumpwise change in aerodynamic loads represents an infinitely stable moment derivative which results in infinite undamping for infinitesimal amplitude oscillation at the jump angle of attack. However, as oscillation amplitude is increased the undamping becomes finite due to the finite moment derivatives on either side of the jump (Refs. 4 and 5). Thus, the damping is a function of oscillation amplitude (Figure 13a). It has been shown that the experimentally observed undamping of the Saturn I vehicle with a Jupiter nose cone (Refs. 5 and 33) was the result of a sudden separation (Figure 13b). Thus, one would expect the sudden leeside separation on the shuttle wings to have equally drastic dynamic effects. That is, limit cycle oscillations in pitch and/or roll would result unless damping were supplied via the control system.

DYNAMIC EFFECTS OF SUDDEN SEPARATION ON BODIES OF REVOLUTION

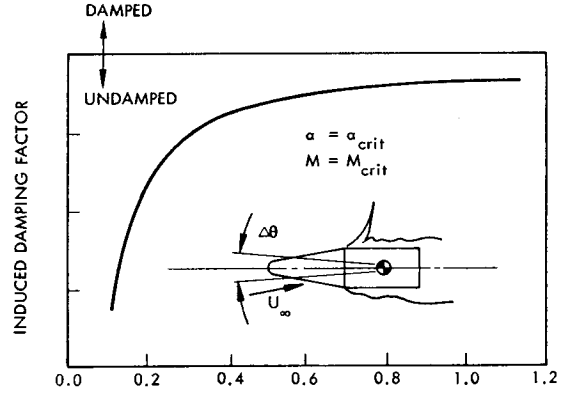

(a) EFFECT OF AMPLITUDE ON DAMPING FOR COLLAPSING SEPARATION (REF. 5)

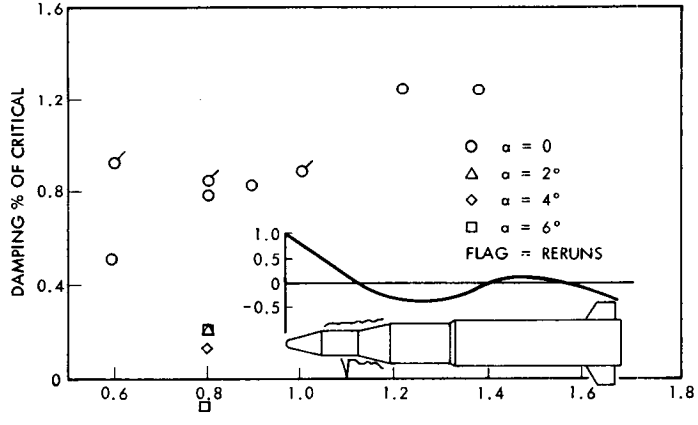

(b) EFFECT OF SUDDEN SEPARATION ON SECOND MODE DAMPING OF SATURN I W/JUPITER NOSE (REF. 33)

Figure 13

DYNAMIC EFFECTS OF MIXED FLOW
(FIGURE 14)

On the swept wing a mixed flow condition can result (Figure 14a, Ref. 34). That is, the inner portion of the wing may be stalled at the leading edge while the flow over the outer wing leading edge is attached with shock induced separation occurring a short distance downstream. In the unsteady case the demarkation line between the flow conditions will oscillate spanwise as the wing pitches or plunges. There will undoubedly be a random (motion independent) oscillation superimposed on the motion dependent oscillation. It is likely that the motion dependent oscillation of this separation boundary was the cause of the large amplitude bending response measured on the wing of the earlier straight wing shuttle (Figure 14b, Ref. 35). Likewise the spanwise, motion dependent, oscillation of the demarkation line can degrade roll damping of the delta wing shuttle. This separation phenomenon also serves to couple the effects of pitch, yaw, and roll motions.

The mixed separated-attached flow condition has not, to the knowledge of the authors, been observed on any of the delta orbiters (possibly because no one has really looked for it), but it is certainly possible that it could occur. It is important to determine whether it is there or not, as its effects can be disastrous, and there are ways to alleviate these effects and possibly avoid the flow phenomena altogether, as will be discussed later.

DYNAMIC EFFECTS OF MIXED FLOW

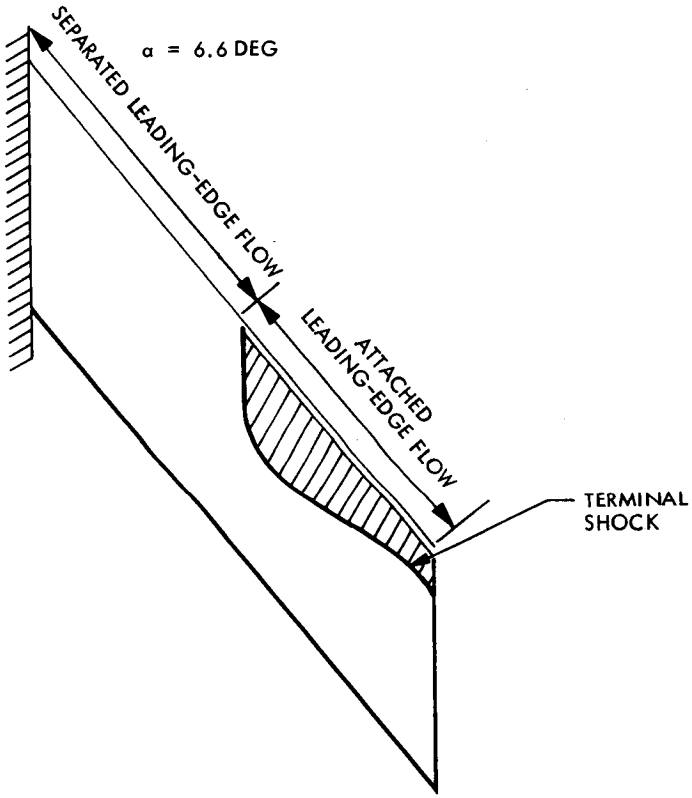

A) MIXED FLOW CONDITION, M = 1.05 (REF. 34)

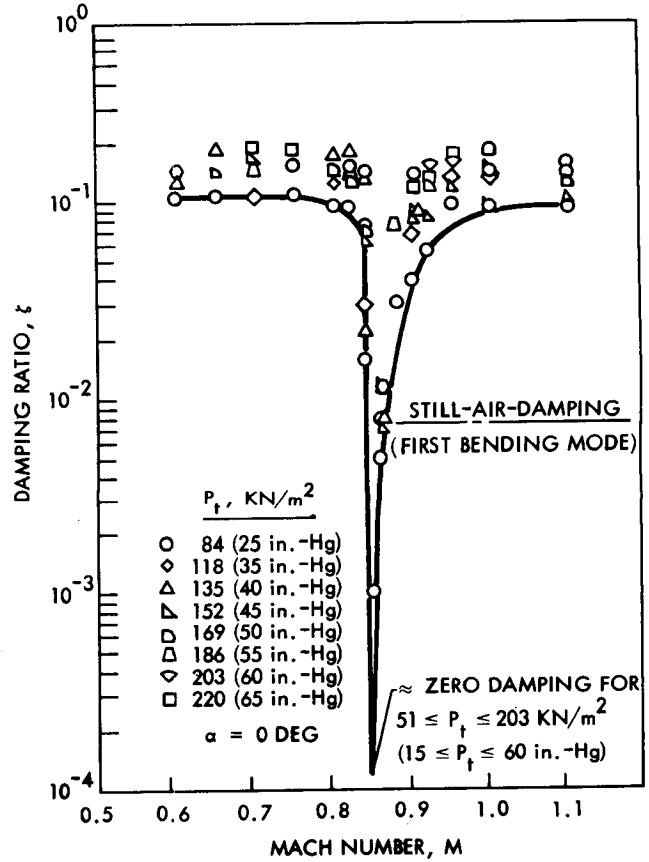

B) EFFECT OF MIXED FLOW ON THE DAMPING OF A STRAIGHT SHUTTLE WING (REF. 35)

Figure 14

VORTEX BURST
(FIGURE 15)

It is well known that vortex lift is a major portion of the lift on delta wings at subsonic speeds. Polhamus' "turned-up" leading edge suction predicts vortex lift and drag quite well (Refs. 36 and 37). However, as yet there is no similarly simple means of predicting vortex burst which has drastic effects on delta wing characteristics. It remains a well documented but still not fully understood phenomenon.

When leading edge vortex breakdown occurs over the delta wing, a loss of lift due to the decreased suction results (Figure 15a, Ref. 38). This usually results in reduced longitudinal and lateral stability (Figure 15b, Ref. 38). There has, therefore, been extensive experimental research aimed at defining the vortex breakdown phenomena for delta wings. Lambourne showed that the delay of vortex breakdown with increasing leading edge sweep could be scaled by using the angle the leading edge forms with the free stream velocity vector (Ref. 39). He found also that vortex breakdown is relatively insensitive to Reynolds number. (As Ludwieg's inviscid analysis, Ref. 40, predicts experimentally observed vortex bursts, this result is not unexpected.) Sideslip effects on vortex breakdown could probably be accounted for by adding the yaw angle to Lambourne's scaling. The effect of yaw is, of course, to cause earlier breakdown on the windward wing-half with its lesser effective sweep angle.

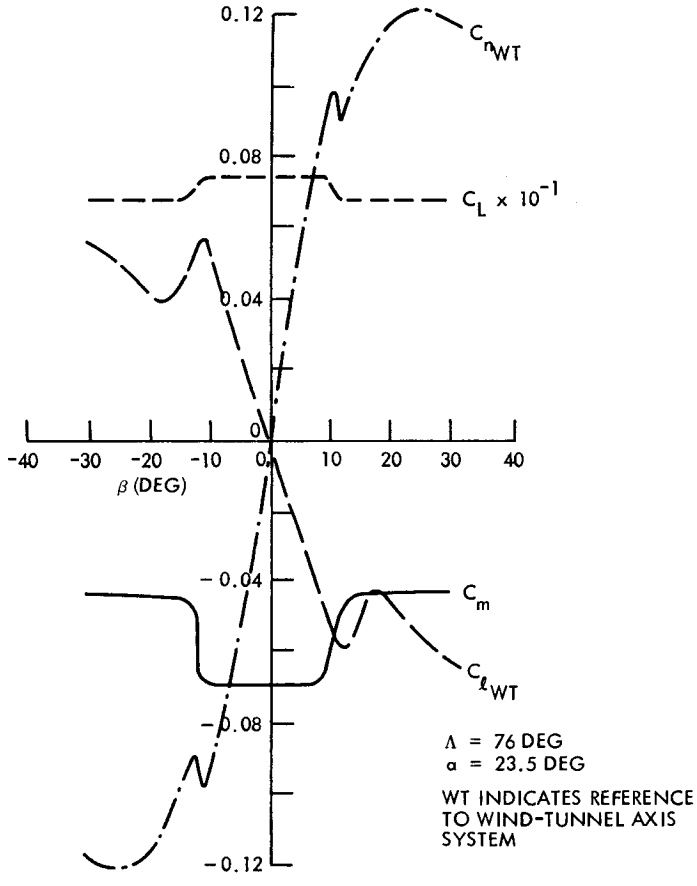

A) EFFECT OF VORTEX BURST ON DELTA WING STABILITY (REF. 38)

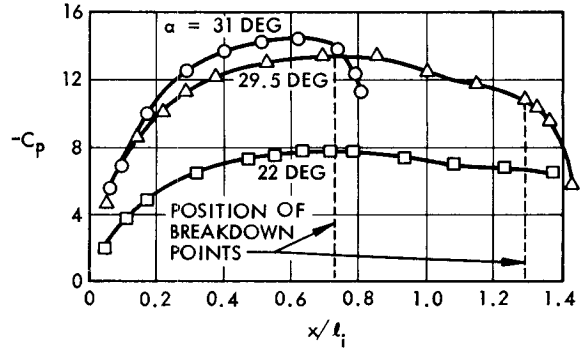

RANGE OF STATIC PRESSURES
$C_p = (p - p_\infty)/q_\infty$ ALONG VORTEX
AXIS AT VARIOUS ANGLES OF INCIDENCE

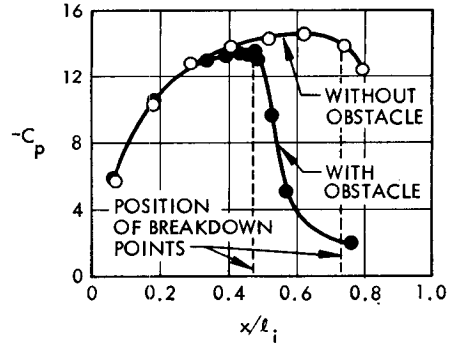

RANGE OF STATIC PRESSURES
$C_p = (p - p_\infty)/q_\infty$ ALONG VORTEX
AXIS AT ANGLE OF INCIDENCE α = 31 DEG
WITH AND WITHOUT OBSTACLES BEHIND WING

B) STATIC PRESSURE DISTRIBUTION ALONG LEADING EDGE VORTEX AXIS (REF. 38)

Figure 15

EFFECT OF ANGLE OF ATTACK ON BURST POSITION
(FIGURE 16)

The vortex breakdown is very sensitive to angle of attack, moving almost jumpwise from trailing edge to 2/3 chord (Figure 16a and Ref. 41), at least for high sweep angles. Lowson finds that he has to "undershoot" angle of attack to bring vortex breakdown back to the "upstroke" position, i.e., there is an α-hysteresis (Figure 16b, Ref. 42). He also finds that the vortex breakdown is asymmetric, i.e., at different axial positions for right and left half span. Which side gets the earlier breakdown is a random event, but once established the asymmetry prevails throughout the angle of attack range. The distance axially between the two breakdowns was in his case approximately the same as their spanwise separation distance. Lowson speculates that his asymmetry may be limited to highly swept delta wings where the two breakdowns get close to each other. This is verified by others' results (Refs. 38 and 41).

This α-sensitivity implies that the down-going wing during roll will get earlier breakdown due to the roll rate induced angle of attack, causing a roll moment that will sustain the roll rate, i.e., an undamping effect. Vortex breakdown plays the same role for delta wings as nose stall does for airfoils. One can, therefore, expect that pitch rate induced camber and accelerated flow effects, which have proven to have a powerful influence on dynamic stall,(Refs. 14-16 and 32) also will dominate dynamic vortex breakdown.

Vortex burst is certainly to be be avoided considering these adverse dynamic effects. Fortunately, all the proposed shuttle vehicles fly at angles of attack well below those for severe vortex burst effects. On the other hand, vortex burst is sensitive to back pressure such as would be produced by the deflection of a trailing edge control surface. Thus, a careful analysis of the problem is needed.

EFFECT OF ANGLE OF ATTACK ON BURST POSITION

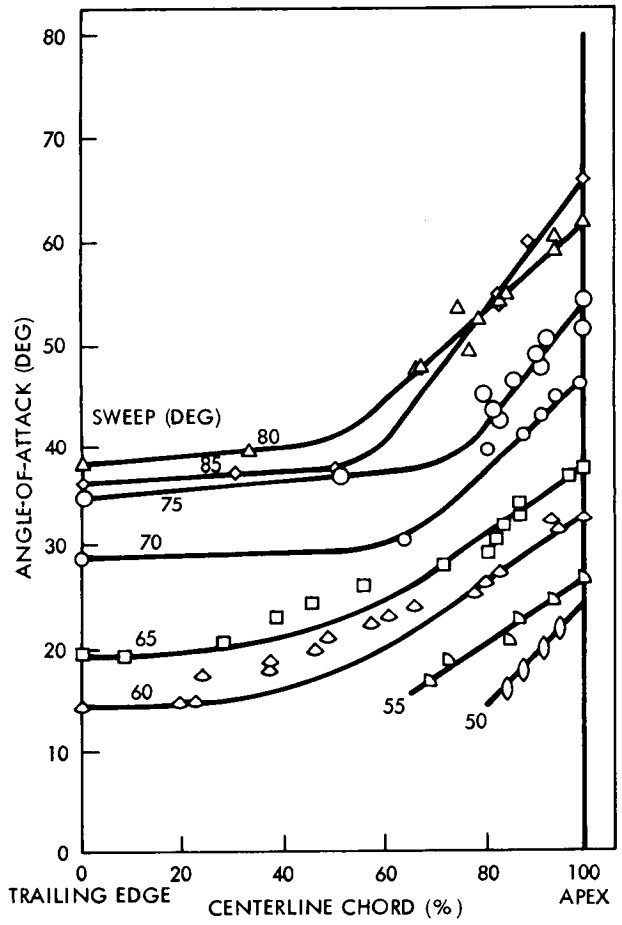

A) VORTEX BREAKDOWN POSITION – DELTA WINGS (REF. 41)

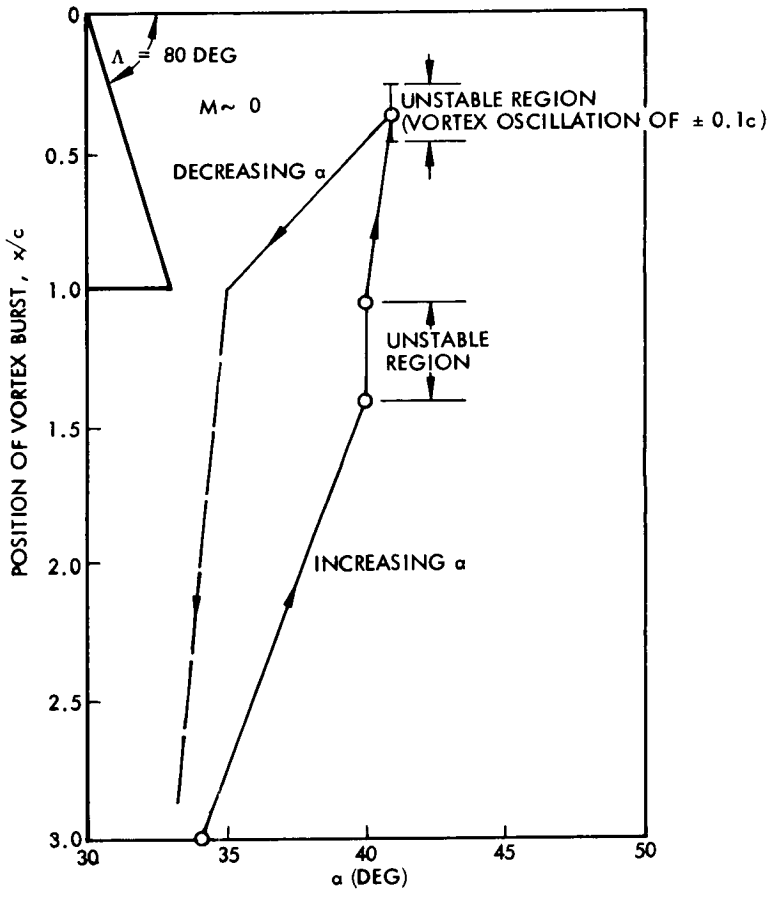

B) HYSTERESIS AND UNSTABLE VORTEX BURST LOCATIONS (REF. 42)

Figure 16

HYPERSONIC CONTROL INTERFERENCE, M = 5.0
(FIGURE 17)

Up until now the effect of back pressure on the leeside flow field of the delta wing has not been considered. It is well known that the extent of shock induced separation is sensitive to back pressure (Ref. 43). Flap controls will often cause boundary layer separation, especially in hypersonic low density flow, where less than 10 degrees flap deflection often will cause boundary layer separation (Refs. 70-73). Thus, the deflection of a trailing edge control surface will affect the extent of shock induced separation. Such back pressure effects are of practical concern since it is desirable to control the shuttle with leeward control deflections, wherever possible, in order to minimize control surface heating. Data obtained on the NAR orbiter (Refs. 21 and 44) show an elevon effectiveness greater than Newtonian for small deflections ($\delta = -10^{\circ}$) at low angles of attack (Figure 17). This is the likely result of shock induced separation of the leeside flow. The separation extent (for fixed flap deflection $\delta = -10^{\circ}$) increases initially with angle of attack. However, the back pressure effect from the flap causes the transition between shock induced separation and leading edge stall to start near the flap and progress forward with increasing angle of attack (see inset sketch in Figure 17); at high angle of attack the positive lift produced by the vortices outweighs the negative lift generated by the flap induced flow separation over the inner wing surface. The result is a loss of flap effectiveness below the Newtonian windward side value (i.e., a more stable ΔC_m than predicted by Newtonian theory for $\delta = -10^{\circ}$). At the high deflection $\delta = -30^{\circ}$ the mixed flow field may still occur, but the overall force data is not sensitive enough to detect it. Generally, the leeside effects seem to vary less drastically and Newtonian theory seems to predict the α -trends rather well.

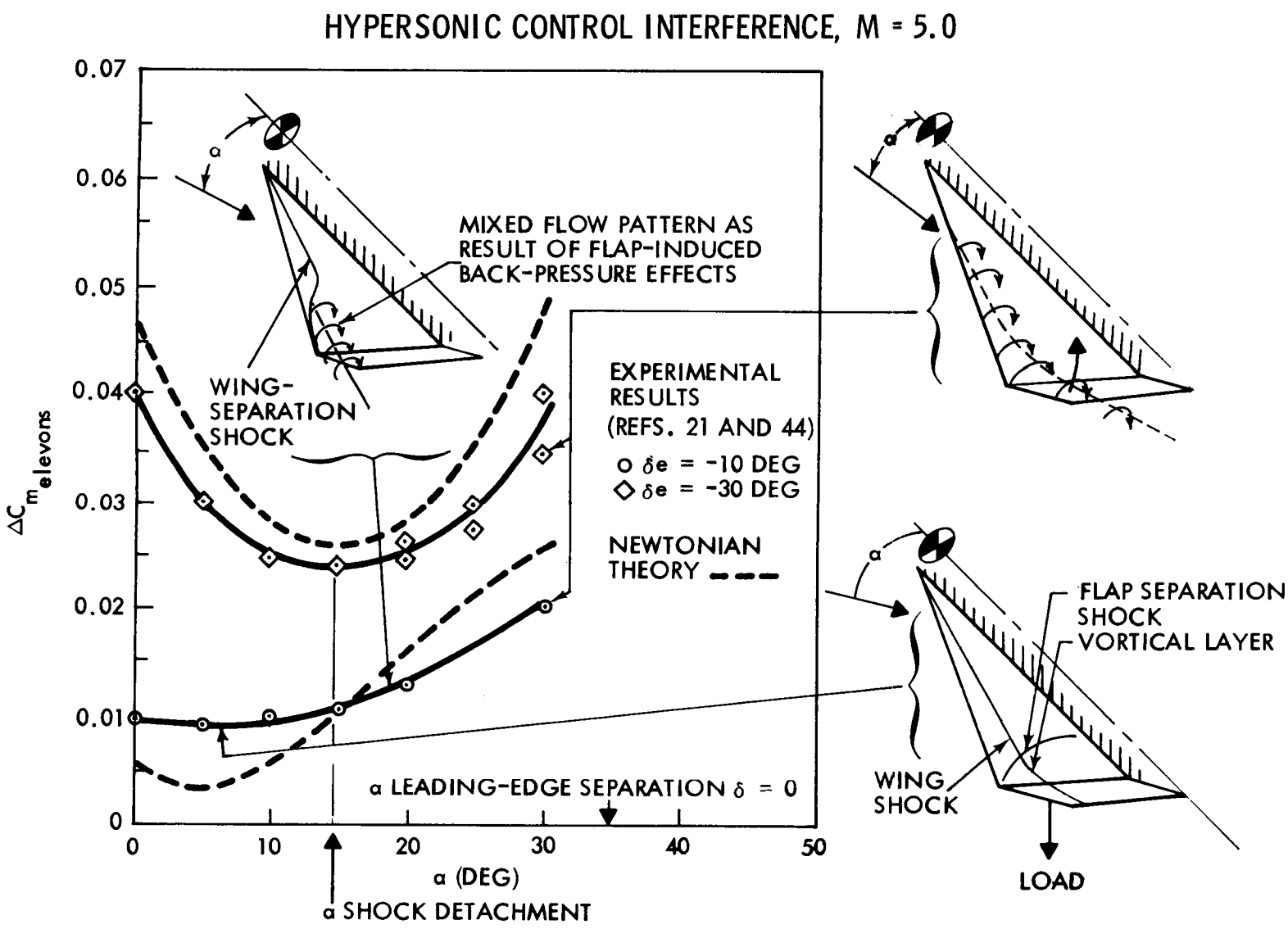
HYPERSONIC CONTROL INTERFERENCE, M = 5.0
0.07
0.06
0.05
0.04
0.03
0.02
0.01
0
$\Delta C_{m_{elevons}}$
0
10
20
30
40
50
α (DEG)
α SHOCK DETACHMENT
α LEADING-EDGE SEPARATION δ = 0
MIXED FLOW PATTERN AS RESULT OF FLAP-INDUCED BACK-PRESSURE EFFECTS
WING-SEPARATION SHOCK
EXPERIMENTAL RESULTS (REFS. 21 AND 44)
o δe = -10 DEG
◇ δe = -30 DEG
NEWTONIAN THEORY
α
FLAP SEPARATION SHOCK
VORTICAL LAYER
WING SHOCK
LOAD

Figure 17

CONTROL INDUCED ROLL REVERSAL AND POSSIBLE HYSTERESIS
(FIGURE 18)

Experimental results also indicate that roll reversal occurs as a result of the back-pressure-induced change in flow field (Figure 18a, Ref. 22). If hysteresis does occur when switching between the various separated flow types, then a residual control force will remain after the control deflection is removed. The control force is made up of two components; the force on the control surface itself and the induced load on the wing due to a control induced change in the flow field (separation type) on the wing. The former will go away when the control deflection is removed. The latter will persist (if flow field hysteresis is present) until the angle of attack is reduced sufficiently to get out of the hysteresis region (Figure 18b).

CONTROL-INDUCED ROLL REVERSAL AND POSSIBLE HYSTERESIS

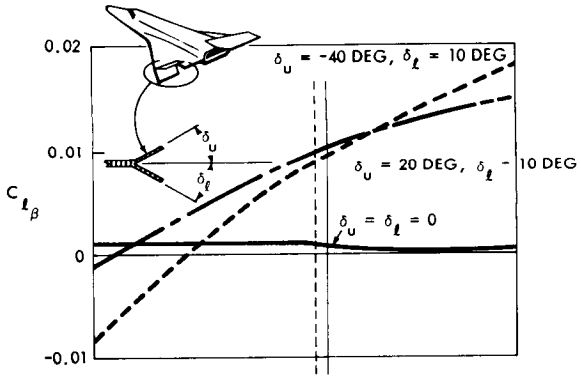

A) ROLL REVERSAL

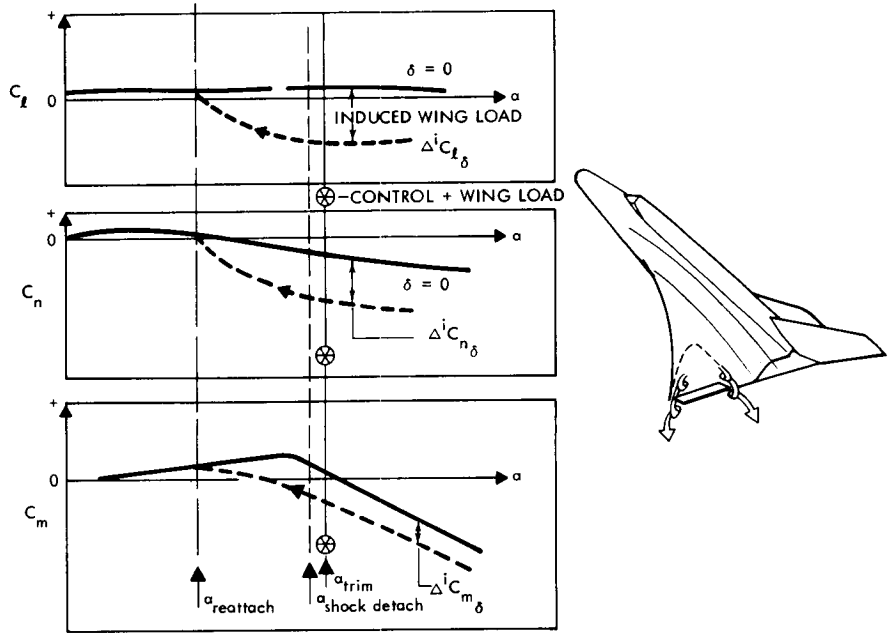

B) POSSIBLE CONTROL INDUCED HYSTERESIS

Figure 18

VORTEX BURST INDUCED BY DOWNSTREAM OBSTACLE
(FIGURE 19)

As one would expect, vortex burst is also sensitive to back pressure. In agreement with Ludwieg's theory, Hummel finds that supplying an adverse pressure gradient by using an obstacle one chord length downstream of the trailing edge on the right half span causes vortex breakdown (Figure 19, Ref. 38). An upward flap deflection, e.g., for a roll maneuver, will of course, have a similar effect, thus causing a "super response" to a roll command. Thus, control deflection will induce burst where ordinarily it would not occur. Furthermore, vortex burst is definitely associated with hysteresis, and subsonic control-induced burst is a problem of serious concern.

VORTEX BURST INDUCED BY DOWNSTREAM OBSTACLE (REF. 38)

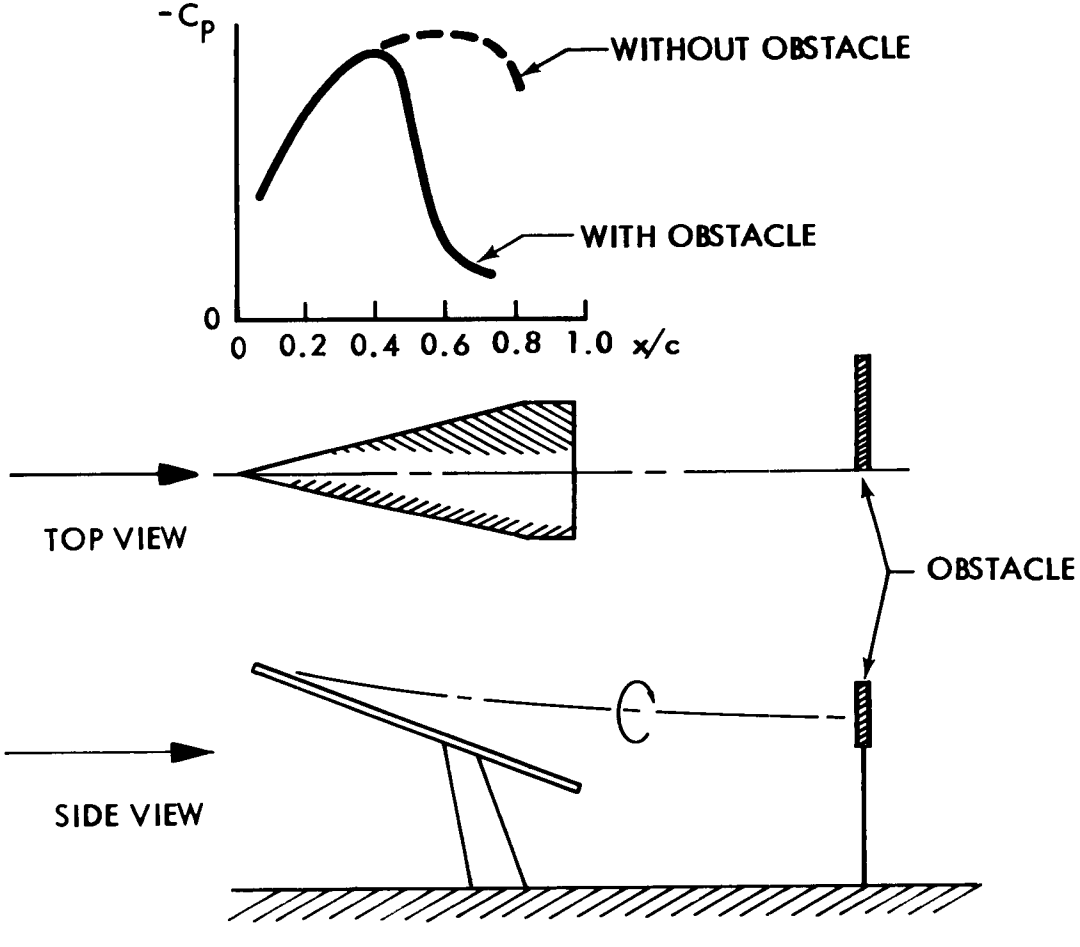

Figure 19

CONTROL INDUCED BURST
(FIGURE 20)

There is experimental evidence of control-induced burst on a proposed shuttle configuration (Figure 29, Ref. 21). At M = 0.6 vortex burst is caused by the left elevon at $\alpha = 12^{\circ}$ for a combined pitch-roll command which results in $\delta_L = -45^{\circ}$. After burst, there is a reduction in control effectiveness until burst is caused also by the right elevon. Nearly all control force is lost when burst occurs near the wing apex. At M = 1.5 the characteristics are similar but less drastic. At M = 2.0 the typical shock induced leeside separation characteristics are evident.

CONTROL INDUCED VORTEX BURST

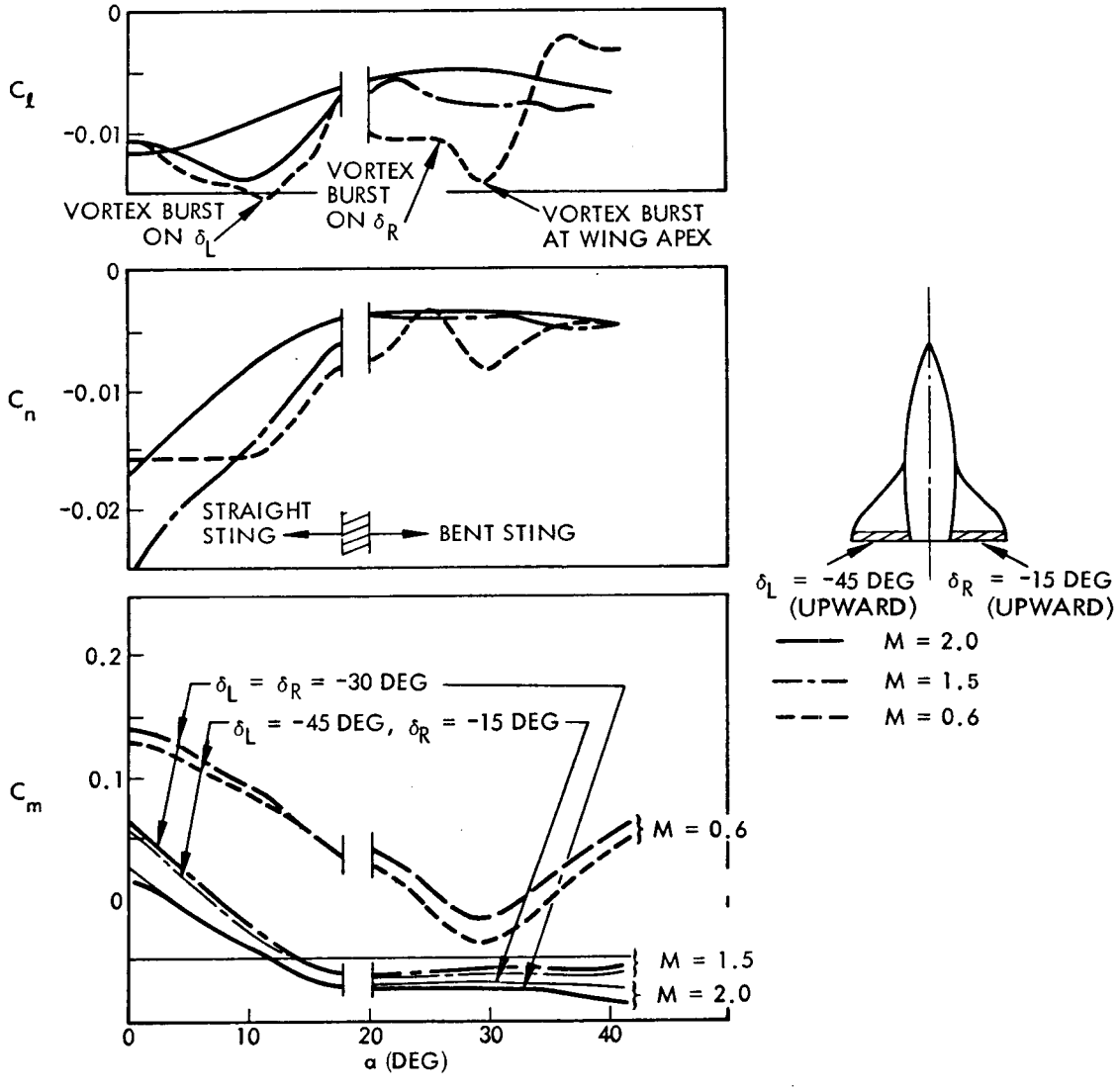

Figure 20

UNSTEADY AERODYNAMIC FLOW BOUNDARIES
SUPERIMPOSED ON A TYPICAL SHUTTLE ENTRY CORRIDOR
(FIGURE 21)

Even though the shuttle vehicle may largely avoid the vortex burst and shock induced separation, control deflection will cause the realization of both, with the attendant undesirable dynamic effects. The NAR orbiter will certainly experience shock induced separation as the result of control deflection, as it flies just below the lower bound of the shock induced separated flow region (Figure 21).

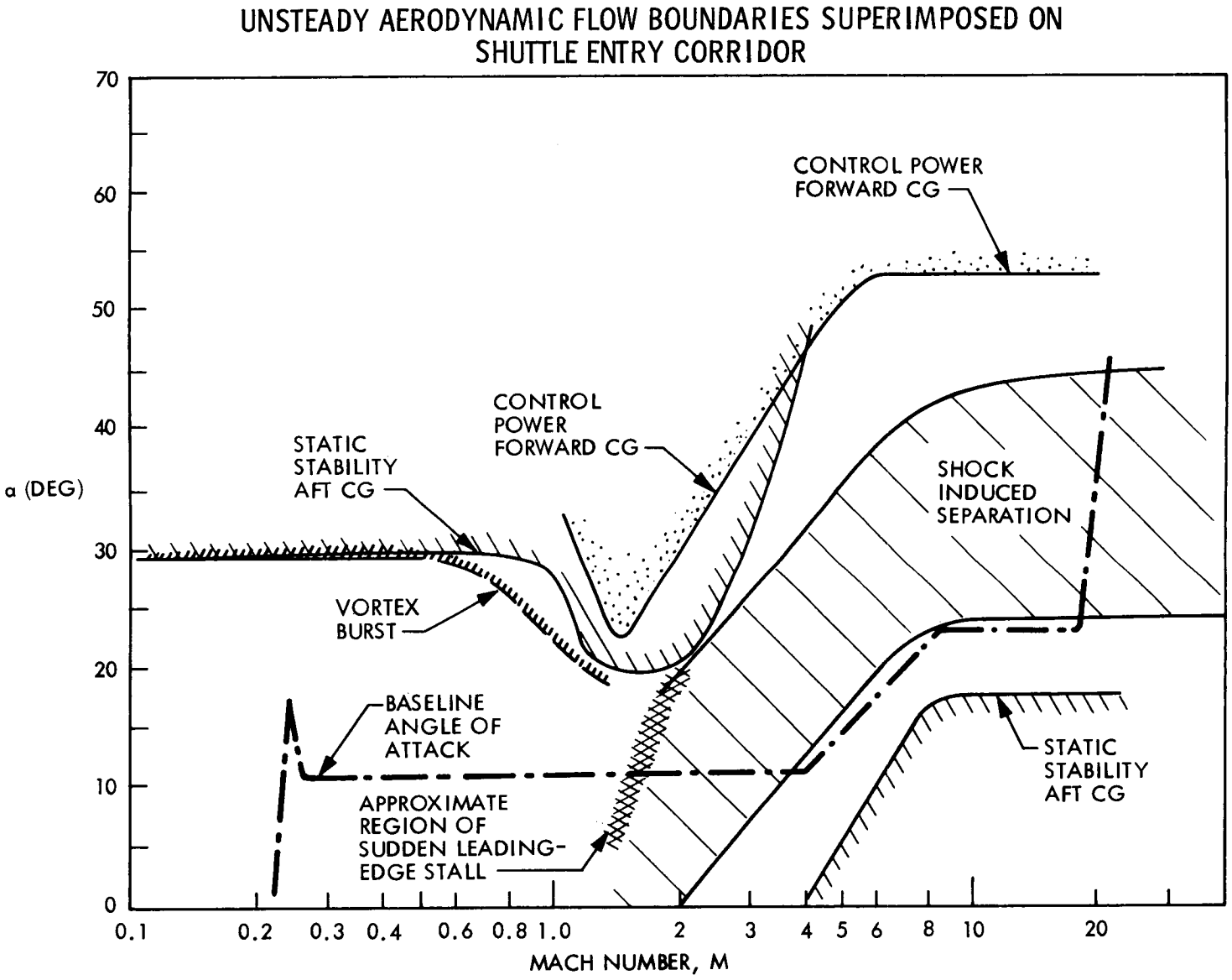
UNSTEADY AERODYNAMIC FLOW BOUNDARIES SUPERIMPOSED ON SHUTTLE ENTRY CORRIDOR
CONTROL POWER FORWARD CG
CONTROL POWER FORWARD CG
STATIC STABILITY AFT CG
SHOCK INDUCED SEPARATION
VORTEX BURST
BASELINE ANGLE OF ATTACK
APPROXIMATE REGION OF SUDDEN LEADING-EDGE STALL
STATIC STABILITY AFT CG
α (DEG)
MACH NUMBER, M
70
60
50
40
30
20
10
0
0.1
0.2
0.3
0.4
0.6
0.8
1.0
2
3
4
5
6
8
10
20

Figure 21

POSSIBLE OCCURRENCE AND RESULT OF BOW SHOCK-FLAP SHOCK INTERFERENCE (FIGURE 22)

Incidentally, there is one other control interference effect worth mentioning, and that is bow shock-flap shock interaction (Refs. 11 and 46-48). Leeward control deflections do not cause bow shock-flap shock interactions, but if the vehicle is trimmed near zero elevator deflection, as indicated from the test data of Ref. 22 (Figure 22a), and a sufficiently large aileron deflection is required, it could happen (Figure 22b). This can result in aerodynamic undamping in pitch (Figure 22c) which is coupled aerodynamically with the two other angular degrees of freedom. Of course, one can through diligent design assure that large aileron deflections are not necessary (in this case $\alpha = 15^{\circ}$ is acceptable). But one must recognize the problem in order to be sure to avoid it. Even for smaller flap deflections than those causing the drastic flap shock-bow shock interaction, the curved bow shock can through the generated inviscid shear flow, the "entropy wake", generate loads on aft body and flap (Ref. 48). "Entropy vortices" generated by discontinuities in the shock envelope are another means of generating loads on the aft body, as Maikapar has shown for a half-cone lifting entry geometry (Ref. 49).

Pitch-roll coupling through bow shock induced crossflow, in addition to the dynamic pressure deficit, could be another entropy wake effect, according to Hart's findings (Ref. 50). The Edney-effect, i.e., bow shock-wing shock interaction, is another interference effect that can cause problems (Ref. 51). However, the problem is mainly one of increased heating and is not causing any substantial vehicle dynamics problem. In addition, it is not likely to occur as readily for the delta winged vehicles as for the straight winged ones, where it is unavoidable unless the angle of attack is very, very large (Refs. 52 and 53).

POSSIBLE OCCURRENCE AND RESULT OF BOW-SHOCK FLAP-SHOCK INTERFERENCE

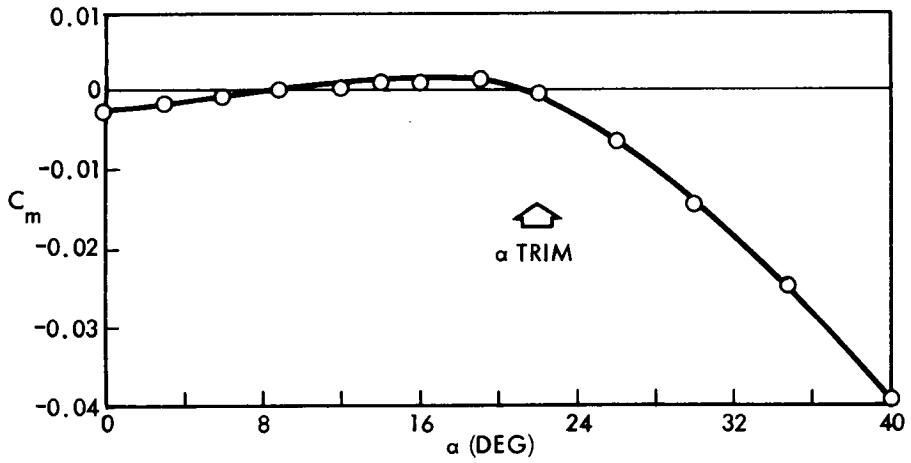

(a) M = 6.0 PITCHING MOMENT

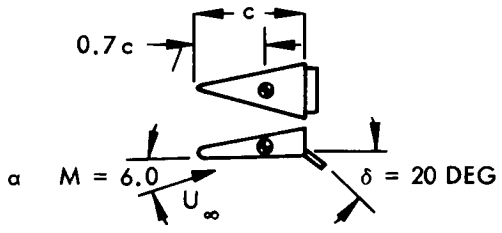

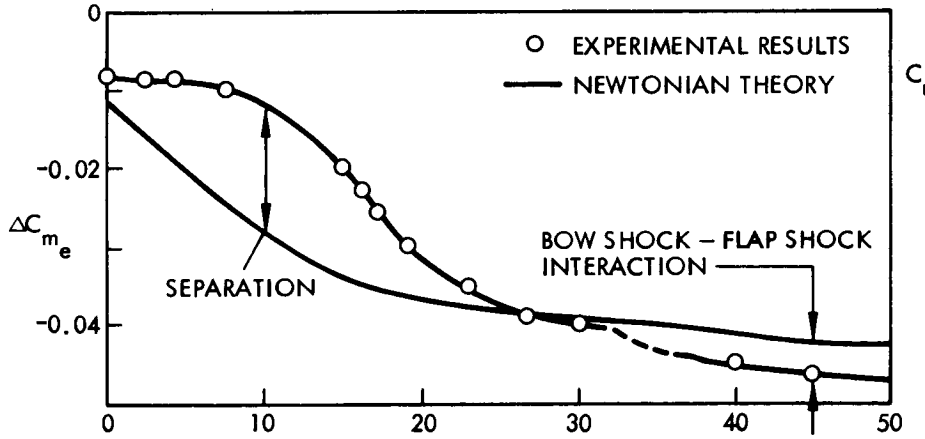

(b) ELEVON INDUCED MOMENT WINDWARD DEFLECTION, δ_e = 15 DEG, (REF. 22)

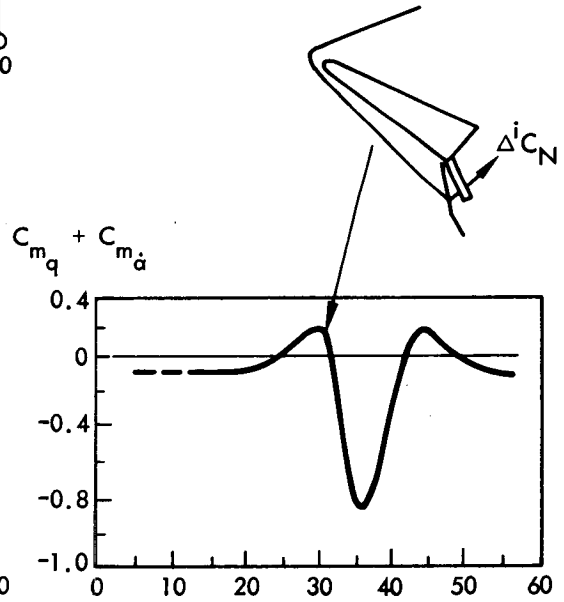

(c) PITCH DAMPING RESULTS (REF. 11)

Figure 22

NONLINEAR YAW CHARACTERISTICS INDUCED BY FOREBODY VORTICES
(FIGURE 23)

It is now well documented that long slender bodies start to develop free vortices at moderate angles of attack, and that the vortex shedding becomes asymmetric at some high angle of attack (Refs. 54-56) with the result that large side forces and yawing moments are generated at zero sideslip (Refs. 57-60, Figure 23a). The phenomenon shows α-hysteresis (Ref. 58). The direction of the side force and moment is determined by minute model asymmetrics as it seems to be body-fixed (Ref. 59). The magnitude is determined by the nose geometry, a slender nose giving larger magnitudes than a more blunt nose, and by the nose boundary layer, mainly because the turbulent boundary layer gives a decreased wake width (Ref. 59). As the angle of attack is increased more vortices are shed, the axial separation distance being that giving the separation in time in the cross flow plane determined by von Karman's theory. At some angle of attack below $\alpha = 90^{\circ}$ this space-time equivalence breaks down and von Karman type vortex shedding starts (Refs. 56 and 59). As a result of this, the direction of the side moment can change sign several times for a long body as vortices are added with increased α (Figure 23b, Refs. 55 and 57).

NONLINEAR YAW CHARACTERISTICS INDUCED BY FOREBODY VORTICIES

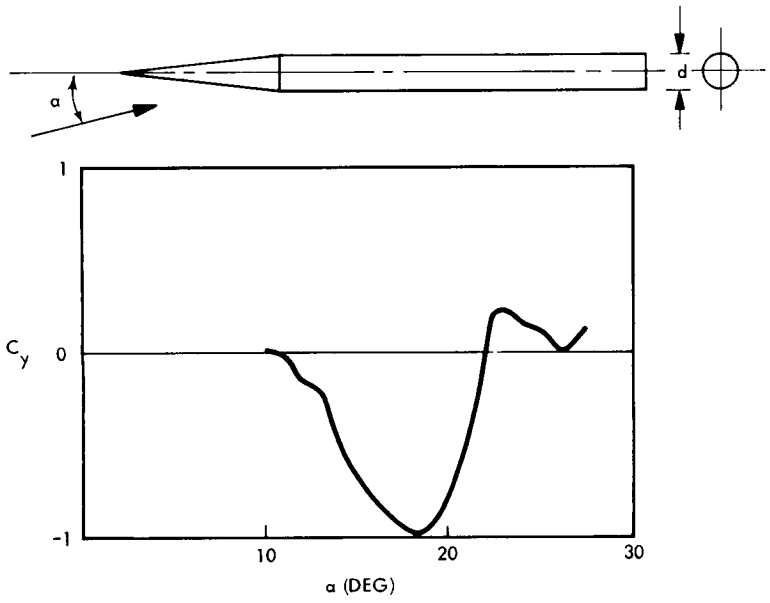

A) SIDE FORCE AT ZERO YAW, M = 2

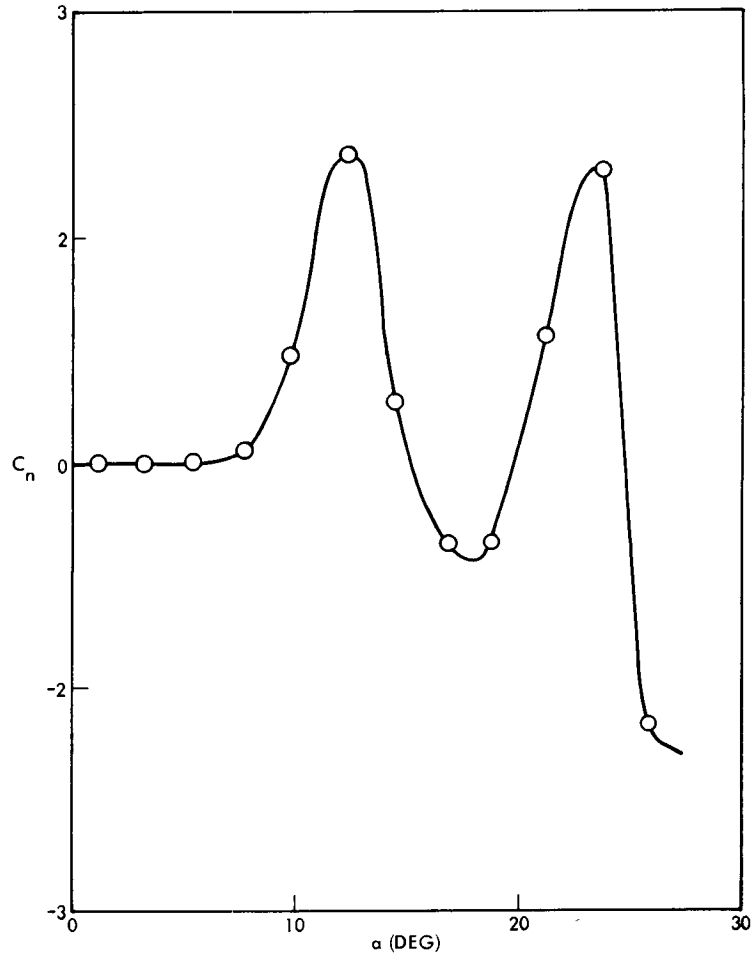

B) SIDE MOMENT AT ZERO YAW, M = 0.5

Figure 23

EFFECTS OF FOREBODY VORTICES ON AIRCRAFT YAW CHARACTERISTICS (FIGURE 24)

It has been recognized for some time now that free vortices from the slender forebody of modern fighters can cause adverse lateral characteristics strong enough to make the flat spin modes unrecoverable (Figure 24a, Refs. 61-63). Again the yaw characteristics are sensitive to seemingly infinitesimal model variations. Repeat runs show quite different results as do the results from several models (Figure 24b, Ref. 63). Furthermore, the effects are extremely large. They have been observed to be an order of magnitude greater than the rudder power (Figure 24b). No wonder they can dominate spin characteristics.

EFFECTS OF BODY VORTICIES ON AIRCRAFT YAW CHARACTERISTICS

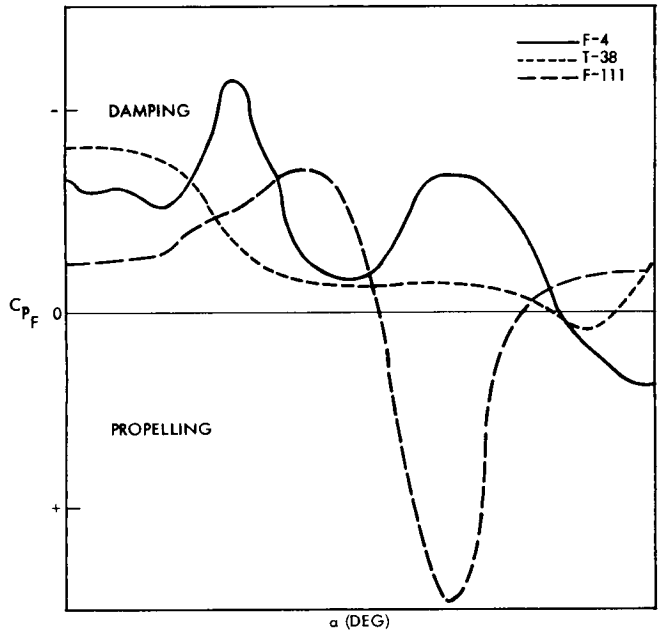

A) YAW RATE DAMPING OF SEVERAL FIGHTER CONFIGURATIONS (REF. 61)

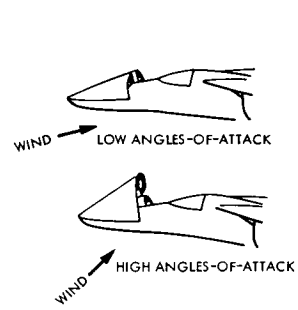

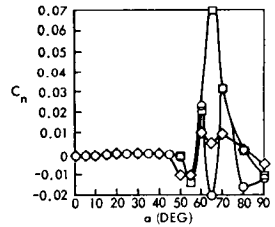

(a) VARIATION OF YAWING-MOMENT COEFFICIENT WITH ANGLE-OF-ATTACK; SYMBOLS INDICATE VALUES OBTAINED IN SEVERAL REPEAT TESTS

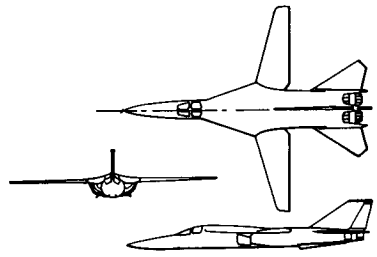

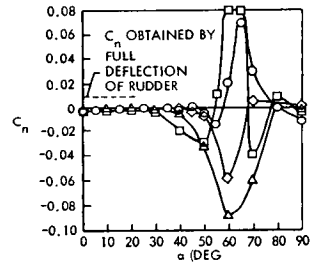

(b) VARIATION OF STATIC YAWING-MOMENT COEFFICIENT WITH ANGLE-OF-ATTACK FOR SEVERAL MODELS OF THE CONFIGURATION; β = 0 DEG

B) REPEATABILITY OF BODY VORTEX INDUCED CHARACTERISTICS (REF. 63)

Figure 24

FOREBODY VORTEX-TAIL INTERFERENCE
(FIGURE 25)

In addition to the local effect at the nose, the forebody vortices can affect the vertical tail loads. The oilflow photograph in Figure 2a shows stagnation region on the leeward fuselage which is the result of the flow entrained by the forebody vortices stagnating on the upper surface (Figure 3). The entrained flow constitutes a region of excess velocity (Figure 25a). Thus, when the vehicle yaws the vertical tail is subjected to decreasing velocities (i.e., decreasing dynamic pressures). The velocity gradient, however, subjects one side of the wedge tail to higher dynamic pressures than the other. As a result, a load is induced in the direction of decreasing velocity. This is similar to the wedge fin submerged in the shear flow generated by nose induced separation (Ref. 64). Thus, for positive β a positive induced side force will result. Increasing the wedge angle effectively increases the average differential dynamic pressure, which increases the induced load (Figure 25b and Ref. 21). The induced load may or may not be larger than the load component due to local angle of attack. In the case of the tail with drag brake the induced load is large enough to cause a reversal in the incremental drag brake load at $M = 2.5$ and to nearly eliminate it at $M = 4.6$. This is not the result of an ordinary loss of tail effectiveness at high angle of attack due to body shielding. Certainly shielding effects would not cause a reversal in the sign of the drag brake load. What is more likely is that the local load vanishes or nearly vanishes due to shielding, allowing the vortex induced load to dominate. The effect of forebody vortices, both the local effect at the nose and the induced effect at the tail, are statically destabilizing in yaw, which can result in a sustained spin or would require large amounts of reaction control propellant to maintain stability (Refs. 65 and 66). Thus, it appears highly desirable to eliminate or minimize these effects, if at all possible.

FOREBODY VORTEX – TAIL INTERFERENCE

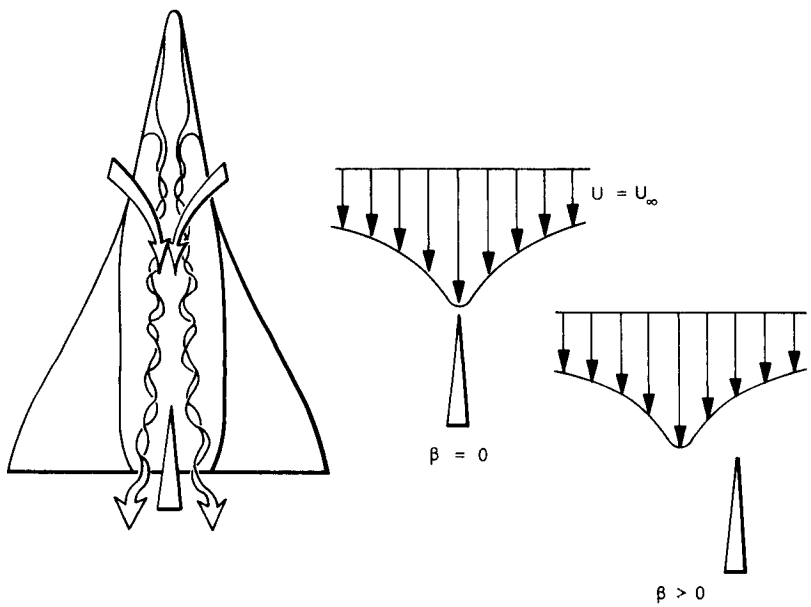

A) EFFECT OF FOREBODY VORTICITY ON VELOCITY PROFILE AT TAIL

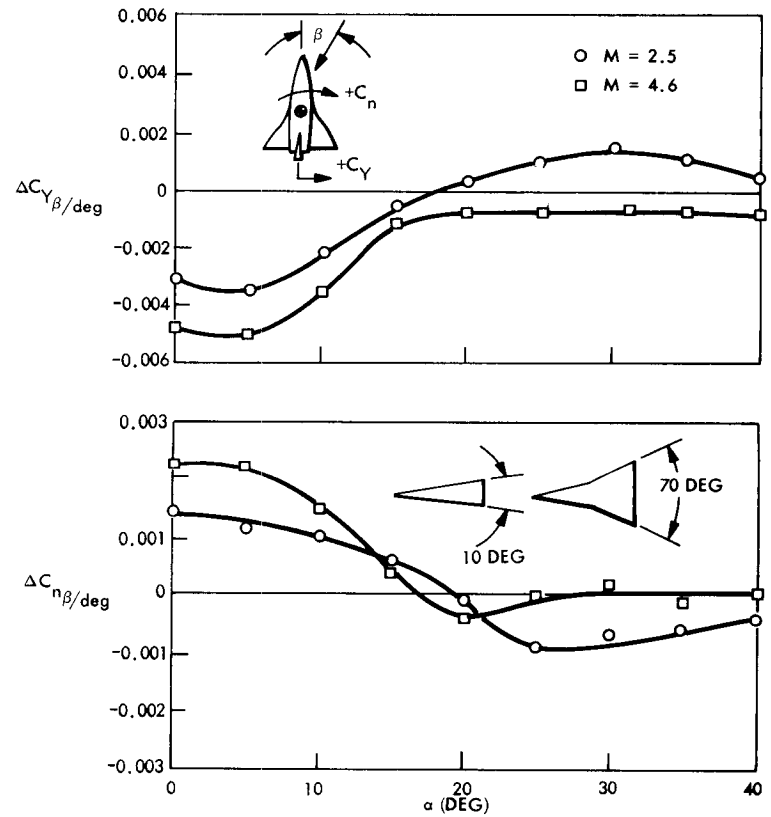

B) EFFECT OF DRAG BRAKE ON DIRECTIONAL STABILITY, NAR ORBITER (REF. 21)

Figure 25

MINIMIZING UNSTEADY AERODYNAMIC PROBLEMS BY TRAJECTORY SHAPING (FIGURE 26)

Perhaps the best way to eliminate these stability problems is to traverse the regions of instability quickly, and to avoid flying close to an unstable flow boundary (see Figure 21); thus avoiding involuntary realization of adverse unsteady flow effects due to control deflection, gust, etc. From the preceding discussions the flow phenomena to avoid are:1.) high speed shock induced separation; 2.) sudden leading edge stall; 3.) vortex burst; 4.) bow shock-flap shock interaction; and 5.) forebody vortices. The last item, the effect of forebody vortices, cannot be avoided by trajectory shaping alone, since the shuttle must fly at high angles of attack because of aerodynamic heating considerations.

A fictitious entry trajectory is superimposed on the boundaries of the NAR entry corridor (Ref. 18) as an illustration of one way of minimizing the deleterious effects of unsteady flow phenomena (Figure 26). The trajectory is fictitious in the sense that it was constructed without regard to meeting cross range and aerodynamic heating requirements. It is only an illustration of the philosophy of avoiding unfavorable flow regions. At any rate, the philosophy is to stay above the region of shock induced separation as long as possible; then to induce separation. In addition, it may be necessary to limit control deflection. The second passage through the shock induced separation region should be made at low angle of attack, thus, avoiding the adjacent region of sudden L.E. stall. At lower Mach number a return to the baseline trajectory seems permissible; however, it may be necessary to limit control deflection to avoid control induced vortex burst.

An alternate scheme that might be applied to a reduced cross range trajectory could be to stay above the shock induced separation region and the control power limit, thus reaching the subsonic cruise attitude at about M = 1.2 (alternate trajectory of Figure 26). This, of course, supposes that a means can be found for moving the aft center of gravity stability boundary upward.

MINIMIZING UNSTEADY AERODYNAMIC PROBLEMS WITH TRAJECTORY SHAPING

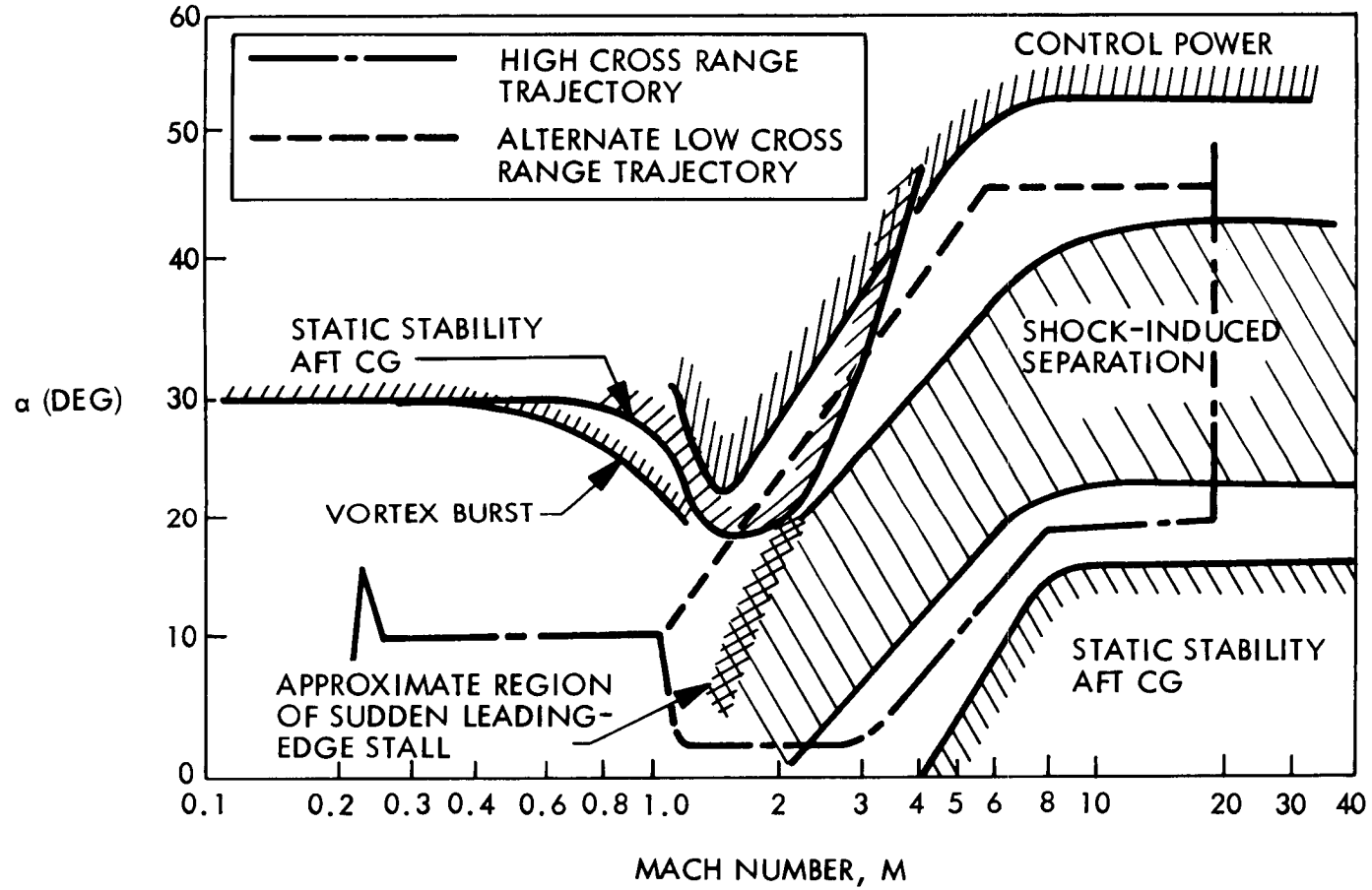

Figure 26

PLANFORM MODIFICATION ALTERING THE STALL BOUNDARIES (FIGURE 27)

It might be possible to gain leeway for a trajectory like this by increasing the leading edge sweep, thereby lowering the upper angle of attack boundary for shock-induced separation. This would also delay vortex burst, thereby widening the space shuttle re-entry corridor by raising the stability and control boundaries to higher angles of attack. Increasing sweep angle delays subsonic vortex burst (Ref. 39). There is no reason to believe it would do otherwise at higher speeds. When L.E. stall occurs the leading edge flow is subsonic, and increased sweep will energize the vortex core flow to delay burst just as in the low speed case.

One would assume that a planform in which the sweep is increasing towards the trailing edge would delay vortex burst, and it does (Figure 27a, Ref. 67). However, the effect is small compared to the beneficial effect of a double delta or ogee planform (compare wings 2 and 5 in Figure 27b) in which case better static stability characteristics is an additional bonus. This delay of vortex burst to a higher angle of attack means also a gain in lift. This is not always true if the delay is accomplished by delaying the initial vortex formation, e.g., by leading edge droop or apex drooping (Refs. 68 and 69). It appears, however, that a combination of curving the leading edge planform and convexing the upper surface could lead to some optimum design (Refs. 69, 70,71). Increasing sweep also eliminates the dangerous mixed leading edge flow condition shown earlier (Ref. 72, Figure 27b).

PLANFORM MODIFICATION ALTERING THE STALL BOUNDARIES

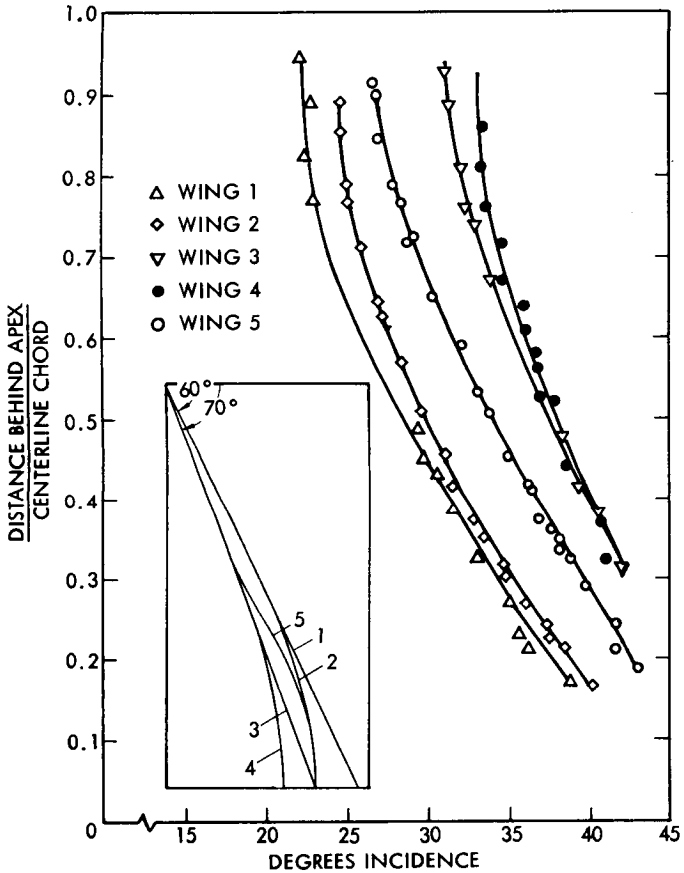

A) EFFECT OF PLANFORM MODIFICATION ON BURST LOCATION

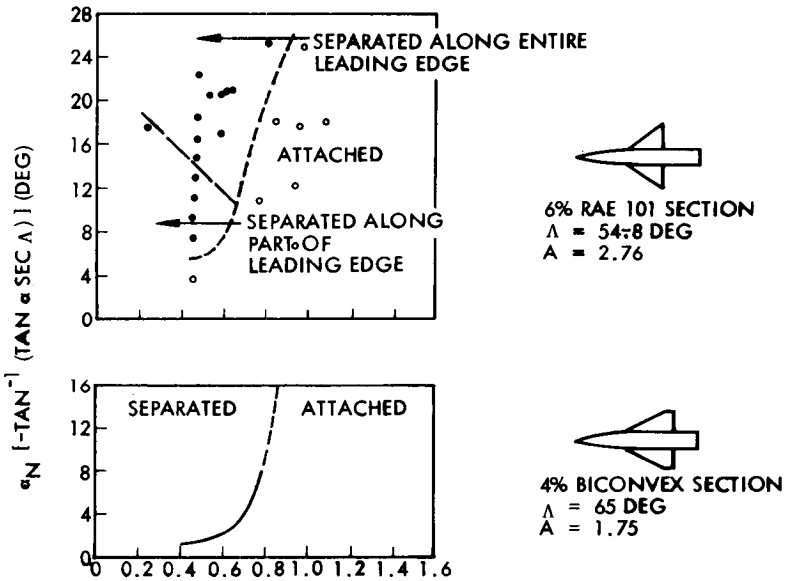

B) EFFECT OF PLANFORM MODIFICATION ON SUDDEN STALL

Figure 27

USE OF STRAKES TO MINIMIZE FOREBODY VORTEX EFFECTS (FIGURE 28)

The effect of forebody vortices is not easy to avoid completely as was discussed earlier. However, it is quite possible to fix the vortex separation point, thus eliminating the asymmetric vortex shedding and thereby the major portion of the destabilizing load. This may be accomplished by fuselage shaping (Ref. 65), strakes (Ref. 73, Figure 28), or a combination of both. The strakes can be designed to form an efficient double delta configuration. This has the added advantage of delaying vortex burst and maintaining good control effectiveness to high angles of attack, as discussed previously.

USE OF STRAKES TO MINIMIZE FOREBODY VORTEX EFFECTS

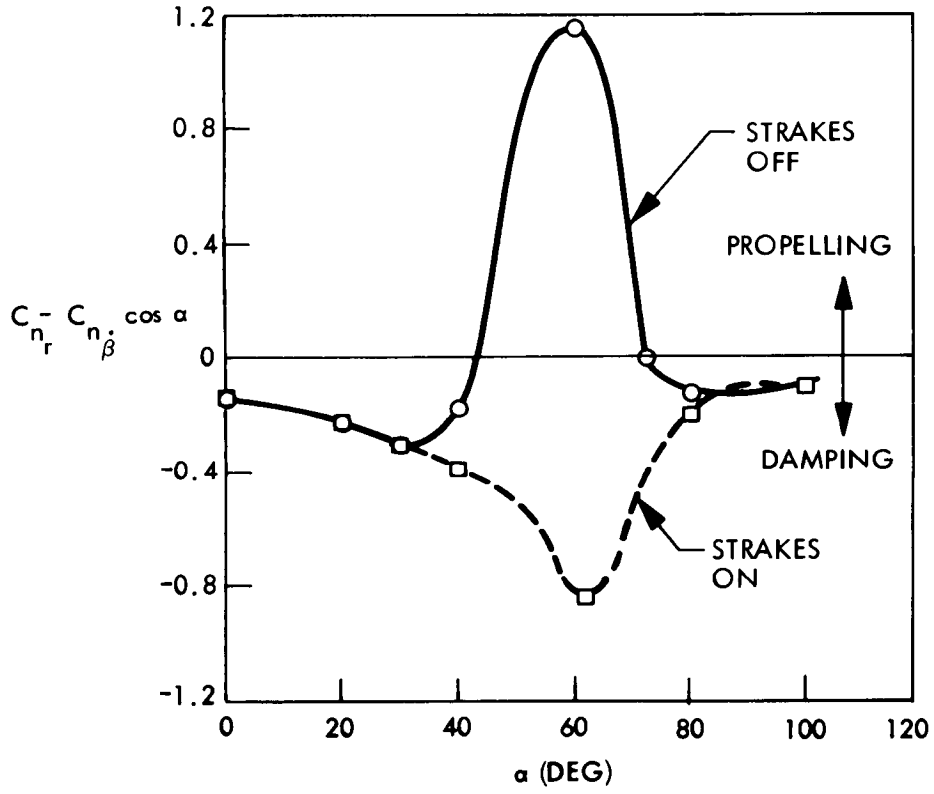

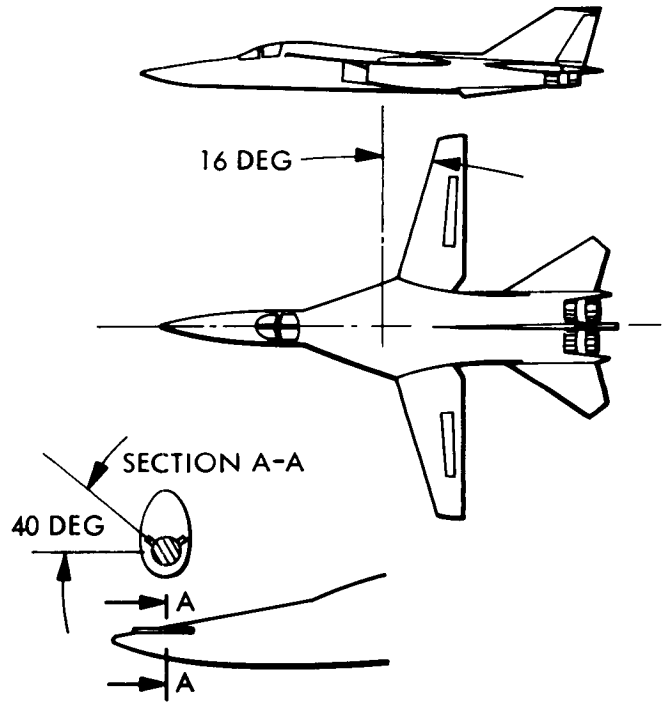

Figure 28

EFFECTS OF VARIOUS CONFIGURATION MODIFICATIONS ON SHUTTLE DIRECTIONAL STABILITY
(FIGURE 29)

Forebody strakes may not completely eliminate the directional instability, as one shuttle contractor has shown (Figure 29, Ref. 65). The hard chine results represent the effect of fixing vortex shedding locations. However, the symmetric vortex shedding from the forebody can also induce significant adverse effects, especially when the vortices can interact with a central vertical tail. Only after the addition of a ventral fin was a stable C_{n_β} measured.

EFFECTS OF VARIOUS CONFIGURATION MODIFICATIONS ON SHUTTLE DIRECTIONAL STABILITY

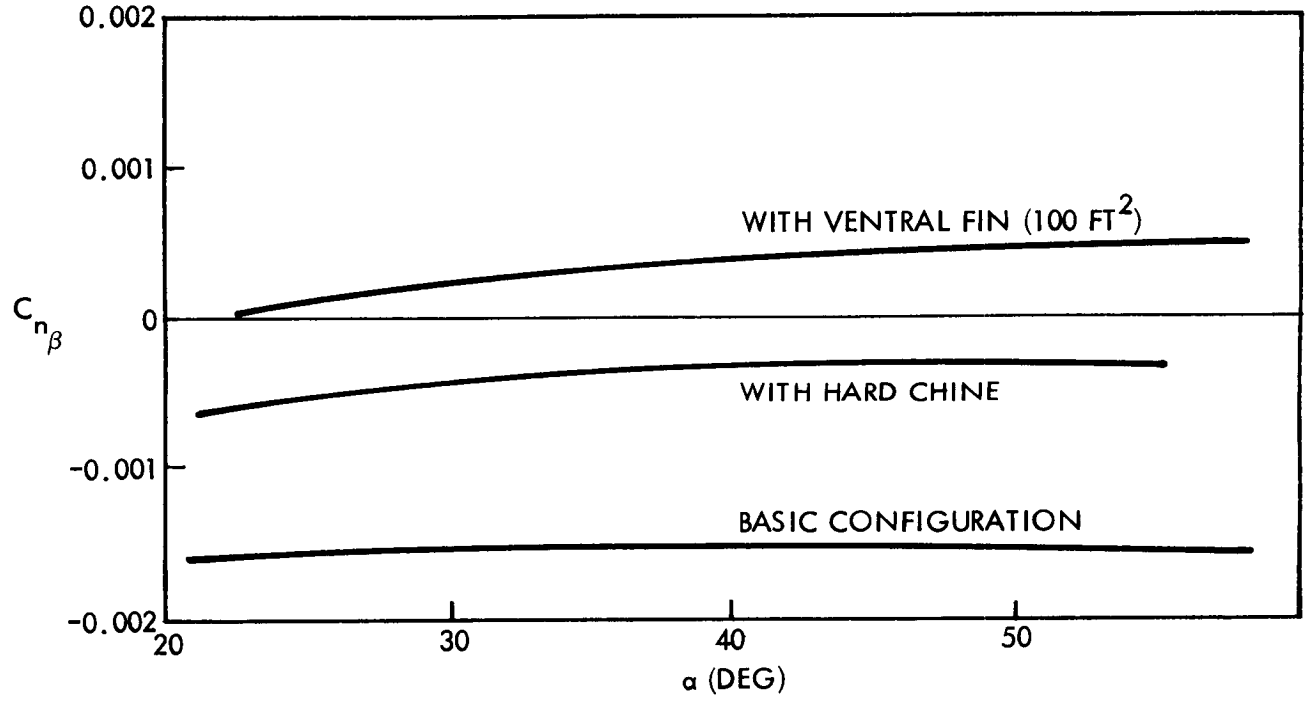

Figure 29

SUMMARY OF SUGGESTED ORBITER MODIFICATIONS
(FIGURE 30)

During the transition maneuver it will be necessary to fix the flow conditions over the wing to avoid the possibility of experiencing snap roll. That is, when traversing the flow boundaries it is likely that one wing will reestablish attached leading edge flow before the other. The results may be an unprogrammed snap roll similar to that experienced with the straight winged shuttle orbiter during the drop tests (Ref. 74). Spoilers are probably providing the simplest means of fixing separation. When the transition maneuver has been completed down to subcritical angles of attack, the spoilers would be retracted, causing instantaneous flow reattachment on both wings simultaneously.

The configuration modifications just discussed are summarized in Figure 30. Like the trajectory modifications, these are fictitious and are meant to illustrate philosophy only. No evaluation of their effects on longitudinal stability, drag, center of gravity location, etc., has been made. Strakes, spoilers, and vertical fins constitute the preferred modifications. The ventral fins would have to be folding or jettisonable for landing. If the ventral fins prove undesirable from aerodynamic heating considerations or negative dihedral effects (Ref. 75), it may be possible to achieve directional stability with two vertical tails.

The two fins will reside in opposite vortex induced velocity fields (Figure 25). Thus the adverse C_{n_β} effects induced by forebody vortices will be cancelled. If the cross range requirements could be relaxed it might be possible to fly the vehicle at very high angles of attack ($\alpha \approx 45^\circ$) over most of the trajectory and delay pitch-over to lower speeds as in the sample low cross range trajectory (Figure 26). This relaxes the lateral stability requirements somewhat (Ref. 66) allowing a negative C_{n_β} at high Mach numbers.

SUMMARY OF SUGGESTED ORBITER MODIFICATIONS

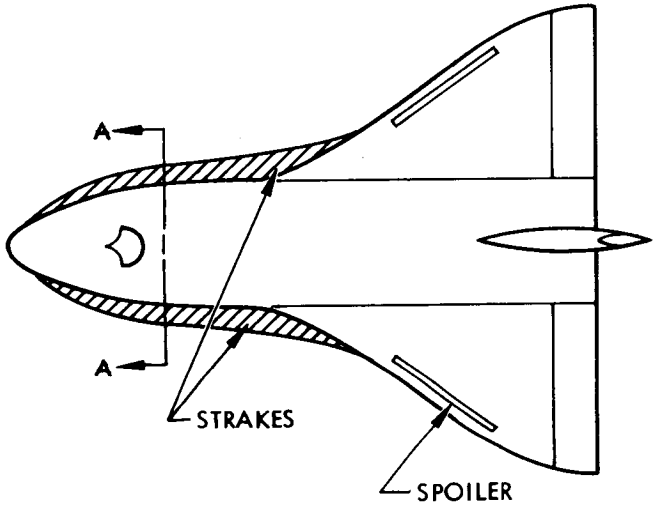

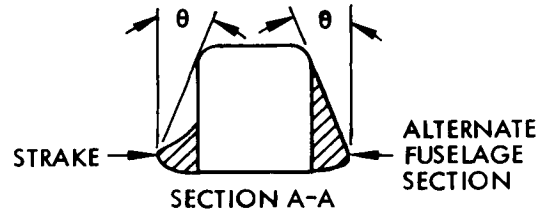

NOTE: θ MUST BE LARGE ENOUGH TO AVOID HYPERSONIC REATTACHMENT

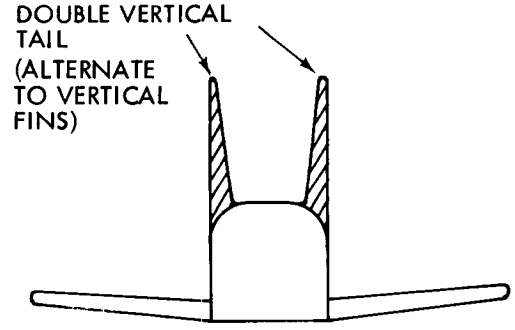

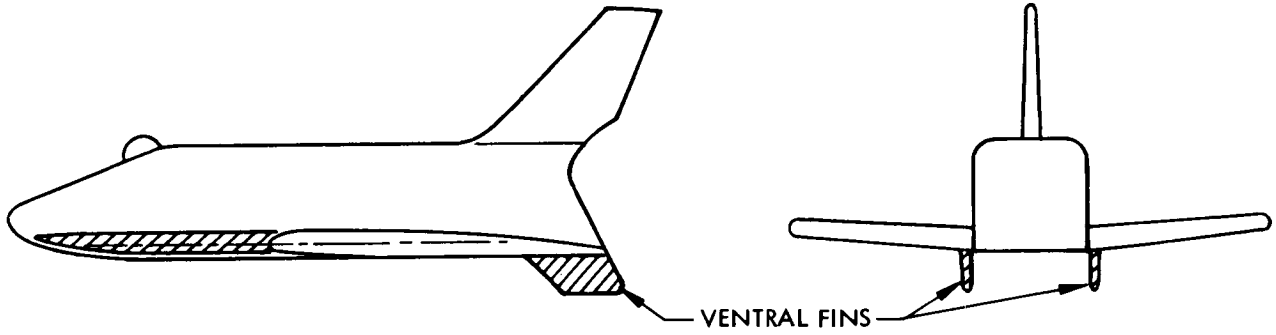

Figure 30

SCALING EFFECTS
(FIGURE 31)

Perhaps the most fundamental problem associated with the unsteady aerodynamics of delta wings is that of scaling of separated flow effects. The shock induced separation is difficult to scale already for stationary flow on airfoils and straight wings (Refs. 76-78, Figure 31a). It is only recently that a criterion for simulation of terminal shock boundary layer interaction in two-dimensional subsonic-transonic flow was established (Ref. 81). Whitehead has shown that transition has a drastic effect on control induced separation on delta wings (Ref. 47). Because the boundary layer approach length varies along the span the leeside separation patterns will exhibit a spanwise variation. Transition also has a significant effect on leading edge vortex formation (Ref. 80 and Figure 31b). Thus, a wind tunnel test must simulate both the spanwise and chordwise position of transition, and at hypersonic down to subsonic speeds in the case of the space shuttle vehicle.

The vortex shedding from slender forebodies is also sensitive to boundary layer conditions, supercritical flow conditions, i.e., turbulent boundary layers, giving significantly smaller induced side moments (Refs. 59 and 81).

As boundary layer transition is very sensitive to accelerated flow effects, it is very much affected by the vehicle motion (Refs. 82 and 83).

In the case of spoiler design great care has to be exercised that it will not revert to a pre-separation device (Refs. 5, 84, and 85). This presents a real problem when covering the $\alpha - \beta$ -M range for the space shuttle vehicle, including the transient effects during the transition maneuver. A "spoiler design" utilizing a flap located at quarter- or mid-chord is probably the best way of avoiding these dangerous preseparation effects.

SCALING EFFECTS

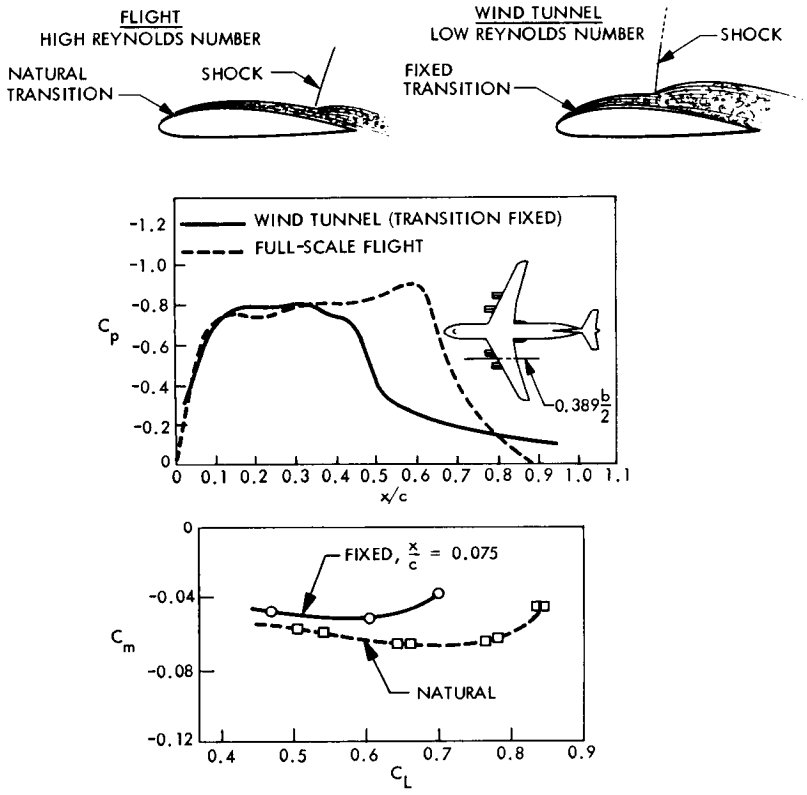

A) EFFECT OF FIXED TRANSITION

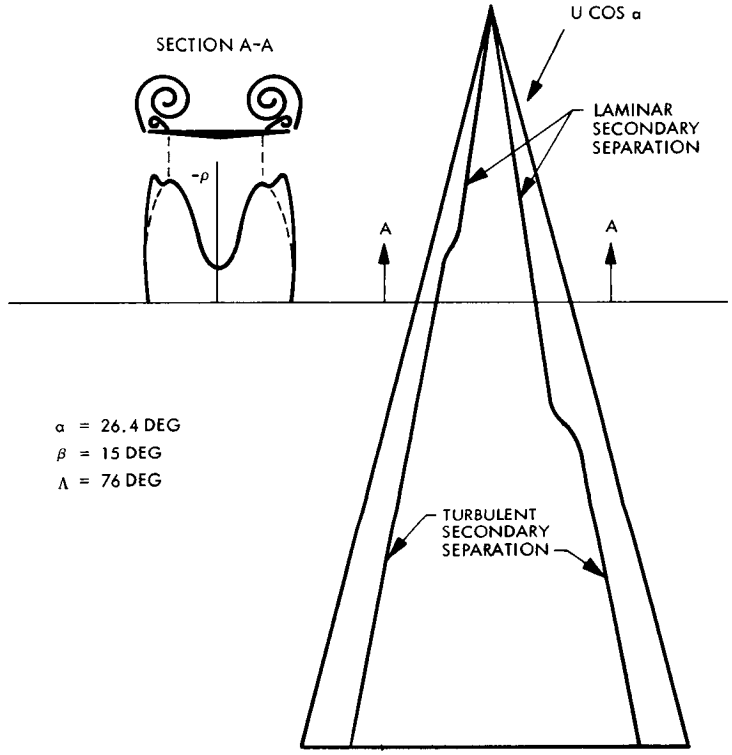

B) EFFECT OF BOUNDARY LAYER TRANSITION ON LEADING EDGE VORTEX FORMATION

Figure 31

CONCLUSIONS

This study of the unsteady aerodynamics of the high cross range, delta planform, shuttle orbiter indicates that the shuttle vehicle will be subject to five unsteady flow phenomena which can have deleterious effects on the flight dynamics: 1.) leeside shock induced separation; 2.) sudden leading edge stall; 3.) vortex burst; 4.) bow shock-flap shock interaction; and 5.) free forebody vortices. Furthermore, many of these undesirable flow conditions may be induced by control deflection.

Because the shuttle enters at a high angle of attack ($\alpha \approx 30^{\circ}$) and eventually must pitch over to a low cruise angle of attack ($\alpha \approx 10^{\circ}$), it will necessarily traverse at least one of the three stall regions (Items 1 through 3). This should be accomplished as quickly as possible. It is essential that stall be controlled (e.g., via spoilers) such that simultaneous reattachment can be accomplished on both wings after traversing stall. This prevents the disastrous snap roll which can result when the flow attaches on one wing while remaining stalled on the other. If necessary, the separation boundaries may be altered by wing planform or section modifications.

The unsteady flow regimes must be well mapped to insure that control deflection will not cause stall. Combined elevator and aileron deflections are particularly dangerous since they may induce stall on only one wing, again subjecting the vehicle to all the dangers of asymmetric stall effects. Bow shock-flap shock interaction may also be avoided by carefully programming control deflection.

Much of the undesirable effects of forebody vortices can be eliminated by fixing vortex locations. This is a relatively simple matter of shaping the body cross section or adding strakes.

A careful review of the unsteady flow problems of the delta wing shuttle orbiters indicates that there is every reason to believe that the problems can be dealt with successfully.

REFERENCES

1. Woods, P. and Ericsson, L. E., "Aeroelastic Considerations in a Slender Blunt-Nose, Multistage Rocket", Aerospace Engineering, Vol. 21, No. 5, May 1962, pp. 42-51.

2. Ericsson, L. E. and Reding, J. P., "Analysis of Flow Separation Effects on the Dynamics of a Large Space Booster", J. Spacecraft and Rockets, Vol. 2, No. 4., July-August 1965, pp. 481-490.

3. Ericsson, L. E. and Reding, J. P., "Dynamics of Separated Flow over Blunt Bodies", Lockheed Missiles & Space Company, Report 2-80-65-1, NASA Contract NAS 8-5338, December 1965.

4. Ericsson, L. E., French, N. J., and Guenther, R. A., "The Aeroelastic Characteristics of the Saturn 1B Launch Vehicle with Biconic Payload Shroud", Lockheed Missiles & Space Company, Report M-37-67-1, NASA Contract NAS 8-11238, CR-61736, July 1967.

5. Ericsson, L. E., "Aeroelastic Instability Caused by Slender Payloads", J. Spacecraft and Rockets, Vol. 4, No. 1, January 1967, pp. 65-73.

6. Ericsson, L. E., and Reding, J. P., "Ablation Effects on Vehicle Dynamics", J. Spacecraft and Rockets, Vol. 3, No. 10, October 1966, pp. 1476-1483.

7. Reding, J. P., and Ericsson, L. E., "Loads on Bodies in Wakes", J. Spacecraft and Rockets, Vol. 4, No. 4, April 1967, pp. 511-518.

8. Ericsson, L. E., and Reding, J. P., "Aerodynamic Effects of Bulbous Bases", NASA CR-1339, August 1969.

9. Ericsson, L. E., and Reding, J. P., "Re-entry Capsule Dynamics", J. of Spacecraft and Rockets, Vol. 8, No. 6, June 1971, pp. 575-586.

10. Jecmen, D. M., Reding, J. P., and Ericsson, L. E., "An Application of Automatic Carpet Plotting to Wind Tunnel Data Reduction", J. Spacecraft and Rockets, Vol. 4, No. 3., March 1967, pp. 408-410.

11. Ericsson, L. E. and Reding, J. P., "Dynamic Stability Problems Associated with Flare Stabilizers and Flap Controls", J. Spacecraft and Rockets, Vol. 7, No. 2., February 1970, pp. 132-137.

12. Ericsson, L. E., "Universal Scaling Laws for Hypersonic Nose Bluntness Effects", AIAA Journal, Vol. 7, No. 12, December 1969, pp. 2222-2227.

13. Ericsson, L. E., "α-Effects are Negligible at Hypersonic Speeds - Fact or Fiction?", Vol. 3, Proceeding of the 19th Congress of the International Astronautical Federation, New York, 13-19 October 1968, pp. 547-561.

14. Ericsson, L. E. and Reding, J. P., "Unsteady Airfoil Stall", NASA CR 66787, July 1969.

15. Ericsson, L. E. and Reding, J. P., "Unsteady Airfoil Stall and Stall Flutter", NASA CR-111906 June 1971.

16. Ericsson, L. E. and Reding, J. P., "Unsteady Airfoil Stall, Review and Extension", Journal of Aircraft, Vol. 8, No. 8, August 1971, pp. 609-616.

17. Reding, J. P. and Ericsson, L. E., "Unsteady Aerodynamics of Manned Space Vehicles; Past, Present Future", Proceedings First Western Space Congress, Santa Maria, California, October 27-29, 1970, pp. 882-893.

18. Young, J. C., "Aerodynamic Comparisons of the Space Shuttle Phase B Two Stage Fully Reusable Vehicles," Aero-Configuration Working Group Meeting, MSFC, Houston, Texas, 16 September 1971.

19. Seegmiller, H. L., "Surface Flow Visualization Investigation of a High Cross Range Shuttle Configuration at a Mach Number of 7.4 and Several Reynolds Numbers", NASA TMX-62036, June 2, 1970.

20. Cross, E. J., "Analytical Investigation of the Expansion Flow Field over a Delta Wing at Hypersonic Speeds", ARL 68-0027, February 1968.

21. Foster, G., Graves, E , NASA Langley Research Center, and Mennell, R., Olsen, D. C., Cameron, B., North American Rockwell Corporation, Private communications, May 1971.

22. Goldberg, G., Emercy, C , NASA Langley Research Center, and Olsen, D. C., Mennell, R., North American Rockwell Corp , Private communication, May 1971

23. Cleary, J. W., "Hypersonic Stability and Control Characteristics of a High-Cross Range Orbital Vehicle," NASA TMX 62065, May 22, 1970

24. Weaver, J., NASA Marshall Space Flight Center, and Allen, E. C., North American Rockwell Corp., Private communication, March 1971.

25. Space Shuttle Aerodynamics Group, "North American Rockwell Space Shuttle Program Aerodynamic Design Data Book, Volume II - Delta Wing Orbiter, DB 2.1.5 - 13000-10", Space Division, North American Rockwell Corporation, May 1971.

26. Lamborne, H. C., "Some Current and Proposed Investigations into the Flow for Slender Delta and Other Wings in Unsteady Motion", ARC 21844, April 1968.

27. Lamborne, N. C., Bryer, D. W., and Mayberg, J. F. M., "A Preliminary Note on the Behavior of the Leading-Edge Vortices of a Delta Wing Following a Sudden Change of Incidence", NPL AERO Note 1006, March 13, 1962.

28. Jones, W. P., "Research on Unsteady Flow", The Sixth Minta Martin Lecture, Journal of Aerospace Sciences, Vol. 29, No. 3, March 1962, pp. 249-263.

29. Hayes, W. D. and Probstein, R. F., "Hypersonic Flow Theory", Vol. 1, Inviscid Flows, Academic Press, 1966, pp. 50-51.

30. Lindsey, W. F., and Landrum, E. J., "Compilation of Information on the Transonic Attachment of Flows at the Leading Edges of Airfoils", NACA TN 4204, February 1958.

31. Chevalier, H. L., and Robertson, J. E., "Pressure Fluctuations Resulting from Alternating Flow Separation and Attachment at Transonic Speeds", AEDC TDR 63-204 (November 1963).

32. Ericsson, L. E., and Reding, J. P., "Dynamic Stall of Helicopter Blades", Preprint No. 422, 26th Annual Forum of the American Helicopter Society, Washington, D. C., June 16-18, 1970.

33. Hanson, P. W. and Dogget, R. V., Jr., "Aerodynamic Damping and Buffet Response of an Aeroelastic Model of the Saturn I Block II Launch Vehicle", NASA TND-2713, March 1965.

34. Rogers, W. E., Berry, C. J., and Townsend, J. E. C., "A Study of the Effect of Leading Edge Modifications on the Flow over a 50-Deg. Sweptback Wing at Transonic Speeds", Great Brit. R&M No. 3270 (1962).

35. Erickson, L. L., Grambucci, B. J., and Wilcox, P. R., "Effect of Space Shuttle Configuration on Wing Buffet and Flutter," NASA Space Shuttle Technology Conference, Vol. II, NASA TMX-2274, 261-229, March 2-4,1971.

36. Polhamus, E. C., "A Concept of the Vortex Lift of Sharp-Edge Wings Based on a Leading Edge Suction Analogy", NASA TND-3767, December 1966.

37. Polhamus, E. C., "Application of the Leading-Edge-Suction Analogy of Vortex Lift to the Drag Due to Lift of Sharp-Edge Delta Wings", NASA TND-4739.

38. Hummel, D., "Untersuchungen über das Aufplatzen der Wirbel an schlanken Deltaflügeln," Z. Flugwiss 13 (1956), pp. 158-168.

39. Lambourne, N. C. and Bryer, D. W., "The Bursting of Leading Edge Vortices - Some Observations and Discussion of the Pehnomenon", Great Brit. R&M No. 3282 (1962).

40. Ludwieg, H., "Zur Erklärung der Instabilitat der über angestellten Deltaflugeln auftretenden freien Wirbelkerne", Zeitschrift fur Flugwissenschaften Vol. 10, 1962, pp. 242-249.

41. Wedtz, W. H., and Kohleman, D. L., "Vortex Breakdown on Slender Sharp-Edged Wings", AIAA 69-778, July 1969.

42. Lowson, M. V., "Some Experiments with Vortex Breakdown", J. Royal Aeronautical Society, Vol. 68, May 1964, pp. 343-346.

43. Needham, D. A., and Stollery, J. L., "Boundary Layer Separation in Hypersonic Flow", AIAA 66-455, June 1966.

44. Freeman, D. C., NASA Langley Research Center, Private communication, June 1971.

45. Rolls, L. S., Koenig, D. G., and Drinkwater, F. J., III, "Flight Investigation of the Aerodynamic Properties of an Ogee Wing", NASA TND-3071, December 1965.

46. Morkovin, M. V., Donahue, J. C., and Larson, H. K., "Exploratory Investigation of the Effects of Gas Injection Through a Porous Model on Separation, Transition, Static Stability, and Control Effectiveness of a Blunt Entry Body at Mach Number 7.3", AIAA 68-27, January 1968,(and Report ER 14598, Contract NAS 2-3873, July 1967, Martin Marietta Corp).

47. Whitehead, A. H., Jr., and Keyes, J. W., "Flow Phenomenon and Separation over Delta Wings with Trailing-edge Flaps at Mach 6", AIAA Journal, Vol. 6, No. 12, December 1968, pp. 2380-2387.

48. Ericsson, L. E., "Unsteady Aerodynamics of an Ablating Flared Body of Revolution Including Effects of Entropy Gradient", AIAA Journal, Vol. 6, No. 12, December 1968, pp. 2395-2401.

49. Maikapar, G. I., "Aerodynamic Heating of Lifting Bodies", Paper Re-126, 19th Congress of the International Astronautical Federation, New York, 13-19 October 1968.

50. Hart, H., "Wing/Tail Interference in Hypersonic Missile Configurations", 8th Navy Symposium on Aeroballistics, Naval Weapons Center, Corona, California, May 6-8, 1969.

51. Edney, B. E., "Effects of Shock Impingement on the Heat Transfer Around Blunt Bodies", AIAA Journal, Vol. 6, No. 1, January 1968, pp. 15-21.

52. Katzen, E. D., Marvin, H. L., Seegmiller, H. L., Ayelson, J. A., Brownson, J. J., Cleary, J. W., Kickman, W. K., and Kaattari, G. E., "Static Aerodynamics, Flow Fields, and Aerodynamic Heating of Space Shuttle Orbiters", Space Transportation System Technology Symposium, Vol. I, NASA TM X-52876, July 15-17, 1970.

53. Edney, B. E., "Shock Interference Heating and the Space Shuttle", Space Transportation System Technology Symposium, Vol. I NASA TM X-52876, July 15-17, 1970.

54. Maltby, R. L., et al., "Low Speed Flow Studies of the Vortex Patterns Above Inclined Slender Bodies Using a New Smoke Technique", RAE-TN-AERO-2482, November 1957.

55. Gapcynski, J. P., "An Experimental Investigation of the Flow Phenomena over Bodies at High Angles of Attack at a Mach Number of 2.01", NACA RML 55H29, October 1955.

56. Fiechter, M., "Über Wirbelsysteme an schlanken Rotationskörpern und ihren Einfluss auf die aerodynamischen Beiwerte", Deutsch-Franzosisches Forchungsinstitut Saint-Louis, Bericht 10/66, December 1966.

57. Astraghji, E. G., "The Influence of Mach Number, Reynolds Number, Semi-Nose Angle and Roll Rate on the Development of the Forces and Moments over a Series of Long Slender Bodies of Revolution at Incidence", NAE Data Report 54510020, Ottawa, 1967.

58. Curry, W. H. and Reed, J. F., "Measurement of Magnus Effects on a Sounding Rocket Model in a Supersonic Wind Tunnel", AIAA 66-754, September 1966.

59. Pick, G. S., "Investigation of Side Forces on Ogive-Cylinder Bodies at High Angles of Attack in the M = 0.5 to 1.1 Range", AIAA 71-570, June 1971.

60. Hall, I. M., Roger, E. W. E., and Davis, B. M., "Experiments with Inclined Blunt-Nosed Bodies at M= 2.45", Great. Brit. R&M No. 3128 (1959)

61. McElroy, G. E. and Sharp, P.S., "An Approach to Stall/Spin Development and Test", AIAA 71-772, July 1971.

62. Casteel, G. R. and Weyl, C. J., "A Design Approach to Provide Satisfactory Spin Characteristics for a Modern Flighter Aircraft", AIAA 70-928, July 1970.

63. Chambers, J. R. and Bowman, J. S., Jr., "Recent Experience with Techniques for Prediction of Spin Characteristics of Fighter Aircraft", Journal of Aircraft, Vol. 8, No. 7, July 1971, pp. 548-553.

64. Treon, S. L., "Effects of Nose-Cone Angle on the Transonic Aerodynamic Characteristics of a Blunt Cone-Cylinder Body Having Acylindrical Flared, or Blunt-Finned Afterbody," NASA TMX-582, October 1961.

65. Raymes, F., "Alternate Space Shuttle Concepts Study, Part II Tech. Summary, Vol. I Orbiter Definitions", Contract NAS 9-11160, Grumman Report DRL M-010-Line Item 11, B 3543RD-12, July 6, 1971.

66. Wawrzyniak, M. E., "To What Extent Should Space Shuttle Stability and Control be Provided Through Stability Augmentation?", Space Transportation Systems Technology Symposium, Vol. I, NASA TMX-52876, July 15-17, 1970.

67. Earnshaw, P. B., "Measurements of Vortex-Breakdown Position at Low Speed on a Series of Sharp-Edged Symmetrical Models", Great Brit. ARC CP No. 828 (1965).

68. Squire, L. C., Jones, J. C., and Stanbrook, A., "An Experimental Investigation of the Characteristics of Some Plane and Cambered 65° Delta Wings at Mach Numbers from 0.7 to 2.0", Great Brit. R&M No. 3305 (1963).

69. Rao, D. M., "Hypersonic Lee-Surface Heating Alleviation on Delta Wing by Apex-Drooping", AIAA Journal, Vol. 9, No. 9, September 1971, pp. 1875-1876.

70. Keating, R. F. A., and Mayne, B. L., "Low-Speed Characteristics of Waverider Wings", Great Brit. RAE Tech. Rpt. 69051. (1969)

71. Whitehead, A. H., Jr., and Bertram, M. H., "Alleviation of Vortex-Induced Heating to the Lee Side of Slender Wings in Hypersonic Flow", AIAA Journal, Vol. 9, No. 9, September 1971, pp. 1870-1872.

72. Stanbrook, A. and Squire, L. C., "Possible Types of Flow at Swept Leading Edges", The Aero. Quarterly, February 1964, pp. 72-82.

73. Kirkpatrick, D. L. I. and Field, J. D., "Experimental Investigation of the Positions of the Leading Edge Vortices Above Slender Delta Wings With Various Rhombic Cross-Sections in Subsonic Conical Flow", Great Brit. RAE Tech. Report No. 66068 (1966).

74. Hamilton, E. J. and Ryals, W. G., "Review of 1/10 Scale Space Shuttle Air Drop Test Results", NASA MSC Internal Document 5-2950-1-NOU-126, June 24, 1970.

75. Moul, M. J. and Paulson, J. W., "Dynamic Lateral Behavior of High Performance Aircraft", NACA RML 58E16, August 1958.

76. Stanewsky, E. and Hicks, G., "Scaling Effects on Shock-Boundary Layer Interaction in Transonic Flow", AFFDL-TR-68-11, March 1968.

77. Zonars, D., Lawndes, H. B., and Kolb, A. W., "Ground Testing", AIAA 68-1084, October 1968.

78. Loving, D. L., "Wind-Tunnel-Flight Correlation of Shock-Induced Separation Flow", NASA TN D-3580, 1966.

79. Blackwell, J. A., Jr., "Preliminary Study of Effects of Reynolds Number and Boundary-layer Transition Location on Shock-Induced Separation", NASA TN D-5003, January 1969.

80. Hummel, D., "Experimentelle Untersuchung der Stromung auf der Saugseite eines Schlanken Deltaflugels", Zeitschrift fur Flugwissenschaften, Vol. 13, No. 7, July 1965, pp. 247-252.

81. Chambers, J. R., Anglin, E. L., and Bowman, J. B., Jr., "Effects of Pointed Nose on Spin Characteristics of a Fighter Airplane Model Including Correlation with Theoretical Calculations", NASA TN-D5921, September 1970.

82. Ericsson, L. E., "Effect of Boundary Layer Transition on Vehicle Dynamics", J. Spacecraft and Rockets, Vol. 6, No. 12, December 1969, pp. 1404-1409.

83. Obremski, H. J and Morkovin, M. V., "Application of a Quasi-Steady Stability Model to Periodic Boundary Layers", AIAA Journal, Vol. 7, No. 7, July 1969, pp. 1298-1301.

84. Ericsson, L. E., "Loads Induced by Terminal-Shock Boundary-Layer Interaction on Cone-Cylinder Bodies", J. Spacecraft and Rockets, Vol. 7, No. 9, September 1970, pp. 1106-1112.

85. Ericsson, L. E., "Unsteady Aerodynamics of Separating and Reattaching Flow on Bodies of Revolution", IUTAM Symposium on Unsteady Boundary Layers, Laval University, Quebec, 24-28 May 1971.

EXPERIMENTS ON THE DYNAMIC STABILITY OF THE SPACE SHUTTLE

by

K.J. Orlik-Rückemann, J.G. LaBerge and E.S. Hanff
National Aeronautical Establishment
National Research Council of Canada
Ottawa, Ontario, Canada

INTRODUCTION

Flight conditions can be envisaged during which dynamic stability information may be important for the design and operation of the shuttle spacecraft. These include the ascent phase, some initial phases of abort separation, and possibly the transitional flight of the orbiter. In general such information may also be required for the final performance analysis of the shuttle during its entire flight. The complexity of the configuration and the often unusual character of the flight conditions render the analytical prediction of the dynamic stability characteristics of the shuttle extremely difficult. Hence in many cases experiments must be relied on as the sole source of information. However, for some of the more complicated flight conditions, even the experimental data may be difficult to obtain if the wind tunnel experiments are limited to the use of only conventional techniques. At the Space Transportation System Technology Symposium in July 1970 (Ref. 1) the senior author recommended the use of a half-model oscillatory technique for certain dynamic stability experiments on the shuttle. In the present paper some experiments using this technique will be discussed and information will be given on the dynamic pitching characteristics of both the orbiter and the booster alone as well as of the two models mated into a single launch configuration, on the static and dynamic interference effects during an abort separation maneuver, and on the dynamic plume interference effect. All the work was performed as part of the internal research program of the National Aeronautical Establishment (N.A.E.) of Canada using models supplied by the National Aeronautics and Space Administration.

MODELS MOUNTED ON REFLECTION PLATE
OF THE NAE 30 INCH TUNNEL
(a) STRAIGHT WING SHUTTLE

(Figure 1)

The dynamic stability characteristics were determined partly for a low cross-range and partly for a high cross-range configuration. The former was represented by the North American Rockwell 130 C straight-wing orbiter with the 130 G wing location (designation B6W10H12V5), and the General Dynamics/ Convair B8B straight-wing booster (designation $B_3W_1^{15}T_1^{45}$). The model scale was 1/360. Both models were cast in stainless steel and were manufactured and supplied by NASA Langley Research Center. The straight-wing configuration was used only for the initial phases of the experiments which involved the determination of the damping-in-pitch for both the orbiter alone and the booster alone as well as the study of the mutual static interference effects on the damping-in-pitch derivative of the two vehicles in 20 different relative positions. The derivative was referred to the wing planform area and the wing mean aerodynamic chord for the orbiter, and the body planform area and the body length for the booster. The distance from the nose to the moment reference center (and axis of oscillation) was 8.89 cm (3.50 in) for the orbiter and 11.57 cm (4.55 in) for the booster.

MODELS MOUNTED ON REFLECTION PLATE OF THE NAE 30 INCH TUNNEL

(a) STRAIGHT WING SHUTTLE

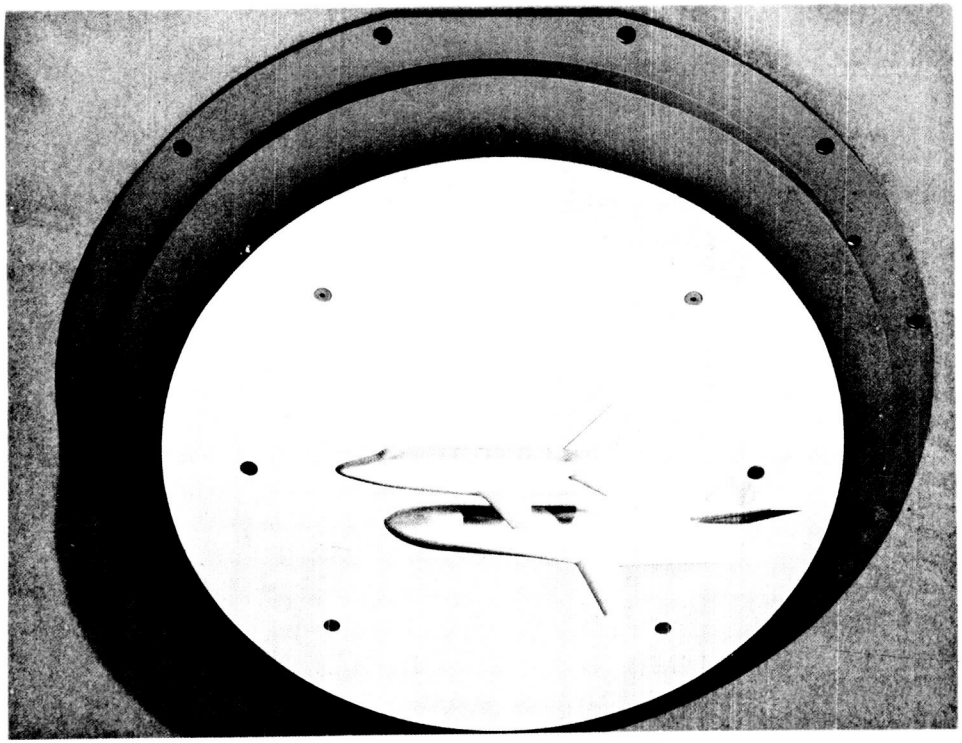

Figure 1

MODELS MOUNTED ON REFLECTION PLATE
OF THE NAE 30 INCH TUNNEL
(b) DELTA WING SHUTTLE

(Figure 2)

The high cross-range configuration was represented by the McDonnell-Douglas delta-wing orbiter 255BJ00050 and the McDonnell-Douglas swept-wing booster configuration 19A but without body base flare or boattail; the vertical tail of the booster was that of configuration 17. The model scale was 1/360. Both models were cast in aluminum alloy and were manufactured and supplied by NASA Langley Research Center. The delta-wing configuration was used for all phases of the program. The pitching moment derivatives were based on the total wing area and the wing mean aerodynamic chord for the orbiter, and the scaled down standard reference area and reference length for the booster, which were, in full scale, 929 m^2 (10,000 ft^2) and 61.0 m (200 ft), respectively. The distance from the nose to the moment reference center (and the axis of oscillation) was 6.33 cm (2.49 in) for the orbiter and 9.53 cm (3.75 in) for the booster.

MODELS MOUNTED ON REFLECTION PLATE OF THE NAE 30 INCH TUNNEL (b) DELTA WING SHUTTLE

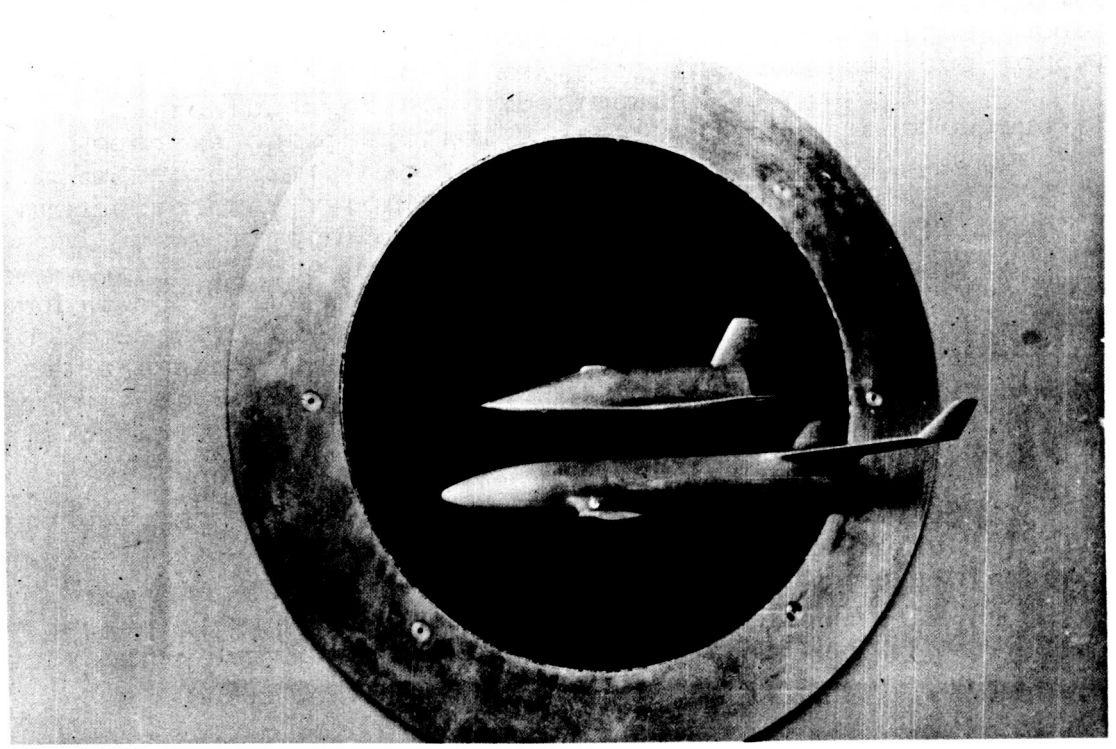

Figure 2

EXPERIMENTAL ARRANGEMENT FOR STATIC AND DYNAMIC INTERFERENCE STUDY ON SHUTTLE ABORT SEPARATION

(Figure 3)

In an abort separation maneuver each component of the shuttle spacecraft will be affected by the interference caused by the proximity of the other component. Two kinds of such interference may be distinguished: static interference, which is caused by the stationary presence of the other component, and dynamic interference, which is caused by the oscillatory motion of the other component.

The experimental arrangement makes use of the half-model technique (Ref. 1). Half-models of the two components of the shuttle spacecraft are mounted very close to a reflection plate which is displaced about 2.5 cm (about 1 in.) from the wind-tunnel wall. The model on which the derivatives are to be measured (orbiter or booster) is attached to an adapter which passes through both the reflection plate and the wind-tunnel wall and which, in turn, is attached to a cruciform spring in the half-model dynamic balance on the outside of the wind tunnel. An oscillatory motion may be imparted to the model by means of an electromagnetic oscillator which consists of a pair of light-weight coils moving in a magnetic field, while a signal proportional to the angular displacement of the model is obtained from a strain-gauge bridge on the spring.

For the static interference experiments the other model is attached to the reflection plate in such a way that its vertical and longitudinal separation distances and the incidence relative to the first model can be easily varied. The incidence of the whole configuration is varied by rotating the wind tunnel plate (with the reflection plate). For the dynamic interference experiments the other model is mounted on a pivot which defines its center of oscillation, while an oscillatory motion of a known amplitude is imparted by means of an eccentric drive connected to a synchronous motor; the two motions can be made synchronous and the phase relationship between them can be varied as required.

Details about the free-oscillation and the forced-oscillation methods of derivative measurements, which both were employed for this program, may be found in Ref. 2.

EXPERIMENTAL ARRANGEMENT FOR STATIC AND DYNAMIC INTERFERENCE STUDY ON SHUTTLE ABORT SEPARATION

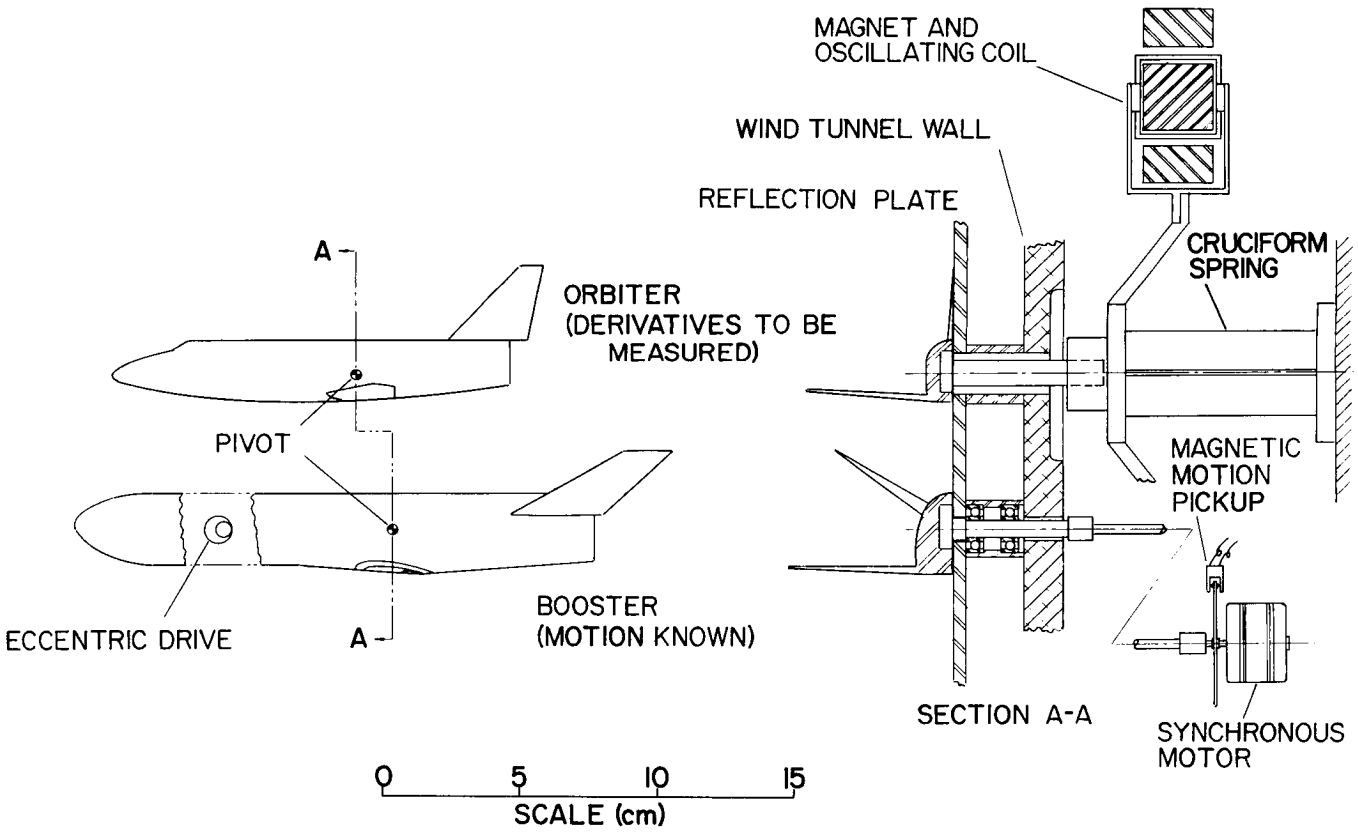

Figure 3

EFFECT OF INCIDENCE ON THE DAMPING-IN-PITCH OF THE STRAIGHT-WING ORBITER ALONE

(Figure 4)

The mean angle-of-attack has only a slight effect on the damping-in-pitch of the orbiter alone, while an increasing Reynolds number seems to increase that quantity in a moderate fashion. The NAE half-model free-oscillation data appear to be in very good agreement with the AEDC full-model forced-oscillation data (Ref. 3), especially when the effect of the difference in the amplitude of oscillation is taken into account. The NAE data represent a mean amplitude of oscillation of 1.12^{o} and as such can be expected (see Fig. 4 in Ref. 3) to be about 10 percent lower than the corresponding AEDC data at 1.6^{o}.

EFFECT OF INCIDENCE ON THE DAMPING-IN-PITCH OF THE STRAIGHT-WING ORBITER ALONE

		M	$R_E \times 10^{-6}$	$\pm\theta°$	x_{CG}/ℓ
●	NAE HALF-MODEL FREE OSC.	1.80	1.8	0.75-1.5	0.612
○	AEDC FULL-MODEL FORCED OSC.	1.76	2.1	1.6	0.601
□	AEDC FULL-MODEL FORCED OSC.	1.76	4.2	1.6	0.601

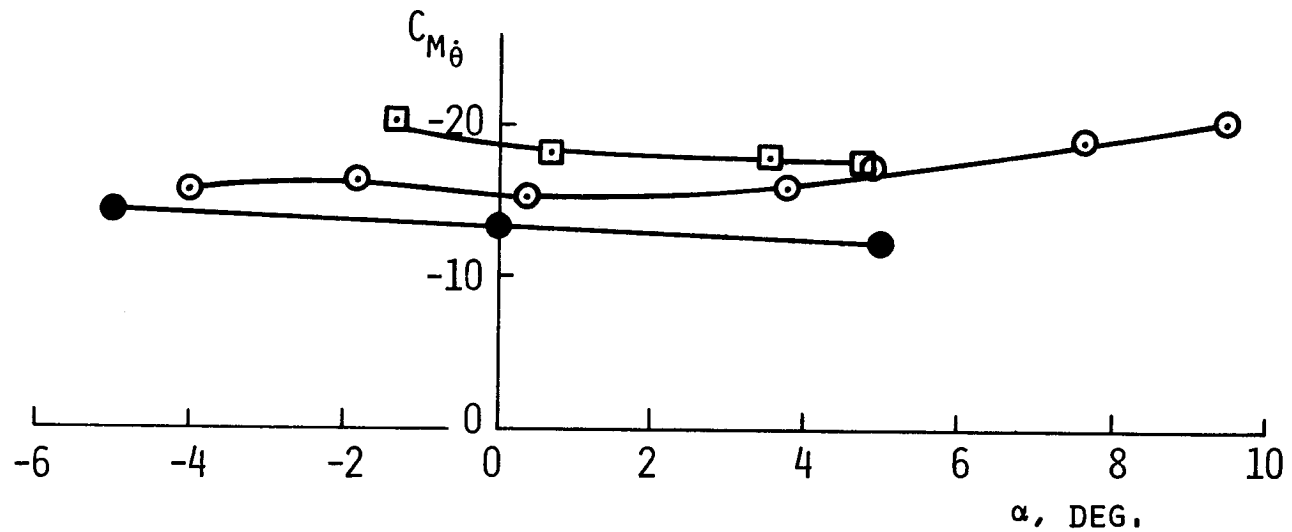

Figure 4

STATIC INTERFERENCE EFFECT ON THE DAMPING-IN-PITCH OF DELTA-WING ORBITER

(Figure 5)

The damping-in-pitch of the delta-wing orbiter in the presence of the stationary swept-wing canard booster was measured for 20 combinations of the angle-of-attack α of the entire configuration and the three separation parameters. These were: the relative incidence i which was equal to the difference between the incidence of the orbiter and that of the booster, the longitudinal separation Δx which was equal to the longitudinal distance of the CG of the orbiter behind the CG of the booster, and the vertical separation Δz, which was equal to the vertical distance of the CG of the orbiter above the CG of the booster. Both separation distances were referred to the length of the booster, ℓ. The effect of varying α, i and $\Delta x/\ell$ around a set of nominal conditions defined by $\alpha=0$, i=0 and $\Delta x/\ell=-.06$ is shown for two values of $\Delta z/\ell$ on the composite diagram in Fig. 5; the static interference effect is then obtained as the difference between these results and the corresponding data for the orbiter alone. It can be seen that this effect is everywhere relatively small and in no case exceeds 29 percent of the interference-free values. An effect of that magnitude is not likely to significantly affect the dynamics of an abort separation maneuver.

STATIC INTERFERENCE EFFECT ON THE DAMPING-IN-PITCH OF DELTA-WING ORBITER

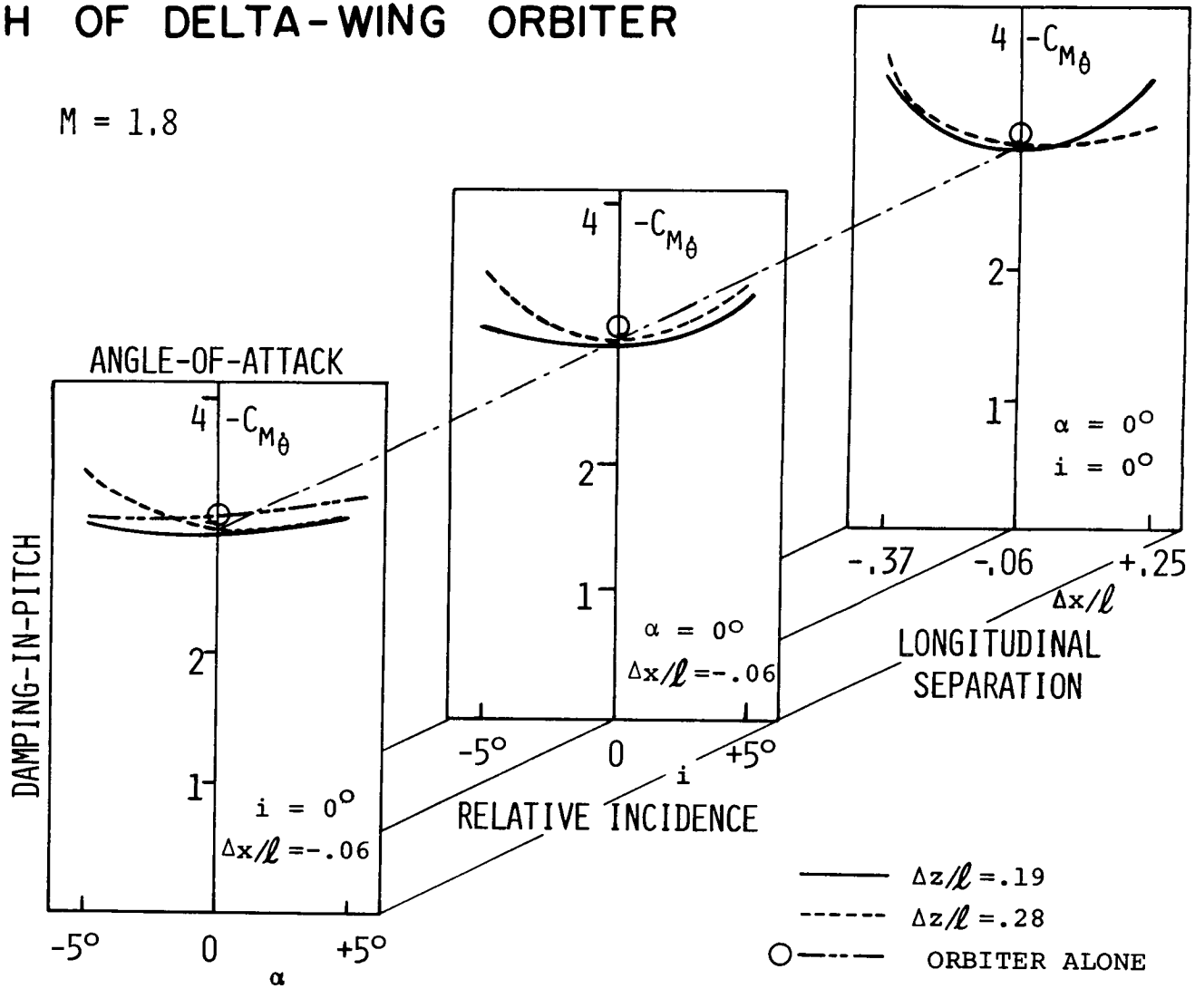

Figure 5

STATIC INTERFERENCE EFFECT ON THE DAMPING-IN-PITCH OF SWEPT-WING CANARD BOOSTER

(Figure 6)

A similar investigation was performed with the roles of the booster and of the orbiter reversed. The effect of the presence of the stationary delta-wing orbiter on the damping-in-pitch of the swept-wing canard booster was found to be of the same order as the one measured for the reverse case. Static interference effects of approximately the same magnitude were also found on the damping derivatives of the straight-wing booster and the straight-wing orbiter (results not shown here). It should be noted, however, that the absolute magnitude of the dimensional damping derivative was four times higher for the canard booster than for the straight-wing booster and twice as high for the delta-wing orbiter as for the straight-wing orbiter. Detailed description of the NAE static interference experiments may be found in Refs. 4 and 5.

STATIC INTERFERENCE EFFECT ON THE DAMPING-IN-PITCH OF SWEPT-WING CANARD BOOSTER

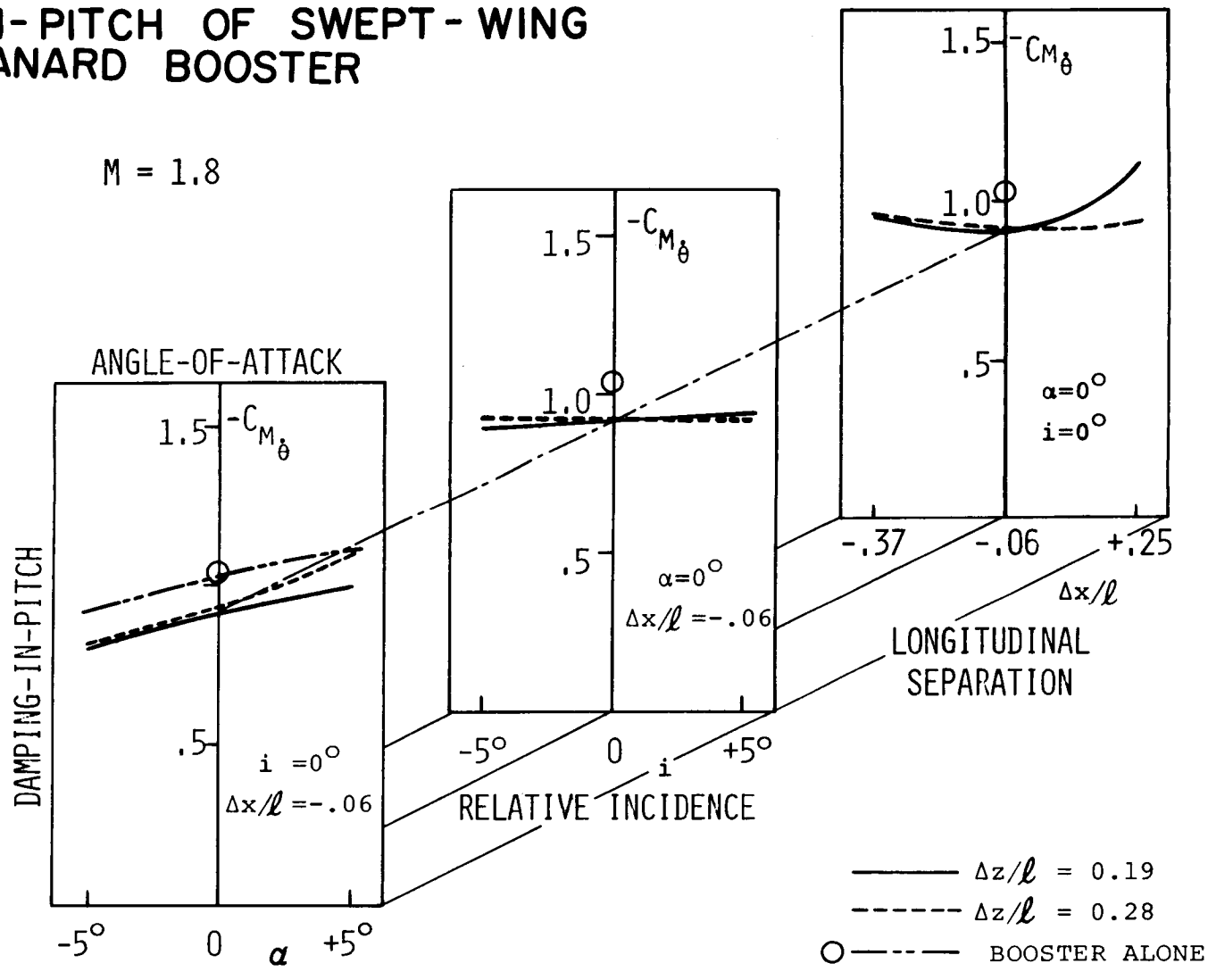

Figure 6

DYNAMIC INTERFERENCE EFFECT ON THE DAMPING-IN-PITCH OF DELTA-WING ORBITER OSCILLATING SYNCHRONOUSLY WITH THE BOOSTER

(Figure 7)

In an actual separation maneuver the two components of the shuttle may be expected to perform oscillatory motions at the same time. It is therefore necessary to establish the effect of the presence of the other vehicle not only when that vehicle is stationary but also when it oscillates. Such an effect is denoted here by the term "dynamic interference". As may be expected, the dynamic interference effect is most pronounced when the two vehicles oscillate with the same frequency. The effect is then a strong function of the phase angle between the two motions. Here the damping-in-pitch derivative of the delta-wing orbiter is shown in the presence of the synchronously oscillating canard booster. Both amplitudes are 1.9^{o}, the frequency is 47 Hz and the separation distances are $\Delta x/\ell = -0.06$ and $\Delta z/\ell = 0.19$. Two different methods were employed for the measurements and the results are highly consistent. The corresponding interference-free value and the static interference effect are also indicated. The dynamic interference effect is found to be up to two orders of magnitude larger than the static interference effect, resulting in values of the damping derivative which are between + 13 and - 8 times the interference-free value. Such large variation in that derivative, and especially the occurrence of large negative damping (positive $C_{m_{\dot{\theta}}}$), could have significant effects on the flight characteristics of the orbiter and, if the two vehicles would indeed perform synchronous oscillation while in close proximity, could affect critically the abort separation maneuver.

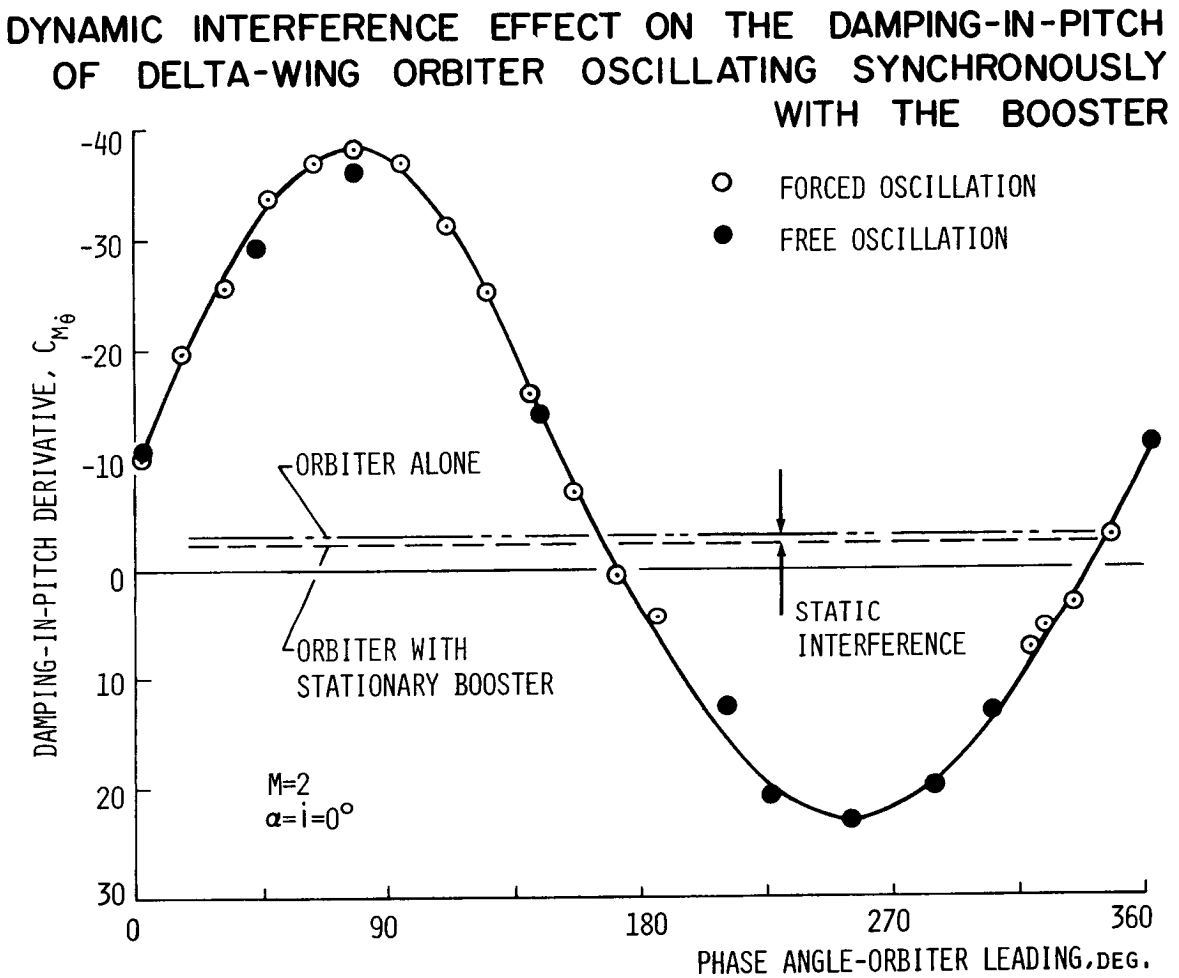
DYNAMIC INTERFERENCE EFFECT ON THE DAMPING-IN-PITCH OF DELTA-WING ORBITER OSCILLATING SYNCHRONOUSLY WITH THE BOOSTER
FORCED OSCILLATION
FREE OSCILLATION
ORBITER ALONE
ORBITER WITH STATIONARY BOOSTER
STATIC INTERFERENCE
M=2
α=i=0°
DAMPING-IN-PITCH DERIVATIVE, $C_{M_{\dot{\theta}}}$
-40
-30
-20
-10
0
10
20
30
0
90
180
270
360
PHASE ANGLE-ORBITER LEADING, DEG.

Figure 7

DYNAMIC INTERFERENCE EFFECT ON THE STATIC PITCHING MOMENT DERIVATIVE OF DELTA-WING ORBITER OSCILLATING SYNCHRONOUSLY WITH THE BOOSTER

(Figure 8)

Since the orbiter is a much smaller vehicle than the booster, its natural frequency under normal interference-free conditions may be expected to be higher than that of the booster. It is shown here that in the presence of the dynamic interference, the static pitching moment derivative+, and therefore the frequency of the orbiter, may be greatly reduced. In the example shown, which applies for the same set of experimental conditions and separation parameters as in the previous figure, this reduction is of the order of up to 50%. This value is probably a strong function of the separation parameters, of which only one set was investigated during the dynamic interference study. It appears therefore quite conceivable that conditions may arise, during which the oscillatory motion of the orbiter is slowed down to such an extent that the orbiter "locks-in" with the oscillatory flow field of the booster. If this in turn happens at a phase angle for which large negative damping of the orbiter has been measured, a serious case of rapidly diverging oscillations may develop. If, furthermore, the procedure for abort separation allows the two vehicles to remain in proximity during a period of time comparable to the time for several cycles of oscillation, this diverging motion may then lead to a collision between the two vehicles during the early stages of separation. The entire question needs further examination, which should include the determination of the effect of the various separation parameters on the experimental data, a dynamic simulation experiment with the inertia properties of the orbiter (or even of both vehicles) correctly scaled, a study of the (probably much smaller but perhaps still significant) dynamic interference effect of the orbiter on the booster and,finally,a realistic analysis of the flight mechanics problem involved.

+ This derivative is presented here without any correction for possible half-model effects, which are not likely to affect the trends discussed in this paper.

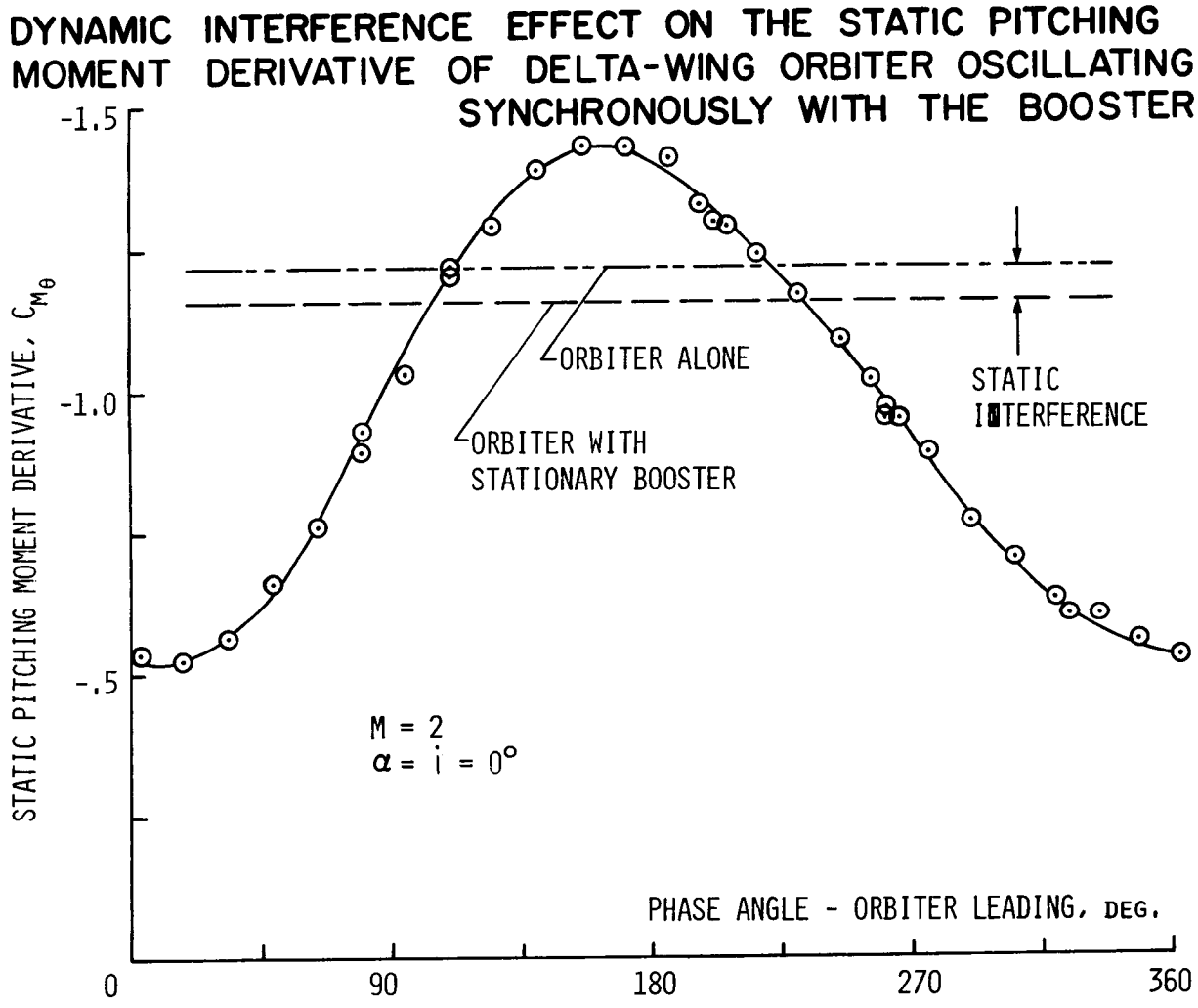
DYNAMIC INTERFERENCE EFFECT ON THE STATIC PITCHING MOMENT DERIVATIVE OF DELTA-WING ORBITER OSCILLATING SYNCHRONOUSLY WITH THE BOOSTER
STATIC PITCHING MOMENT DERIVATIVE, C_{M_θ}
-1.5
-1.0
-.5
ORBITER ALONE
STATIC INTERFERENCE
ORBITER WITH STATIONARY BOOSTER
M = 2
$\alpha = i = 0°$
PHASE ANGLE - ORBITER LEADING, DEG.
0
90
180
270
360

Figure 8

EFFECT OF ORBITER AMPLITUDE ON ORBITER DAMPING
FOR THE TWO MODELS IN SYNCHRONOUS OSCILLATION

(Figure 9)

Two experimental parameters, the effects of which have been investigated, are the orbiter amplitude and the angle-of-attack of the entire configuration. The results are shown here for otherwise the same conditions as on the previous two figures. It may be seen that, although the interference-free values of the damping derivative and the static interference effect are almost independent of the orbiter amplitude, the dynamic interference effect increases greatly with decreasing amplitude, especially so for zero or small overall incidence. Increasing the overall incidence reduces this effect, with $\alpha=-5^{o}$ values located between $\alpha= 0^{o}$ and $\alpha= 5^{o}$. The two phase angles for which the results are shown, represent the two conditions for which the maximum positive damping and the maximum negative damping have been observed. All data were obtained with the free-oscillation method and the amplitude of the booster was everywhere 1.9^{o}.

The NAE study of the dynamic interference effect on the damping-in-pitch of the shuttle orbiter is described in detail in Ref. 6.

EFFECT OF ORBITER AMPLITUDE ON ORBITER DAMPING FOR THE TWO MODELS IN SYNCHRONOUS OSCILLATION

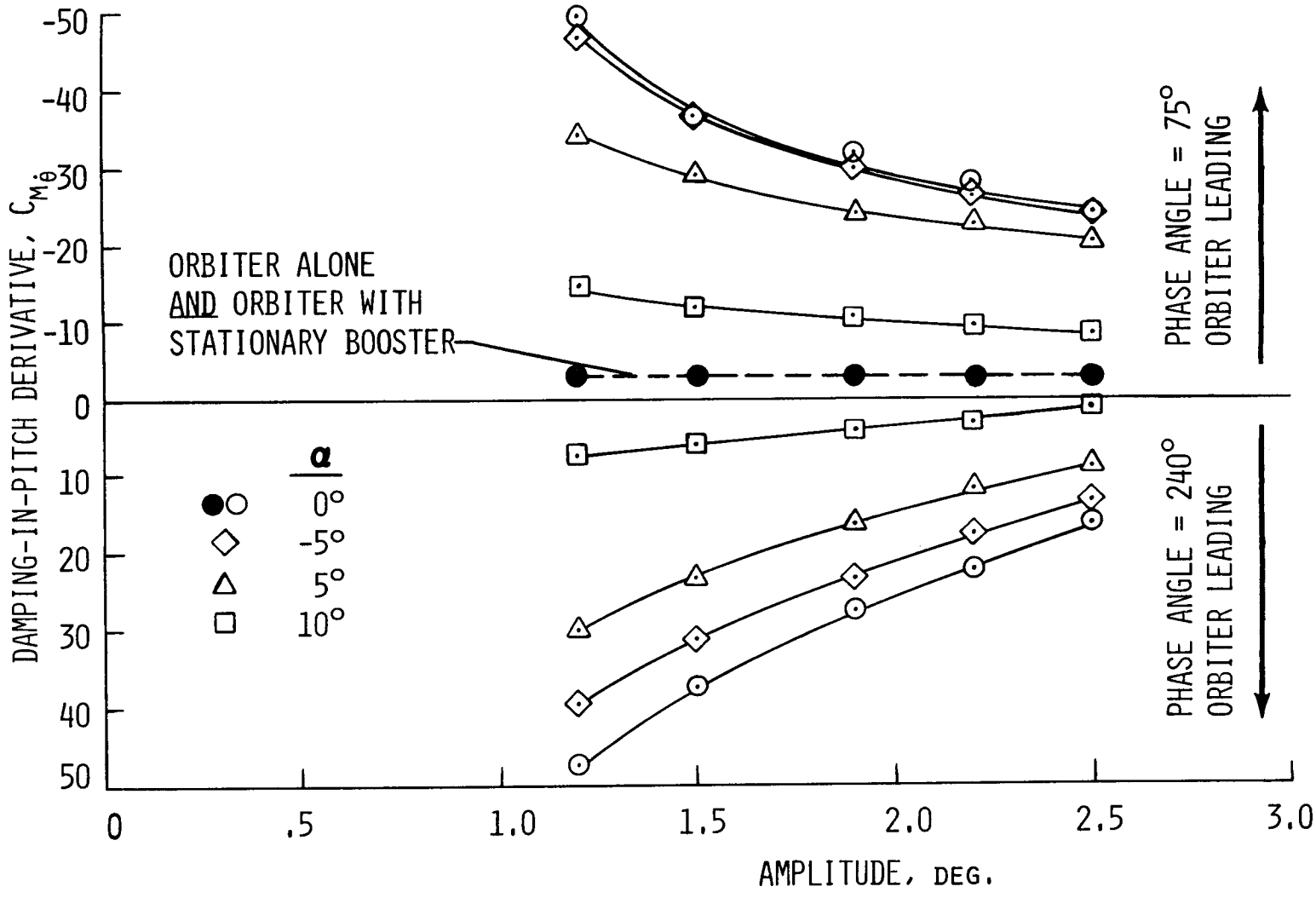

Figure 9

OIL FLOW VISUALIZATION. STRAIGHT WING SHUTTLE IN ABORT SEPARATION AT MACH 1.8, $\Delta z/\ell = 0.2$ $\Delta x/\ell = -0.4$ $\alpha = i = 0^{\circ}$

(Figure 10)

Oil flow visualization studies were conducted in order to obtain detailed pictures of the interacting flow patterns over the two-model configuration at various separation attitudes, to assess the importance of the interaction between the model bow shock and the plate boundary layer and to ascertain that upstream flow on the reflection plate was uniform. A 1:3 mixture of titanium dioxide and vacuum pump oil and a small quantity of oleic acid was used for these experiments.

A typical photograph is shown in Figure 10 with the straight-wing orbiter mounted well forward of the straight-wing booster. A strong effect is visible of the booster bow shock on the orbiter body ahead of the wing and of the leading edge shock from the orbiter wing on the booster forebody. Also, the separation lines around the orbiter canopy and the interaction between the wing trailing edge shock and the leading edge shock of the horizontal stabilizer of the orbiter or the V-shaped stabilizer of the booster can be clearly seen.

As far as the flow on the reflection plate is concerned one can observe the bow-shock-induced separation of the plate boundary layer and its subsequent re-attachment and in some cases its secondary separation and secondary re-attachment. These phenomena, however, seem to be confined to a layer immediately adjacent to the plate and no effects of the plate boundary layer can be discerned on the flow characteristics over the bodies, wings or stabilizers of the two shuttle models.

OIL FLOW VISUALIZATION. STRAIGHT WING SHUTTLE IN ABORT SEPARATION AT MACH 1.8, $\Delta z/\ell = 0.2$ $\Delta x/\ell = -0.4$ $\alpha = i = 0°$

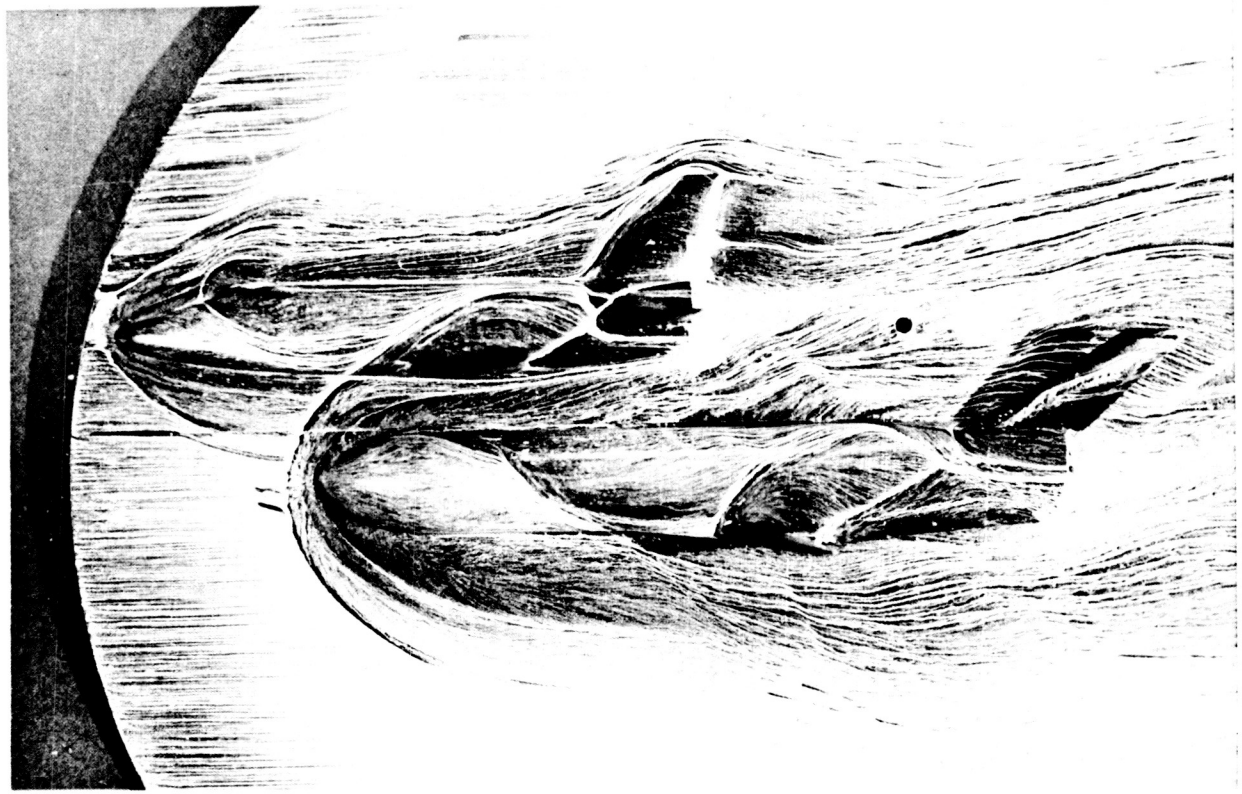

Figure 10

OIL FLOW VISUALIZATION. LAUNCH CONFIGURATION OF DELTA WING SHUTTLE AT MACH 2 AND $\alpha=0^{\circ}$

(Figure 11)

Another example of oil flow visualization is given in Figure 11. This time the models are those of the delta-wing orbiter and the swept-wing canard booster combined into a single launch configuration. Surface flow features, similar to those described in Figure 10 are again visible. Especially, a clear picture is provided of the shock-wave-induced separation and subsequent re-attachment in front of and behind the forward wing of the booster. The leading-edge shock of the main wing of the booster is also clearly visible.

In both figures, the interaction between the plate boundary layer and the various shock waves emanating from the models can be observed as inflections in the plate streamlines, which may be used to study the propagation of these shock waves. The flow ahead of the models appears fully uniform everywhere with the possible exception of the area in the vicinity of the orbiter nose in Figure 10, where a slight disturbance associated with the very close edge of the reflection plate can be discerned.

OIL FLOW VISUALIZATION. LAUNCH CONFIGURATION OF DELTA WING SHUTTLE AT MACH 2 AND $\alpha = 0°$.

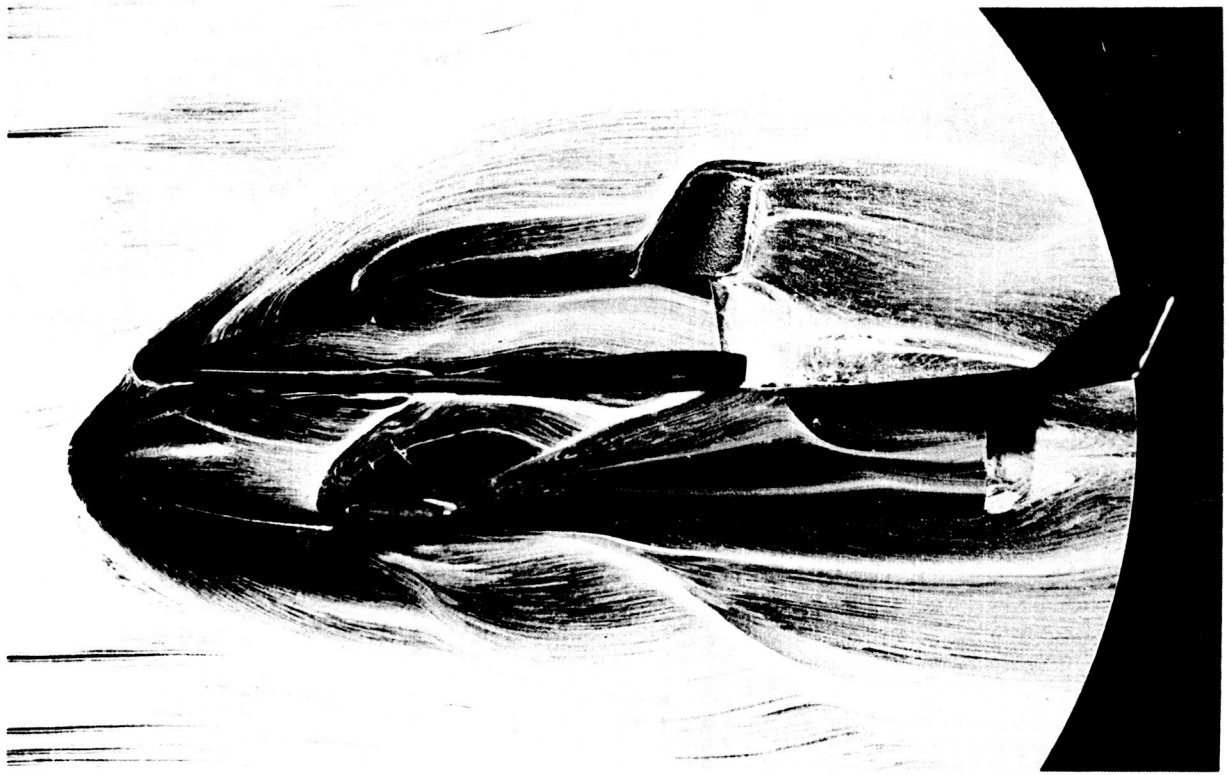

Figure 11

EXPERIMENTAL ARRANGEMENT FOR DYNAMIC EXHAUST PLUME INTERFERENCE STUDY

(Figure 12)

Proper knowledge of the damping derivatives may be particularly important during the ascending flight of the shuttle when the destabilizing effect of the negative density gradient may render the vehicle quite sensitive to its inherent aerodynamic stability characteristics. An analytical determination of the damping derivatives for a configuration as complex as the mated launch configuration is, of course, extremely complicated. In addition, during the ascending portion of the flight, the rocket exhaust plume, which oscillates together with the vehicle, may also influence to some extent the aerodynamic stability characteristics of the vehicle, including its aerodynamic damping. An experimental determination of the damping derivative of the launch configuration, including a study of the plume interference effect, is therefore highly desirable.

The previously described (Figure 3) experimental arrangement and delta-wing shuttle models were modified in order to allow simulation of the rocket exhaust plume on an oscillating model of the mated launch configuration. A high pressure (up to 15 Mn/m^2 or 2200 psi) nitrogen supply line was incorporated, in a frictionless fashion, in the half-model dynamic balance and an adapter, containing a high pressure chamber and an exhaust nozzle, was inserted in the body of the booster. The half-model technique is most suitable for such an investigation since it eliminates entirely the large reaction which may be expected to exist between the oscillating plume and the stationary sting of a conventional sting support. It also makes possible, without any problems, the correct positioning of the center of oscillation of the mated launch configuration.

EXPERIMENTAL ARRANGEMENT FOR DYNAMIC EXHAUST PLUME INTERFERENCE STUDY

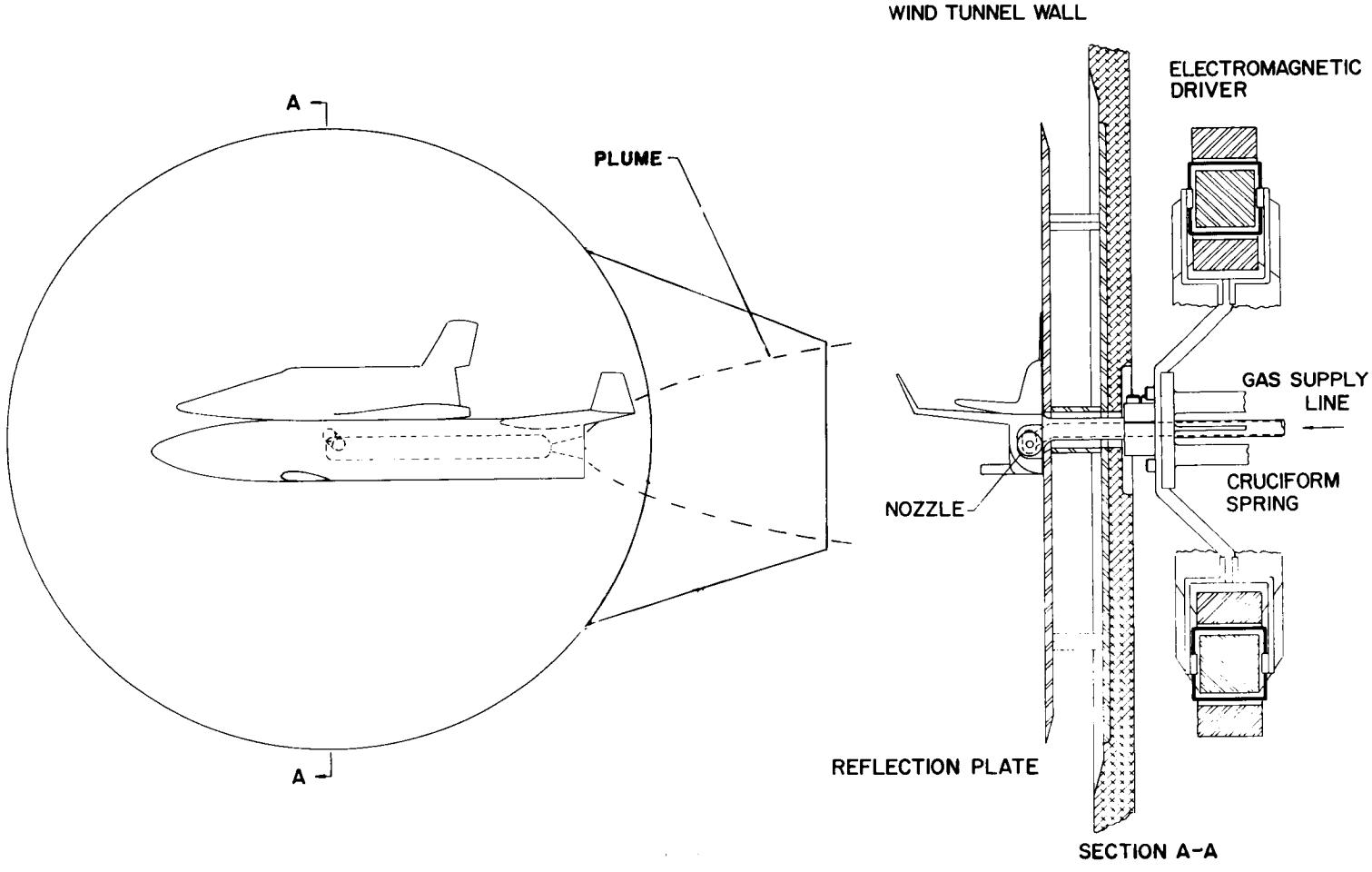

Figure 12

OIL FLOW VISUALIZATION. LAUNCH CONFIGURATION OF DELTA-WING SHUTTLE WITH SIMULATED EXHAUST PLUME AT MACH 2 AND $\alpha = 0^{\circ}$.

(Figure 13)

The simulation of the shape and size (but not the momentum) of the exhaust plume was achieved by using methods and charts from NASA-MSC (J.L. Sims) i.e. by duplicating the nozzle-exit wall angle, the initial plume boundary angle and the ratio of the initial plume boundary Mach number to the specific heat ratio. Thus, using dry nitrogen at 8.6 MN/m^2 (1250 psi), nozzle wall angle of 14° and nozzle area-ratio of 11.9 (exit Mach number of 4.1) the full-scale conditions were simulated of a booster with nozzle area-ratio 34 flying at Mach 2 at 17.4 km (57,000 ft) and with 50% thrust level [10.3 MN/m^2 (1500 psi) chamber pressure]. One nozzle only was used on the half-model with a throat area corresponding to one half of the scaled-down total throat area on the full-scale vehicle.

The reflection plate was extended (by installing an extra flat plate which was removable for calibration) in the downstream direction, and oil flow visualization was employed to confirm the shape and the size of the exhaust plume. The conditions on the photograph represent flow at Mach 2 and the nozzle-exit to freestream pressure ratio of 6.5, which was close to the highest pressure ratio tested. Streamlines on the model are also visible. No oil was applied to the main part of the reflection plate.

OIL FLOW VISUALIZATION. LAUNCH CONFIGURATION OF DELTA-WING SHUTTLE WITH SIMULATED EXHAUST PLUME AT MACH 2 AND $\alpha = 0°$.

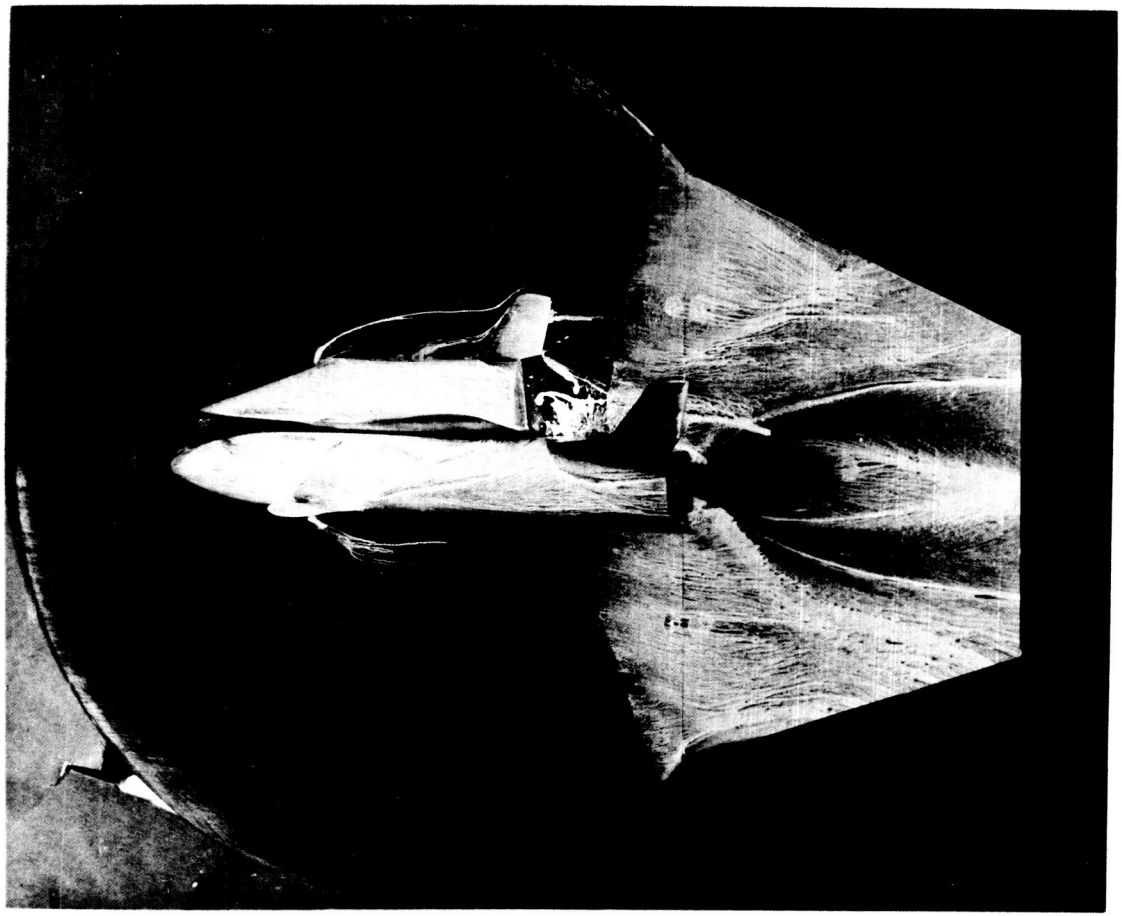

Figure 13

DELTA-WING SHUTTLE LAUNCH CONFIGURATION
EFFECT OF MACH NUMBER ON THE DAMPING-IN-PITCH

(Figure 14)

The damping-in-pitch derivative of the launch configuration decreases significantly with increasing supersonic Mach number, while its variation with angle-of-attack is far less pronounced. The information presented here is for the delta-wing shuttle oscillating with an amplitude of $\pm$ 2.5°. Similar data for the booster alone at Mach 1.80 are included for comparison. Although it would appear that the addition of a piggy-back orbiter has only a small effect on the damping derivative, this may be coincidental, since the positions of the axes of oscillation for the launch configuration and for the booster alone are different. These positions, which correspond to the positions of the centers of gravity of the full-scale vehicles, are given by x_{CG}/ℓ and z_{CG}/ℓ, which are distances behind the booster nose and above the booster CG, respectively, both expressed in terms of the booster length.

DELTA-WING SHUTTLE LAUNCH CONFIGURATION
EFFECT OF MACH NUMBER ON THE DAMPING-IN-PITCH

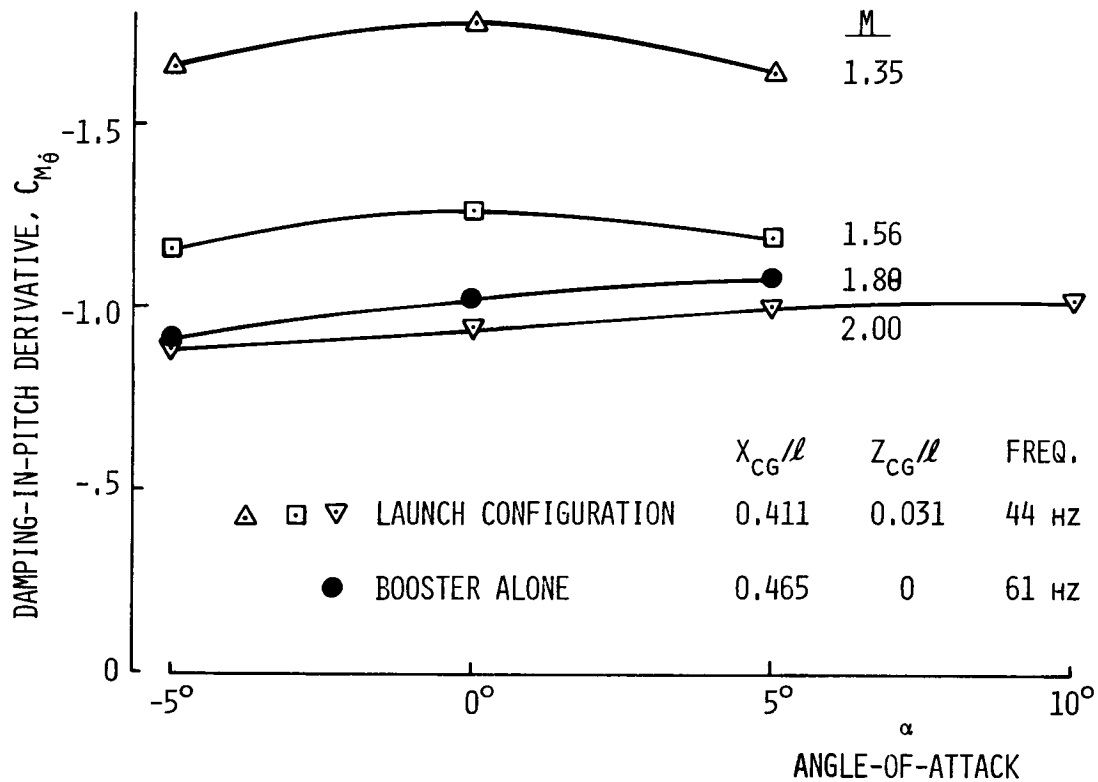

Figure 14

DELTA-WING SHUTTLE LAUNCH CONFIGURATION

PLUME INTERFERENCE EFFECT ON DAMPING-IN-PITCH

(Figure 15)

Plume interference effect on the damping-in-pitch derivative may be obtained from the following expression:

$$\Delta(C_{m_{\dot\theta}})_{\text{plume int.}} = (C_{m_{\dot\theta}})_{\text{plume}} - \Delta(C_{m_{\dot\theta}})_{\text{plate, plume}} - (C_{m_{\dot\theta}})_{\text{no plume}} - \Delta(C_{m_{\dot\theta}})_{\text{jet,vac.}}$$

$$\begin{bmatrix}\text{PLUME}\\ \text{INTERFERENCE}\end{bmatrix} = \begin{bmatrix}\text{WITH}\\ \text{PLUME}\end{bmatrix} - \begin{bmatrix}\text{WITHOUT}\\ \text{PLUME}\end{bmatrix} - \begin{bmatrix}\text{JET IN}\\ \text{VACUUM}\end{bmatrix}$$

where the first and the third term on the RHS are usual damping derivatives measured with and without the plume during a tunnel run, and the remaining terms are calibration terms obtained with no flow in the tunnel but expressed here, for convenience, in the form of equivalent derivatives. $\Delta(C_{m_{\dot\theta}})_{\text{jet,vac.}}$ represents the internal effect of the nitrogen flow inside the model (a characteristic of the experimental arrangement) and is determined from the difference in damping measured in vacuum with and without the jet. $\Delta(C_{m_{\dot\theta}})_{\text{plate, plume}}$ represents the effect of the reflection plate on the plume and is obtained at a pressure equal to the static pressure during a run from a difference in damping measured with and without the reflection plate extension.

Preliminary results indicate that the plume interference effect on the damping-in-pitch derivative is quite small, of the order of ten percent or so for the configuration and conditions tested. The effect of the internal nitrogen flow, however, is significantly larger and, although this quantity was not simulated in the present experiments, it may be worth considering this effect for a full-scale rocket engine flow. The effect of the reflection plate extension on the plume is very small, confirming the suitability of half-model oscillatory techniques for this type of experiment.

DELTA-WING SHUTTLE LAUNCH CONFIGURATION

PLUME INTERFERENCE EFFECT ON DAMPING-IN-PITCH

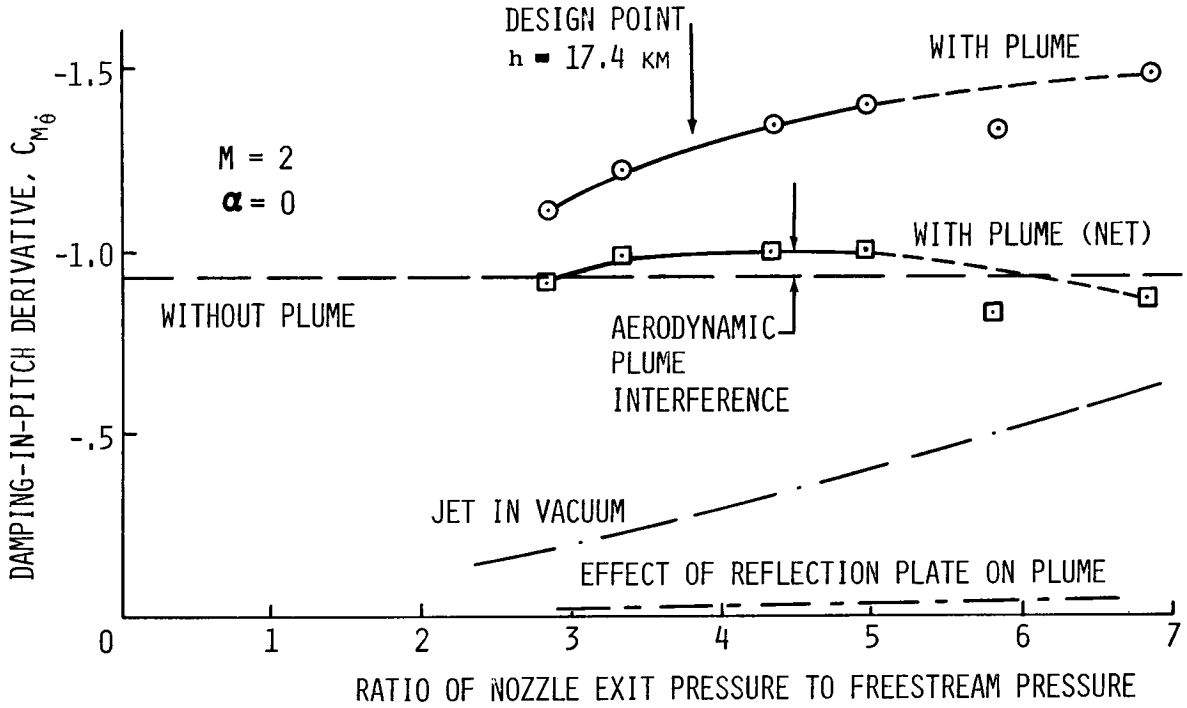

Figure 15

SHADOWGRAPH HIGH SPEED MOTION PICTURE
OF DELTA-WING ORBITER AND BOOSTER
IN SIMULTANEOUS OSCILLATION
(Figure 16)

By inserting a flat front surface mirror into the reflection plate and an optical window into a specially prepared circular cut-out in the Mach 2 nozzle liner, it was possible to use a double-pass optical system during the half-model experiments. Aerodynamic considerations prevented the use of a thick enough mirror to entirely avoid structural vibrations; the optical system was therefore mainly used in the shadowgraph mode of operation. A high speed motion picture film revealing the complex oscillating shock wave pattern during the dynamic interference experiments has been taken for the following eight cases:

	orbiter	booster	phase angle	α
1)	stationary	stationary	-	0°
2)	47 Hz; $\pm 2.5^{\circ}$	stationary	-	0°
3)	stationary	47 Hz; $\pm 1.9^{\circ}$	-	0°
4)	47 Hz; $\pm 2.5^{\circ}$	47 Hz; $\pm 1.9^{\circ}$	0°	0°
5)	47 Hz; $\pm 2.5^{\circ}$	47 Hz; $\pm 1.9^{\circ}$	75°	0°
6)	47 Hz; $\pm 2.5^{\circ}$	47 Hz; $\pm 1.9^{\circ}$	250°	0°
7)	47 Hz; $\pm 2.5^{\circ}$	47 Hz; $\pm 1.9^{\circ}$	250°	10°
8)	47 Hz; $\pm 2.5^{\circ}$	23.5Hz; $\pm 1.9^{\circ}$	-	0°

4X Reversal film at 1500 frames per second was used for the entire film. The Mach number was 2.0 and the Reynolds number per meter was 12 million. A single frame from case no. 4 is shown here.

SHADOWGRAPH HIGH SPEED MOTION PICTURE OF DELTA-WING ORBITER AND BOOSTER IN SIMULTANEOUS OSCILLATION

Figure 16

CONCLUSIONS

IN THE RANGE OF EXPERIMENTAL CONDITIONS INVESTIGATED THE FOLLOWING APPLIES:

1. INTERFERENCE-FREE DIMENSIONAL DAMPING IS SUBSTANTIALLY HIGHER FOR THE HIGH-CROSS-RANGE SHUTTLE THAN FOR THE LOW-CROSS-RANGE CONFIGURATION.
2. FOR BOTH CONFIGURATIONS DURING ABORT SEPARATION THE STATIC INTERFERENCE EFFECTS ON DAMPING ARE RELATIVELY SMALL.
3. FOR THE TWO VEHICLES IN SYNCHRONOUS OSCILLATION THE DYNAMIC INTERFERENCE EFFECTS ARE VERY LARGE AND MAY LEAD TO NEGATIVE DAMPING CONDITIONS. THE POSSIBILITY OF THE ORBITER "LOCKING-IN" WITH THE OSCILLATORY FLOW FIELD OF THE BOOSTER AND DEVELOPING RAPIDLY DIVERGING OSCILLATION THAT COULD LEAD TO COLLISION DURING ABORT SEPARATION CANNOT BE RULED OUT AND SHOULD BE INVESTIGATED FURTHER. MORE EXPERIMENTAL DATA AS WELL AS A REALISTIC FLIGHT MECHANICS ANALYSIS ARE NEEDED.
4. THE DAMPING OF THE DELTA-WING LAUNCH CONFIGURATION AND OF THE BOOSTER ALONE ARE OF THE SAME ORDER OF MAGNITUDE.
5. PLUME INTERFERENCE EFFECTS ON DAMPING APPEAR TO BE SMALL. EFFECTS OF THE INTERNAL FLOW IN ROCKET ENGINES MAY BE SUBSTANTIAL.
6. THE HALF-MODEL TECHNIQUE APPEARS TO BE UNIQUELY SUITABLE FOR OSCILLATORY EXPERIMENTS INVOLVING TWO MODELS IN SIMULTANEOUS MOTION AND/OR MODELS WITH SIMULATED PLUME EFFECT.

REFERENCES

(1) Orlik-Rückemann, K.J.: Possible Use of Half-Model Oscillatory Techniques for the Study of Shuttle Abort Separation Dynamics. Space Transportation System Technology Symposium, Volume I, pp. 99-118. NASA TM X-52876, July 1970.

(2) Orlik-Rückemann, K.J., Adams, P.A. and LaBerge, J.G.: On Dynamic Stability Testing of Unconventional Configurations. AIAA Paper No. 71-276, 1971.

(3) Uselton,R. and Wallace, A.R.: Dynamic Stability Testing of Space Shuttle Configurations During Abort Separation at Mach Numbers 1.76 and 2. AEDC-TR-71-198, October, 1971.

(4) Orlik-Rückemann, K.J. and LaBerge, J.G.: Dynamic Stability Experiments on Straight Wing Space Shuttle Abort Separation at M=1.80. National Research Council of Canada Report NAE LTR-UA-16, May 1971.

(5) LaBerge, J.G.: Dynamic Stability Experiments on Delta-Wing Space Shuttle in Abort Separation at M=1.80. National Research Council of Canada Report LTR-UA-17, July 1971.

(6) Orlik-Rückemann, K.J. and LaBerge, J.G.: Dynamic Interference Effect on Dynamic Stability of Delta-Wing Shuttle in Abort Separation at M=2.0. National Research Council of Canada Report NAE LTR-UA-18, November, 1971.

Aerospace Transporter and Lifting Body Activities in Europe and Potential Participation in the Development of the Space Shuttle Orbiter

by

M. Fuchs

J. Haseloff

G. Peters

ERNO Raumfahrttechnik GmbH

Bremen, W.-Germany

1. General Remarks

In order to be able to understand Germany's great interest in a participation in the Space Shuttle system, at first some remarks should be made regarding the work so far performed in Europe.

Stimulated by professor Sänger's concept of a space glider at the end of the Second World War, German space activities started approximately in 1962 with first studies on a space transporter system within our national program. (Fig. 1)

These studies, which went more into depth from year to year, showed that the costs of such a European Space Shuttle (Fig. 2) were definitely too high. In 1966 a further joint German/French study (Fig. 3) investigated, besides the financial problems, also the technical aspects. The estimated costs at that time, amounting to approximately

20 billion German marks (approximately 5 billion $,), were extremely high for European standards. At the same time, the structural weight uncertainties became quite evident during the layout of an orbiter, thus adding to the overall technical uncertainties. The orbiter, envisioned at that time, should have been capable of transporting a payload of approximately 3 tons into a 500-km circular orbit. However, the great uncertainties concerning structure, engines and thermal insulation did not justify a continuation in this direction.

For these reasons, all plans so far made have been changed completely. The new course was directed to detail investigations in the field of re-entry vehicles, as the basis for future design and development concepts in the direction of a space shuttle. Fundamental investigations concerning re-entry vehicles have been performed in the fields of:

- aerodynamics,
- aerothermodynamics,
- flight mechanics,
- attitude control,
- flight control,
- structures, and
- free-flight tests.

This program permitted the continuation of work to acquire realistic data in the field of aero-space transporters.

This program offered also the opportunity to test the wind tunnels, which have been rebuilt between 1960 and 1970, thus step by step measurements, from subsonic to hypersonic speed, could be made (Fig. 4, Fig. 5, Fig. 6).

2. Preliminary Work Regarding Re-Entry Problems

In 1966 extensive theoretical investigations started regarding the configuration of re-entry vehicles. The first comprehensive computer programs in the field of aerodynamics and aerothermodynamics have been furnished. Then the first configuration of a lifting body configuration - LB 1 - (Fig. 7) has been elaborated to such a degree that wind tunnel measurements (Fig. 8) could be made. These wind tunnel measurements showed that, in particular, the lateral stability was insufficient, which necessitated improvements of the stabilizers. Further developments and improvements led to the version LB 10 (Fig. 9), which was also tested in the wind tunnel. The lateral stability was, indeed, improved, but further modifications were necessary, thus, finally, the configuration LB 21 (Fig. 10) led to satisfactory results. LB 21 was tested under sub-, trans-, super- and hypersonic conditions. During all tests, LB 21 showed sufficient stability (Fig. 11). For subsonic flight an additional central fin became necessary, which had not been foreseen in the original concept.

Apart from the aerodynamic investigations, flight mechanical analyses have been conducted, utilizing comprehensive computer programs. The first subsonic flight tests with a 10 ft. free-flight model (Bumerang) for parachute landing (Fig. 12) have been successfully completed off Heligoland (North Sea/Germany) and Sardenia (Mediterranian/Italy) (Fig. 13, 14, 15). The flight tests and their evaluation showed an excellent flight behavior for a center of gravity location at 52 %. The results of the flight tests exceeded, particularly in the case of high angles of incidence, all expectations with regard to the flight quality

The Fig. 16 - 17 show the recuperation phase of the lifting body "Bumerang".

For hypersonic flight we regarded aerothermodynamic investigations as very essential. Therefore, computer programs were established for the calculation of temperature distributions on the flight vehicle; moreover, corresponding wind tunnel measurements have been made (Fig. 18). In addition to these investigations, first steps towards the development of a re-usable thermal insulation system were made, especially regarding the hot nose region. (Fig. 19, 20, 21). Various materials on the basis of ceramics were tested in the exhaust of a rocket in a horizontal test stand and evaluated.

All these activities were directed towards the construction and testing of a re-entry vehicle of approximately 3.10 m length and a weight of approximately 600 kg - to establish a basis for a potential future design of a space shuttle system.

When in 1969 the first news about an American Space Shuttle arrived and the American invitation for a cooperation was received, there were already existing teams, at least in Germany, with considerable experiences in this field. It may well be that our national program, which foresees subsonic to supersonic free flights in the following years, will be reduced or even stopped in favor of a full participation in the Space Shuttle program.

These were, in general, the background and prerequisites, which have led to our involvement and participation in the US Space Shuttle Program.

3. Cooperation with MDC in the Space Shuttle Phase B.

The objective of our cooperation with MDC during Phase B was to obtain in-depth first-hand impressions of the problems related to the Space Shuttle. Only if the real problems are identified, precise ideas can be conceived, as to the contributions Europe is factually able to make - and ought to make. An effective cooperation had, therefore, to be established, in order to become really well acquainted with the new problems.

This goal was achieved in the following manner:

a) Full integration of ERNO personnel into the MDC project teams (Fig. 22), where our team leader was participating in all essential meetings;

b) Construction of wind tunnel models for wind tunnel measurements in Germany and preparation of free-flight tests on an orbiter model;

c) elaboration of proposals, as to which parts can be built in Europe.

Thus effective contributions have been made during Phase B, carefully avoiding duplication of work.

Furthermore, it was demonstrated that, on the other side of the Atlantic, wind tunnel models (Figs. 23 and 24) can be built in very short periods of time, and wind tunnel tests data can be

transmitted quickly and efficiently. These tests have been made at (Fig. 25) the DFVLR (Deutsche Forschungs- und Versuchsanstalt für Luft- und Raumfahrt = German Research and Test Establishment for Aeronautics and Astronautics) in Porz-Wahn and, later, in Göttingen. The test data were transmitted daily by telex.

The following test programs have been performed:

- 6-component measurement with 3 alternate wing configurations and 2 different vertical tails in the DFVLR low speed tunnel;

- 6-component measurements with engine simulation;

- flow field visualizations;

- boundary layer measurements;

- at present, preparations for transsonic measurements are under way.

Additional free-flight tests will support the aerodynamic and aeromechanic investigations in critical flight regimes (Fig. 26).

Apart from this immediate support during Phase B, our most essential aim, namely the "determination of potential German or European orbiter components", has been consistently pursued. Speaking in more detail, the work performed has been based on the following philosophy; after an initial cooperation period of about 6 months, a carefully selected additional group was assigned to MDC, to identify orbiter structural components, which could realistically be built in Europe or Germany, respectively, within the time schedule and on the basis of the technology requirements. This second team, which consisted of specialists in the fields of manufacturing, design, materials and structures, selected the following components: (Fig. 27)

- Vertical Tail
- Payload Door
- Nose Section
- Wing Structure (as a joint European project).

A corresponding report was submitted to the Federal German Ministry of Education and Science, and, in October 1971, a presentation of the preliminary results has been made.

The careful selection of components, regarding the existing technical and financial potentials, has considerably strengthened the credibility that a substantial contribution is feasible, especially, since the sizes of the components selected are of the same order of magnitude as the components for the European Airbus (Fig. 28, 29)

4. Conclusion

The example of the ERNO-VFW-FOKKER activities should serve to demonstrate the work so far done and the potentials existing in Europe for a Space Shuttle participation.

From the technical point of view, a European, respectively, German participation should come to existence. This necessitates a participation in the orbiter development with regard to technology, management and experience. A participation would , furthermore, enable Europe or Germany to contribute experiences in the fields of aerodynamics and aerothermodynamics.

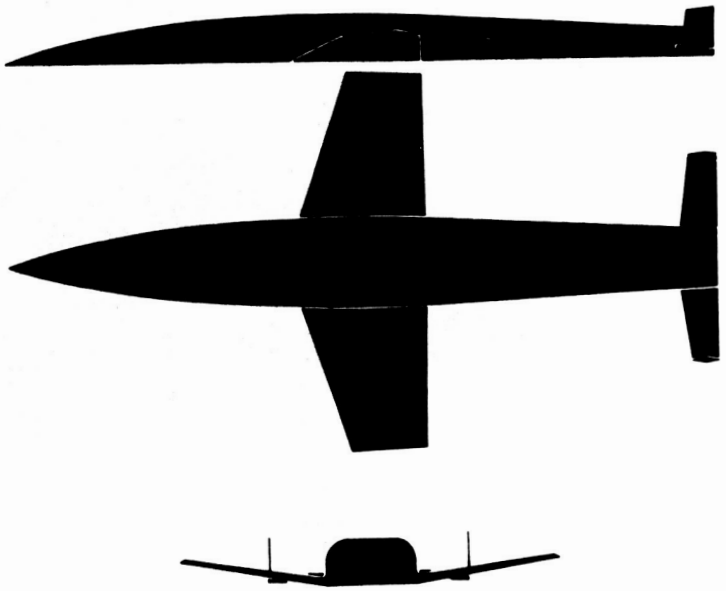

FIG. 1 E. SÄNGERS CONCEPT OF A SPACE GLIDER (1944)

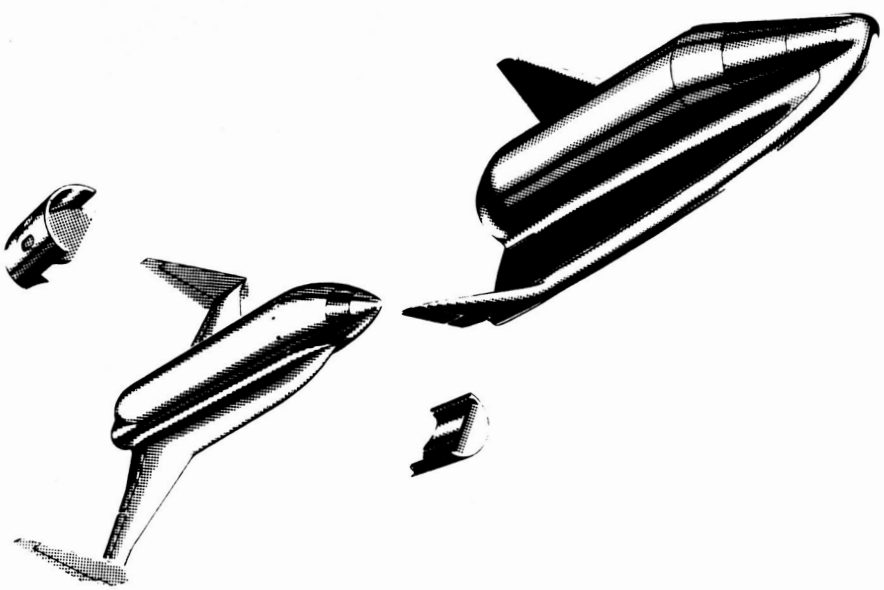

FIG. 2 ERNO SPACE SHUTTLE CONCEPT (1963)

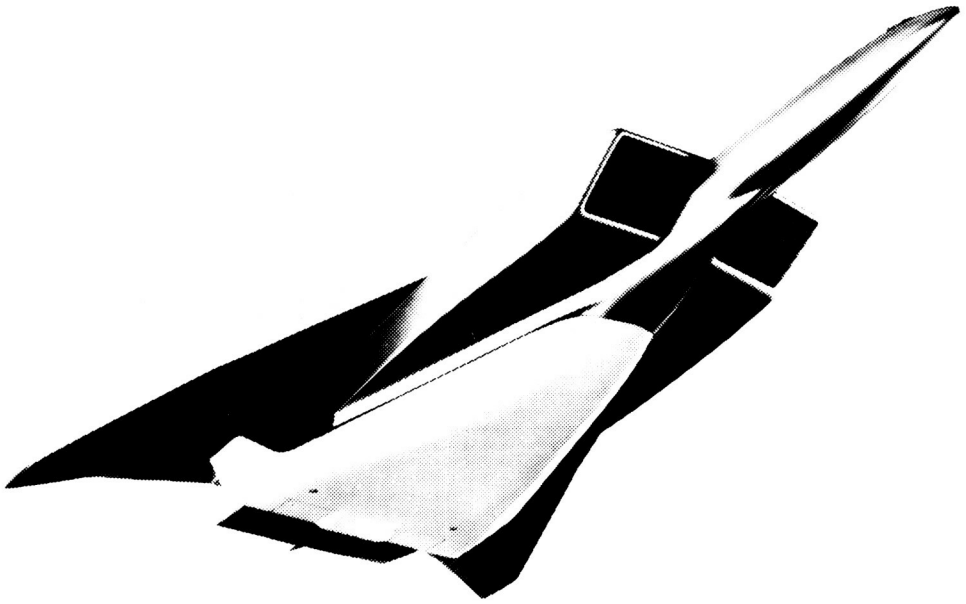

FIG. 3 NA-SNECMA- ERNO HORIZONTAL TAKE-OFF
SPACE SHUTTLE CONCEPT 1966

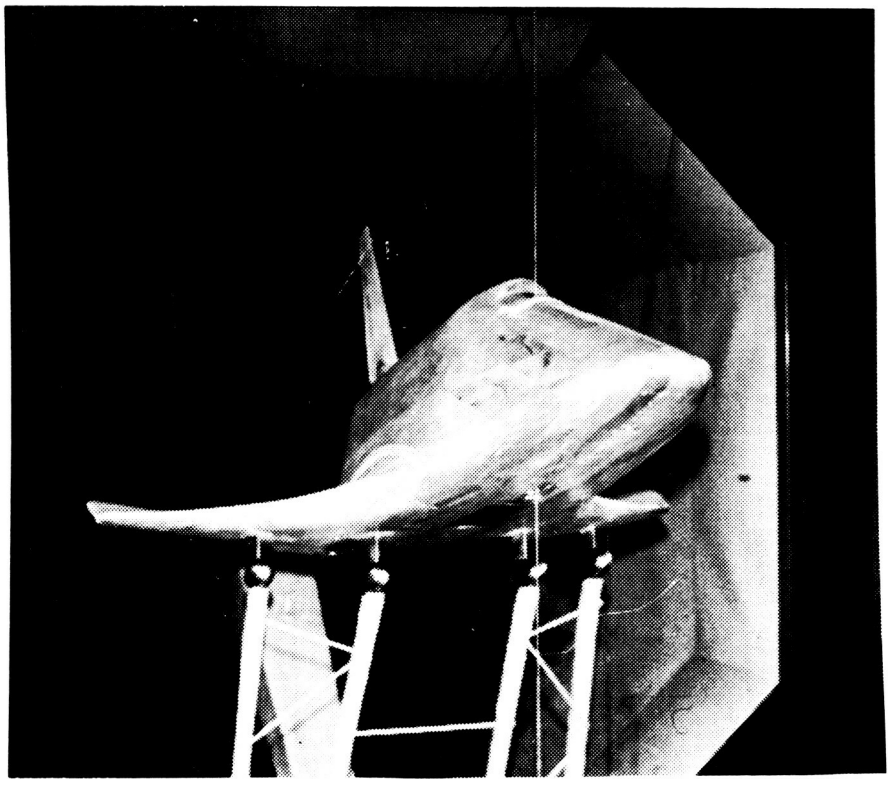

FIG. 4 SUBSONIC WIND TUNNEL DFVLR PORZ-WAHN

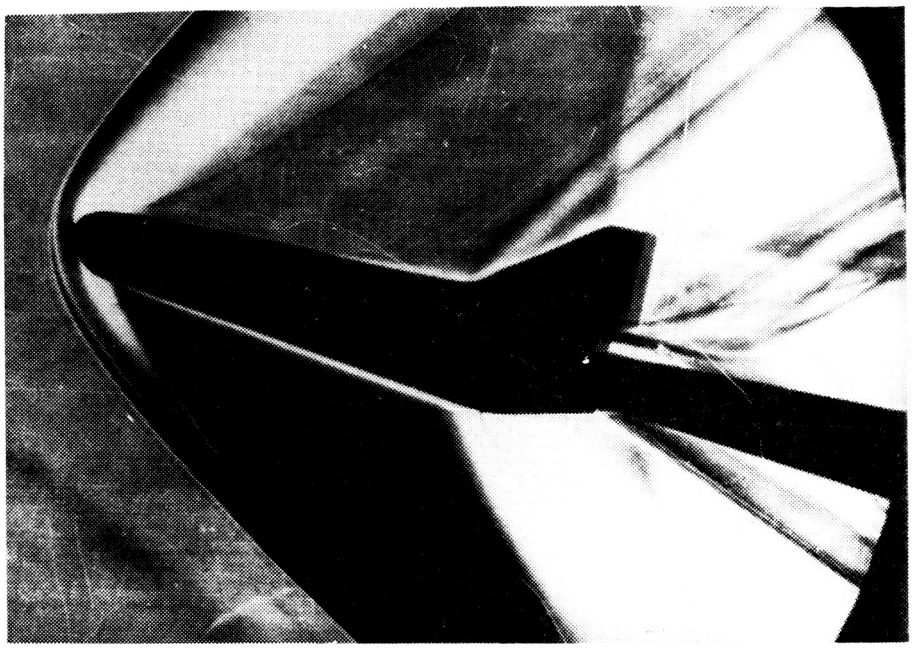

FIG. 5 TRISONIC WIND TUNNEL DFVLR- PORZ-WAHN

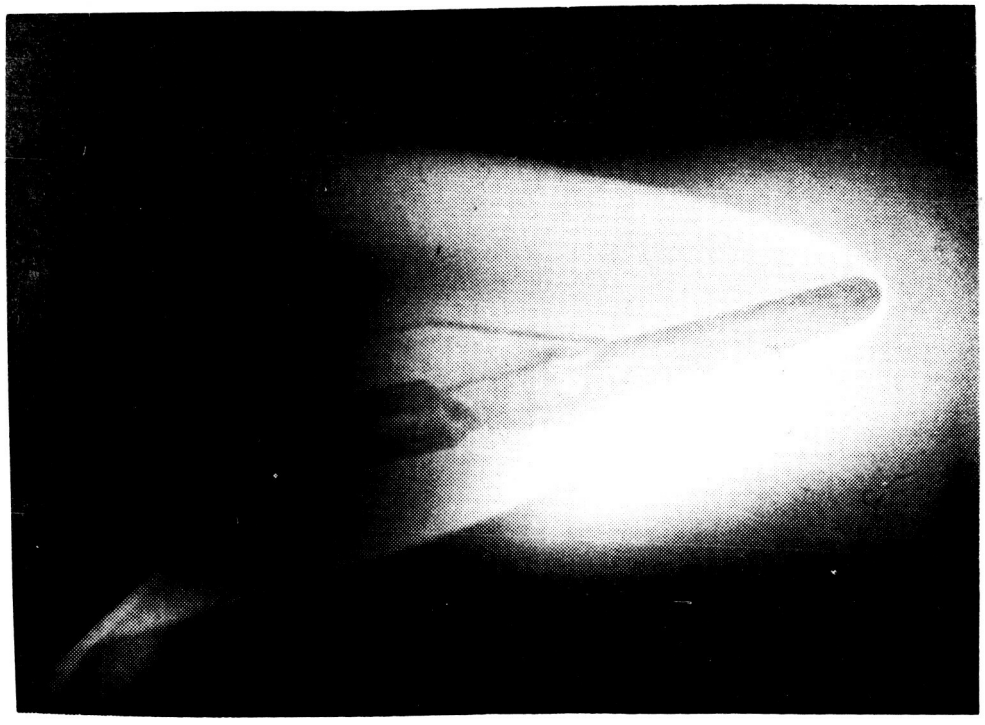

FIG. 6 HYPERSONIC WIND TUNNEL
DFVLR-AVA-GÖTTINGEN

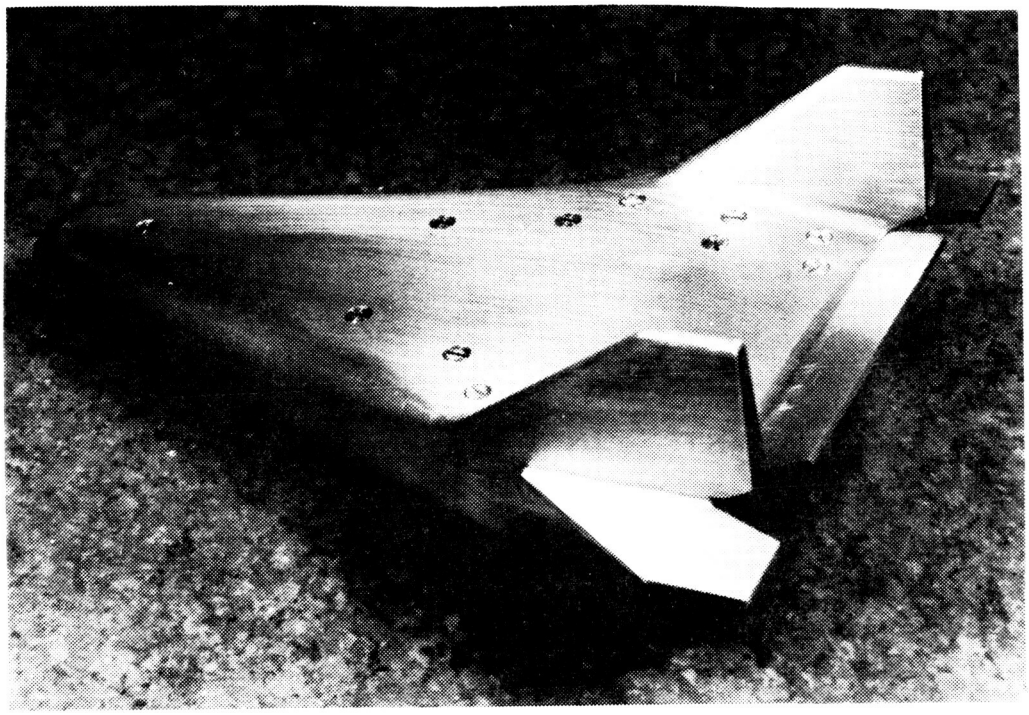

FIG. 7 LIFTING BODY CONFIGURATION LB-1

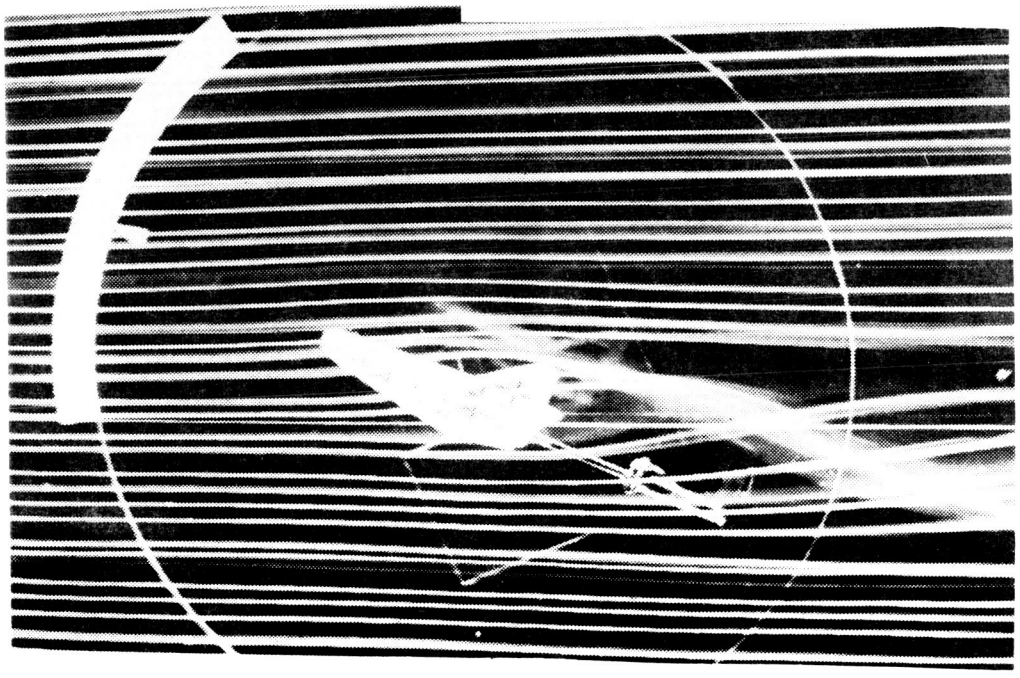

FIG. 8 SMOKE TUNNEL MEASUREMENTS
ERNO-VFW/FOKKER

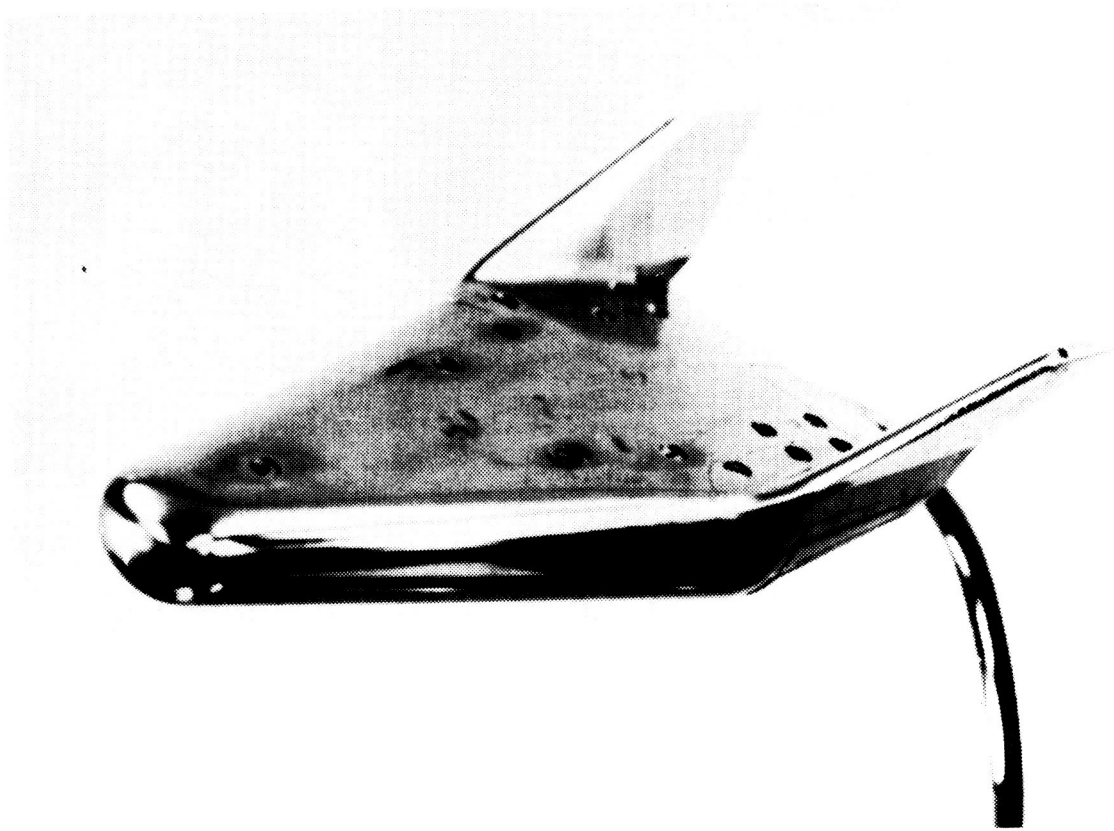

FIG. 9 LIFTING BODY CONFIGURATION LB 10

FIG. 10 LIFTING BODY CONFIGURATION LB-21

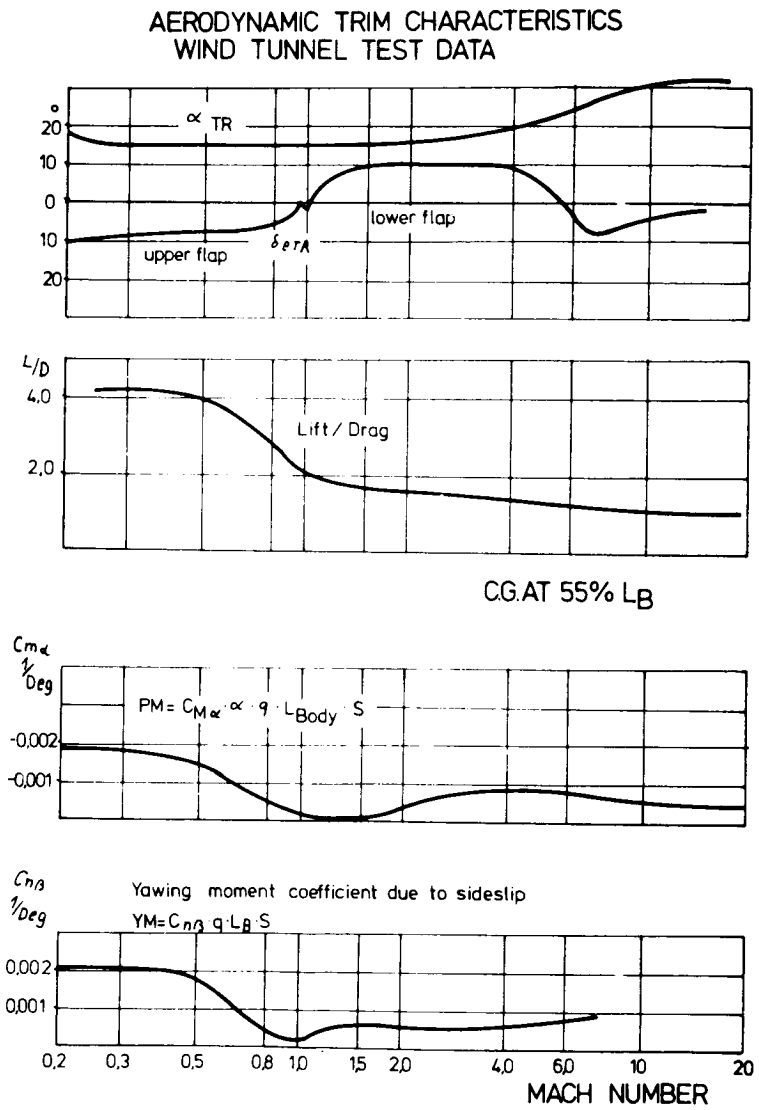

FIG. 11 LB-21 WIND-TUNNEL-TEST-DATA

FIG. 12 FREE-FLIGHT-MODEL LB-21 BUMERANG

FIG. 13

FIG. 14

FIG. 15

FREE-FLIGHT OF L.B 21 BUMERANG

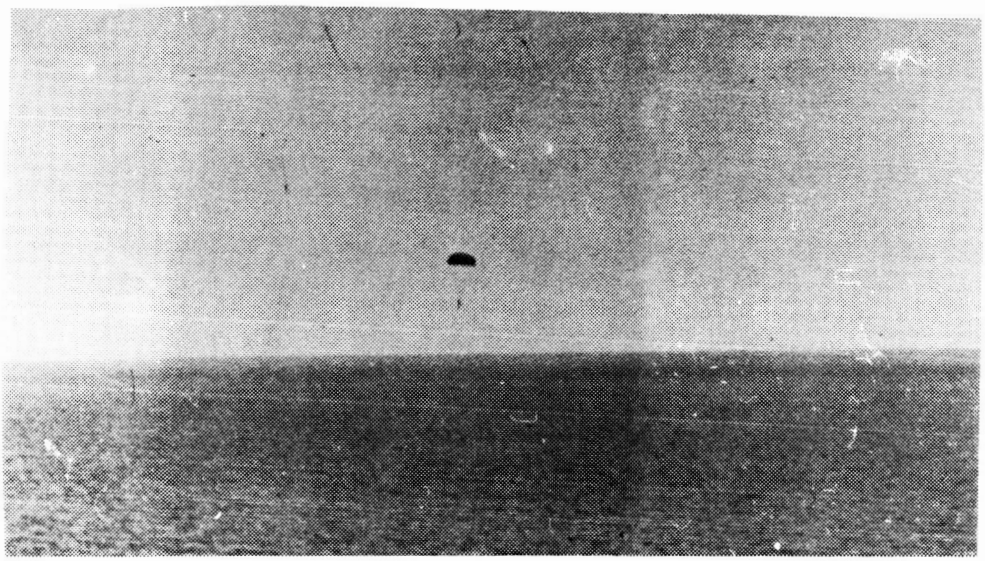

FIG. 16 LB-21 BUMERANG ON A PARACHUTE SYSTEM

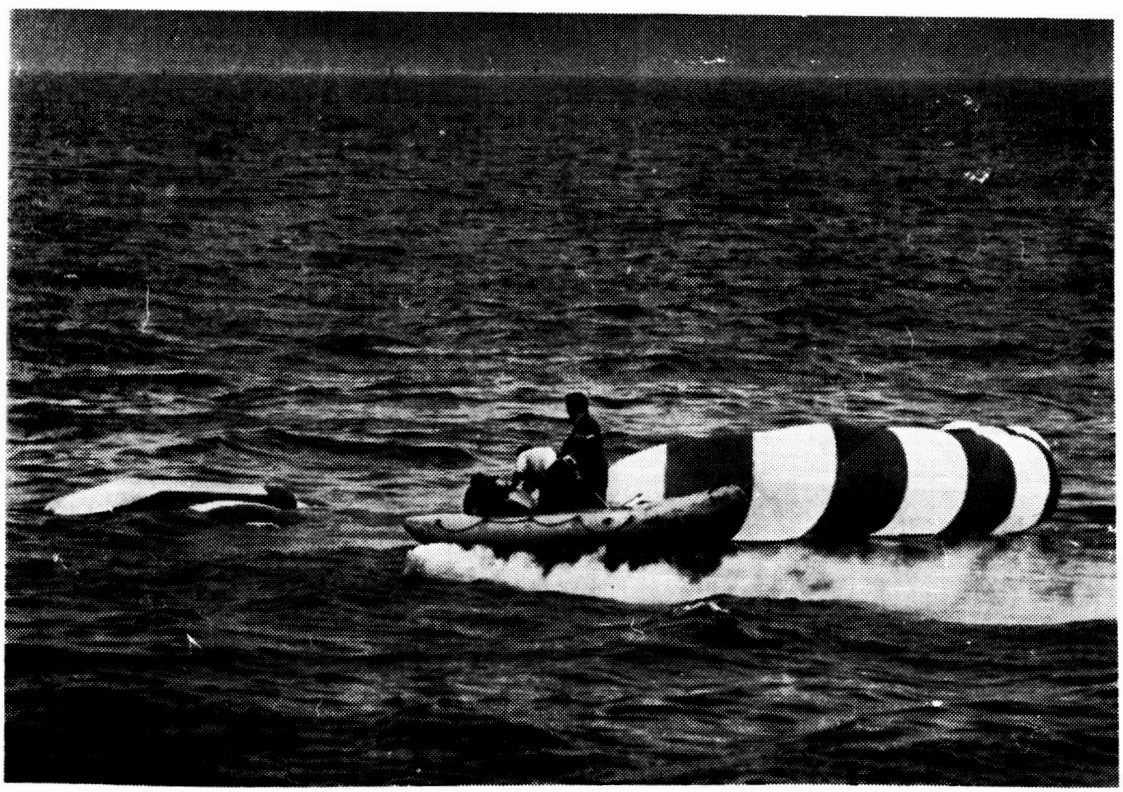

FIG. 17 RECUPERATION OF LB-21 BUMERANG

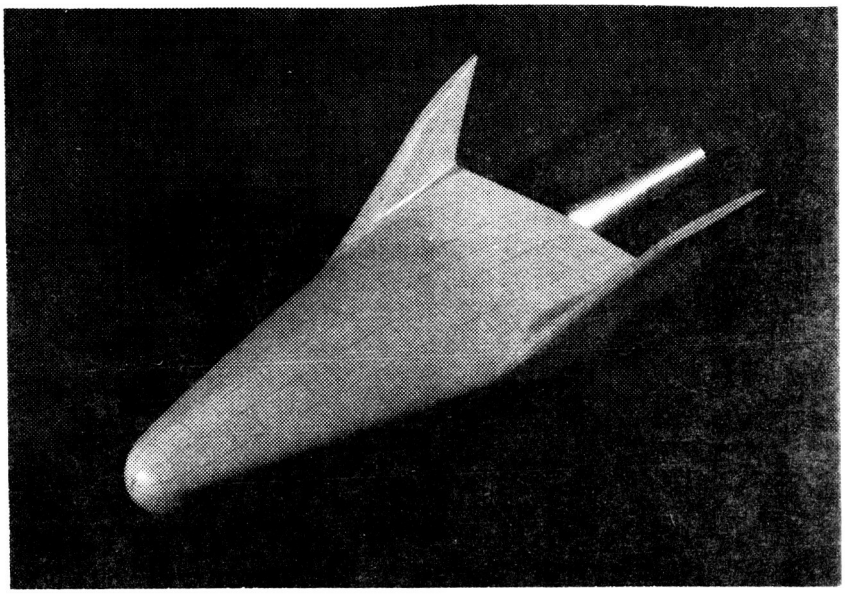

FIG. 18 LB-21 SILICON RUBBER MODEL FOR THERMAL MAPPING TESTS

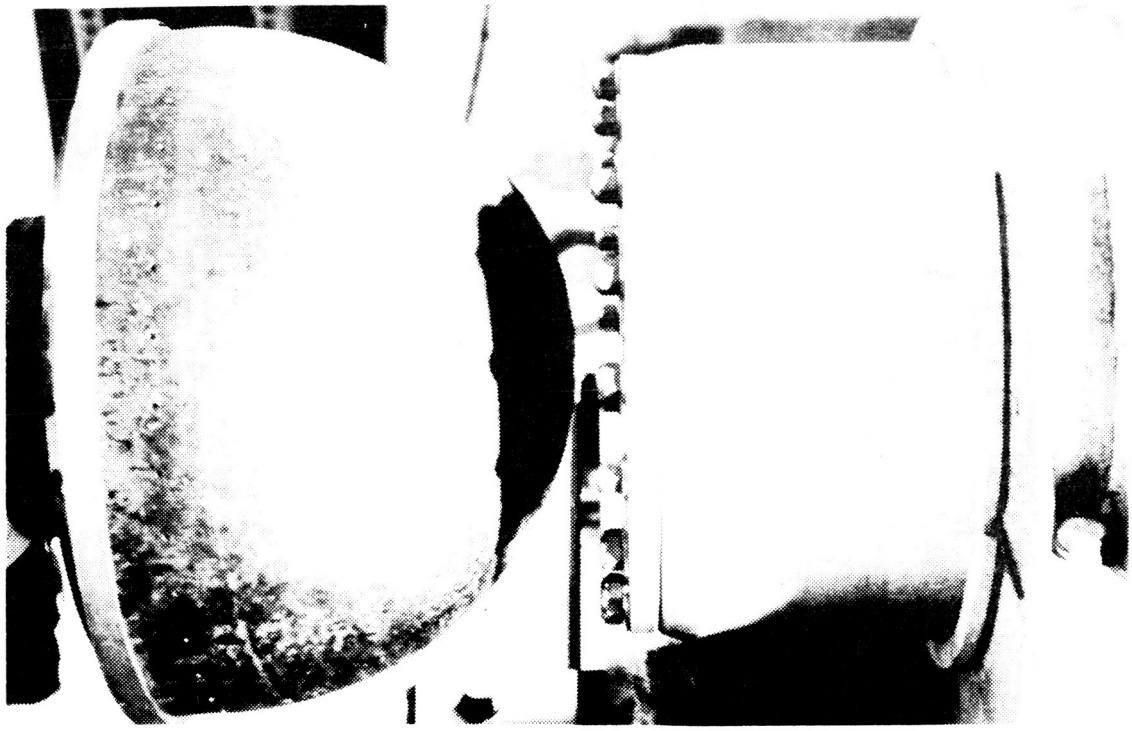

FIG. 19 CERAMIC TPS ON ROCKET TEST STAND

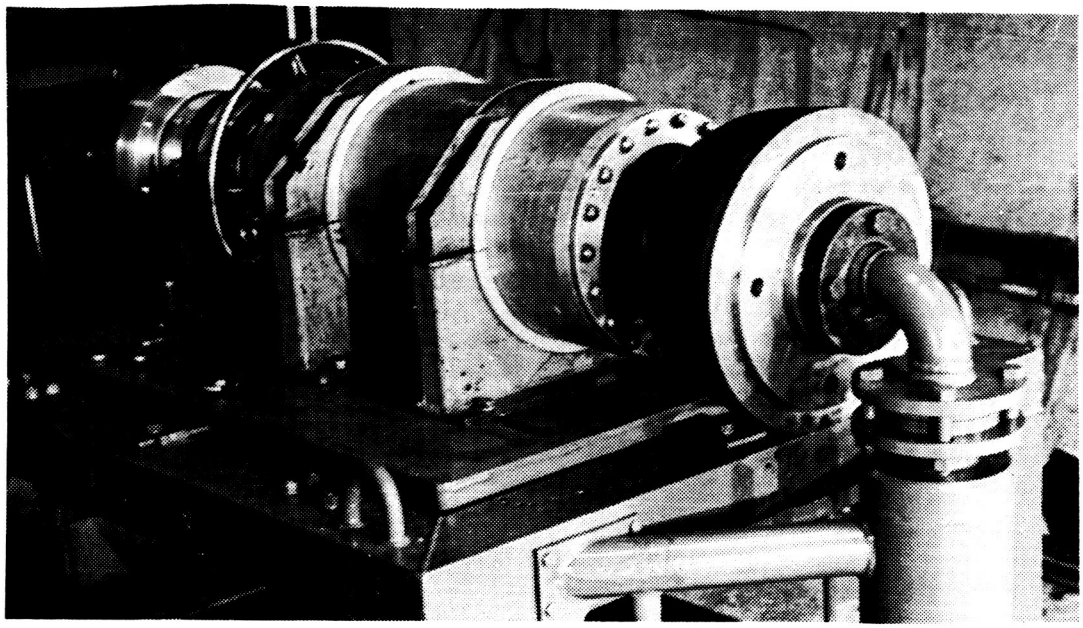

FIG. 20 GENERAL VIEW OF THE EXPERIMENTAL ROCKET SET UP FOR TPS-TEST

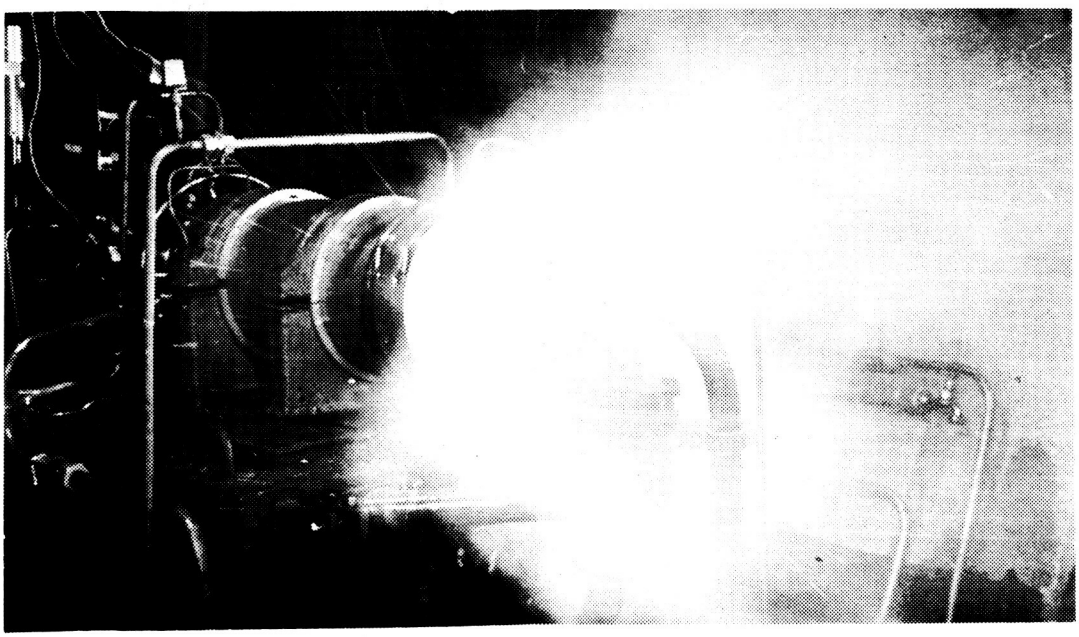

FIG. 21 TPS TEST RUN

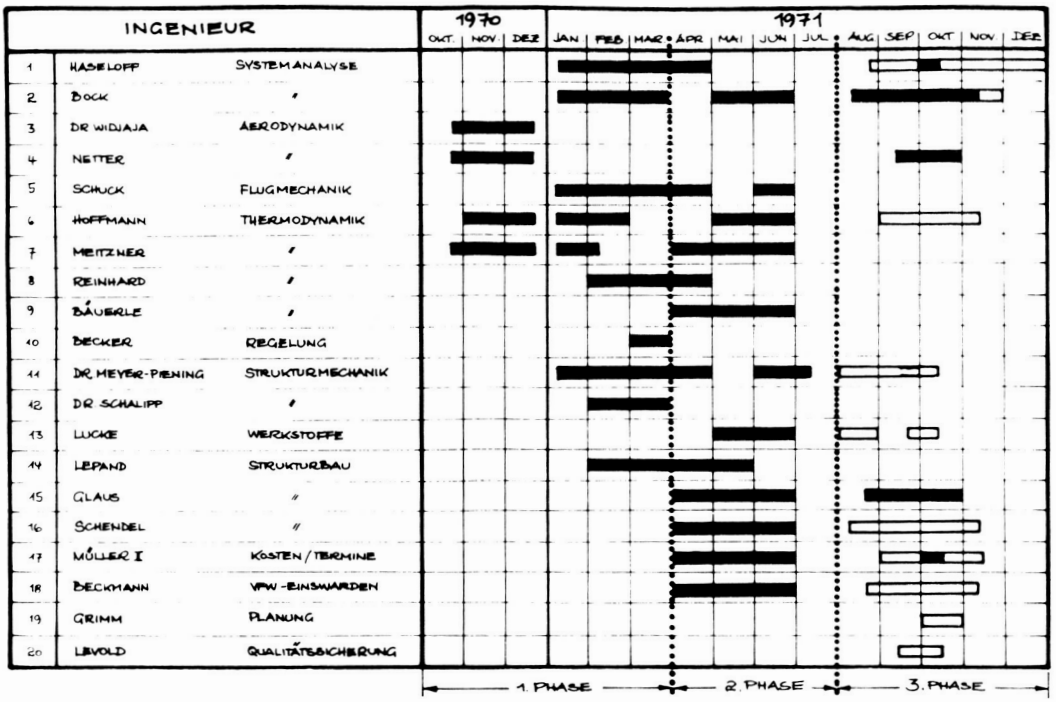

FIG. 22 ERNO PERSONNEL ASSIGNED TO THE MDC SPACE SHUTTLE PROJECT TEAM

FIG. 23 ERNO SUBSONIC WIND TUNNEL MODEL OF THE MDC ORBITER

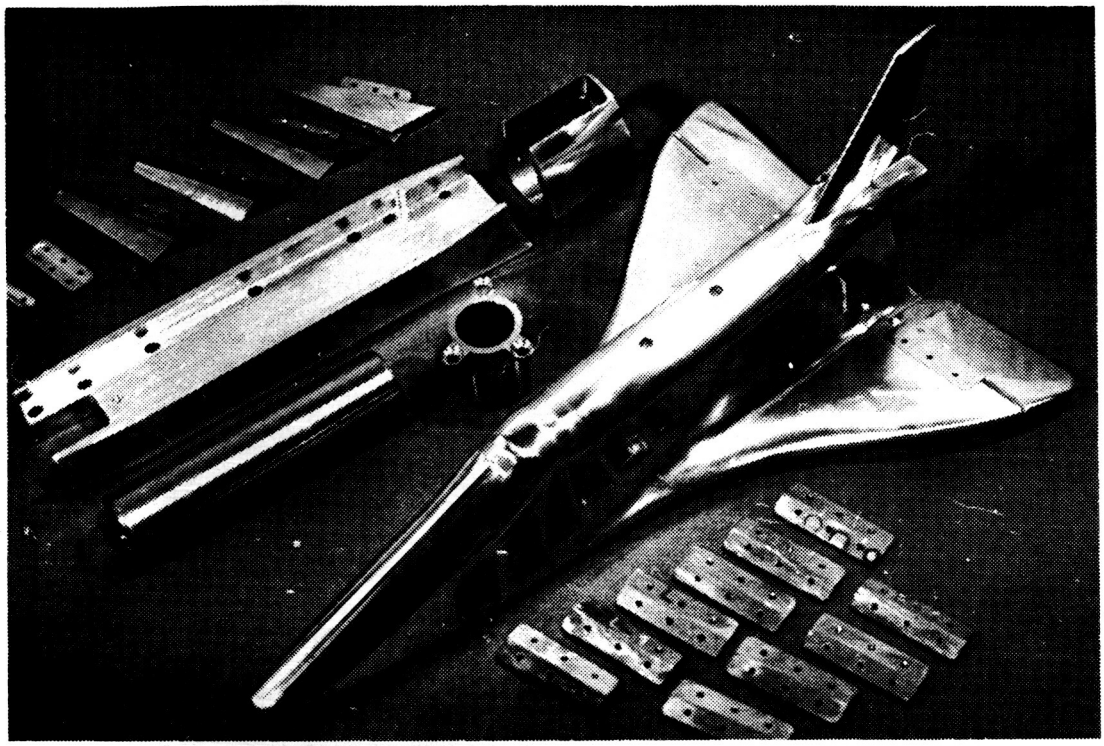

FIG. 24 ERNO TRANS-/SUPERSONIC WIND TUNNEL MODEL OF THE MDC ORBITER

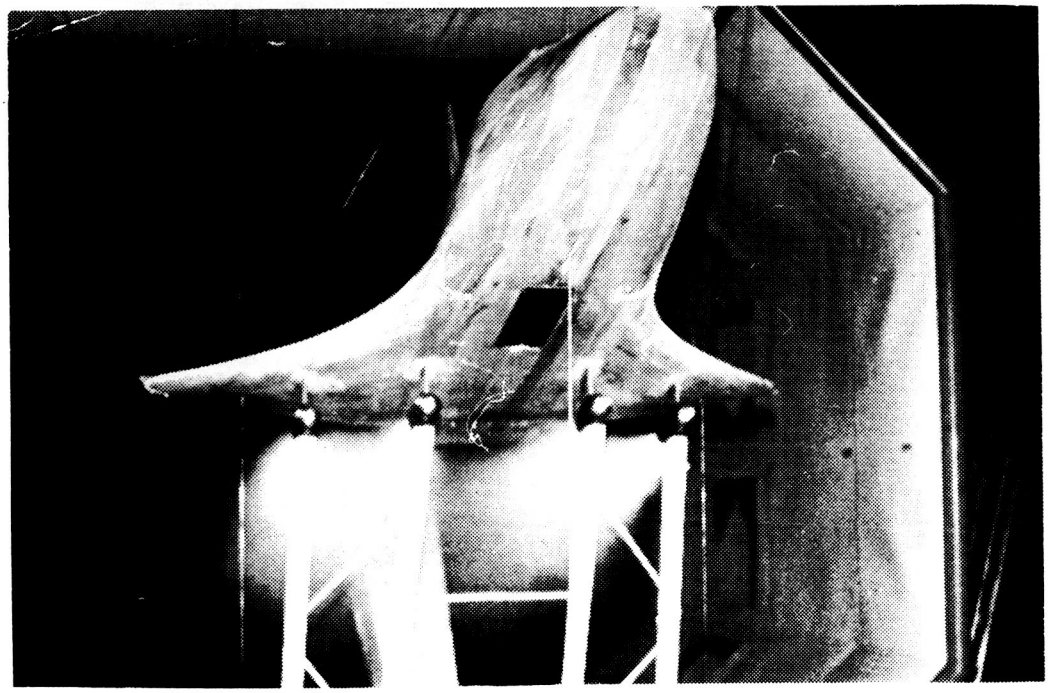

FIG. 25 SUBSONIC WIND TUNNEL TEST WITH ABES SIMULATION AT DFVLR PORZ-WAHN

FIG. 26 SUBSONIC FREE-FLIGHT MODEL (MDC-ORBITER)

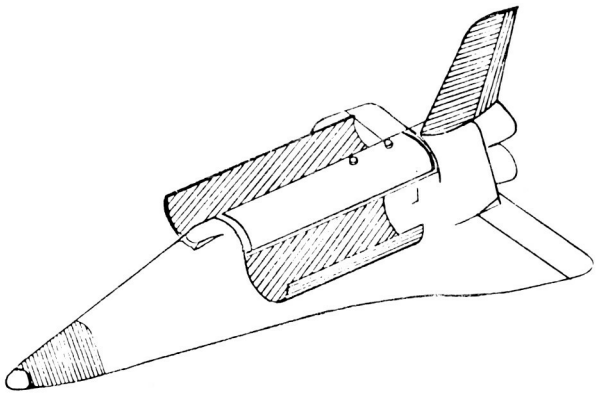

FIG. 27 SELECTED GERMAN STRUCTURE COMPONENTS ON ORBITER

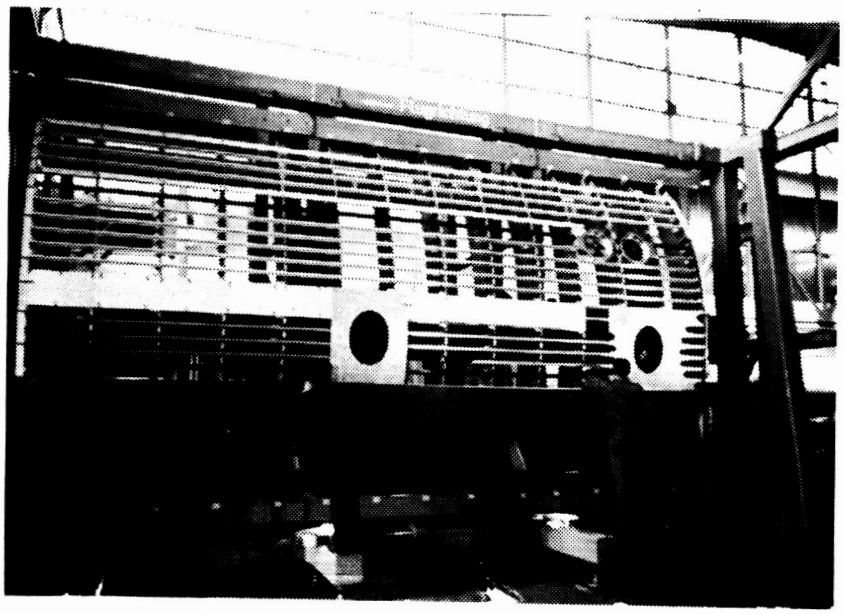

FIG. 28 EXAMPLE OF A SUBASSEMBLY JIG
(AIRBUS A 300 B)

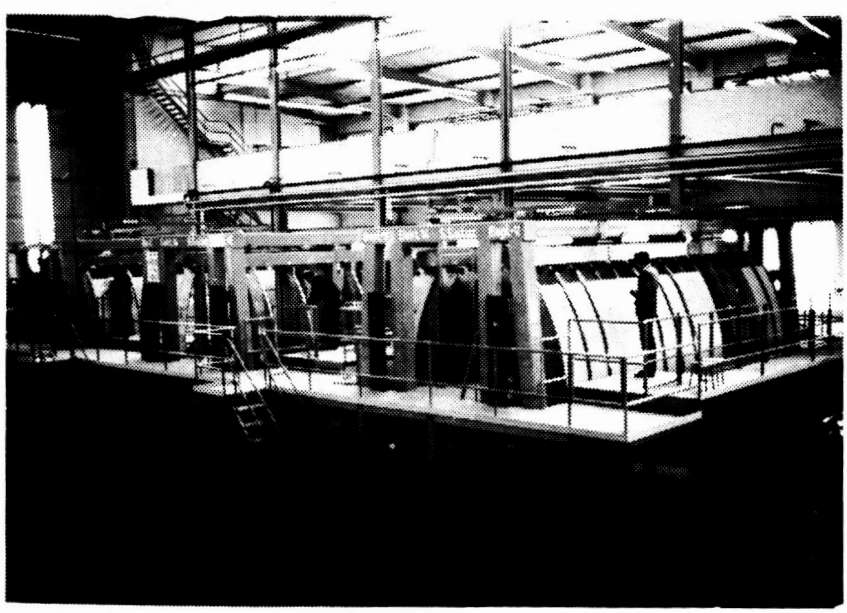

FIG. 29 SKIN PANEL ADAPTION AND DRILL JIG
(AIRBUS A 300 B)

AERODYNAMICS SESSION

SUMMARY REMARKS OF SESSION CHAIRMAN

By Beverly Z. Henry
NASA Langley Research Center

I would like to add a few remarks of my own – some of a summary nature – and others perhaps more in the nature of a personal assessment of the current status from an aerodynamic point of view. I think the papers presented in the session this morning are reasonably representative of the aerodynamic status of the shuttle. I think the papers also indicate a reasonably mature understanding of most of the problems from the aerodynamicists' viewpoint.

We have, in the past 2 years or so accumulated an impressive data base. So impressive that it's assimilation and application becomes perhaps a problem in itself. Without the SADSAC data system this problem may well have been an untenable situation.

Although configurations sometimes vary in significant detail, the generic class – particularly the orbiters – remains the same, and the data base is appropriate. There still remains, of course, more than adequate room for innovations and unique solutions for troublesome problems.

I think the question one should always ask at the conclusion of a conference such as this is – are we ready to proceed with a vehicle? To me, the answer is yes. This answer is particularly firm in my mind relative to the orbiter. I think the HO type orbiter as represented by

the O4OA is a reasonable point of departure; it can, with the inevitable modifications, do the mission, and I think, do it very well. There are known problem areas and some question marks, but we understand the fundamentals which lead to the solutions. Many of these solutions will not be forthcoming in finite form until the concept and configuration are fixed; then we can do the detailed work to provide the necessary answers – a transition, if you will, from parametrics to specific, detailed examinations.

We have improved our techniques for obtaining experimental information as indicated by Orlik-Rückemann's paper and, as you will see, in papers to be presented later today. We are approaching an understanding of the various loadings on the vehicles and the application of the various control modes.

Papers such as that of Reding and Ericsson have raised caution flags as to some problems which can arise, but at the same time have demonstrated an understanding of the source of these problems. With this understanding, comes a solution. Similarly, potential problems such as discussed by Orlik-Rückemann, et al. relative to the dynamic effects during separation on $C_{m_{\dot{\theta}}}$ – the possible "lock in" of the oscillatory motions of the two vehicles – are possibly solvable by control surface setting and thrust vectoring – as will be discussed in a paper by Decker, et al.

Some areas requiring a better understanding were not discussed today, but hopefully will be in the next conference. Two of these areas come to mind:

(1) The effects of ablator surface roughness on the flying characteristics of the vehicles – as might be experienced in a Mark I – Mark II approach.

(2) The interactive effects of attitude control jet exhausts on the aerodynamic characteristics of the vehicles.

Ways are now being sought to examine these effects. We have to date utilized thousands of wind-tunnel hours in facilities across the country and in Europe. There have been uncounted parametric studies and analyses made. I think we know how to configure the vehicle.

Although many areas remain for improvement, when I ask myself the question – are we ready to proceed? I still get the answer – yes.